



Durham E-Theses

Understanding the properties and stabilities of emulsions

Day, James P.R.

How to cite:

Day, James P.R. (2009) *Understanding the properties and stabilities of emulsions*, Durham theses, Durham University. Available at Durham E-Theses Online: <http://etheses.dur.ac.uk/2127/>

Use policy

The full-text may be used and/or reproduced, and given to third parties in any format or medium, without prior permission or charge, for personal research or study, educational, or not-for-profit purposes provided that:

- a full bibliographic reference is made to the original source
- a [link](#) is made to the metadata record in Durham E-Theses
- the full-text is not changed in any way

The full-text must not be sold in any format or medium without the formal permission of the copyright holders.

Please consult the [full Durham E-Theses policy](#) for further details.

Understanding the properties and stabilities of emulsions

James P. R. Day

The copyright of this thesis rests with the author or the university to which it was submitted. No quotation from it, or information derived from it may be published without the prior written consent of the author or university, and any information derived from it should be acknowledged.

Department of Chemistry



February 2009



16 MAR 2009

for Laura

Abstract

Our knowledge of the behaviour of emulsions and the oil–water interface at the molecular level is relatively sparse when compared to the huge importance of these systems in everyday life. This thesis describes the development of several techniques that have the potential to extend this knowledge further.

Ellipsometry is exquisitely sensitive to density variations across a fluid–fluid interface, but the interpretation of the ellipsometric response from the oil–water interface, both in the absence and presence of adsorbed species, is nontrivial. The responses from the interface between simple linear alkanes and water suggest that these interfaces are more complex than the air–water interface. The results are indicative of a “drying layer” and a model based on the hard sphere repulsion of a hydrocarbon surface is developed to explain these results.

The conclusions from this study on the pristine oil–water interface are used as a basis for the interpretation of the ellipsometric response of a surfactant monolayer at the oil–water interface. The results suggest that the nonionic hydrocarbon surfactant $C_{10}E_8$ forms a disordered monolayer with partially-hydrated headgroups. The structure of this film is largely independent of the nature of the superphase; whether air, hexadecane or triolein.

The competitive adsorption of the milk proteins β -casein and β -lactoglobulin with $C_{10}E_8$ at the hexadecane–water interface is also studied. At low and high concentrations of $C_{10}E_8$, the measured ellipticity is indicative of an unperturbed protein and surfactant film, respectively. At intermediate concentrations, the measured ellipticity suggests a mixed surfactant/protein film.

Raman spectroscopies deliver considerably more data than ellipsometry, but the difficulties of delivering and collecting light from a buried interface require more sophisticated experimental engineering. An attempt is made to sandwich a 100-nm-thick oil film between water and silica in order to probe the oil–water interface by evanescent wave Raman scattering employing a visible excitation source. Unfortunately this procedure has proved unsuccessful to date.

The requirement for a thin oil film can be bypassed if the signal from the adsorbed species is enhanced. The design and construction of an ultra-violet resonance Raman microspectrometer is described to achieve this aim. This instrument also has the potential to probe proteins and peptides adsorbed in lipid bilayers.

The commissioning and development of a combined *in-situ* confocal Raman-tribometer is also presented. This instrument is capable of determining the composition of emulsions under shear within a soft elastohydrodynamic contact, as well as the morphology of the soft, deformed surface and the thickness of the lubricating film.

Acknowledgments

I am indebted to my supervisor, Professor Colin Bain, for his enthusiasm, insight, ingenuity and friendship throughout my degree. His guidance repeatedly served to reinvigorate my enthusiasm whenever things were not progressing. Thanks to him, I feel I have learnt an incredible amount during my time in the group, having studied a wide variety of topics and learnt to use many different techniques.

I thoroughly enjoyed working with Dr Eric Tyrode on the UV resonance Raman project. Eric is an incredibly enthusiastic and dynamic scientist and I hope that I have picked up at least some of his practical expertise.

During my three-month placement at Unilever, Colworth, I was fortunate enough to work with Dr Paul Pudney and Dr Jeroen Bongaerts. I am indebted to them for all their help and for allowing me to work on the tribo-Raman project. I am also thankful to Paul for all his hard work as my industrial supervisor, not least arranging for me to experience science in industry. I also thank Unilever itself for granting me a CASE award.

I am thankful to all the members of the Bain group in Durham and Oxford with whom I have worked over the past five years. There are too many to name individually, but I have enjoyed all our discussions, scientific and otherwise!

The importance of the love and support of my fiancée, Laura, my parents and my brother could not be adequately described in only a few lines, but I am utterly grateful to you all for everything.

Publications List

The following publications have arisen from the work described within this thesis:

1. “Ellipsometric study of depletion at oil–water interfaces”
J. P. R. Day and C. D. Bain
Physical Review E, **76**, 041601 (2007)
2. “*In situ* confocal Raman spectroscopy of lubricants in a soft
elastohydrodynamic tribological contact”
J. H. H. Bongaerts, J. P. R. Day, C. Marriott, P. D. A. Pudney and A.-M.
Williamson
Journal of Applied Physics, **104**, 014913 (2008)

Contents

1. INTRODUCTION	1
1.1. Food emulsions	1
1.2. Interfaces and surfactants	3
1.3. Proteins	7
1.4. Experimental studies of protein-stabilized emulsions	13
1.5. Emulsion formation, stabilization and coalescence	25
1.6. Thesis outline	28
2. THEORY	32
2.1. Introduction	32
2.2. Light and interfaces	32
2.3. Raman scattering	44
3. ELLIPSOMETRIC STUDY OF DEPLETION AT OIL-WATER INTERFACES	60
3.1. Introduction	60
3.2. Experimental	62
3.3. Results	67
3.4. Discussion	73
3.5. Conclusion	87

4. ADSORPTION OF SURFACTANTS AND PROTEINS TO THE OIL–WATER INTERFACE	92
4.1. Introduction	92
4.2. Experimental	93
4.3. Adsorption of C ₁₀ E ₈ to hexadecane– and triolein–water interfaces	94
4.4. Protein adsorption to the hexadecane–water interface	108
4.5. Surfactant and protein coadsorption	115
4.6. Conclusion	123
4.7. Outlook	124
5. DEVELOPMENT OF EVANESCENT WAVE RAMAN SCATTERING AT THE OIL–WATER INTERFACE	129
5.1. Introduction	129
5.2. Thin oil film concept and theory	132
5.3. Spin coating	136
5.4. Hydrophobing optical substrates	139
5.5. Outlook	149
6. DEVELOPMENT OF A UV RESONANCE RAMAN MICROSPECTROMETER	152
6.1. Introduction	152
6.2. Development of the optical bench	155
6.3. UV resonance Raman spectra from an unenhanced monolayer	182
6.4. Design of the prism prefilter	183
6.5. Spectrometer throughput and resolution	190
6.6. Truncated hemisphere design	191
6.7. Indolicidin adsorbed in a planar-supported lipid bilayers	192
6.8. Spatial filter	195
6.9. Comparison with other UV Raman spectrometers	196
6.10. Conclusion	198

7. CONFOCAL RAMAN SPECTROSCOPY OF LUBRICANTS IN A SOFT ELASTOHYDRODYNAMIC TRIBOLOGICAL CONTACT	201
7.1. Introduction	201
7.2. Experimental rig	205
7.3. Materials and methods	208
7.4. Confocality of the microscope objective	210
7.5. Single phase lubricants	213
7.6. Emulsions	223
7.7. Conclusion	230

Chapter 1

Introduction

1.1 Food emulsions

The ever-growing global population continues to drive increased food production. Allied to this increase, the market continually demands improvements in the taste, texture, shelf life and nutritional quality of food products. Furthermore, current estimates suggest 1–2% of adults and 5% of children in the US suffer from a food allergy and the prevalence of these allergies are rising [1]. All these drivers necessitate an increased understanding of the physical properties governing the behaviour of food during production, storage, intake and digestion.

Many of the most common foodstuffs consist of either droplets of oil dispersed in a continuous aqueous phase or water droplets dispersed in oil. These foods include dairy spreads and margarines, creams, cheeses, salad creams and salad dressings, cooking sauces, yoghurts and even ice-creams [2]. These heterogenous mixtures of oil and water are known as emulsions and are thermodynamically unstable with respect to separation into two continuous bulk phases. In this respect emulsions should be distinguished from microemulsions which *are* thermodynamically stable [3]. Phase separation of these food products is obviously undesirable to both the food industry and the consumer and consequently the emulsions must be kinetically stabilized by proteins and surfactants. These compounds adsorb to the oil–water interface, form films between the immiscible phases and serve to prevent coalescence, albeit by different mechanisms. Although a considerable amount of work has been done to understand the phenomenological aspects of emulsion stabilization, as warranted by the importance and ubiquity of these systems, relatively little is known about the behaviour of emulsifiers at the molecular level.

The overriding aims of this thesis are to use existing techniques and to develop new techniques that are capable of probing emulsifier films at the oil–water interface, in order to further our knowledge of the stability of emulsions. Ellipsometry has been used extensively at the air–water interface to quantify adsorption, to study adsorption



kinetics and, to a lesser extent, to help discern the structure of surfactant films (in conjunction with other techniques), but its application to the oil–water interface is in its infancy. I aim to develop the quantitative interpretation of the ellipsometric response from the oil–water interface in the presence and absence of adsorbed species. Previous studies have shown that even the pristine interface displays complex behaviour, so I will investigate these clean interfaces first before extending my studies to the adsorption of surfactants and proteins.

Vibrational spectroscopy can give much more structural detail about adsorbed protein or surfactant films, but because the interface is buried, using conventional external reflection or attenuated total internal reflection infrared spectroscopies is not trivial. Evanescent wave Raman scattering would give more detail about film structure than ellipsometry or tensiometry, however this technique has never been demonstrated at the oil–water interface. I aim to develop an experimental procedure to allow us to use Raman spectroscopy to probe surfactant and protein adsorption at the oil–water interface.

Ultraviolet resonance Raman (UVRR) spectroscopy has been used to amplify the Raman response from proteins and peptides in bulk solution but this technique has never been employed at any interface. In order to use this technique, I will have to build a UVRR microspectrometer with sufficient sensitivity to study the behaviour of adsorbed species. I subsequently intend to use this spectrometer to study the structure of peptides and proteins adsorbed in phospholipids bilayers and at the oil–water interface.

At a more applied level, the behaviour of food emulsions under shear is critical to the way in which these foods are appreciated by the consumer, but again most of our knowledge comes by extrapolation from friction data. Confocal Raman spectroscopy would deliver information about the behaviour of emulsion films under shear. The aim of this section of my work is to determine the composition of emulsions within a soft tribological contact.

In the remainder of this chapter, I will present an overview of the knowledge contained in the literature about the stabilization of emulsions. First I will present

general information about proteins and surfactants before focussing on various studies that highlight the suite of techniques currently used to investigate emulsions. I will then discuss the mechanisms of emulsion stabilization and breakdown in light of these studies. Finally I will describe the layout of the remainder of this thesis.

1.2 Interfaces and surfactants

An interface is the common boundary between two phases. In this thesis, I will use the term surface to indicate an interface between air and a condensed phase, and the term interface in all other cases. The lateral extent of these interfaces can be either macroscopic, such as the solid–solid interfaces in industrial bearings, or mesoscopic, such as the air–water and oil–water interfaces in foams and emulsions. The influence of this region on the properties of a system belies the relatively small number of molecules located at the interface compared to in the bulk. Some processes such as corrosion, adhesion, detergency and heterogenous catalysis can only occur at interfaces, whereas emulsions and foams enclose large interfacial areas within relatively small volumes.

Interfacial properties differ markedly from bulk properties. Molecules close to an interface experience anisotropic intermolecular forces because they are surrounded by fewer near neighbours than in the bulk phase. The excess in the free energy, G , at the surface gives rise to an interfacial tension, γ , defined as [3]

$$\gamma = \left(\frac{\partial G}{\partial A} \right)_{T,p,n_i} \quad (1)$$

where A is the interfacial area, T is the temperature and p is the pressure.

The theory of van der Waals elucidates the behaviour of the bulk phases as they approach the interface. This theory uses thermodynamic considerations to describe the density profiles, $\rho(z)$, of each bulk phase at the interface, as follows [4]. $\psi(z)$ is defined as the free energy surface density as a function of the interface normal, z . The variation of ψ as a function of the density is shown in figure 1.

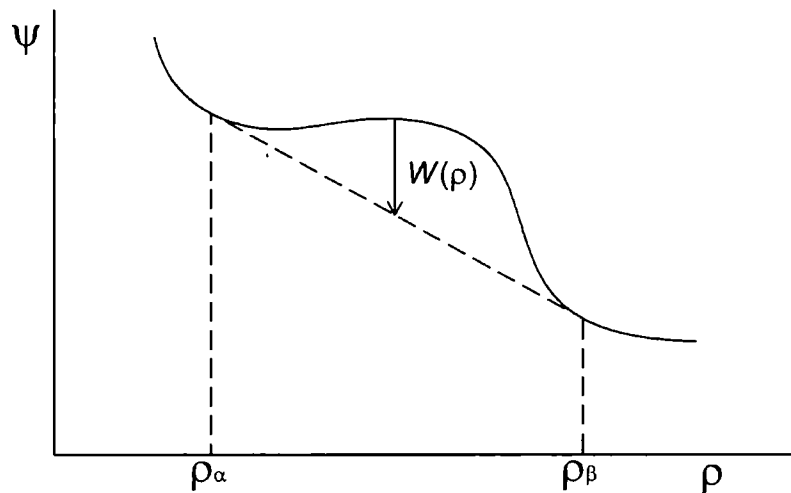


Figure 1. Free energy surface density and the common tangent construction. Adapted from ref. [4].

The common tangent construction depicted in figure 1 gives the densities of the adjacent phases α and β . A further free energy functional, $W(\rho(z))$ is defined as the difference between the common tangent and $\psi(z)$.

There is an excess in the free energy surface density, $\Psi(z)$, due to inhomogeneity at the interface compared to the value that would be expected if the bulk phases met unaltered, $\psi_{\alpha,\beta}$. This excess is defined to be [4]

$$\Psi(z) = \psi(z) - \psi(\rho_{\alpha,\beta}) \quad (2)$$

With the Gibbs dividing surface chosen so that there is no net adsorption, the surface tension is given by [4]

$$\gamma = \int_{-\infty}^{\infty} \Psi(z) dz \quad (3)$$

If $\Psi(z)$ is equivalent to $-W(\rho(z))$ alone, the surface tension vanishes and the density profile is a step function, as shown in figure 2(a). This picture is physically unreasonable and consequently van der Waals augmented $\Psi(z)$ with a square-density-gradient term, such that [4]

$$\Psi(z) = -W[\rho(z)] + \frac{1}{2}m\left(\frac{d\rho}{dz}\right)^2 \quad (4)$$

where m is a coefficient that is independent of the density gradient. In contrast, if $\Psi(z)$ was solely dependent upon the square-density-gradient the density profile would be infinitely diffuse (see figure 2(b)). The combination of these terms generates an interface of non-zero but finite thickness over which the bulk properties change between their limiting values (see figure 2(c)).

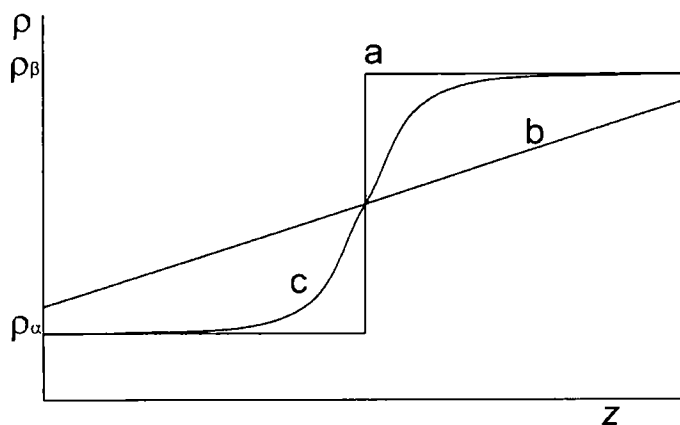


Figure 2. Density profiles arising from the three free-energy functionals described in the text. Adapted from ref [4].

For an optically sharp surface such as the oil–water interface, the density profile and associated parameters like the refractive index change between their limiting values over a few Ångstroms. In contrast, as a system tends towards the critical point, the thickness of the interface tends to infinity [5].

The behaviour of interfaces is typically controlled by molecules named surfactants. The term surfactant is a contraction of *surface active agent* [6] and describes the ability of these molecules to adsorb to an interface and alter its properties. The simplest surfactants in aqueous solution are amphiphilic molecules comprised of a polar headgroup and a nonpolar tail. The polar section can be cationic, anionic, non-ionic or amphoteric whereas the nonpolar section can consist of hydrocarbon, fluorocarbon or polysiloxane groups [7]. Surfactants can adsorb to the oil–water

interface to form monolayer films and in some cases can cluster together in aqueous solutions above a distinct bulk concentration to form micelles. This concentration is termed the critical micelle concentration (cmc) and is characteristic to each surfactant. The formation of monolayers and micelles is driven predominantly by the hydrophobic effect, whereby the entropy of the solution is maximized when the fewest water molecules are organized into a solvent cage around the hydrophobic section of the surfactant. When a surfactant molecule adsorbs to an interface, it modifies the interfacial tension by reducing the anisotropy in the intermolecular forces. The link between the composition and free energy of the interface is provided by the Gibbs isotherm, which is derived as follows. A general change in the free energy of the system is given by [8]

$$dG = -SdT + Vdp + \gamma dA + \sum_i \mu_i dn_i \quad (5)$$

where S is the entropy, V is the volume and μ_i and n_i are the chemical potential and number of moles of component i . The excess free energy at an interface, G^σ , is the difference between the total free energy and the free energy of the adjacent phases, thus [8]:

$$dG^\sigma = -S^\sigma dT + \gamma dA + \sum_i \mu_i dn_i^\sigma \quad (6)$$

Equation 6 integrates at constant temperature to give [8]:

$$G^\sigma = \gamma A + \sum_i \mu_i n_i^\sigma \quad (7)$$

Equation 6 constrained at constant temperature and the derivative of equation 7 are compared to give the Gibbs isotherm [8]:

$$d\gamma = \sum_i \Gamma_i d\mu_i \quad (8)$$

where the surface excess, Γ , is defined as n_i^σ/A ; the surface density of a component at the interface compared to the amount expected if the bulk phases continued unchanged up to the interface. For a single component surfactant solution at a concentration, c , the change in the chemical potential is given by $d\mu = RTd \ln c$ for

dilute solutions, where R is the gas constant. The interface, in the form of a Gibbs dividing surface, can be located arbitrarily. Under the approximation that only the surfactant accumulates at the interface, the surface excesses of the bulk phases are zero and equation 8 simplifies to [8]

$$\Gamma = -\frac{1}{kRT} \left(\frac{\partial \gamma}{\partial \ln c} \right)_T \quad (9)$$

where k is the number of species per surfactant molecule (e.g. $k = 1$ for nonionic surfactants and $k = 2$ for 1:1 ionic surfactants). Thus the surface excess can be determined directly from a surface tension isotherm.

Many proteins are also surface active. The charge distribution on the protein's surface is heterogenous, with a distribution of hydrophobic and hydrophilic patches. Furthermore proteins are also capable of changing their morphology upon adsorption. Consequently they behave differently to surfactants at interfaces. These molecules will now be described in more detail.

1.3 Proteins

Proteins are essential to life and play a wide variety of roles within the body. Structural proteins such as keratin, collagen and elastin support biological tissue; enzymes catalyze chemical reactions; transport enzymes such as haemoglobin carry small molecules around the body; immunoglobulins protect the body from foreign bacteria and viruses and hormones coordinate actions between different cells [9, 10]. Proteins are constructed within cells from a set of twenty naturally-occurring α -L-amino acids. Nine of these amino acids (the essential amino acids) cannot be synthesized by humans [10] and thus along with water, carbohydrates, lipids, vitamins and minerals, proteins are an essential constituent of diet.

The generic structure of an α -L-amino acid is shown in figure 3.

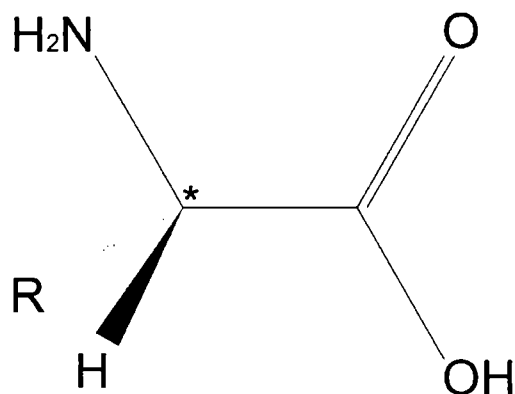


Figure 3. Generic structure of an α -L-amino acid, with side-chain R.

The side-chain, R, differs for each amino acid, and except in the case of glycine, the carbon atom marked by an asterisk is a chiral centre. Each side-chain has different physico-chemical properties but the amino acids can be conveniently classed into groups depending on the nature of the side-chain. The twenty amino acids, their side chains and classifications are given in table 1.


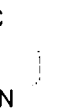
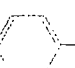
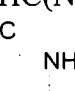
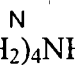
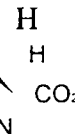
Name	3-letter symbol	1-letter symbol	Side-chain	Classification
Alanine	Ala	A	CH ₃	Hydrophobic-aliphatic
Isoleucine*	Ile	I	CH(CH ₃)CH ₂ CH ₃	
Leucine*	Leu	L	CH ₂ CH(CH ₃) ₂	
Valine*	Val	V	CH(CH ₃) ₂	
Phenylalanine*	Phe	F	H ₂ C 	Hydrophobic-aromatic
Tryptophan*	Trp	W	H ₂ C 	
Tyrosine	Tyr	Y	HN 	
Asparagine	Asn	N	CH ₂ CONH ₂	Polar
Cysteine	Cys	C	CH ₂ SH	
Glutamine	Gln	Q	CH ₂ CH ₂ CONH ₂	Acidic
Methionine*	Met	M	CH ₂ CH ₂ SCH ₃	
Serine	Ser	S	CH ₂ OH	
Threonine*	Thr	T	CH(CH ₃)OH	
Aspartic acid	Asp	D	CH ₂ CO ₂ H	
Glutamic acid	Glu	E	CH ₂ CH ₂ CO ₂ H	
Arginine	Arg	R	(CH ₂) ₃ NHC(NH)NH ₂	
Histidine*	His	H	H ₂ C 	
Lysine*	Lys	K	 (CH ₂) ₄ NH ₂	Unique
Glycine	Gly	G	H	
Proline ^a	Pro	P		

Table 1. The twenty naturally-occurring α -amino acids. ^aComplete structure. *Essential amino acid.

Each protein or peptide comprises a distinct sequence of amino acid residues, however it is not merely the residue sequence that determines the functionality of a protein. The polypeptide chain is folded within a cell to generate a unique three-dimensional conformation. The morphology of a protein is conveniently split up into a hierarchy of structures. The primary structure of a protein consists of the amino acid sequence of the polypeptide chain. This sequence may also be cross-linked by

disulfide bonds between cysteine residues. The secondary structure refers to the arrangement of residues that are nearby to one another within the chain and is exemplified by the α -helix, β -sheet and β -turn structures. The α -helix is formed by intramolecular hydrogen bonding between the carbonyl oxygen of an amino acid and the amide hydrogen four residues ahead in the sequence. Consequently the α -helix is a right-handed spiral with a repeat distance of 5.4 Å or 3.6 residues [10]. The β -sheet is also formed by intramolecular hydrogen bonding between adjacent β -strands to form a pleated structure. The adjacent strands can run in the same direction or in opposite directions to give a parallel or antiparallel β -sheet, respectively. β -turns are used by the protein to make hairpin bends and are typically used to connect antiparallel β -strands. The β -turn is constructed by a hydrogen bond between a carbonyl group and the N–H group of the amino acid that is three residues ahead in the polypeptide sequence. The tertiary structure refers to the arrangement of residues that are far apart within the chain and gives rise to further folding. Finally, when the protein consists of more than one polypeptide chain, the arrangement of these subunits is termed quaternary structure. Proteins are typically classified as either globular proteins or fibrous proteins. Globular proteins exhibit pronounced folding and an approximately spherical shape, whereas fibrous proteins like collagen form extended rod-like or wire-like structures.

Milk proteins

It is apparent from the list of products above that the majority of food emulsions are derived from milk. Indeed, milk itself is an oil-in-water emulsion and is one of only two foods (along with honey) produced in nature whose sole function is sustenance. Milk consists of ~87% water, ~4% triglyceride fats and ~3% protein, with the remainder comprising lactose, salts, acids, dissolved gases and vitamins [11]. The pH of milk is 6.5–6.7 but acidifying milk to pH 4.6 causes precipitation. The precipitate contains the predominant class of proteins in milk: the caseins, whereas the supernatant contains the remainder, known as whey proteins. These two sets of proteins are significantly different and also stabilize emulsions by different mechanisms.

Caseins

Caseins make up ~80% of milk proteins [11]. There are several variants, namely α_{s1} -, α_{s2} -, β - and κ -casein. They behave like denatured globular proteins, with no distinct secondary structure, no tertiary structure and no disulfide bonds. This lack of structure is caused by the high number of proline residues. The cyclic structure of proline prevents rotation about the C–N bond and hence proline is restricted in the number of structures that it can form. Caseins are resistant to thermal denaturation as there is so little structure to unfold. The lack of structure also exposes a considerable number of hydrophobic residues to the water solvent. Caseins are also conjugated proteins, whereby the serine side-chains are esterified with phosphate groups. In milk the caseins interact with calcium phosphate and each other to form casein micelles which range in diameter from ~30–300 nm. In this work I use β -casein as a representative of the general characteristics of these proteins. β -casein consists of 209 residues and has a molecular weight of $\sim 25000 \text{ g mol}^{-1}$. It has a highly-charged N-terminal region containing the phosphoserine groups whereas the C-terminal region is very hydrophobic.

Whey proteins

The remaining 20% of milk proteins are the whey proteins [11]. These globular proteins exhibit considerably more structure than the caseins and can be denatured readily by heat. Furthermore this structure buries the majority of the hydrophobic residues inside the protein so the whey proteins are more soluble in water than the caseins and exhibit less interaction in their native state. In this thesis I use β -lactoglobulin. This protein makes up half of the whey protein fraction. It consists of 162 residues and has a molecular weight of $\sim 18,400 \text{ g mol}^{-1}$. It has two intramolecular disulfide bonds and a free cysteine residue and at physiological pH and room temperature it exists as a dimer [12]. The structure of β -lactoglobulin is shown in figure 4.

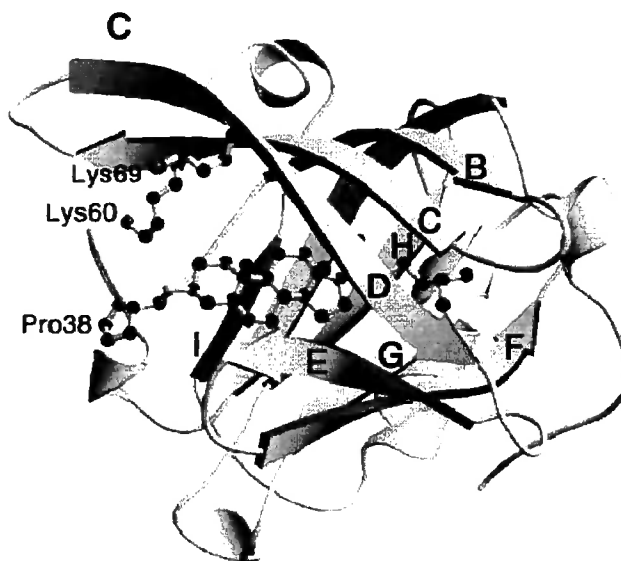


Figure 4. Structure of β -lactoglobulin. In this image the protein is complexed to cholesterol, which is bound in the calyx. Reproduced from ref [13].

Eight β -strands (A–H) are collected into a calyx, or β -barrel. A ninth β -strand (I) and a three-turn α -helix are located on the outer surface of the calyx. This calyx is a ligand-binding site and entry to the site is controlled by the loop between the E and F β -strands. The calyx is a conical cavity that is used to transport small hydrophobic molecules, and consequently β -lactoglobulin is a member of the lipocalin family [13].

1.4 Experimental studies of protein-stabilized emulsions

I will now present a brief literature review of studies concerning the stabilization of emulsions by proteins, both in the presence and absence of surfactants.

Interfacial tension studies of protein films

Recent advances in computers and image-capture technology have enabled researchers to move away from invasive, force-based techniques for measuring surface tension such as the Wilhelmy plate and du Nouy ring. Axial drop-shape analysis captures the cross-sectional image of a pendant or rising drop of one phase immersed in a bath of the other phase. The surface tension of the drop serves to contract the interface and this force is balanced by the excess pressure, Δp , within the drop according to the Laplace equation [3]:

$$\Delta p = \gamma \left(\frac{1}{r_1} + \frac{1}{r_2} \right) \quad (10)$$

where the shape of the drop is defined by two radii of curvature, r_1 and r_2 . The pressure difference for an axially-symmetric drop is dependent upon the difference in the densities of the two phases, thus $\Delta p = \Delta \rho g h$, where g is the acceleration due to gravity and h is the height within the drop. In practice, the image of the drop is fitted in terms of the laboratory coordinates x and z , and the Bashforth–Adams equation is used to yield the interfacial tension:

$$2 + \frac{\beta z}{b} = \frac{b}{r} + \frac{b \sin \varphi}{x} \quad (11)$$

where the bond number, $\beta = \frac{\Delta \rho g b^2}{\gamma}$, r is the radius of curvature of the drop meridian,

b is the radius of curvature at the drop apex and φ is the angle between the surface normal and the z axis. This technique does not perturb the interface and has a time resolution of < 1 s. Consequently it has found much use in the acquisition of dynamic interfacial tension measurements. Beverung *et al* measured the adsorption of several

proteins to the heptane–water interface over several hours [14]. They studied both β -casein as an example of a random coil protein and lysozyme and ovalbumin as examples of globular proteins. The dynamic interfacial tension decay of all the proteins followed a characteristic shape, as shown in figure 5.

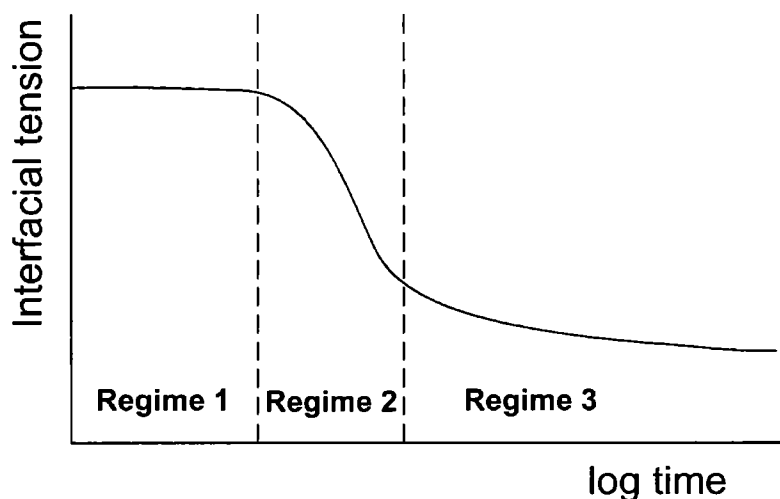


Figure 5. Schematic of the typical dynamic interfacial response of a protein adsorbing to the oil–water interface. Adapted from ref [14].

Beverung *et al* divided this response into three regimes. In the first regime, termed the induction phase, the protein diffuses to the interface but does not affect the interfacial tension appreciably. This response was attributed to adsorption induced by hydrophobic interactions between the oil and hydrophobic residues on the surface of the protein. The restricted number of contact points between the protein and the interface means that the change in the interfacial tension is limited. In the second regime, named the monolayer saturation phase, there is a large drop in the interfacial tension. This drop was ascribed to the protein unfolding at the interface and the rearrangement of secondary and tertiary structure to expose hydrophobic residues to the hydrophobic phase. This unfolding permits more contact points between the protein and the interface so the interfacial tension is reduced. Furthermore, any hydrophobic groups on the unfolded protein that were prevented from orienting themselves to the oil phase provide a foundation for further adsorption. They found

that β -casein unfolded faster than the globular proteins, as expected from its lack of secondary and tertiary structure. Finally in the third regime, called the interfacial gelation regime, there is a slow change in the conformation of the layer and the formation of a gel-like network through intermolecular interactions including ionic or hydrophobic interactions, or disulfide or hydrogen bonds. The rheology of these gel networks has been studied extensively, as discussed below. Each additional layer of protein unfolds less until eventually the environment encountered by newly-adsorbed protein resembles the bulk and adsorption ceases.

Krägel *et al* studied the dynamic interfacial tension decay of β -lactoglobulin and sodium dodecyl sulfate mixtures [15]. They found that the surfactant and protein formed a complex that is more hydrophobic than the natural protein. Furthermore, even at a large excess of SDS, the oil-water interface was still covered by the complex rather than the surfactant alone.

Rodríguez Patino *et al* investigated the effect of processing conditions upon the adsorption of a whey protein isolate containing a high proportion of β -lactoglobulin to the triolein–water interface [16]. They found that heating the protein at 80°C for one hour caused the surface pressure to increase more rapidly than for the untreated protein. Heating the protein breaks the intramolecular interactions and causes the protein to denature. Consequently the denatured protein can adsorb and gelate more rapidly.

Surface rheology of protein films

The shear and dilatational rheology of protein films have been extensively studied as these properties give information about the dynamic response of the films. The structural properties of the film can be inferred from this behaviour. The shear response reports on lateral interactions and the structure of the film whereas the dilatational response gives information on the exchange of matter between the surface and the bulk and on processes going on within the film. The complex interfacial dilatational modulus, \hat{E} , is the proportionality factor between a periodically applied strain serving to vary the surface area, A , and the ensuing stress response. The real part, E' describes the elastic response of the interface to variations in surface area whereas the imaginary part, E'' is the viscous response accounting for the energy that is dissipated by the film.

Similarly the complex interfacial shear modulus, \hat{G} , can be described in terms of a storage modulus, G' , accounting for recoverable energy stored during shear deformation and a loss modulus, G'' , accounting for energy dissipated in shear processes.

Surface rheology experiments highlight the difference between films formed from disordered proteins such as β -casein and those films formed from globular proteins like β -lactoglobulin. Freer *et al* investigated the rheology of lysozyme and β -casein at the hexadecane–water interface [17]. They found that under shear the film formed from the random-coil protein was fluid-like and dominated by viscous dissipation whereas the lysozyme film exhibited an elastic response. This result points towards the formation of a glassy interfacial network by the globular protein. The dilatational response of β -casein exhibited a strong frequency dependence; at low frequencies the response was dominated by diffusion dissipation (suggesting that the adsorption of β -casein is reversible on the timescales probed by these low frequencies) and at higher frequencies by viscous dissipation. In contrast, lysozyme showed only a weak frequency dependence. These results suggest that the lysozyme film is irreversibly adsorbed whereas the β -casein film can desorb, provided that the dilatational timescale is slower than the timescale for diffusion. In a related study, the same group

investigated the effect of surface age on the shear moduli of the same proteins [18]. They found that the shear moduli of the lysozyme film grew with age; in regimes one and two the film was fluid-like but became more solid-like in regime three. The protein initially adsorbs in a state similar to its native conformation. This state is stabilized by intramolecular interactions which provide a kinetic barrier to unfolding. As these barriers are overcome and the protein unfolds, these interactions form intermolecular linkages that strengthen the film network. In contrast, the moduli of the β -casein film were practically independent of surface age, indicating the lack of structure in the native protein and the adsorbed film.

Romoscanu *et al* studied the rheology of the same proteins at the interface between water and a mixture of medium-chain triglycerides [19]. They used glutaraldehyde to form cross-links between protein molecules in adsorbed films. They found that densifying the β -casein film increased the elasticity of the film, which is indicative of either additional cross-linking or a thicker layer. In contrast, densifying the β -lactoglobulin film reduced the elasticity, suggesting that a folded interface is created by the glutaraldehyde.

Murray *et al* compared both random-coil and globular proteins at the air–water and oil–water interface [20]. The rheological responses suggested that the proteins were more unfolded and more flexible at the oil–water interface, which is possibly due to the superior solvation of the hydrophobic residues by the oil phase. The same group investigated the dilatational response of β -lactoglobulin at the air–water and oil–water interface in the presence of the nonionic surfactant $C_{12}E_6$ [21]. They found a slight maximum in the dilatational moduli at equimolar ratios which is concomitant with an increase in foam stability.

Ellipsometry

Ellipsometry is an optical technique that reports on the profile of the refractive index across an interface. Thus it is very sensitive to adsorption at interfaces, although the response cannot be unequivocally ascribed to the precise amount of the adsorbate and a model is required to interpret the results. The problem arises that, for films much thinner than the wavelength of the incident light, the thickness and refractive index of the adsorbed layer cannot be uniquely determined. Russev *et al* studied the adsorption kinetics of β -casein at the oil–water and air–water interfaces [22]. They overcame the problem of correlation between the refractive index and layer thickness by assuming that the protein behaved identically at both interfaces. They interpreted their results in terms of a double layer model; the protein initially adsorbs as a dense layer and subsequently a second, more diffuse layer adsorbs. At long times, the surface coverage of the second layer approaches that of the first layer although the second layer is still more diffuse.

Beaglehole *et al* studied the adsorption of the globular protein bovine serum albumin (BSA) to the oleyl alcohol–water interface [23]. In this brief investigation, they determined the variation of the dielectric constant of the protein with concentration in solution. With this parameter, and using the assumption that the adsorbed amount was small, they were able to relate the ellipsometric response to the surface excess of the protein. They found that the protein adsorbed to the interface with a surface excess of 0.45 mg m^{-2} at a bulk concentration of 3.5 mg mL^{-1} . Bylaite *et al* compared the adsorption of β -lactoglobulin to the interface between water and either olive oil or caraway essential oil [24]. They found that the protein adsorbed in a similar quantity to each interface. They fitted their ellipsometry data and found that the protein film formed a dense layer with a surface excess of $1.60\text{--}1.65 \text{ mg m}^{-2}$ and a thickness of 20 \AA . The techniques employed by these groups to extract the quantitative data from the ellipsometric responses will be discussed in further detail in chapter 4.

Nuclear magnetic resonance spectroscopy

Nuclear magnetic resonance (nmr) spectroscopy is not a surface-sensitive technique, however the signal from protein adsorbed to the oil–water interface in emulsions can be readily detected. ter Beek *et al* investigated the conformation and dynamics of β -casein in a tetradecane–water emulsion by ^{13}C and ^{31}P nmr [25]. They found that the protein films were fairly stiff and moved on a nanosecond timescale, consistent with motions of entire protein tails. They rationalized their results by a “hairy sphere” model where the hydrophilic N-terminal tails extend from the surface of the emulsion droplets. Thus the phosphoserine groups are not immobilized but in a flexible part of the protein away from the site of adsorption. Mine studied the adsorption behaviour of casein-stabilized emulsions by ^{31}P nmr [26]. He found that the line widths of the spectra increased with increased loading of protein at the interface, which is consistent with reduced mobility of the phosphoserine moieties. Barros *et al* used low-resolution ^1H nmr relaxometry to investigate the dynamics of a water-in-decane emulsion stabilized by β -casein [27]. They used spin-spin relaxation time constants to determine the relative mobility of the emulsion constituents. Most of the oil behaved like bulk solvent, with a minority with reduced mobility ascribed to oil molecules closer to the interface. The majority of protein molecules exhibited a significantly decreased mobility compared to those in the bulk, and most of the water was significantly restricted owing to the high concentration of interfacial water in the water-in-oil emulsion.

Fourier transform infrared spectroscopy

Fourier transform infrared (FTIR) spectroscopy suffers from similar restrictions to nmr as it is not inherently surface-sensitive, nonetheless it can offer significant information about the structure of proteins in emulsions. The amide I band (1600 – 1700 cm^{-1}) is a sensitive reporter of the secondary structure of proteins [28]. This band arises from the carbonyl stretch of the peptide bond, coupled with in-plane N–H bending and C–N stretching modes. The exact position of the band is perturbed by the degree of hydrogen bonding between the amide carbonyls and N–H bonds of

separate residues. The secondary structure of a protein determines the degree of hydrogen bonding and the interatomic distances between nonadjacent atoms and consequently α -helices, β -sheets, β -turns and random coil structures are resonant at slightly different frequencies. Typically, individual peaks are not explicitly resolved within the amide I band, but nevertheless the fractions of each secondary-structure motif within a protein can be determined by curve fitting and comparison with spectra from known structures.

Lefèvre and Subirade probed the amide I' region in oil-in-D₂O emulsions stabilized by β -lactoglobulin [29]. They separated the emulsion oil droplets from the bulk protein solution in order to compare the spectra from bulk and adsorbed protein. Protein remaining in the bulk exhibited no spectral change, unlike adsorbed protein which showed spectra characteristic of intermolecular anti-parallel β -sheets. Fang and Dalgleish also studied the conformation of β -lactoglobulin by FTIR spectroscopy and compared the effect of denaturation by heat and by adsorption [30]. Whereas both treatments proceeded via similar intermediate structures and involved the loss of β -sheet structure, heating generated more intermolecular β -sheet and less unordered structure than adsorption. Furthermore denaturation by adsorption proceeded more slowly than thermal denaturation.

Scattering techniques

Scattering techniques such as dynamic light scattering (DLS) and neutron reflectance (NR) are used to determine the dimensions of adsorbed layers and hence, in the case of proteins, these methods provide information about the degree of unfolding. NR delivers information about the distribution of mass near the interface whereas DLS experiments inform upon the hydrodynamics of the emulsion droplets, thus these two sets of techniques are complementary [31]. Dickinson *et al* used specular neutron reflectivity to study β -casein films adsorbed at the hexane–water interface [32]. A two-layer model consisting of a 2-nm thick, dense inner layer and a more diffuse, 5–7-nm thick secondary layer described their data well. Light scattering can be used to determine the size of emulsion droplets [33, 34] and Fang and Dalgleish used quasi-

elastic light scattering to study the breakdown of adsorbed β -casein films by proteolysis [35]. At low surface coverages of protein they found that the hydrodynamic thickness of the adsorbed layer was at a minimum, suggesting that the protein molecules were stretched out on the surface. This layer was only reduced by 5 nm during proteolysis by trypsin. In contrast, the layer thickness increased to 10 nm at the plateau surface coverage of 3 mg m^{-2} as the proteins protruded into the aqueous phase.

Imaging studies

Atomic force microscopy (AFM) and Brewster angle microscopy (BAM) are imaging techniques which can be used to determine the topology of surfaces. Imaging is particularly useful in the study of adsorbed protein films as these surfaces are heterogenous at mesoscopic lengthscales. Whereas ellipsometry and FTIR spectroscopy generate a response that is integrated over the cross-section of the light beam ($\text{mm}^2 - \text{cm}^2$), AFM can provide lateral resolution down to molecular lengthscales. However AFM is not able to distinguish between different chemical species. BAM only offers a lateral resolution of $\sim 1 \text{ }\mu\text{m}$ but is very sensitive to surface composition.

AFM involves scanning a sharp silicon nitride cantilever across the surface of a sample. The force between the tip and the sample is kept constant by a feedback loop and the movements of the scanner required to maintain this deflection are converted into an image that reveals the topography of the surface of the sample. Mackie *et al* have used AFM to probe the mechanism of protein displacement from the oil–water interface by surfactants [36]. They formed films of β -lactoglobulin and β -casein at the tetradecane–water interface, exposed the films to an aqueous solution of Tween 20 and transferred the films by Langmuir–Blodgett deposition onto freshly-cleaved mica. They found that heterogeneity in the protein films allowed surfactant to adsorb into the film. These regions then expanded and compressed the protein network. Above a critical surface pressure, the film thickened and eventually broke up and the protein desorbed into the bulk. This mechanism has been termed “orogenic

displacement". Both proteins followed this mechanism, but the displacement of β -lactoglobulin occurred over a much narrower range of surface pressure than the displacement of β -casein. The same group investigated the orogenic displacement of β -lactoglobulin from the oil–water interface by bile salts as a model for duodenal digestion [37]. The bile salts were able to displace the protein film almost completely from the interface but the morphology of the film during displacement was different to the morphology of a film displaced by simple surfactants.

BAM relies on the restriction that at the Brewster angle no p -polarized light is reflected from a bare interface. However, the presence of a film at the interface breaks this restriction. Thus in BAM a beam is scanned across an interface and the reflected intensities are captured by an array detector to form an image. Although the reflected intensity increases with increasing optical density and thickness of the film, it is not possible to determine these parameters quantitatively by BAM [38]. Furthermore, the limited spatial resolution means that BAM is not suitable to the study of mixed protein–surfactant films, and the low optical contrast precludes the study of mixed protein films [39]. Xu *et al* have studied films of β -lactoglobulin and α_{s1} -, β - and κ -casein at the polydimethylsiloxane–water interface [40]. The films were formed in a Langmuir trough in order to subject them to compression–expansion and heating–cooling cycles. The β -lactoglobulin films exhibited considerable structuring and the films became more coherent at increased bulk concentrations. Upon compression the films formed ridges and cracks. In contrast, the β -casein films exhibited no structuring at all, although the other casein fractions exhibited some limited structure. Overall they found that the films became highly inhomogeneous during these thermal and mechanical perturbations.

Miscellaneous studies

A number of other experimental techniques have been used to investigate protein adsorption at the oil–water interface. Corredig and Dalgleish employed differential scanning microcalorimetry (DSC) to determine the structural characteristics of lysozyme and β -lactoglobulin adsorbed at the oil–water interface [41]. DSC probes thermal transitions and hence is particularly useful for studying the denaturation of proteins. Thermograms of adsorbed protein were markedly different from bulk protein, suggesting adsorption caused considerable changes in the conformation of the protein. Adsorbed β -lactoglobulin displayed no thermal transition which indicated that the protein is denatured at the interface. The transition did not reappear once the protein was displaced from the interface by Tween 60, which suggests that the protein was not restored to its native state in solution.

Dickinson and Matsumura investigated the kinetics of formation of intermolecular disulfide bonds in β -lactoglobulin films [42]. The protein film was displaced by sodium dodecyl sulfate from emulsion droplets and analyzed by polyacrylamide gel electrophoresis. Immediately after adsorption the protein film consisted solely of protein monomers, but the amount of polymerized β -lactoglobulin increased over time. N-ethylmaleimide prevents the formation of disulfide bonds and in the presence of this reagent no polymerization was seen. Thus the formation of disulfide linkages was found to be a key stage in the creation of the viscoelastic protein film.

Dimitrova *et al* used the magnetic chaining technique (MCT) and the Mysels cell to investigate the repulsive interaction profiles between protein films at the oil–water interface [43]. These repulsive interactions are critical to the prevention of coagulation of emulsion droplets. The magnetic chaining technique involves the application of a magnetic field to an emulsion containing a paramagnetic oil (in this case a 10% v/v dispersion of Fe_2O_3 particles in octane). The applied field generates a magnetic dipole in each droplet and causes the droplets to align in linear arrays. The spacing of these arrays is measured by Bragg diffraction of a white light source, and as the system is in equilibrium the attractive forces from the magnetic dipoles are balanced by the repulsive forces between the droplets. In the Mysels cell, an emulsion

film is formed in a circular porous plate. The thickness of the film is measured by white light interferometry and the disjoining pressure is measured by a transducer. The repulsive forces for films stabilized by the globular protein bovine serum albumin were long-ranged, probably from the formation of multiple protein layers. The interactions between β -casein layers were governed by electrostatic repulsion. This group also employed the MCT to compare the threshold flocculation force for β -casein and β -lactoglobulin emulsions. They found that this force was lower and the flocs were more rigid for β -lactoglobulin than β -casein.

Theoretical studies

In addition to the experimental studies discussed above, there have been a number of papers presenting theoretical simulations of proteins at the oil–water interface. Anderson *et al* modeled a protein-like heteropolymer at the oil–water interface by dynamic lattice Monte Carlo simulation [44]. In aqueous solution the 27-residue polymer folded into a globular state below a critical temperature and denatured above this temperature. Irreversible adsorption of the protein is driven by the reduction in unfavourable interactions between the oil and the water phase and results in the protein adopting an unfolded conformation at the interface. The majority of the protein penetrates the water phase with less than 10% in the oil phase. The same group extended this study by varying the parameters governing the behaviour of the oil phase [45]. They found that the average residue–water interaction needs to be repulsive to create compact, folded protein conformations and adsorption to the oil–water interface was most favourable when the average residue–water interaction was slightly more repulsive than the average residue–oil interaction.

1.5 Emulsion formation, stabilization and coalescence

As discussed above, emulsions are metastable dispersions of water-in-oil or oil-in-water that usually contain emulsifiers to prevent phase separation. They are typically formed through mechanical agitation of the bulk phases by stirrers or homogenizers. The turbulent flows created by this process exert shearing forces on the liquid droplets and cause them to break up. Mechanical stirring produces emulsions with a fairly broad distribution of droplet sizes. The energy required to break up emulsion droplets can also be produced chemically. For example, neutralization of oleic acid in mineral oil by an aqueous alkali solution generates gradients in the interfacial tension. The interfacial tension is reduced sufficiently to allow thermal fluctuations to emulsify the system. As another example, the free energy of mixing of ethanol and water can drive the emulsification of a toluene–ethanol solution with water. The ethanol diffuses into the aqueous phase and the toluene left behind emulsifies with water close to the interface [3].

The breakup of an emulsion proceeds via a variety of mechanisms [3]. The first stage is flocculation, which is a reversible association between emulsion droplets caused by a weak secondary minimum in the interaction potential–separation curve. During this stage, the difference in density between the two phases also causes creaming, whereby a concentration gradient is created by the gravitational field. Once the droplets have become more concentrated thanks to creaming and flocculation, they can coagulate into the primary minimum of the interaction potential–separation curve. This stage is irreversible. Finally, the droplets coalesce to form two separate bulk phases. This coalescence process proceeds in the following manner. Coagulated droplets have flat surfaces separated by a film of the continuous medium. In order for coalescence to occur, the droplets must fuse across this film to form a neck linking the two droplets. Finally this neck enlarges until the droplets fuse completely.

If the two phases possess an appreciable mutual solubility, the emulsion can also age by the Ostwald ripening mechanism. Large emulsion droplets have a smaller surface area–volume ratio. As it is energetically more favourable for a molecule to be in the interior of a particle rather than at the surface, large droplets are more favourable than

small droplets. Thus molecules will diffuse from the small to the large droplets until eventually all small droplets disappear.

Milk proteins alone are insufficient to maintain a stable emulsion over the months and years required for a typical food product [2]. Thus small molecule surfactants are used to enhance shelf life. Proteins and emulsifiers stabilize emulsions by different mechanisms; proteins form an adsorbed layer with lateral interactions between molecules which prevents the emulsion coalescing mechanically, whereas emulsifiers exhibit minimal lateral interactions but can reduce the interfacial tension to lower values and rely on charge repulsion or the Gibbs-Marangoni effect to stabilize the emulsion [46]. These two mechanisms are frequently antagonistic so I will now describe each in more detail.

The studies described above present the following picture for the mechanism of emulsion stabilization by proteins. The films formed from β -casein and β -lactoglobulin differ. Although β -casein is disordered in its native form, at the interface some ordered secondary structure can arise in the form of α -helix. Its amphiphilic nature means that it behaves more like a surfactant molecule, whereby the hydrophobic region is anchored at the surface and the hydrophilic region extends into the aqueous phase [47]. The five charged phosphoserine residues are anchored at the surface and serve to prevent coalescence through electrostatic repulsion. In contrast the films formed from β -lactoglobulin exhibit more intermolecular interactions and over time the protein molecules form a two-dimensional gel network. This network has a more viscoelastic character than the casein film [47].

In contrast, emulsifying surfactants are considerably more surface-active than proteins and can lower the interfacial free energy from $\sim 50 \text{ mJ m}^{-2}$ to $\sim 5 \text{ mJ m}^{-2}$ for a typical alkane–water interface. This reduction in the surface free energy reduces the driving force for a system to lower its overall energy by reducing the total interfacial area. Adsorption of soluble surfactants is also a reversible process, whereas protein adsorption can be reversible or irreversible, depending on the nature of the protein. Finally, surfactants can also diffuse readily in the interfacial plane. As described above, emulsions can only coalesce if a neck can be formed between droplets.

Attractive van der Waals forces draw the droplets together, but the presence of surfactant molecules (or proteins) creates a repulsive barrier. Thus the formation of this neck requires adjacent patches on the surface of the droplets that are devoid of surfactant. Thermal fluctuations can perturb the interface to create bare patches, but the resulting gaps are readily filled, either slowly by surfactant diffusing to the surface and adsorbing from bulk solution, or more rapidly by the Gibbs–Marangoni effect. Variations in the surface excess create local surface tension gradients. Surfactant molecules on the surface are driven by these gradients to regions of higher surface tension (less adsorption). Consequently the Marangoni effect acts to heal any gaps in the surface coverage and limit coalescence.

Surfactants can also delay coalescence by preventing the growth of the neck. A free energy barrier for the growth of the neck exists if the spontaneous curvature of the emulsion droplet is towards the dispersed phase, whereas there is no barrier if the spontaneous curvature is towards the continuous phase. The spontaneous curvature is governed by the architecture of the surfactant as well as other factors such as the temperature and ionic strength of the emulsion. Thus emulsions are often quite sensitive to these parameters and a small change can rapidly lead to the breakdown of the emulsion.

Although each of these mechanisms is effective at stabilizing an emulsion in isolation, when proteins and surfactants are both present these mechanisms are antagonistic, which can lead to emulsion breakdown. This destabilization of emulsions by competitive adsorption operates in the following manner [46, 47]. The proteins saturate the interface at a much lower concentration than surfactants, thus when the surfactant concentration is low, protein adsorption dominates and the lateral interactions between protein molecules stabilize the emulsion. However at higher surfactant concentrations the surfactant molecules compete with proteins for interfacial area. The surfactants penetrate into the defects in the interfacial protein film. The presence of the surfactant molecules weakens the lateral interactions between protein molecules, and the protein molecules inhibit the lateral migration of surfactant molecules. Thus neither species is able to stabilize the emulsion as efficiently as in isolation. Surfactant molecules continue to adsorb, creating

surfactant-rich and protein-rich domains at the interface. Eventually sufficient surfactant adsorbs such that the surface pressure in the surfactant-rich domain is greater than the surface pressure and elastic resistance of the protein-rich domain. The protein film crumples and thickens and is eventually displaced from the interface. In general nonionic water-soluble surfactants are found to be more effective at displacing proteins from oil–water interfaces than oil-soluble surfactants.

1.6 Thesis outline

The remainder of this thesis is presented as follows. In chapter 2, I describe the electromagnetic theory underlying ellipsometry and Raman spectroscopy. The ellipsometric response from protein and surfactant films at the oil–water interface can only be understood once the response from a pristine interface has been interpreted. Therefore in chapter 3 I have measured the ellipsometric response from the interface between water and a series of nonpolar and polar oils. I compare these results to complementary studies in the literature and propose two alternative models to describe the structure at the pristine oil–water interface. In chapter 4 I present results from the adsorption of surfactants and proteins to the oil–water interface. In chapter 5 I describe my attempts to take Raman spectra of surfactants at an oil–water interface. In chapter 6 I describe the construction of a UV resonance Raman microspectrometer to acquire spectra of proteins and peptides adsorbed at the oil–water interface and in planar supported lipid bilayers. Finally in chapter 7 I describe the commissioning of a combined tribometer and confocal Raman spectrometer to study emulsions within a soft elasto-hydrodynamic contact.

References

- 1 R. S. Kagan, *Environmental Health Perspectives* **111**, 223 (2003).
- 2 Overview of Food Emulsifiers, G. L. Hasenhuettl, in *Food emulsifiers and their applications*, edited by G. L. Hasenhuettl and R. W. Hartel (Chapman and Hall, New York, 2008).
- 3 D. F. Evans and H. Wennerstrom, *The Colloidal Domain* 2nd ed. (Wiley-VCH, New York, 1999).
- 4 J. S. Rowlinson and B. Widom, *Molecular Theory of Capillarity* 1st ed. (Dover Publications, Inc., Mineola, N. Y., 2002).
- 5 J. Schulz, A. Hirtz, and G. H. Findenegg, *Physica A* **244**, 334 (1997).
- 6 M. R. Porter, *Handbook of Surfactants* 2nd ed. (Blackie Academic and Professional, Glasgow, 1994).
- 7 M. J. Rosen, *Surfactant and Interfacial Phenomena* 2nd ed. (Wiley, New York, 1989).
- 8 P. W. Atkins, *Physical Chemistry* 6th ed. (Oxford University Press, Oxford, 1999).
- 9 Amino Acids, Peptides and Proteins, J. C. Cheftel, J.-L. Cuq, and D. Lorient, in *Food Chemistry*, edited by O. R. Fennema (Marcel Dekker, Inc., New York, 1985).
- 10 L. Stryer, *Biochemistry* 4th ed. (W. H. Freeman and Company, New York, 1996).
- 11 Milk, H. E. Swaisgood, in *Food Chemistry*, edited by O. R. Fennema (Marcel Dekker, Inc., New York, 1985).
- 12 S.-Y. Wu, M. Dolores Perez, P. Puyol, and L. Sawyer, *J. Biol. Chem.* **274**, 170 (1999).
- 13 G. Kontopidis, C. Holt, and L. Sawyer, *J. Dairy Sci.* **87**, 785 (2004).
- 14 C. J. Beverung, C. J. Radke, and H. W. Blanch, *Biophysical Chemistry* **81**, 59 (1999).
- 15 J. Kragel, M. O'Neill, A. V. Makievski, M. Michel, M. E. Leser, and R. Miller, *Colloids and Surfaces B: Biointerfaces* **31**, 107 (2003).

- 16 J. M. Rodriguez Patino, M. R. Rodriguez Nino, and C. C. Sanchez, *J. Agric. Food Chem.* **47**, 2241 (1999).
- 17 E. M. Freer, K. S. Yim, G. G. Fuller, and C. J. Radke, *Langmuir* **20**, 10159 (2004).
- 18 E. M. Freer, K. S. Yim, G. G. Fuller, and C. J. Radke, *J. Phys. Chem. B* **108**, 3835 (2004).
- 19 A. I. Romoscanu and R. Mezzenga, *Langmuir* **21**, 9689 (2005).
- 20 B. S. Murray, M. Faergemand, M. Trotreau, and A. Ventura, *Special Publication - Royal Society of Chemistry* **227 (Food Emulsions and Foams)**, 223 (1999).
- 21 B. S. Murray, A. Ventura, and C. Lallemand, *Colloids and Surfaces A: Physicochemical and Engineering Aspects* **143**, 211 (1998).
- 22 S. C. Russev, T. V. Arguirov, and T. D. Gurkov, *Colloids and Surfaces B: Biointerfaces* **19**, 89 (2000).
- 23 D. Beaglehole, F. Lawson, G. Harper, and M. Hossain, *J. Colloid Interf. Sci.* **192**, 266 (1997).
- 24 E. Bylaite, T. Nylander, R. Venskutonis, and B. Jonsson, *Colloids and Surfaces B: Biointerfaces* **20**, 327 (2001).
- 25 L. C. ter Beek, M. Ketelaars, D. C. McCain, P. E. A. Smulders, P. Walstra, and M. A. Hemminga, *Biophysical J.* **70**, 2396 (1996).
- 26 Y. Mine, *J. Agric. Food Chem.* **45**, 68 (1997).
- 27 C. N. Barros, E. P. G. Areas, E. N. Figueiredo, and J. A. G. Areas, *Colloids and Surfaces B: Biointerfaces* **48**, 119 (2006).
- 28 S. Ngarize, H. Herman, A. Adams, and N. Howell, *J. Agric. Food Chem.* **52**, 6470 (2004).
- 29 T. Lefevre and M. Subirade, *J. Colloid Interf. Sci.* **263**, 59 (2003).
- 30 Y. Fang and D. G. Dalgleish, *J. Colloid Interf. Sci.* **196**, 292 (1997).
- 31 D. G. Dalgleish, *Food Research International* **29**, 541 (1996).
- 32 E. Dickinson, D. S. Horne, J. S. Phipps, and R. M. Richardson, *Langmuir* **9**, 242 (1993).
- 33 J.-L. Courthaudon and E. Dickinson, *J. Agric. Food Chem.* **39**, 1365 (1991).

- 34 D. G. Dalgleish, M. Srinivasan, and H. Singh, *J. Agric. Food Chem.* **43**, 2351 (1995).
- 35 Y. Fang and D. G. Dalgleish, *J. Colloid Interf. Sci.* **156**, 329 (1993).
- 36 A. R. Mackie, A. P. Gunning, P. J. Wilde, and V. J. Morris, *Langmuir* **16**, 2242 (2000).
- 37 J. Maldonado-Valderrama, N. C. Woodward, A. P. Gunning, M. J. Ridout, F. A. Husband, A. R. Mackie, V. J. Morris, and P. J. Wilde, *Langmuir* **24**, 6759 (2008).
- 38 R. Xu, E. Dickinson, and B. S. Murray, *Langmuir* **23**, 5005 (2007).
- 39 L. A. Puglanoni, E. Dickinson, R. Ettelaie, A. R. Mackie, and P. J. Wilde, *Adv. Coll. Interface Sci.* **107**, 27 (2004).
- 40 R. Xu, E. Dickinson, and B. S. Murray, *Langmuir* **24**, 1979 (2008).
- 41 M. Corredig and D. G. Dalgleish, *Colloids and Surfaces B: Biointerfaces* **4**, 411 (1995).
- 42 E. Dickinson and Y. Matsumura, *Int. J. Biol. Macromol.* **13**, 26 (1991).
- 43 T. D. Dimitrova, F. Leal-Calderon, T. D. Gurkov, and B. Campbell, *Adv. Coll. Interface Sci.* **108-109**, 73 (2004).
- 44 R. E. Anderson, V. S. Pande, and C. J. Radke, *J. Chem. Phys.* **112**, 9167 (2000).
- 45 K. Leonhard, J. M. Prausnitz, and C. J. Radke, *Langmuir* **22**, 3265 (2006).
- 46 P. Wilde, A. Mackie, F. Husband, P. Gunning, and V. Morris, *Adv. Coll. Interface Sci.* **108-109**, 63 (2004).
- 47 E. Dickinson, *Colloids and Surfaces B: Biointerfaces* **20**, 197 (2001).

Chapter 2

Theory

2.1 Introduction

The aim of this thesis is to investigate the behaviour of proteins and emulsifiers at the oil–water interface. Films of these molecules may extend to human length scales in two dimensions but in the third dimension normal to the interface these films are typically only a few nanometers thick. Spectroscopic techniques are capable of determining molecular-scale information about these films. I have principally used ellipsometry, vibrational Raman spectroscopy and vibrational resonance Raman spectroscopy in this work. All these techniques employ laser beams as the incident light source, so I begin this chapter with a discussion of the propagation and polarization of light and the interaction of light with matter. Next I describe the reflection and refraction of light from an interface with particular emphasis on the phenomenon of total internal reflection (TIR), as we employ a TIR geometry to ensure that our Raman techniques are surface-sensitive. Next, I discuss molecular vibrations and symmetry before I address the origin of the Raman effect and the theory behind both normal and resonance vibrational Raman spectroscopy. Raman spectroscopy is a particularly rich source of data and without sufficient knowledge of the underlying theory significant information may be lost.

2.2 Light and interfaces

The wave equation and the propagation of light

The most complete description of light and its interaction with matter is provided by the quantum field theory of quantum electrodynamics (QED). Although QED is currently believed to be wholly accurate, the calculations involved in its implementation are extremely complex for any but the most simple systems. I will therefore start my discussion of the propagation of light with the classical equations of Maxwell. Maxwell's equations are given below in differential form [1]:

$$\nabla \times \mathbf{E} = -\frac{\partial \mathbf{B}}{\partial t} \quad (1a)$$

$$\nabla \times \mathbf{H} = \mathbf{J} + \frac{\partial \mathbf{D}}{\partial t} \quad (1b)$$

$$\nabla \cdot \mathbf{D} = \rho \quad (1c)$$

$$\nabla \cdot \mathbf{B} = 0 \quad (1d)$$

where \mathbf{J} is the current density and ρ is the electric charge density. The electric displacement, \mathbf{D} , is related to the electric field vector, \mathbf{E} , by the polarization, \mathbf{P} and similarly the magnetic flux density, \mathbf{B} , is related to the magnetic field vector, \mathbf{H} , by the magnetization, \mathbf{M} [1]:

$$\mathbf{D} = \epsilon_0 \mathbf{E} + \mathbf{P} \quad (2a)$$

$$\mathbf{B} = \mu_0 (\mathbf{H} + \mathbf{M}) \quad (2b)$$

where ϵ_0 and μ_0 are the permittivity and permeability of free space, respectively. In a vacuum, $\mathbf{P} = \mathbf{M} = \mathbf{J} = \rho = 0$ so the Maxwell equations become [1]

$$\nabla \times \mathbf{E} = -\frac{\partial \mathbf{B}}{\partial t} \quad (3a)$$

$$\nabla \times \mathbf{B} = \epsilon_0 \mu_0 \frac{\partial \mathbf{E}}{\partial t} \quad (3b)$$

$$\nabla \cdot \mathbf{E} = 0 \quad (3c)$$

$$\nabla \cdot \mathbf{B} = 0 \quad (3d)$$

Taking the curl of equation 3a and making use of the identity $\nabla \times (\nabla \times \mathbf{A}) = \nabla(\nabla \cdot \mathbf{A}) - \nabla^2 \mathbf{A}$, equation 3a becomes [1]:

$$\nabla(\nabla \cdot \mathbf{E}) - \nabla^2 \mathbf{E} + \nabla \times \frac{\partial \mathbf{B}}{\partial t} = 0 \quad (4)$$

This equation can be simplified by substitution of equation 3c and the partial time derivative of equation 3b to give the wave equation [1]:

$$\nabla^2 \mathbf{E} = \epsilon_0 \mu_0 \frac{\partial^2 \mathbf{E}}{\partial t^2} \quad (5)$$

The electromagnetic disturbance in equation 5 propagates with a phase velocity $c = (\epsilon_0 \mu_0)^{-1/2}$.

The work in this thesis is primarily concerned with monochromatic plane waves and in this case the solution to equation 5 is given by [2]

$$\mathbf{E} = \mathbf{E}_0 e^{i(\mathbf{k} \cdot \mathbf{r} - \omega t + \varphi)} \quad (6)$$

where \mathbf{E}_0 is the amplitude, \mathbf{k} is the propagation vector with magnitude $k = 2\pi/\lambda$ (λ is the wavelength), \mathbf{r} is the position vector, ω is the angular frequency and φ is the phase angle.

Polarization of light

The electromagnetic disturbance that is described by Maxwell's equations consists of mutually sustaining electric and magnetic fields that are orthogonal to the direction of propagation of energy. These fields can each be described by the field vectors \mathbf{E} and \mathbf{B} and the propagation of energy is described by the Poynting vector, $\mathbf{S} = \left(\frac{1}{\mu_0}\right) \mathbf{E} \times \mathbf{B}$ [2]. The orientation of the field vectors defines the polarization of the light. In the simplest case of linear polarization the orientation of the vector is constant; however, in more general cases the orientation of the vector varies as the beam propagates through space such that the head of the field vector describes a circle or ellipse. This situation is described mathematically by two orthogonal linearly polarized waves in which one wave lags the other [2]:

$$E_x = E_{0x} e^{i(\mathbf{k} \cdot \mathbf{r} - \omega t)} \quad (7a)$$

$$E_y = E_{0y} e^{i(\mathbf{k} \cdot \mathbf{r} - \omega t + \varphi)} \quad (7b)$$

Consequently the difference in their phase angles can be used to describe the state of polarization of the light beam, as shown in figure 1.

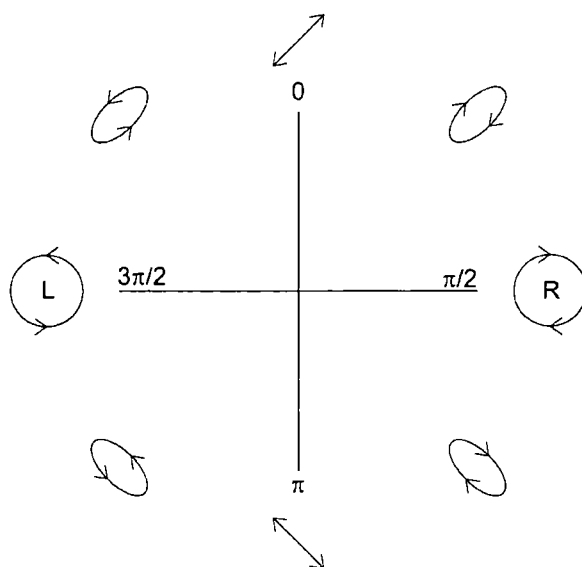


Figure 1. Schematic showing various polarizations of light in terms of the phase lag between two linearly polarized waves. $E_{0x} = E_{0y}$.

If the two waves are in phase or antiphase, the light is linearly polarized. When the amplitudes of the two waves are equal and the waves are out-of-phase by $\pi/2$ or $3\pi/2$ radians then the light is right- or left-circularly polarized. For all other phase differences or amplitude ratios the light is elliptically polarized.

Interaction of light with matter

When light interacts with a molecule, the electron distribution responds to the local electric field of the light. To a first approximation (neglecting higher order electric and magnetic multipoles) this response is characterized by the dipole moment, μ . The dipole moment is given by the infinite sum [3]:

$$\mu = \alpha \cdot \mathbf{E} + \frac{1}{2} \beta : \mathbf{E}\mathbf{E} + \frac{1}{6} \gamma : \mathbf{E}\mathbf{E}\mathbf{E} + \dots \quad (8)$$

where α , β , and γ are the molecular polarizability, hyperpolarizability and second hyperpolarizability tensors, respectively. The second and higher nonlinear terms only become appreciable if the electric field of the incident light is comparable to the

electric fields within the molecule itself. This situation occurs with intense pulsed lasers and can lead to nonlinear effects such as second harmonic generation and stimulated Raman scattering. The remainder of this discussion will focus on linear effects only, as they are the most relevant to my work.

In a condensed medium, the electric field experienced by the molecule does not arise solely from the incident light, but is modified by the local field produced by the surrounding dipoles. Thus it is more usual to describe the effect of the electric field in terms of the macroscopic parameters of polarization, \mathbf{P} , and susceptibility, χ , such that [4]

$$\mathbf{P} = \varepsilon_0 \chi \cdot \mathbf{E} \quad (9)$$

The susceptibility of a material is linked to the polarizability according to $\chi = N\langle\alpha\rangle/\varepsilon_0$ where N is the number of molecules per unit volume and the angle brackets indicate that α is averaged over all molecular orientations. The exact nature of the local field correction is a complicated subject that depends on the structure of the material, but for isotropic media the local field is increased by $\mathbf{P}/3\varepsilon_0$ over the incident field and equation 9 is modified to give [5]

$$\mathbf{P} = \frac{N\langle\alpha\rangle\mathbf{E}}{1 - (N\langle\alpha\rangle/3\varepsilon_0)} \quad (10)$$

Following a similar approach to that used to find the wave equation in vacuum, one finds that wave equation in an isotropic medium is given by [1]:

$$\nabla^2 \mathbf{E} = \frac{1}{v^2} \frac{\partial^2 \mathbf{E}}{\partial t^2} \quad (11)$$

where the phase velocity, v , is given by [1]:

$$v^2 = \frac{c^2(1 - (N\langle\alpha\rangle/3))}{1 + (2N\langle\alpha\rangle/3)} \quad (12)$$

The refractive index, n , is defined as the ratio of the phase velocity in vacuum and in a medium, and we acquire the Clausius-Mossotti equation [5]:

$$\frac{n^2 - 1}{n^2 + 2} = \frac{N\langle\alpha\rangle}{3\epsilon_0} \quad (13)$$

This equation relates the microscopic property of polarizability to the macroscopic property of the refractive index. Furthermore it can be used to determine the effect on the refractive index of a change in the density of a material.

Dispersion

The electron distribution of a molecule can be treated classically as a damped harmonic oscillator. In one dimension, x , the solution to the equation of motion for an oscillator with charge q , mass m , resonant frequency ω_0 and damping coefficient Γ is [6]

$$x = \frac{q/m}{\omega_0^2 - \omega^2 + i\Gamma\omega} E \quad (14)$$

The dipole moment, μ , is equal to the product qx and by comparison with equation 8 one finds that [6]

$$\alpha(\omega) = \frac{q^2/m}{\omega_0^2 - \omega^2 + i\Gamma\omega} \quad (15)$$

The polarizability and hence the refractive index are complex numbers that are functions of the frequency of the incident light. This variation of the refractive index with frequency is known as dispersion. From equations 13 and 15 the refractive index is a complex number $\hat{n} = n + ik$. At frequencies that are far from an absorption band $k \approx 0$ and the refractive index is approximately constant. Close to an absorption band both n and k vary rapidly with wavelength.

Reflection and refraction

The work described in this thesis is primarily concerned with the interaction of light with matter at interfaces. When a light beam is incident on an interface it is common to describe the polarization of the light beam in relation to the plane of incidence. This description results in a basis set that names light polarized perpendicular to the plane of incidence as *s*-polarized (from the German *senkrecht*, perpendicular) and parallel-polarized light as *p*-polarized. This convention is shown pictorially in figure 2.

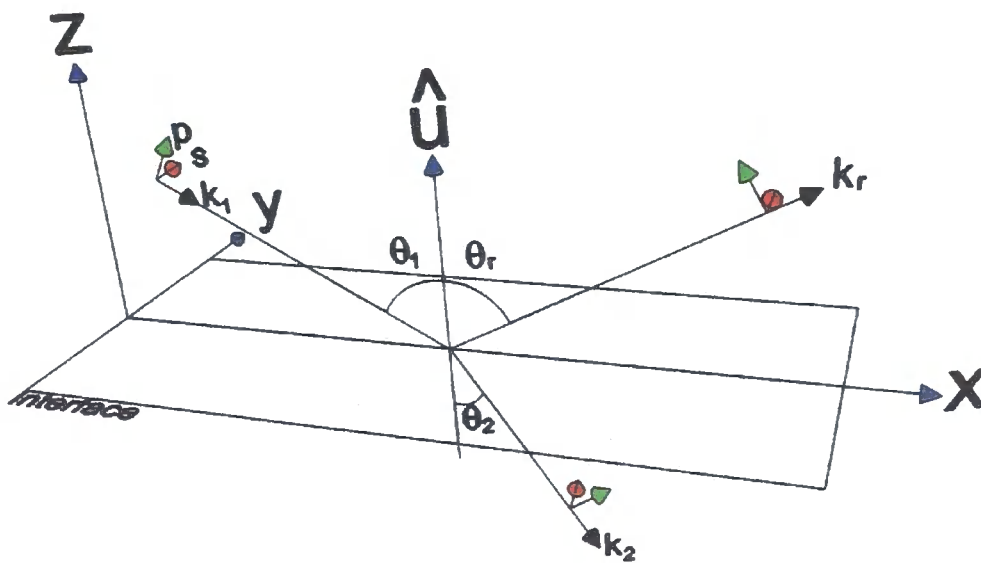


Figure 2. Reflection and refraction of a light beam at an interface. θ_1 , θ_r and θ_2 are the angles of incidence, reflection and refraction, respectively and $\hat{\mathbf{u}}$ is the surface normal.

For an interface that is smooth on the order of the wavelength of the incident light, the incident beam is scattered into a reflected and refracted part, as shown in figure 2. The electric fields of the incident, \mathbf{E}_1 , reflected, \mathbf{E}_r , and refracted light, \mathbf{E}_2 , can each be described by a formula akin to equation 6, whereby [2]

$$\mathbf{E}_1 = \mathbf{E}_{01} e^{i(\mathbf{k}_1 \cdot \mathbf{r} - \omega_1 t)} \quad (16a)$$

$$\mathbf{E}_r = \mathbf{E}_{0r} e^{i(\mathbf{k}_r \cdot \mathbf{r} - \omega_r t + \epsilon_r)} \quad (16b)$$

$$\mathbf{E}_2 = \mathbf{E}_{02} e^{i(\mathbf{k}_2 \cdot \mathbf{r} - \omega_2 t + \varepsilon_2)} \quad (16c)$$

The energy of the electromagnetic field must be conserved across the interface, which leads to the boundary condition that the tangential components of the electric and magnetic fields must be continuous across the interface, as follows. Consider a rectangular loop, Γ , that straddles the interface in figure 2. Combining equation 3a with Stokes theorem [5]:

$$\oint \mathbf{E} \cdot d\mathbf{r} = -\frac{d}{dt} \int \mathbf{B} \cdot \hat{\mathbf{u}} dS \quad (17)$$

where $d\mathbf{r}$ is a line element and dS is a surface element. As the lateral extent of the loop is reduced, $dS \rightarrow 0$, and equation 17 reduces to:

$$\hat{\mathbf{u}} \times \mathbf{E}_1 + \hat{\mathbf{u}} \times \mathbf{E}_r = \hat{\mathbf{u}} \times \mathbf{E}_2 \quad (18)$$

Combining equations 16 and 18 one finds that [2]

$$k_1 \sin \theta_1 = k_r \sin \theta_r \quad (19a)$$

$$\omega_1 = \omega_r = \omega_2 \quad (19b)$$

$$k_1 \sin \theta_1 = k_2 \sin \theta_2 \quad (19c)$$

As the incident and reflected waves propagate in the same medium $k_1 = k_r$ and equation 19a implies $\theta_1 = \theta_r$. The equivalence of the incident and reflected angles is known as the law of reflection. Combining equations 19b and 19c and noting that $n = kc/\omega$ one obtains Snell's law, given by [2]

$$n_1 \sin \theta_1 = n_2 \sin \theta_2 \quad (20)$$

The proportion of light that is reflected or refracted for a given polarization is described by the Fresnel equations. The ratio of the complex amplitude of reflected light to the complex amplitude of incident light is termed the reflection coefficient, r . The reflection coefficients for s - and p -polarized waves can be determined in an analogous manner to the procedure used above, with the additional boundary condition that the tangential components of the magnetic field must also be continuous across the interface. One obtains [2]:

$$r_s = \frac{n_1 \cos \theta_1 - n_2 \cos \theta_2}{n_1 \cos \theta_1 + n_2 \cos \theta_2} \quad (21a)$$

$$r_p = \frac{n_1 \cos \theta_2 - n_2 \cos \theta_1}{n_1 \cos \theta_2 + n_2 \cos \theta_1} \quad (21b)$$

The reflectivity, $R = r^*r$ is shown in figure 3 for a typical oil-water interface at $\lambda = 633$ nm. At this frequency, absorption is negligible and the refractive index of each phase can be assumed to be a real number. If the interface is also assumed to be step-like, at Brewster's angle, $\theta_B = \arctan(n_2/n_1)$, all the p -polarized light is transmitted into the second medium.

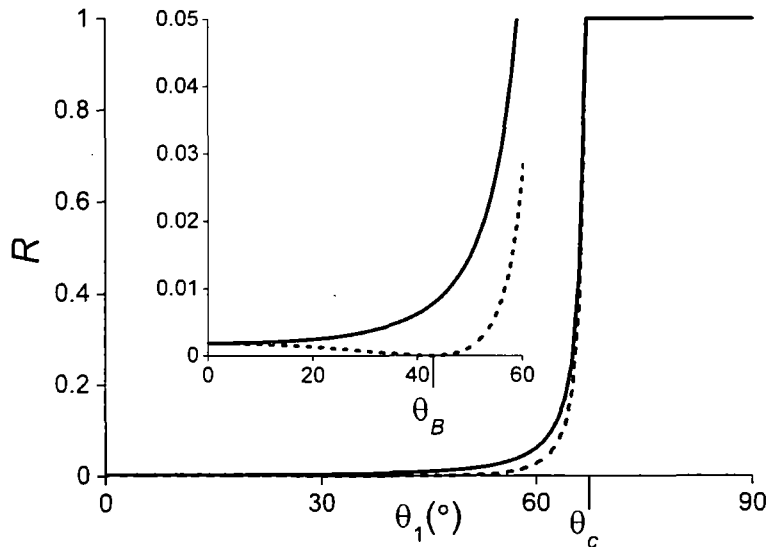


Figure 3. Reflectivity of (solid line) s - and (dashed line) p -polarized light ($\lambda = 633$ nm) at an oil-water interface that is step-like. The inset is an expansion of the main graph at low angles of incidence.

Total internal reflection

Under the assumptions discussed above, above the critical angle, $\theta_c = \arcsin(n_2/n_1)$, all the light that is incident upon the interface is reflected. This phenomenon is termed total internal reflection (TIR) and is very useful for the study of films at interfaces.

Although there is no net energy transfer into the optically rarer medium, the boundary conditions described above must still be met and consequently an electromagnetic field does exist in the second medium, given by [2]

$$\mathbf{E}_2 = \mathbf{E}_{02} e^{i(\mathbf{k}_2 \cdot \mathbf{r} - \omega t)} \quad (22)$$

The components of \mathbf{k}_2 for a p -polarized wave are [2]

$$k_{2x} = k_2 \sin \theta_2 \quad (23a)$$

$$k_{2z} = k_2 \cos \theta_2 \quad (23b)$$

Above the critical angle, θ_2 is a complex number. Snell's law still applies and equation 20 can be substituted into equation 23 to give [2]

$$k_{2x} = \frac{k_2 n_1 \sin \theta_1}{n_2} \quad (24a)$$

$$k_{2z} = ik_2 \sqrt{\frac{n_1^2 \sin^2 \theta_1}{n_2^2} - 1} = i\beta \quad (24b)$$

Consequently the transmitted electric field is given by [2]

$$\mathbf{E}_2 = \mathbf{E}_{02} e^{-\beta z} e^{i\left(\frac{k_2 n_1 \sin \theta_1 x}{n_2} - \omega t\right)} \quad (25)$$

This electromagnetic field propagates along the interface and the amplitude decays exponentially with increasing distance from the interface into the optically rarer phase, and as such the field is known as an evanescent wave. The penetration depth, d_p , of the evanescent wave is

$$d_p = \frac{1}{\beta} = \frac{\lambda_0}{2\pi n_1} \left(\frac{n_1^2 \sin^2 \theta_1}{n_2^2} - 1 \right)^{-1/2} \quad (26)$$

where λ_0 is the wavelength of the incident light *in vacuo*. Raman scattering is proportional to the square of the incident electric field hence the penetration depth of the square of the electric field is $d_p/2$. $d_p/2$ at the hexadecane–water interface for light with $\lambda_0 = 532$ nm is plotted in figure 4 as a function of the angle of incidence.

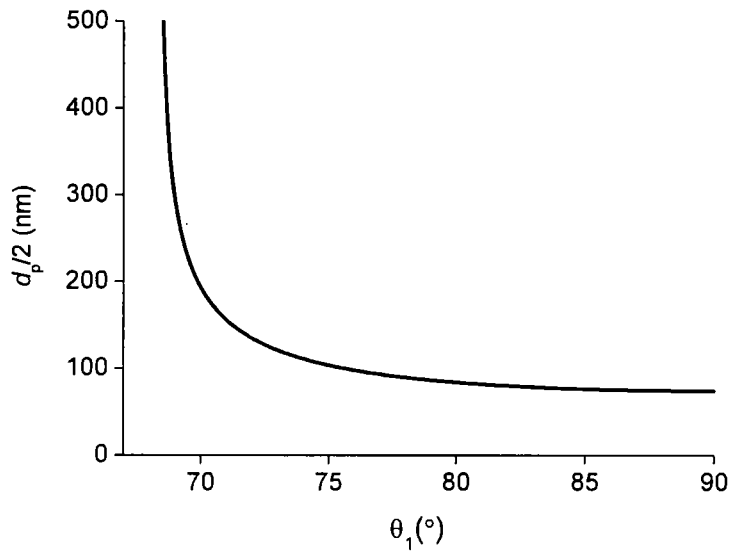


Figure 4. Penetration depth, d_p , plotted as a function of angle of incidence, θ_1 , at the hexadecane–water interface. $n_1 = 1.435$, $n_2 = 1.333$, $\theta_c = 68.3^\circ$.

Therefore the first benefit of the TIR geometry is the volume of the second medium that is influenced by the electric field only extends away from the interface a distance that is the order of the wavelength of the incident light. Consequently this geometry imparts sensitivity to Raman spectroscopy for studying species adsorbed to a surface. The second benefit is the enhancement of the electric field at the interface from the overlap of the incident and reflected beams. The ratios of the components of the electric field at the interface relative to the total electric field in the bulk incident medium are given by the Fresnel factors, K . In the absence of a monolayer at the interface the fields at the interface are given by

$$\begin{aligned}
 E_x &= (1 - r_p) E_p \cos \theta_1 \\
 E_y &= (1 + r_s) E_s \\
 E_z &= (1 + r_p) E_p \sin \theta_1
 \end{aligned}
 \tag{27}$$

so the Fresnel factors are [7]

$$\begin{aligned}
K_{px} &= \frac{2n_1 \cos \theta_1 \cos \theta_2}{n_1 \cos \theta_2 + n_2 \cos \theta_1} \\
K_{sy} &= \frac{2n_1 \cos \theta_1}{n_1 \cos \theta_1 + n_2 \cos \theta_2} \\
K_{pz} &= \frac{2n_2 \cos \theta_1 \sin \theta_1}{n_1 \cos \theta_2 + n_2 \cos \theta_1} \\
K_{sx} &= K_{py} = K_{sz} = 0
\end{aligned} \tag{28}$$

Above the critical angle these factors become complex, so that [7]

$$\begin{aligned}
K_{px} &= \frac{2 \cos \theta_1 (\sin^2 \theta_1 - n_{21}^2) + 2i n_{21}^2 \cos \theta_1 \sqrt{(\sin^2 \theta_1 - n_{21}^2)}}{n_{21}^4 \cos^2 \theta_1 + \sin^2 \theta_1 - n_{21}^2} \\
K_{sy} &= \frac{2 \cos^2 \theta_1 - 2i \cos \theta_1 \sqrt{(\sin^2 \theta_1 - n_{21}^2)}}{1 - n_{21}^2} \\
K_{pz} &= \frac{2n_{21}^2 \cos^2 \theta_1 \sin \theta_1 - 2i \cos \theta_1 \sin \theta_1 \sqrt{(\sin^2 \theta_1 - n_{21}^2)}}{n_{21}^4 \cos^2 \theta_1 + \sin^2 \theta_1 - n_{21}^2}
\end{aligned} \tag{29}$$

where $n_{21} = n_2 / n_1$. The absolute values of these Fresnel factors are plotted in figure 5.

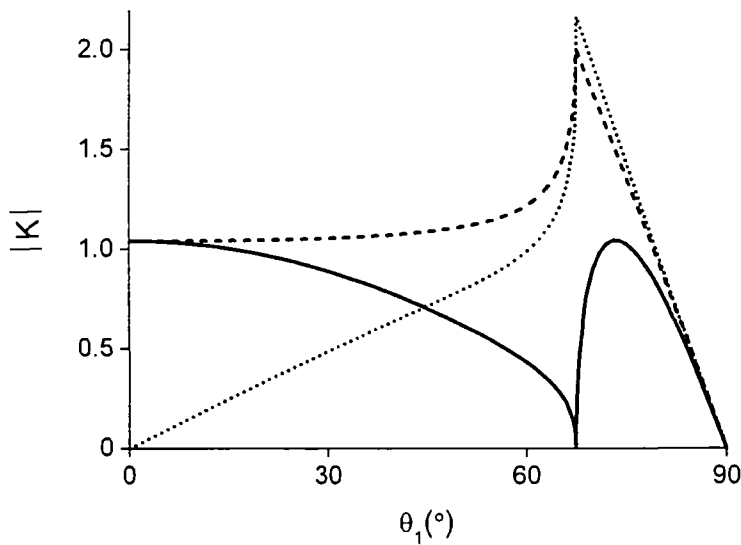


Figure 5. Plots of absolute values of the Fresnel factors, $|K|$, as a function of incident angle at the hexadecane–water interface. (Solid line) px , (dashed line) sy , (dotted line) pz . See figure 4 for conditions.

It is apparent that the overlap of the incident and reflected beam at the interface causes an enhancement in K_{pz} and K_{sy} at the critical angle, whereas K_{px} is zero at this angle. Therefore, operating at the critical angle will cause an enhancement in the electric field and hence an enhancement in the Raman signal. Furthermore, operating at this angle will simplify spectra as p -polarized light creates an interfacial electric field that consists solely of a z -component. This result means that Raman light will only be scattered by certain oscillators in the interfacial region. In practice it is desirable to work a few degrees above the critical angle to limit the penetration depth of the electric field, so the interfacial field created by the p -polarized light will not consist purely of a z -component. Nonetheless detailed orientational information can still be determined from TIR Raman spectra, as discussed below.

2.3 Raman scattering

Molecular vibrations

I have exclusively used vibrational Raman spectroscopies in this work, thus I will now give a short description of the quantum-mechanical theory of molecular vibrations. A nonlinear molecule consisting of N atoms possesses $3N$ degrees of freedom. Six of these degrees of freedom are assigned to translational and rotational motion, which leaves a total of $3N-6$ vibrational modes. In the quantum-mechanical formulation the total energy of an atom or molecule, \mathbf{E} , is determined via the Hamiltonian operator, $\hat{H} = \hat{T} + \hat{V}$, and the time-independent Schrödinger equation, given by [1]

$$\hat{H}\psi = \mathcal{E}\psi \quad (30)$$

For the displacement of a constituent atom, i , with mass m along the coordinate x_i , the kinetic energy operator of the molecule, \hat{T} , is given by [1]

$$\hat{T} = -\frac{\hbar^2}{2} \sum_i \frac{1}{m_i} \frac{\partial^2}{\partial x_i^2} \quad (31)$$

For small displacements from equilibrium, the atoms in a bond respond harmonically and the potential energy operator, \hat{V} , is given by [1]

$$\hat{V} = \frac{1}{2} \sum_{i,j} k_{ij} x_i x_j \quad (32)$$

where the force constant, k_{ij} , is given by [1]

$$k_{ij} = \left(\frac{\partial^2 V}{\partial x_i \partial x_j} \right)_0 \quad (33)$$

The cross-terms in equation 32, $x_i x_j$, can be eliminated by a change of coordinates so that the vibrations are expressed in terms of an orthogonal basis set. This basis set constitutes the normal modes of the molecule, Q_i , which can be determined by group theory. As the new basis set is orthogonal, the Hamiltonian operator, the energy and the wavefunction for each mode are separable, and each normal mode satisfies the following Schrödinger equation [1]

$$-\frac{1}{2} \hbar^2 \frac{\partial^2 \psi_i(Q_i)}{\partial Q_i^2} + \frac{1}{2} \kappa_i Q_i^2 \psi(Q_i) = \mathcal{E} \psi(Q_i) \quad (34)$$

Equation 34 can be solved analytically to give the energy levels for each mode [1]:

$$\mathcal{E} = (v + \frac{1}{2}) \hbar \kappa_i^{1/2} \quad (35)$$

where v is the vibrational quantum number. The effective force constant, κ_i , for a given mode varies depending upon the strength of the bonds and the masses of the atoms involved in the vibration, so different species will vibrate at different characteristic energies. These energies can be probed by vibrational spectroscopies like Raman scattering to gain information about the constituents and environments of molecules.

Equation 35 was derived by assuming that each mode behaves as a harmonic oscillator. In reality equation 32 is only the first term in a power series that reflects the anharmonicity inherent in a chemical bond. Consequently the evenly-spaced hierarchy of vibrational energy levels that is described by equation 35 actually

converges at high ν . Anharmonicity also allows the formation of combination, overtone and Fermi resonance bands, as discussed below.

The Raman effect

Light incident upon a molecule is either scattered or adsorbed. Light is adsorbed if the frequency of the incident photon coincides with the difference in energy between two of the quantum states of the molecule (a situation known as resonance) and if the transition between states causes a change in the dipole moment of the molecule. When these conditions are not met the light is scattered. In a scattering event, the light merely polarizes the electron cloud and the molecule is said to be in a virtual state. These virtual states are not eigenstates of the molecule and the incident photon is rapidly re-emitted. In the vast majority of cases no nuclear motion occurs during the lifetime of the virtual state, there is no change in the populations of the vibrational quantum states and the scattered light has the same energy as the incident light. This elastic scattering process is termed Rayleigh scattering. However, in some cases nuclear motion does occur during the lifetime of the virtual state, there is a change in the populations of the vibrational quantum states and the scattered light has a different frequency to the incident light. This inelastic scattering process is termed Raman scattering and the Raman photons report on the nuclear motion of the molecule. Photons that result from the transition $\Delta\nu = +1$ are termed Stokes bands and those photons that result from the transition $\Delta\nu = -1$ are termed anti-Stokes bands. In spontaneous Raman scattering Stokes bands are observed at a lower frequency than the incident light and anti-Stokes bands are observed at a higher frequency than the incident light. Raman spectra are typically reported as a function of the Raman shift: the difference in wavenumbers between the incident and scattered light. Thus Rayleigh light has a Raman shift of zero, Stokes band exhibit a positive Raman shift and anti-Stokes band have a negative Raman shift. This convention will be adopted throughout this thesis. The number of Raman photons is greatly enhanced if the frequency of the incident radiation coincides with an electronic transition within the molecule. This scenario is termed resonance Raman scattering. The energy level

diagrams for Rayleigh scattering, normal vibrational Raman scattering (Stokes and anti-Stokes bands) and vibrational resonance Raman scattering are shown in figure 6.

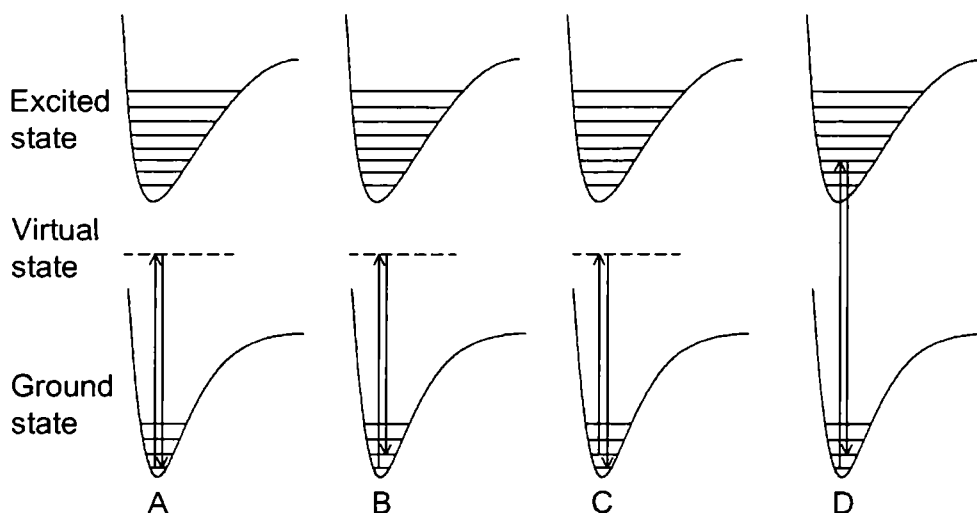


Figure 6. Comparison of the energy level diagrams for (A) Rayleigh scattering, normal Raman scattering ((B) Stokes and (C) anti-Stokes bands) and (D) resonance Raman scattering. Adapted from ref [3].

The normal Raman effect can be well-described by treating both the incident light and the molecule classically. However the classical theory cannot account for excited electronic states and thus it is unable to predict or analyse resonance Raman effects. Therefore I will restrict my discussion to the quantum mechanical description of the molecules, though the light itself will still be treated classically.

Dipole emission

A scattering event, whether Rayleigh or Raman scattering, proceeds via the formation of an induced dipole by the incident field according to equation 8. The induced dipole oscillates at a certain frequency and acts as a source for an electromagnetic field. The radiant intensity, I , produced by a dipole oriented along the z axis and oscillating at a wavenumber $\bar{\nu}$ with amplitude μ can be determined classically and is given by

$$I = \frac{\pi^2 c}{2\epsilon_0} \bar{\nu}^4 \mu^2 \sin^2 \theta \quad (36)$$

where θ is the zenith angle. In the case of Stokes Raman scattering $\bar{\nu} = \bar{\nu}_0 - \bar{\nu}_i$, where $\bar{\nu}_0$ is the incident wavenumber and $\bar{\nu}_i$ is the Raman shift: i.e. the vibrational frequency of a normal mode within a molecule.

Raman scattering is an incoherent process so the emitted intensity is additive and the detected signal scales linearly with the number of scatterers. In practice, the strength of a Raman band is measured from the number of photoelectrons produced by photons striking a charge-coupled device camera, rather than the radiant intensity itself. The number of photons per second, \mathcal{N} , incident upon a detector within an element of solid angle $d\Omega = dA/r^2$ is related to the radiant intensity according to

$$d\mathcal{N} = \frac{I d\Omega}{hc\bar{\nu}} \quad (37)$$

Consequently the count rate is proportional to $\bar{\nu}^3$. As evinced by equation 36, light is not emitted isotropically from a single dipole. A cut-through of isosurfaces of the factor $\sin^2\theta/r^2$ are plotted in figure 7.

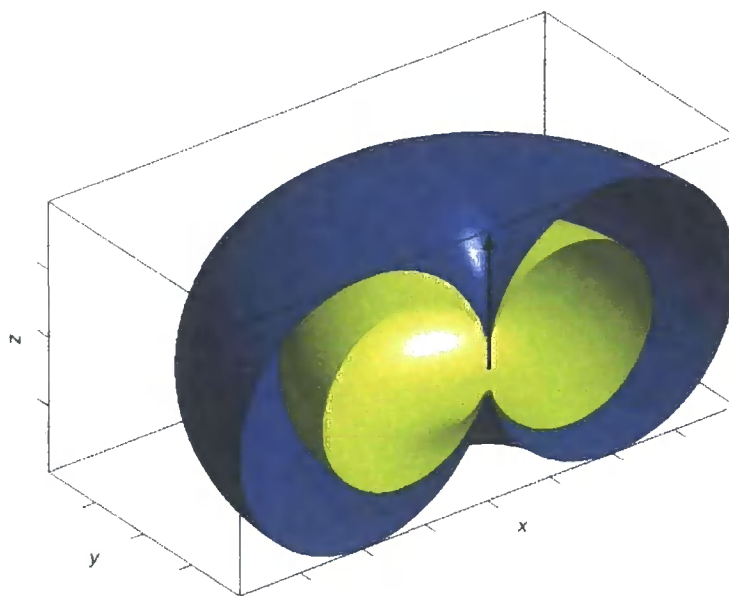


Figure 7. Cut-through of isosurfaces of the factor $\sin^2\theta/r^2$ representing the time-averaged radiation of an oscillating dipole moment aligned along the z -axis. The arrow designates the dipole moment vector.

Figure 7 demonstrates that the energy radiated by an electric dipole is predominantly emitted perpendicular to the dipole moment, with no energy emitted parallel to the dipole. This point is very important when considering the orientational information from Raman spectra of films at interfaces, as described in more detail below.

Selection rules

The electric field vector of light incident upon a molecule can induce a transition between quantum states if the transition dipole moment, $\mu = \langle f | \hat{\mu} | i \rangle$, is nonzero [1]. $\hat{\mu}$ is the electric dipole moment operator and $|i\rangle$ and $|f\rangle$ are the initial and final wavefunctions, respectively. In Raman spectroscopy the electric dipole is induced by the incident field according to equation 8, and the transition dipole moment is given by [1]

$$\boldsymbol{\mu} = \langle f | \hat{\boldsymbol{\alpha}} | i \rangle \mathbf{E} \quad (38)$$

where $\hat{\boldsymbol{\alpha}}$ is the transition polarizability tensor operator. An element of the polarizability tensor, $\alpha_{\rho\sigma}$, can be expanded in a Taylor series in terms of the normal coordinates defined above. To second order [3]:

$$\boldsymbol{\mu} = \left(\left(\frac{\partial \alpha_{\rho\sigma}}{\partial Q_i} \right)_0 \langle f | Q_i | i \rangle + \frac{1}{2} \left(\frac{\partial^2 \alpha_{\rho\sigma}}{\partial Q_i \partial Q_j} \right)_0 \langle f | Q_i Q_j | i \rangle \right) \mathbf{E} \quad (39)$$

Thus a transition is only Raman active if the polarizability varies during a vibration along a normal coordinate. Neglecting anharmonicity and the second order term, the transition is only Raman active for $\Delta\nu = \pm 1$ when $\langle f | Q_i | i \rangle$ is nonzero. This selection rule is relaxed when anharmonicity is included, leading to overtone bands where $|\Delta\nu| > 1$. These overtones are much weaker than the fundamental bands for normal Raman scattering but can become equivalent in intensity for resonance Raman scattering. Anharmonicity also allows more than one mode to be excited simultaneously as exhibited by the cross-terms $Q_i Q_j$ in equation 39. Finally, higher order anharmonicity terms can lead to Fermi resonance bands that are formed by mixing between a fundamental and a combination or overtone band.

Linewidths

Raman spectroscopic lines are not infinitely sharp. As well as the physical and technical issues inherent in the imaging of diffracted light onto a detector, there are also underlying physical restrictions that tend to broaden the lineshapes. These processes can be conveniently divided into homogeneous and inhomogeneous broadening effects, depending on whether they affect all atoms equally or otherwise. All spectroscopic lines experience lifetime broadening. An excited state does not return to the ground state instantaneously but decays exponentially with a time constant, τ . The range of energies, δE , present in the excited state can be determined from the spectral density function [1] whose width at half-height is equal to $\hbar/2\tau$. Thus the lifetime of the excited state broadens the energy of the state according to the

relationship: $\tau\delta E \approx \hbar/2$. Lifetime-broadened peaks are Lorentzian functions, as exemplified by equation 40 below. As the virtual states accessed by Raman scattering are not eigenstates these lifetimes are O(ps) so the lifetime broadening is O(cm^{-1}).

Inhomogeneous broadening in gaseous media occurs principally via the Doppler effect, where the velocity of the molecules relative to the detector causes a spread of frequencies in the detected light. In condensed media the dominant broadening mechanism arises from the molecules finding themselves in a range of environments which experience different inter- and intramolecular interactions. These interactions can also cause the peak positions to shift in a spectrum. Consequently the lineshapes and peak positions in a spectrum can be used to report on the molecular environment. Inhomogeneous broadening in spectra is typically modelled by a Gaussian function, but this assumption is only an estimate as there can be many different factors affecting this type of broadening.

Polarizability tensor elements

The full quantum-mechanical derivation of the polarizability tensor elements follows from time-dependent perturbation theory. From this technique of approximation, $\alpha_{\rho\sigma}$ is given by [3]

$$\alpha_{\rho\sigma} = \frac{1}{\hbar} \sum_{ev} \left\{ \frac{\langle f | \hat{\mu}_\rho | ev \rangle \langle ev | \hat{\mu}_\sigma | i \rangle}{\omega_{ev} - \omega_0 - i\Gamma_{ev}} + \frac{\langle f | \hat{\mu}_\sigma | ev \rangle \langle ev | \hat{\mu}_\rho | i \rangle}{\omega_{ev} + \omega_0 - i\Gamma_{ev}} \right\} \quad (40)$$

where $|i\rangle$ and $|f\rangle$ are the initial and final vibrational wavefunctions in the ground electronic state and $|ev\rangle$ is an excited state. ω_0 and ω_{ev} are the angular frequencies of the incident light and the excited state and Γ_{ev} is the homogenous linewidth of the transition. Far from resonance, $\omega_0 \ll \omega_{ev}$ and the polarizability of a mode is dependent upon the transition moments in the numerator of equation 40. As ω_0 tends to ω_{ev} the first term in equation 40 dominates the expression. Consequently in resonant Raman spectroscopy individual bands can be significantly enhanced, greatly simplifying the spectra.

The origin of the resonant enhancement in equation 40 can be better understood if the vibronic transition moment elements are factored into separate electronic and vibrational components. The polarizability tensor becomes the sum of three terms:

$\alpha_{p\sigma} = A + B + C$, where A is given by [3]:

$$A = \frac{1}{\hbar} \langle g | \hat{\mu}_p | e \rangle \langle e | \hat{\mu}_\sigma | g \rangle \sum_{ev} \frac{\langle f | v \rangle \langle v | i \rangle}{\omega_{ev} - \omega_0 - i\Gamma_{ev}} \quad (41)$$

and $|g\rangle$ and $|e\rangle$ are the ground and excited electronic states and $|v\rangle$ is the vibrational level in the excited electronic state. These three terms demonstrate different enhancement mechanisms. The A -term transition is allowed if the vibrational wavefunctions are not orthogonal so that the Franck-Condon factors, $\langle f | v \rangle \langle v | i \rangle$, are nonzero. This non-orthogonality can arise in two ways: either the vibrational frequency is different in the ground and excited electronic state and/or there is a displacement of the potential energy minimum along the normal coordinate, Q_i . This displacement can only occur for totally symmetric modes unless the symmetry is broken in the excited state by, for example, a Jahn-Teller distortion. The four situations that can arise are shown in figure 8.

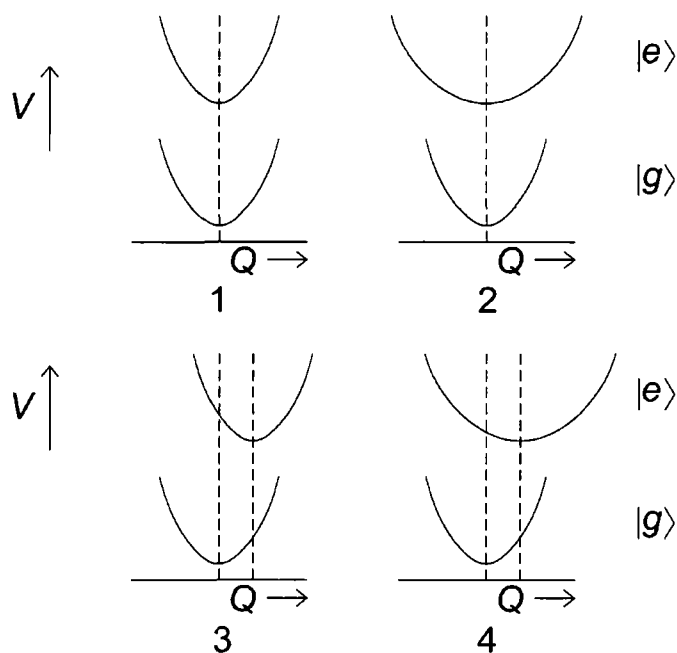


Figure 8. Schematics of the four potential energy diagrams associated with A -term resonant enhancement. Adapted from ref [3].

In case 1 in figure 8, the wavefunctions are orthogonal and the A term in this case is zero. The remaining cases all lead to A -term enhancement, but case 3 is the most common.

B -term enhancement occurs through the dependence of the transition moments upon vibrational motion, such as through Herzberg-Teller vibronic coupling, and can occur for both symmetric and nonsymmetric transitions. In Herzberg-Teller vibronic coupling an electronically forbidden transition steals intensity from an electronically-allowed transition. Finally, C -term enhancement involves the enhancement of overtone or combination bands. If allowed, the A -term is the dominant term, but for nonsymmetric transitions where this term is forbidden the intensity attributed to the B - and C -terms becomes appreciable.

The intensities of vibrational resonance Raman bands are dependent upon the electronic states of a molecule. Thus by varying the frequency of the incident beam

one can generate a resonance Raman excitation profile. These profiles inform upon the excited state dynamics for gas-phase studies.

Molecular orientation information from TIR Raman spectra

Molecules confined at an interface may orient in a repeatable and consistent manner over lengthscales that are larger than the wavelength of incident light. The presence of a well-defined interfacial plane and plane of incidence provides a link between the molecular coordinates and the lab-based coordinates. Thus if the molecules are illuminated by polarized light and the polarization of the scattered light is similarly analyzed, it is possible to infer information about the orientation of the confined molecules. This process proceeds as follows. One acquires a series of spectra with different polarization combinations of the incident and scattered light. The signal levels for the different peaks within the spectrum are related to the polarizability tensor elements in laboratory-based coordinates according to the collection geometry and via equation 36. One then compares the experimentally-determined tensor elements in lab-based coordinates with a model of the tensor elements in molecule-based coordinates generated by each mode within a scattering molecule. This model can then be compared to the experimental data in order to draw conclusions on the orientation of the scattering molecules relative to the interface. I will first describe the polarization combinations that are accessible in TIR Raman scattering and I will then describe the generation of a typical model.

The polarizability tensor is a second-rank tensor, thus in lab-based coordinates equation 8 is given explicitly by

$$\begin{bmatrix} \mu_x \\ \mu_y \\ \mu_z \end{bmatrix} = \begin{bmatrix} \alpha_{xx} & \alpha_{xy} & \alpha_{xz} \\ \alpha_{yx} & \alpha_{yy} & \alpha_{yz} \\ \alpha_{zx} & \alpha_{zy} & \alpha_{zz} \end{bmatrix} \begin{bmatrix} E_x \\ E_y \\ E_z \end{bmatrix} \quad (42)$$

The subscripts $\rho\sigma$ denote the direction of the polarizability response and the incident field, respectively.

All the Raman spectra in this thesis are collected via a microscope with the optical axis in the z -direction (see figure 4 in chapter 6 in particular). The microscope objective collects a cone of light with a half-angle, β , whose extent is determined by the numerical aperture, NA . For an air-immersion objective with $NA = 0.5$, $\beta = \sin^{-1} 0.5 = 30^\circ$. A dipole aligned along the z -axis does not emit in the z -direction (see figure 7). Thus in this geometry we collect the following proportion of light from dipoles aligned along the z -axis:

$$\frac{\int_0^{\pi/2} \int_0^{2\pi} \sin^3 \theta d\theta d\phi}{\int_0^{\pi} \int_0^{2\pi} \sin^3 \theta d\theta d\phi} = \frac{\left(\frac{4}{3} - \frac{3\sqrt{3}}{4}\right)\pi}{8\pi/3} = 0.013 \quad (43)$$

To determine the proportion of light that we collect from dipoles oriented along either the x or y axis, we proceed as follows. We maintain the same geometry as shown in figure 7 with the dipole aligned along the z axis but we align the axis of the objective along the x axis as shown in figure 9.

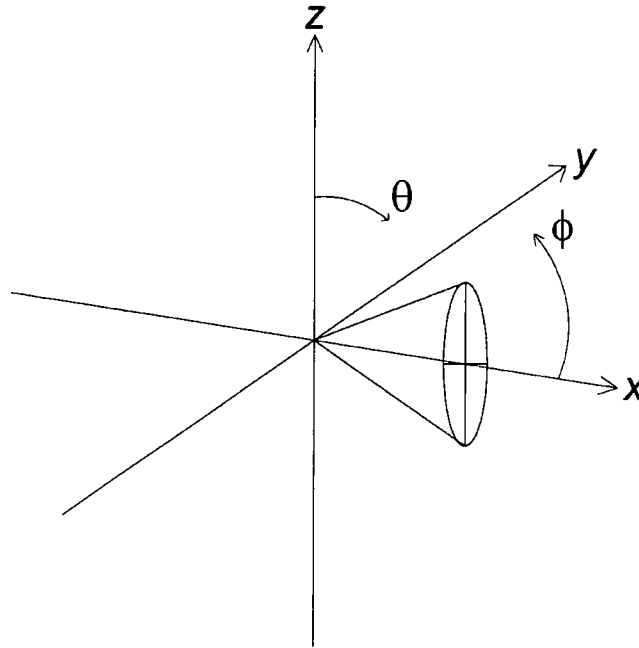


Figure 9. Geometry of acceptance cone of objective aligned along x axis.

To solve the problem we must recalculate the limits of the integral. We use the symmetry of the base of the acceptance cone and determine the limits for the shaded quadrant in figure 9. θ varies between $\frac{\pi}{3}$ and $\frac{\pi}{2}$ but the limits of ϕ are a function of θ . The formula for the base of the acceptance cone of the objective (with unit radius) is:

$$z^2 + y^2 = \cos^2 \theta + \sin^2 \theta \sin^2 \phi = \frac{1}{4} \quad (44)$$

so $\phi = \cos^{-1} \left[\frac{\sqrt{3}}{2 \sin \theta} \right]$. Thus the fraction of light collected by the objective in this configuration is:

$$\frac{4 \int_{\frac{\pi}{3}}^{\frac{\pi}{2}} \sin^3 \theta d\theta \int_0^{\cos^{-1} \left(\frac{\sqrt{3}}{2 \sin \theta} \right)} d\phi}{\int_0^{\pi} \int_0^{2\pi} \sin^3 \theta d\theta d\phi} = \frac{4 \int_{\frac{\pi}{3}}^{\frac{\pi}{2}} \sin^3 \theta \cos^{-1} \left(\frac{\sqrt{3}}{2 \sin \theta} \right) d\theta}{8\pi/3} = \frac{0.786}{8\pi/3} = 0.094 \quad (45)$$

where the integral in the numerator has been calculated numerically. Therefore, in this geometry we collect over seven times as much light from dipoles oriented along

either the x or y axis: μ_x and μ_y will dominate the spectra in this geometry. In order to collect more of the light from dipoles oriented along the z -axis one must move the collection optics towards the xy plane.

The four polarization combinations that we define in a TIR geometry are sx , sy , px and py , where the indices denote the polarization of the incident and scattered light respectively. At an interface for a film with uniaxial symmetry illuminated by light that is far from resonance, there are only four independent components of α : $\alpha_{xx} = \alpha_{yy}$, $\alpha_{zx} = \alpha_{xz} = \alpha_{yz} = \alpha_{zy}$, $\alpha_{xy} = \alpha_{yx}$ and α_{zz} . (n.b. At resonance, the assumption $\alpha_{\rho\sigma} = \alpha_{\sigma\rho}$ breaks down, as exemplified by equation 40) For the four possible polarization combinations the linear equations in equation 42 are reduced to the expressions in table 1.

Polarization combination	Detected dipole moment response
sx	$\mu_x = \alpha_{xy} E_y$
sy	$\mu_y = \alpha_{xx} E_y$
px	$\mu_x = \alpha_{xx} E_x + \alpha_{xz} E_z$
py	$\mu_y = \alpha_{xy} E_x + \alpha_{xz} E_z$

Table 1. Dipole moment responses for the four polarisation combinations accessible in a TIR Raman experiment.

Every molecule can be assigned to a certain point group, depending upon which symmetry operations leave the molecule unchanged. Individual moieties within a molecule can also be crudely associated with point groups, for example the CH_2 group in an alkane chain has C_{2v} symmetry whereas the indole ring in the amino acid tryptophan has C_s symmetry. Each vibrational normal mode can be associated with an irreducible representation of the point group, for example the methylene antisymmetrical stretch has B_1 symmetry. A mode will only be Raman-active if the mode belongs to the same symmetry species as a component of the electric polarizability. This property follows from the fact that the Dirac bracket in equation 37 will only be non-zero if the integrand is even. The three terms in the integral are

the ground state, which is always totally symmetric, the polarizability operator and the excited state. The product of these final two terms, and hence the integrand as a whole, will only be even if both terms belong to the same irreducible representation. This symmetry restriction reduces the number of independent elements in the Raman polarizability tensor. In the case of the methylene antisymmetrical stretch there is only one Raman-active element: α_{ac} where a is perpendicular to the CH_2 plane and c is parallel to the C_2 rotation axis. The molecular tensor elements are then rotated in terms of the Euler angles into the lab-based basis set. These three Euler angles are variables in the model and for scattering from multiple sources the angles will be a spread over a distribution. Thus the tensor elements from the model must be orientationally averaged for comparison with experimental results.

References

- 1 P. W. Atkins and R. S. Friedman, *Molecular Quantum Mechanics* 3rd ed. (Oxford University Press, Oxford, 1997).
- 2 E. Hecht, *Optics* 3rd ed. (Addison Wesley Longman, Inc., Reading, MA, 1998).
- 3 D. A. Long, *The Raman Effect* 1st ed. (John Wiley and Sons, Ltd., Chichester, 2002).
- 4 Non-linear optical techniques, C. D. Bain, in *Modern characterization methods of surfactant systems*, edited by B. P. Binks (Marcel Dekker, Inc., New York, 1999).
- 5 R. P. Feynman, R. B. Leighton, and M. Sands, *The Feynman Lectures on Physics, Volume II* 6th ed. (Addison-Wesley, Reading, MA, 1977).
- 6 R. P. Feynman, R. B. Leighton, and M. Sands, *The Feynman Lectures on Physics, Volume I* 6th ed. (Addison-Wesley, Reading, MA, 1977).
- 7 D. A. Beattie, S. Haydock, and C. D. Bain, *Vib Spectrosc* **24**, 109 (2000).

Chapter 3

Ellipsometric study of depletion at oil–water interfaces

3.1 Introduction

The density profile at a fluid interface is not a step; the density variation typically occurs over a few molecular diameters as predicted by classical van der Waals theory [1]. At the air–water interface this profile is monotonic. Lum, Chandler and Weeks have postulated that at the interface between water and a hydrophobic solute, anisotropy in the intermolecular forces may lead to depletion (reduced water density) or accretion (increased water density), depending on the size of the solute [2]. For a planar interface, a depletion or ‘drying’ layer was predicted. In this work, I have employed ellipsometry to investigate density profiles at oil–water interfaces and the effect of the molecular structure of the oil on these profiles.

The nature of the pristine interface between oil and water has been extensively investigated by various experimental techniques, including x-ray [3] and neutron reflection [4], sum-frequency [5, 6] and second harmonic generation [7] and ellipsometry [5, 8], as well as by molecular dynamics simulations [9-13]. Nevertheless, the debate in the literature as to the nature of the density profile at the oil–water interface continues [14-16]. My work was stimulated by the observation that the ellipticity of the hexadecane–water interface is of opposite sign to that expected for a simple, thermally roughened interface. Ellipsometry is exquisitely sensitive to the optical density profile at an interface and, although the interpretation of ellipsometry measurements is model-dependent, the reversal of the sign itself suggests that ellipsometry may be a useful tool to investigate the behaviour of the mass density profile at the oil–water interface.

In ellipsometry, a polarized light beam is reflected from a surface and the change in the polarization of the light is detected [17]. The coefficient of ellipticity, $\bar{\rho}$, is defined as $\text{Im}(r_p/r_s)$ at the Brewster angle, θ_B , where r_p and r_s are the reflection coefficients for p and s-polarized light and θ_B is the angle where $\text{Re}(r_p/r_s) = 0$. When

the thickness of the interfacial region is much less than the wavelength, λ , of the incident light, a single interfacial parameter, η , with dimensions of length and known as the ellipsometric thickness, determines $\bar{\rho}$ [18]:

$$\bar{\rho} = \frac{\pi}{\lambda} \frac{\sqrt{\varepsilon_1 + \varepsilon_2}}{(\varepsilon_1 - \varepsilon_2)} \eta \quad (1)$$

where ε_1 and ε_2 are the relative permittivities of oil and water, respectively, at wavelength, λ . In the presence of a thin isotropic film, the Drude equation relates η to the permittivity profile normal to the surface [18, 19]:

$$\eta = \int \frac{(\varepsilon - \varepsilon_1)(\varepsilon - \varepsilon_2)}{\varepsilon} dz \quad (2)$$

The Drude equation can also be extended to describe a uniaxial film with different permittivities parallel, ε_o , and perpendicular, ε_e , to the interface [20, 21]:

$$\eta = \int \frac{(\varepsilon_e - \varepsilon_1)(\varepsilon_e - \varepsilon_2)}{\varepsilon_e} + (\varepsilon_o - \varepsilon_e) dz \quad (3)$$

There are two alternative ways to treat thermal roughening of the interface; either as a modulation of the shape of a sharp interface by capillary waves or as a smooth monotonic variation in the density profile between bulk values. In the first instance, coupled mode theory predicts the roughness contribution to the ellipticity, $\bar{\rho}_{r1}$, to be [22]

$$\bar{\rho}_{r1} = -\frac{3\pi(\varepsilon_1 - \varepsilon_2)}{2\lambda\sqrt{\varepsilon_1 + \varepsilon_2}} \sqrt{\frac{\pi k_B T}{6\gamma_{ow}}} \quad (4)$$

where γ_{ow} is the interfacial tension. At the air–water surface, $\varepsilon_1 < \varepsilon_2$ and equation 4 predicts that the ellipticity of the pristine surface is positive. In contrast, for the oil–water interfaces studied in this work, $\varepsilon_1 > \varepsilon_2$ and equation 4 predicts negative ellipticities. This formula has been used extensively to describe roughening at the air–liquid interface and gives the correct sign and variation with temperature and surface tension, although it overestimates the ellipticity of the air–water interface by 40% [22]. In the second instance, a suitable functional form is chosen for the density

profile normal to the interface and an effective medium approximation (EMA) is used to calculate the permittivity profile. This profile is used in the Drude equation to calculate η . While one can debate the meaning of a local dielectric function on a length-scale smaller than that of a molecule, the treatment of ellipsometry in terms of a continuously varying dielectric constant is well-established in the literature [23, 24]. Lekner has derived equation 2 to second order in the interface thickness for an arbitrary dielectric profile [19].

In the Results and Discussion sections, I first present ellipsometric data for a series of non-polar and polar oils on water. I then use two alternative models to provide a quantitative microscopic description of these results within a simple physical framework. Finally, I will place my work into context with other related studies on the oil–water interface.

3.2 Experimental

Materials

Octane ($\geq 99\%$), tridecane ($\geq 99\%$), tetradecane ($\geq 99\%$), hexadecane ($\geq 99\%$), isooctane (99.8%), squalane (99%), 2,2,4,4,6,8,8-heptamethylnonane (98%), 1,3-dimethyladamantane (DMA) ($\geq 99\%$), *cis*-decalin (99%), *trans*-decalin (99%), toluene ($\geq 99.9\%$), 1,2,3,4-tetrahydronaphthalene (99%), squalene ($\geq 98\%$), dibutyl ether (99.3%), 5-nonanone (98%), cyclohexylacetate (99%), ethyl acetate (99.8%) and 3-pentanone ($\geq 99\%$) were purchased from Aldrich. Butyl butanoate ($\geq 99\%$) and 5-nonanol ($\geq 99.5\%$) were purchased from Fluka. All oils were purified by passing three times through a column of activated neutral alumina. The purity of the alkanes was checked by a Zisman test [25]. A small drop of the oil was placed on the surface of acidic ($\text{pH} < 4$) and basic ($\text{pH} > 10$) aqueous solutions and the flask covered with a watch glass to limit evaporation. The oil was classed as pure if the diameter of the lens did not increase visibly over a period of several hours. To check the purity of the other oils, the oil–water interfacial tension was monitored as a function of time; for all the oils, the time-averaged interfacial tension varied by less

than 0.1 mN m^{-1} over ten minutes. Interfacial tensions were measured at 293 K by axisymmetric drop shape analysis (FTA200, First Ten Ångstroms) on a rising bubble of oil in water. Polar oils with appreciable mutual solubility with water were shaken with water and stored in contact with water overnight to equilibrate. Ultrahigh purity (UHP) water from a Millipore MilliQ system was used throughout. Glassware and the ellipsometry cell were cleaned by sonication in alkaline detergent (Decon 90) followed by rinsing in UHP water, sonication in acetone, thorough rinsing in UHP water and finally drying in a stream of dry air.

Ellipsometry

The Beaglehole Picometer is a phase-modulated ellipsometer. This design differs from the more conventional null ellipsometer as it uses a birefringence modulator and lock-in amplifiers to extract the small ellipticities commonly measured for monolayers at liquid surfaces. A schematic of the ellipsometer is shown in figure 1.

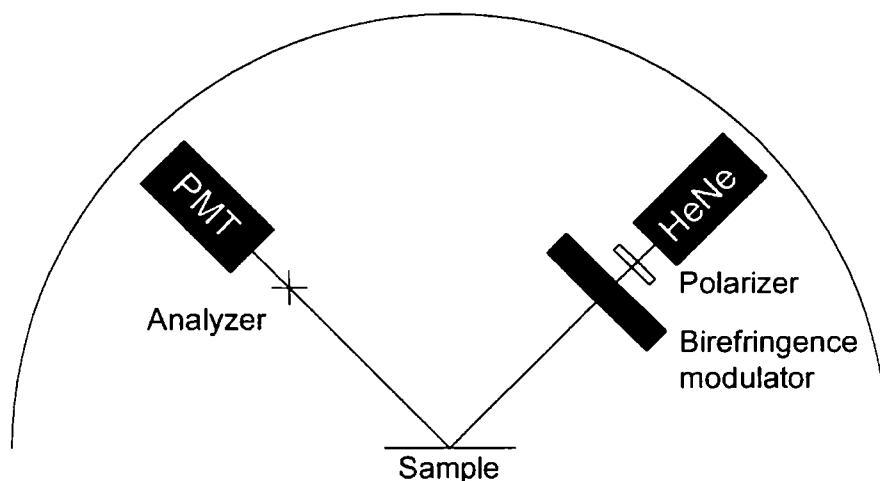


Figure 1. Schematic of the Beaglehole Picometer ellipsometer.

The ellipsometer consists of a large disc mounted vertically in the laboratory plane. Two rotating arms are mounted on the disc and these arms are driven by stepper motors to vary the angle of incidence. A 3-mW continuous-wave plane-polarized

HeNe laser beam ($\lambda = 633 \text{ nm}$) is mounted on one rotating arm of the ellipsometer and directed towards the sample which is positioned at the centre of the disc. The laser is mounted with the polarization of the electric field vector at 45° to the vertical. The polarizer is mounted vertically in front of the laser, so that equal intensities of p - and s -polarized light are transmitted through the polarizer. The light beam then passes through the birefringence modulator. This component consists of a slab of isotropic fused silica of thickness d which is connected at either end to two piezoelectric quartz crystals. An ac voltage is applied to one of the piezoelectric quartz crystals which causes the fused silica to vibrate at a frequency, ω , of 50 kHz. The other crystal is part of a feedback loop which maintains the oscillation at a constant amplitude. The 50 kHz vibration creates a periodic strain on the fused silica slab which modulates the refractive index of the fused silica. This modulation is principally along the axis of the vibration. Consequently the fused silica slab becomes birefringent, with the phase shift, δ , varying sinusoidally at 50 kHz according to [26]:

$$\delta = \frac{2\pi\Delta n d}{\lambda} = \delta_0 \sin(\omega t) \quad (5)$$

where Δn is the maximum difference in the refractive indices perpendicular and parallel to the axis of vibration, δ_0 is the phase amplitude and t is the time. Consequently the light striking the sample is elliptically polarized with the degree of ellipticity varying at 50 kHz.

The light reflected by the sample passes through the analyser, which consists of two orthogonal polarizer plates angled at 45° to the vertical. These plates are attached to an arm that alternates which plate lies in the beam at a frequency of 1.5 Hz. The analyzer is modulated to correct small offsets caused by stray birefringence or the lock-in amplifiers. Finally the light strikes a photomultiplier tube (PMT) and the intensity of the signal is detected. The real and imaginary parts of the ellipticity are extracted from the PMT signal by two lock-in amplifiers and read out on a PC.

As noted above, one of the key benefits of using a phase-modulation technique is that small changes in the ellipticity can be readily extracted from a large background by

the lock-in amplifiers. The intensity of light measured by the PMT is converted to ellipticity in the following manner. The light intensity is given by [27]:

$$I = \frac{I_0 \rho_s^2}{4} (1 + \rho^2 + 2\rho \cos(\Delta + \delta)) \quad (6)$$

where $r = r_p / r_s$, $\rho = |r|$, ρ_s is the ellipticity caused by stray birefringence (for perfect optics, $\rho_s = 1$) and $\Delta = \delta_s - \delta_p$ is the difference in the phase angles for light s and p -polarized light. Expanding the cosine sum in equation 6 and substituting equation 5 one obtains

$$I = \frac{I_0 \rho_s^2}{4} (1 + \rho^2 + 2 \operatorname{Re}(r) (J_0(\delta_0) + 2J_2(\delta_0) \cos(2\omega t)) - 2 \operatorname{Im}(r) (2J_1(\delta_0) \sin(\omega t))) \quad (7)$$

where $\cos(\delta_0 \sin \omega t)$ and $\sin(\delta_0 \sin \omega t)$ have been expanded in terms of the n -th order spherical Bessel functions, J_n [28].

This expression contains a time-invariant dc component, a component varying at $\omega = 50$ kHz, $ac(\omega)$, and a component varying at $2\omega = 100$ kHz, $ac(2\omega)$. These components are extracted by the lock-ins and sent to a PC. The PC program that controls the ellipsometer normalizes the ac terms by the dc term to give [27]:

$$Y = \frac{ac(\omega)}{dc} = \frac{-4J_1(\delta_0) \operatorname{Im}(r)}{1 + \rho^2 + 2J_0(\delta_0) \operatorname{Re}(r)} \quad (8)$$

$$X = \frac{ac(2\omega)}{dc} = \frac{4J_2(\delta_0) \operatorname{Re}(r)}{1 + \rho^2 + 2J_0(\delta_0) \operatorname{Re}(r)} \quad (9)$$

In operation, δ_0 is adjusted to ~ 2.4 radians so that J_0 is zero. The ellipsometer is calibrated by driving the arms to an angle of incidence equal to 90° (straight through) and a quarter-wave plate is inserted into the beam so that $\rho = 1$, $r = i$, and $Y_{cal} = 2J_1(\delta_0)$. When a measurement is taken, the angle of incidence is adjusted so that $X = \operatorname{Re}(r) = 0$. For all the measurements in this thesis ρ is small so that $\operatorname{Im}(r) = Y / 2Y_{cal}$, except for the case of multiple angle-of-incidence ellipsometry where the full expression $Y / Y_{cal} = 2 \operatorname{Im}(r) / (1 + \rho^2)$ is used.

Ellipsometry cell

The ellipsometry cell was based on a design by Benjamins [29] to ensure a planar interface between the oil and water phases. The cross-section of the cell is shown in figure 2.

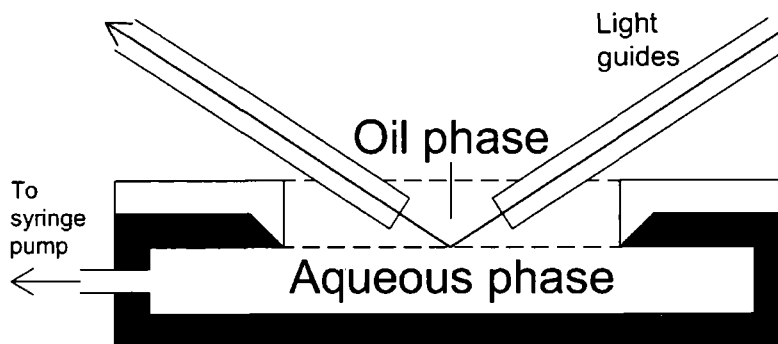


Figure 2. Cross-section of the ellipsometry cell and light guides. The white region is manufactured from Teflon and the black region from stainless steel. Not to scale.

The stainless steel body of the cell has an overhanging lip and is capped by a tight-fitting Teflon ring, so that the interface is pinned at the steel–Teflon intersection. The aqueous phase was introduced into the stainless steel body from a 5-ml gas-tight syringe (Hamilton, Reno, NV) via a sidearm and the precise volume was controlled by an infuse–withdraw syringe pump (11 Plus, Harvard Apparatus, Holliston, MA). The cell was filled with water to the bottom of the overhanging lip, and the oil phase was introduced on top with a pipette. The volume of the aqueous phase was adjusted until the reflected laser beam had a circular cross-section, indicative of a planar interface. The laser beam passed through two light guides immersed in the oil phase, as described by Benjamins [29]. The guides were constructed from 5-mm o.d. nmr tubes with their ends ground flat and glued to sections of optical microscopy coverslips with Araldite. The coefficient of ellipticity of pure water in the cell was measured to check the cleanliness of the cell. The effect of the light guides on the ellipticity was determined in the same way. In both cases, the ellipticity was measured to be within the range $\bar{\rho} = (3.8 \pm 0.3) \times 10^{-4}$, a typical level of experimental

precision for this ellipsometer. The ellipticity of each oil–water interface was measured three times for two minutes at a time. The cell was then cleaned and reassembled and the procedure repeated for the same oil twice more, giving a total of three sets of three readings for each oil. All experiments were performed at room temperature (293 K).

3.3 Results

Figure 3 displays the coefficients of ellipticity, $\bar{\rho}$, measured for the linear alkanes (■), as a function of refractive index of the oil phase, $n_1 = \sqrt{\epsilon_1}$, given in table 1.

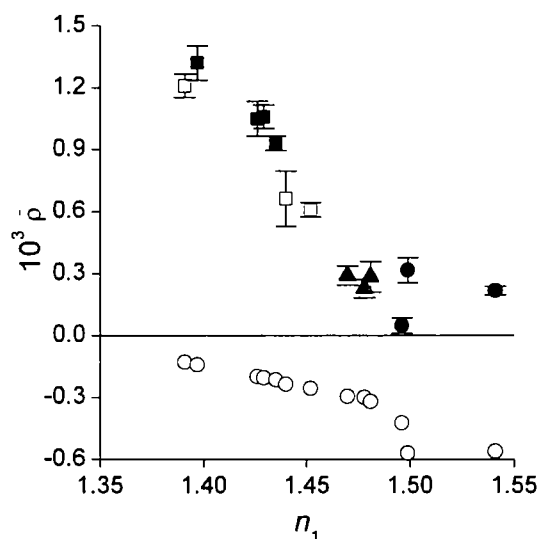


Figure 3. Coefficient of ellipticity, $\bar{\rho}$, of the oil–water interface as a function of refractive index of the oil phase, n_1 , for series of linear alkanes (■), branched alkanes (□), cyclic alkanes (▲) and unsaturated oils (●). The expected roughness contribution from coupled-mode capillary wave theory is also shown for each oil (○).

Oil	n_1	$10^3 \bar{\rho}$	γ_{ow} (mN m ⁻¹)	$10^3 \bar{\rho}_{r1}$
Octane	1.397 ^a	1.32	51.7 ^e	-0.14
Tridecane	1.426 ^a	1.05	52.2 ^f	-0.20
Tetradecane	1.429 ^a	1.06	53.3 ^e	-0.21
Hexadecane	1.435 ^a	0.93	53.8 ^e	-0.22
Isooctane	1.391 ^b	1.21	49.3 ^g	-0.13
Heptamethylnonane	1.440 ^c	0.66	48.8 ^f	-0.24
Squalane	1.452 ^a	0.61	52.3 ^h	-0.26
<i>trans</i> -Decalin	1.470 ^a	0.29	51.4 ^e	-0.30
DMA	1.478 ^d	0.23	56.7 ^f	-0.30
<i>cis</i> -Decalin	1.481 ^a	0.29	51.7 ^e	-0.32
Toluene	1.496 ^a	0.05	35.7 ^g	-0.42
Tetrahydronaphthalene	1.541 ^a	0.22	33.0 ^f	-0.56
Squalene	1.499 ^a	0.32	20.3 ^f	-0.57

Table 1. Refractive index, n_1 , coefficient of ellipticity, $\bar{\rho}$, interfacial tension, γ_{ow} and roughness contribution to ellipticity (eq. 4), $\bar{\rho}_{r1}$, for series of non-polar oils. n_1 is given for $\lambda = 589$ nm whereas the ellipsometer uses a HeNe laser at 633 nm; none of the oils have significant dispersion at visible wavelengths. ^a D. L. Lide, *Handbook of Chemistry and Physics* (CRC Press, Boca Raton, 1993). ^b H. Kalall, F. Kohler, and P. Suejda, *J. Chem. Eng. Data* **37**, 133 (1992). ^c G. Korosi, and E. Kovats, *J. Chem. Eng. Data* **26**, 323 (1981). ^d A. Schneider, R. W. Warren, and E. J. Janoski, *J. Am. Chem. Soc.* **65**, 5365 (1964). ^e F. M. Fowkes, *J. Phys. Chem.* **84**, 510 (1980), ^f this work, ^g J. E. Shewmaker, C. E. Vogler, and E. R. Washburn, *J. Phys. Chem.* **58**, 945 (1954). ^h F. L. Riddle, and F. M. Fowkes, *J. Phys. Chem.* **112**, 3259 (1990).

I calculated the expected contribution to $\bar{\rho}$ from thermal roughening with equation 4, the values of n_1 in table 1 and a value of ϵ_2 for water of 1.774; these values are shown in figure 3 as open circles (\circ). It is immediately evident that the simple picture of a sharp interface between two homogeneous bulk phases roughened by capillary waves does not explain the experimental results: not even the sign of $\bar{\rho}$ is correct. A positive value of $\bar{\rho}$ can conceivably arise from three sources: alignment of

molecules, a dip in the density profile in the aqueous phase or a peak in the density profile of the oil phase. Molecular dynamic simulations often predict oscillations in the water and oil densities at the interface [10, 12, 13]. These oscillations arise from packing effects and vary around a mean density. Ellipsometry is not sensitive to the oscillations themselves, only to the mean density upon which the oscillations are superimposed.

To assess the possible role of anisotropy in yielding positive values of $\bar{\rho}$ for alkanes, I selected a series of hydrocarbons with different molecular architectures. Anisotropy in the refractive indices of a uniaxial linear alkane film arises from the difference in the polarizability of these molecules along and perpendicular to the principal molecular axis. If hydrocarbon chains were to have a preferential alignment normal to the interface, then ϵ_e would be greater than ϵ_o and the ellipticity would be negative. For chains lying parallel to the interface $\epsilon_o > \epsilon_e$, resulting in a positive contribution to $\bar{\rho}$. Branched or cyclic alkanes exhibit a more nearly spherical polarizability ellipsoid, hence if the positive ellipticity of linear alkanes is caused by a uniaxial film at the interface I should see a reduction in the ellipticity for cyclic and branched alkanes. The measured ellipticities for a series of cyclic (\blacktriangle) and branched alkanes (\square) are also plotted in figure 3. Although the absolute magnitude of the ellipticity for most of these oils is lower than for the linear alkanes, all the data fall on the same line when plotted against the refractive index of the oil phase (*vide infra*). To assess the effect of architecture, it is instructive to consider two pairs of oils. First, the structural isomers octane and isooctane have very similar refractive indices and ellipticities that differ by less than 1×10^{-4} . For heptamethylnonane and hexadecane again with similar refractive indices – the variation in ellipticity is slightly larger, but still less than 3×10^{-4} . The close agreement between the linear and highly branched alkanes suggests that anisotropy is not the major factor determining the positive ellipticities. Indeed, the ellipticity for 1,3-dimethyladamantane (DMA) is still positive, despite the fact that this molecule is nearly spherical and hence is unable to form an optically anisotropic layer at the interface. I also measured $\bar{\rho}$ for the interfaces between pure water and two aromatic oils and one olefin (\bullet). All three of these oils give small

positive values for $\bar{\rho}$; the behaviour is not dramatically different from the saturated alkanes.

If the origin of the positive ellipticity for the simple hydrocarbon–water interface is related to the hydrophobicity of the interface then I expect that increasing the polarity of the oil phase will cause the ellipticity of the interface to approach the capillary wave prediction. To test this hypothesis, I measured the ellipticity for a series of alkanes functionalized with polar ether, ketone and ester groups (table 2). As ellipsometry is so sensitive to anisotropy at the interface, I chose molecules that are not potentially amphiphilic. I have plotted $\bar{\rho}$ for these compounds as a function of n_1 in figure 4A and as a function of interfacial tension, γ_{ow} , in figure 4B; the datum for hexadecane is included in the plots for comparison.

Oil	$10^3 \bar{\rho}$	γ_{ow} (mN m ⁻¹)	$10^3 \bar{\rho}_{r1}$
Ethyl acetate	-0.15	6.80	-0.21
3-pentanone	0.09	9.00	-0.29
Dibutyl ether	0.83	27.6	-0.20
Butyl butanoate	0.27	21.4	-0.25
5-nonanone	0.57	22.8	-0.28
5-nonanol	0.13	18.3	-0.35
Cyclohexyl acetate	-0.15	17.8	-0.39

Table 2. Measured ellipticity, $\bar{\rho}$, interfacial tension, γ_{ow} , and contribution to ellipticity from thermal roughening, $\bar{\rho}_{r1}$, for a series of polar oils.

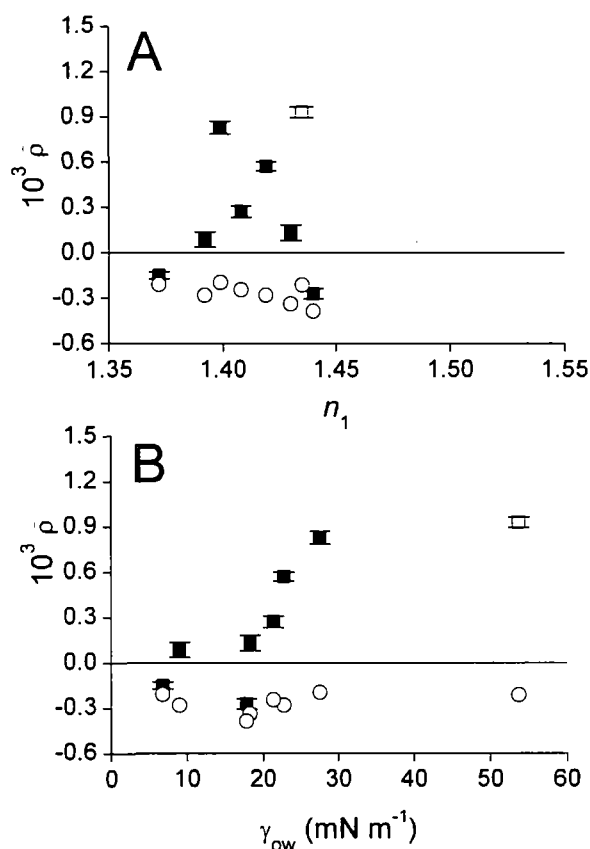


Figure 4. (A) Coefficient of ellipticity, $\bar{\rho}$, of the oil–water interface as a function of the refractive index of the oil phase, n_1 , for a series of polar oils (■) and hexadecane (□). The expected roughness contribution from coupled-mode capillary wave theory is also shown for each oil (○). (B) The same data plotted as a function of the interfacial tension, γ_{ow} .

There is no correlation between $\bar{\rho}$ and n_1 for these oils (figure 4A), in contrast to nonpolar hydrocarbons in figure 3. For polar oils, the mutual solubility of the oil and water phases is no longer negligible and the formation of two mixed bulk phases, one rich in oil and one rich in water, alters the refractive indices relative to the pure liquids. The relative permittivities of these solutions can be approximated by the Lorentz–Lorenz effective medium approximation [30]:

$$\left(\frac{\varepsilon - 1}{\varepsilon + 2}\right) = \varphi_1 \left(\frac{\varepsilon_1 - 1}{\varepsilon_1 + 2}\right) + \varphi_2 \left(\frac{\varepsilon_2 - 1}{\varepsilon_2 + 2}\right) \quad (10)$$

where ε is the permittivity of the mixed phase and φ_1 and φ_2 are the volume fractions of oil and water, respectively, such that $\varphi_1 + \varphi_2 = 1$. The mutual solubilities and the calculated refractive indices of the adjoining phases are given in table 3. The mutual solubility has a small effect on the refractive indices of the ethyl acetate, 3-pentanone and 5-nonanol systems and a negligible effect on all other systems. I have also plotted the capillary wave prediction for each interface in figure 4 using the data from table 2. Figure 4B shows that as the interfacial tension decreases, the values of $\bar{\rho}$ approach the capillary wave prediction.

Oil	n_1	Solubility of water in oil (wt %)	Solubility of oil in water (wt %)	n_{water}	n_{oil}
Ethyl acetate	1.372	2.88	7.79	1.335	1.371
3-pentanone	1.392	2.00	5.30	1.336	1.391
Dibutyl ether	1.399	0.27	0.02	1.332	1.399
Butyl butanoate	1.408	0.44	0.07	1.332	1.408
5-nonanone	1.420	0.44	0.05	1.332	1.420
5-nonanol*	1.430	3.14*	0.04	1.332	1.427
Cyclohexyl acetate	1.440	0.71	0.30	1.332	1.439

Table 3. Refractive index of pure oil phase, n_1 , mutual solubility and adjusted refractive indices of the water, n_{water} , and oil, n_{oil} , phases for a series of polar oils. ^a R. Stephenson, and J. Stuart, *J. Chem. Eng. Data* **31**, 56 (1986). R. Stephenson, *J. Chem. Eng. Data* **37**, 80 (1992). *In the absence of mutual solubility data for 5-nonanol, data for 2-nonanol have been used.

3.4 Discussion

Ellipsometry of an oil–water interface yields only a single independent parameter: the ellipsometric thickness, η . Given that η is a function of the roughness of the interface as well as the refractive index, thickness and anisotropy of any structured layer at the interface, it might at first sight appear that to attempt an interpretation of ellipsometry in terms of a physical model of the interfaces is futile. For the oil–water interface, however, I have established experimentally that optical anisotropy alone cannot describe my results and that the measured ellipticity differs from the capillary wave prediction not merely in magnitude but in sign. With the aid of some simple assumptions, it is possible to derive useful physical insights. To proceed with my model building, I will first describe two alternative formalisms for calculating the contribution of thermal roughening to the ellipticity and then use these formalisms to evaluate the extent of any depletion layer at the interface between oil and water. In the notation of Mecke and Dietrich [31], Model 1 is similar to the Buff, Lovett and Stillinger (BLS) approach, where the interfacial profile is considered as a steplike interface roughened by thermally excited capillary waves. Model 2 is related to the approach of van der Waals where the density profile normal to the interface varies smoothly between the two phases. While these two models are, in principle, equivalent, they make different assumptions about the nature of the interface on a molecular length scale. It is therefore instructive to interpret the ellipsometric results within both conceptual frameworks.

Model 1

A sharp interface is modulated by capillary waves and coupled mode theory is used to arrive at equation 4. Local structure at the interface is treated by a stratified-layer model and the Drude equation used to determine the ellipsometric thickness. The contributions to $\bar{\rho}$ from the roughness and local structure are then summed [22]. I will first consider the case where the positive ellipticity of a hydrocarbon–water interface arises from a thin layer of structured, ice-like water at the interface. To

estimate the refractive index of the ice-like layer, I have employed the Clausius–Mossotti equation in the form

$$\left(\frac{\varepsilon - 1}{\varepsilon + 2}\right)\frac{1}{\rho} = \text{constant} \quad (11)$$

where ρ is the density. Using a value for the density of ice of 0.917 g cm^{-3} [32], the refractive index of ice at 293 K is 1.303. Taking the hexadecane–water interface as a typical example, the layer of ice-like water between the bulk phases would have to be $\sim 21 \text{ \AA}$ thick to explain the measured ellipticity. An intermediate structure between bulk ice and water would be even thicker. Such a thick layer at the interface would be clearly manifested in x-ray reflectivity if it existed: no such layer has been observed [3].

I will next consider a denser oil phase at the interface with the same protocol described above and I will take the hexadecane–water interface as a representative example. The density of solid hexadecane is 0.926 g cm^{-3} [33]. From the Lorentz–Lorenz relationship, the (isotropic) refractive index of a solid layer would be 1.537 and the layer would have to be $\sim 5 \text{ \AA}$ thick to describe the measured ellipticity. Crystalline hydrocarbons are, however, optically anisotropic and it is known from ellipsometric studies of surface freezing at the oil–water interface that the anisotropic contribution to the ellipticity is larger than the isotropic contribution [34]. While it is possible that the effects of the increased density and anisotropy are balanced so perfectly that branched and linear alkanes behave alike ellipsometrically, such a serendipitous outcome is very unlikely. A small increase in density of an alkane might be accommodated without pronounced anisotropy, but then the region of increased density increase would have to extend implausibly far into the bulk oil phase. Hence I conclude that densification of the oil at the interface is unlikely to be the origin of the positive ellipticity.

Finally, I consider the case where the hydrophobic interface leads to a depleted water layer of greatly reduced density at the interface, as depicted in figure 5 – a situation known as “drying”.

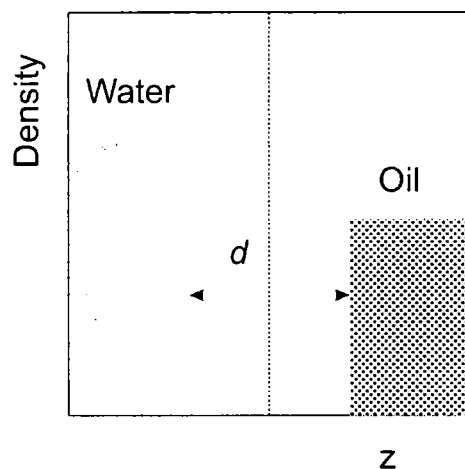


Figure 5. Density profile through the interface for model 1. z is the coordinate normal to the interface.

In the limit of total drying, this depletion layer will have a refractive index of unity. After accounting for the capillary wave contribution, I calculate the thickness of the depletion layer, d , that would generate the experimental ellipticity for each oil. These thicknesses are plotted as a function of interfacial tension in figure 6. The absolute values of d are extremely small — all are less than 0.5 \AA .

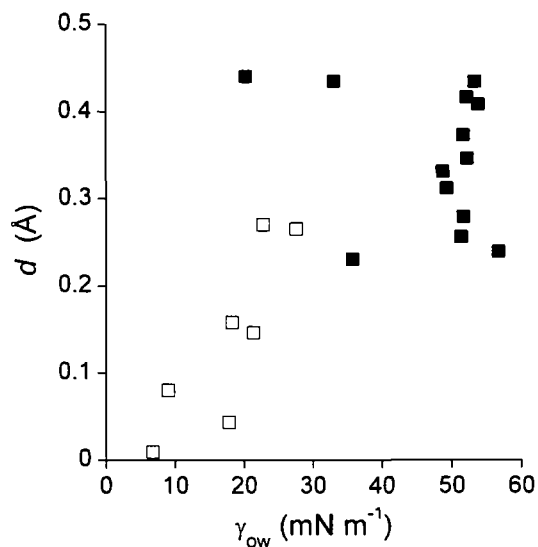


Figure 6. Thickness of depleted layer determined using model 1, d , as a function of interfacial tension, γ_{ow} , for a series of polar (\square) and non-polar (\blacksquare) oils.

To understand why a density gap of this magnitude might arise, it is instructive to compare d with the gap between layers in orthorhombic crystals of long-chain, odd-numbered linear alkanes. In figure 7 I have plotted the c lattice parameter (along the chain axis) of the crystal unit cell as a function of chain length: the intercept is 3.6 Å.

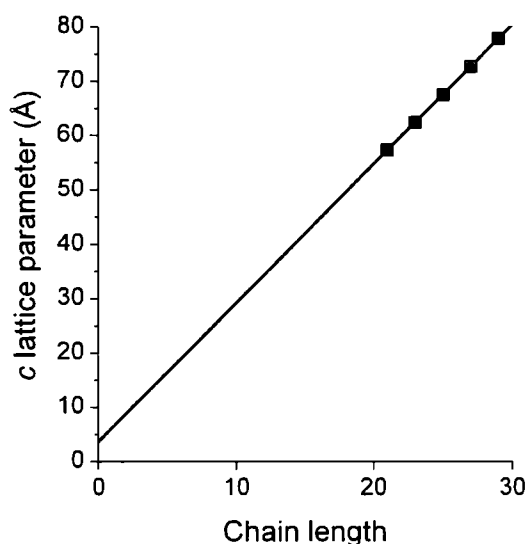


Figure 7. *c* lattice parameter of orthorhombic alkanes plotted against chain length. Data taken from D. E. Small, *The Physical Chemistry of Lipids* (Plenum, New York, 1985).

This non-zero intercept arises because the van der Waals diameter of a methyl group is much larger than the methylene repeat distance (1.27 Å). The region between the terminal methyl groups of two adjacent layers is sketched in figure 8. Since the unit cell contains two layers of alkanes, the ‘gap’ between layers is 1.8 Å, or 0.9 Å per surface. The electron density of the terminal hydrogen of the methyl group is much less than that of a methylene group. Consequently, for a truncated crystalline alkane next to a water surface, I would expect a deficit in the electron density corresponding to a ~0.9 Å void, purely due to the excluded volume of the terminal methyl group – even without any structuring of the interfacial water.

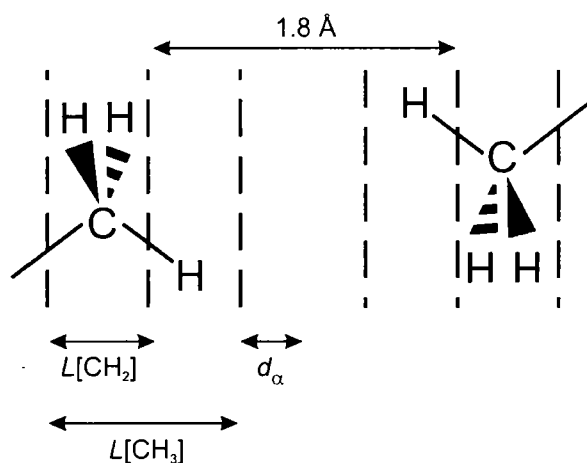


Figure 8. Schematic showing the polarizability gap, d_α , expected between a truncated alkane crystal and water.

The effect of the terminal methyl groups on ellipsometry is more complicated than on x-ray reflectivity since the polarizability of the terminal C–H bond is not negligible compared to a methylene group; consequently the ‘polarizability deficit’ will be smaller than the electron density deficit at the interface. Nevertheless, the excluded volume of the methyl group still results in a region of reduced polarizability compared to the hydrocarbon chains. To quantify this effect, I treated the methyl group as having a thickness $L[\text{CH}_3]$ of equal polarizability density to that of a methylene group. The ‘gap’ d_α sensed by ellipsometry is then given by

$$d_\alpha = 0.9 + L[\text{CH}_2] - L[\text{CH}_3] \quad (12)$$

where $L[\text{CH}_2] = 1.27 \text{ \AA}$ is the CH_2 repeat length from crystallographic studies (see figure 8). $L[\text{CH}_3]$ can be expressed in terms of the molar refractivities, R_m , of methyl and methylene groups by

$$L[\text{CH}_3] = L[\text{CH}_2] \times R_m[\text{CH}_3]/R_m[\text{CH}_2] \quad (13)$$

R_m is an additive property that is related to the polarizability volume, α' , by the relationship $R_m = 4\pi\alpha'N_A/3$, where N_A is Avogadro’s number. I determined R_m for methyl and methylene groups from the bond refractivities of C–C bonds ($1.20 \text{ cm}^3 \text{ mol}^{-1}$) [35] and C–H bonds ($1.65 \text{ cm}^3 \text{ mol}^{-1}$) [35] to give $R_m[\text{CH}_3] = 5.55 \text{ cm}^3 \text{ mol}^{-1}$

and $R_m[\text{CH}_2] = 4.50 \text{ cm}^3 \text{ mol}^{-1}$. Hence $L[\text{CH}_3] = 1.57 \text{ \AA}$ and $d_\alpha = 0.6 \text{ \AA}$, only slightly larger than the value of d I have deduced from ellipsometric measurements on the simple hydrocarbons. I am, of course, studying liquid hydrocarbons that do not expose an oriented layer of methyl groups at the oil–water interface. Nevertheless, I expect the excluded volume effect of methylene groups to be similar to that of methyl groups and so the polarizability gap for a liquid hydrocarbon will not be much smaller than the value of d_α calculated for crystalline alkanes.

For the alkanes, alkene and aromatics the density profiles show regions of reduced polarizability density of similar magnitudes, but these deficits decrease for the polar oils. The oxygenated functional groups of these oils can form hydrogen bonds with water molecules at the interface, reducing the excluded volume between the oil and the water. Hydrogen bonding between the polar oils and the water is one of the primary reasons for the reduction in interfacial tension: the lower the interfacial tension, the more hydrogen bonds and the smaller the value of d . The interfacial tension is not solely dependent on hydrogen bonding and hence the correlation between γ_{ow} and d is not perfect. For oils with π -systems (squalene, toluene and tetrahydronaphthalene) the greater polarizability of the π -electrons reduces the interfacial tension due to dipole-induced dipole interactions, without having a measurable effect on d compared to the saturated hydrocarbons.

Model 2

In the second model I have considered, I specify the density profiles of both phases at the interface. Following the formalism of Senapati and Berkowitz, the density profiles of the two phases are expressed as [13]:

$$\begin{aligned} \rho_1(z) &= \frac{1}{2} \rho_1 \left[1 - \operatorname{erf} \left(\frac{z - w_0}{\sqrt{2} w_c} \right) \right] \\ \rho_2(z) &= \frac{1}{2} \rho_2 \left[1 + \operatorname{erf} \left(\frac{z}{\sqrt{2} w_c} \right) \right] \end{aligned} \tag{14}$$

where ρ_1 and ρ_2 are the densities of the bulk phases, z is the coordinate normal to the interface, w_c is the width of the interface due to thermal roughening and w_0 defines the relative positions of the midpoints in the oil and water distributions. w_0 is the parameter that characterizes the extent of interfacial drying. Density profiles derived from model 2 are shown in figure 9A and 9B for $w_0 = 0$ and $w_0 = w_c$, respectively.

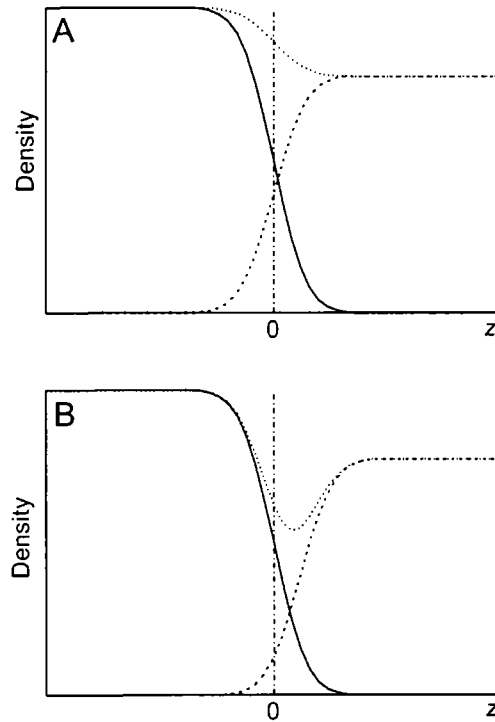


Figure 9. (A) Model 2 density profile, $w_0 = 0$. (B) Model 2 density profile, $w_0 > 0$; $w_0 / w_c = 1$. (Solid line) water density, (dashed line) oil density, (dotted line) total density, (dash-dotted line) $z = 0$.

w_c is typically derived from the capillary wave theory of independent waves and is given by [1]

$$w_c^2 = \frac{k_B T}{2\pi\gamma} \ln\left(\frac{L_{\max}}{L_{\min}}\right) \quad (15)$$

where L_{\max} and L_{\min} are related to the longest and shortest wavelength capillary waves that the interface can support. However, to maintain consistency with model 1, I have

derived an alternative expression for w_c based on the coupled-mode theory of Meunier [22]. This approach has the added advantage that the cut-off L_{\min} arises naturally in coupled-mode theory, reducing the number of fitting parameters.

I follow the formalism of Meunier [22]. An infinitely thin, sharp interface with no bending rigidity ($K = 0$) is modulated by a spectrum of capillary waves driven by thermal energy. The mean square amplitude of the roughness, w_c^2 , is given by

$$w_c^2 = \sum_q \langle \zeta_q^2 \rangle \quad (16)$$

where ζ_q is the amplitude of the mode of wavevector q . Employing a mode coupling theory, the mean square amplitude of mode q is given by Meunier as

$$\langle \zeta_q^2 \rangle = \frac{1}{A} \frac{k_B T}{\Delta \rho g + \gamma(q) q^2} \quad (17)$$

where $\Delta \rho$ is the density difference between the adjacent phases, g is the acceleration due to gravity, $\gamma(q) = \gamma + a q^2$, $a = 3k_B T / 8\pi$ and A is the area of the interface. Converting the summation in equation 16 into an integral over q space, one obtains

$$w_c^2 = \frac{k_B T}{2\pi} \int_{q_{\min}}^{q_{\max}} \frac{q \, dq}{\Delta \rho g + \gamma q^2 + a q^4} \quad (18)$$

The integration limits are defined by the longest and shortest wavelengths that the interface can support. In practice, ellipsometry is insensitive to capillary wavelengths longer than λ as these waves will scatter the light in an off-specular direction and will not be detected in a specular reflection experiment. This restriction places a lower limit of $q_{\min} = 2\pi/\lambda$. $q_{\max} = 2\pi/L_{\min}$ where L_{\min} is of the order of a molecular length. Consequently, the $\Delta \rho g$ term is negligible over the range of q of interest and the integral simplifies to

$$w_c^2 \approx \frac{k_B T}{2\pi} \int_{q_{\min}}^{q_{\max}} \frac{dq}{\gamma q + a q^3} = \frac{k_B T}{2\pi \gamma} \left[\ln \left(\frac{q}{\sqrt{\gamma + a q^2}} \right) \right]_{q_{\min}}^{q_{\max}} \quad (19)$$

Making the reasonable assumptions that $aq_{\min}^2 / \gamma \ll 1$ and $aq_{\max}^2 / \gamma \gg 1$ the integrand simplifies to:

$$w_c^2 = \frac{k_B T}{4\pi\gamma} \ln\left(\frac{\gamma}{aq_{\min}^2}\right) = \frac{k_B T}{4\pi\gamma} \ln\left(\frac{2\gamma\lambda^2}{3\pi k_B T}\right) \quad (20)$$

This derivation assumes that the interface has no rigidity – this approximation has been used successfully in the study of air–liquid interfaces. To approximate the effect of a nonzero bending modulus, I note that in the independent mode approximation the variation of the ellipticity is proportional to $K^{-1/2}$ and that if the interface does have a bending modulus, the constant a is replaced by the bending modulus in equation 18 [22]. Therefore for a rigid interface, the ellipticity is effectively reduced by a factor $(a/K)^{1/2}$. In the absence of ordered surfactant layers, K is typically $< k_B T$, whereas $a = 3k_B T/8\pi$. The bending modulus of the interface will reduce somewhat the roughness contribution to the ellipticity, but cannot change its sign.

At fixed T and λ , the value of w_c from equation 20 depends only on the interfacial tension, in an analogous manner to equation 4. I use the density profile from equation 14 in conjunction with the Lorentz-Lorenz EMA (equation 10) to determine the optical profile across the interface, and finally calculate the ellipticity from the Drude equation (equation 2). When $w_0 = 0$, the density profile corresponds to a simple interface roughened by capillary waves and I expect the calculated ellipticity, $\bar{\rho}_{r2}$, to be similar to the value for the roughness calculated from equation 4 (model 1). I have compared the contribution of the roughness to the ellipticity from model 1 and model 2 in table 4 — for most liquids the predictions are in quantitative agreement and the largest deviation is 4×10^{-5} , which is close to the experimental precision.

The values of w_0 required to fit the experimental values of $\bar{\rho}$ are given in table 4 and plotted in figure 10.

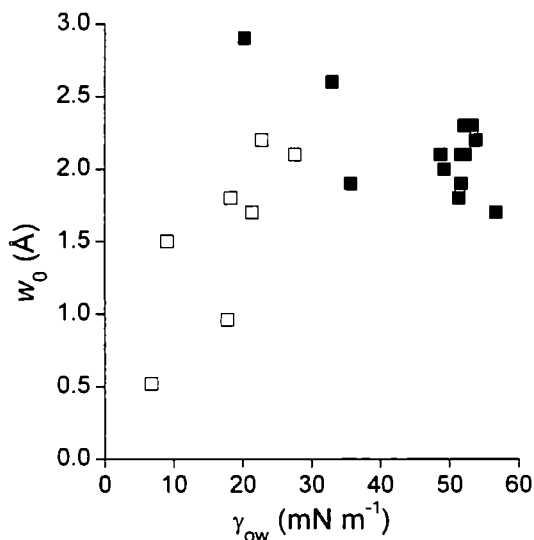


Figure 10. Separation between oil and water phases, w_0 , calculated using model 2 as a function of interfacial tension, γ_{ow} , for series of polar (□) and non-polar (■) oils.

I note two points about the results from model 2. First, the values of w_0 from model 2 vary from 0.5–3 Å and are substantially larger than the values of d from model 1. Although w_0 introduces a separation between the phases akin to d in model 1, the intermediate layer has a refractive index much closer to those of the bulk phases and therefore a value of w_0 larger than d is required to generate the same ellipticity (see equation 2). Second, the correlation between w_0 and γ_{ow} in figure 10 is less apparent than that between d and γ_{ow} in figure 6. In model 2, w_0 and w_c are coupled by equation 14. A dip in the permittivity profile – which is an essential requirement in the Drude model for a positive ellipticity – only occurs for values of $w_0/w_c > 0.1$. The lower the interfacial tension, the rougher the interface and hence the larger the value of w_0 that is required in this model to generate a layer of depleted density at the interface.

The differences between the density profiles derived from Models 1 and 2 are a consequence in part of the fact that ellipsometry is unable to distinguish between a narrow, deep notch in the density profile and a broad and shallow density deficit.

Oil	w_c (Å)	$10^3 \bar{\rho}_{r1}$	$10^3 \bar{\rho}_{r2}$	d (Å)	w_0 (Å)
Octane	3.0	-0.14	-0.15	0.37	2.1
Tridecane	3.0	-0.20	-0.21	0.42	2.3
Tetradecane	2.9	-0.21	-0.22	0.43	2.3
Hexadecane	2.9	-0.22	-0.23	0.41	2.2
Isooctane	3.0	-0.13	-0.14	0.31	2.0
Heptamethylnonane	3.0	-0.24	-0.25	0.33	2.1
Squalane	3.0	-0.26	-0.28	0.35	2.1
<i>trans</i> -Decalin	3.0	-0.30	-0.32	0.26	1.8
DMA	2.8	-0.30	-0.32	0.24	1.7
<i>cis</i> -Decalin	3.0	-0.32	-0.34	0.28	1.9
Toluene	3.5	-0.42	-0.45	0.23	1.9
Tetrahydronaphthalene	3.7	-0.56	-0.60	0.44	2.6
Squalene	4.6	-0.57	-0.58	0.42	2.9
Ethyl acetate	7.6	-0.21	-0.21	0.01	0.5
3-pentanone	6.6	-0.29	-0.28	0.08	1.5
Dibutylether	4.0	-0.20	-0.21	0.27	2.1
Butyl butanoate	4.5	-0.25	-0.26	0.15	1.7
5-nonanone	4.3	-0.28	-0.29	0.27	2.2
5-nonanol	4.8	-0.35	-0.35	0.16	1.8
Cyclohexyl acetate	4.9	-0.39	-0.40	0.04	1.0

Table 4. Capillary wave thickness, w_c , roughness contributions to ellipticity calculated by model 1, $\bar{\rho}_{r1}$, and model 2, $\bar{\rho}_{r2}$, depletion layer thickness, d , and separation between oil and water phases, w_0 , for series of non-polar and polar oils.

I will now place my results in the context of previous experimental studies of water at solid hydrophobic interfaces and oil interfaces. The interaction of water with hydrophobic monolayers on solid substrates is closely related to the interaction of water with hydrophobic liquids. Mao et al [36] have taken ellipsometric measurements on the interface between water and hydrophobic silicon and found that their results disagreed with a model of bulk water adjacent to the solid. To fit their data, a uniform drying film ($\epsilon = 1$) would have to be 0.4 Å thick — in quantitative agreement with my measurements and with the excluded volume of the hydrophobic surface. They rationalized their result by invoking the presence of ‘nanobubbles’ of

air on the solid as have been observed by AFM [37]. They did, however, find similar disagreement for measurements at the interface between hexane and hydrophobic silicon, where nanobubbles have not been observed.

Neutron reflectivity from the interface between D₂O and perdeuterated polystyrene spin-coated onto silicon showed a region of reduced scattering length density at the interface which was interpreted as a depleted layer 20–50 Å thick acting as a precursor to the formation of nanobubbles [38]. A similar study on the interface between water and hydrophobic self-assembled monolayers on gold also noted an extended region of water at the interface (~40 Å thick) with a density of ~85–90% compared to pure water [39]. The presence of an interfacial depleted layer in hydrophobic nanochannels of mesoporous silica approximately 6 Å thick has been invoked to explain the reduced pore volume available to water in comparison to nitrogen gas [40]. Depletion layers of this magnitude are not consistent with my ellipsometric measurements on liquid hydrocarbon – water interfaces. Recent synchrotron x-ray reflectivity results by Mezger *et al.* [41] and Poynor *et al.* [42] of the interface between water and octadecylsilane monolayers show an electron density deficit at the interface that is 2–4 Å and 1–6 Å thick, respectively.

Conversely, Jensen *et al.* measured the x-ray reflectivity from a water surface covered by a solid monolayer of hexatriacontane [43]. They inverted the reflectivity curves to obtain an electron density deficit at the interface of 1 Å, a value that is well-described by the electron density deficit at a methyl-terminated alkane (figure 8). Reflectivity measurements of water covered in solid monolayers of the long-chain alcohol 1-triacontanol and the saturated triglycerides mono-, di- and tri-palmitoyl glycerol ester gave no electron density deficit. In addition to the results presented above, I have also measured the ellipticity of the interface between water and glyceryl trioleate; an unsaturated triglyceride molecule that remains a liquid at room temperature. The experimental ellipticity was -0.60×10^3 in comparison to the capillary wave prediction from equation 4 of -0.38×10^3 : this is the only oil I have measured that gave an ellipticity more negative than the capillary wave prediction. The behaviour of glycerol trioleate is consistent with Jensen's results with the saturated analogue, glycerol tripalmitate, with the small negative deviation from the capillary wave

prediction suggesting a slight optical anisotropy at the interface. Beaglehole measured the ellipticity of the heptane–electrolyte and carbon tetrachloride–electrolyte interfaces and observed the sign of the ellipticity was opposite to that required by capillary wave theory, in agreement with my more recent results [8]. He observed that the discrepancy between the capillary wave prediction and the experimental result was larger for heptane than for carbon tetrachloride and suggested that the heptane chains may be structuring at the interface. My results with a range of hydrocarbons, including octane, suggest that such structuring is unlikely to be a major contributor to $\bar{\rho}$.

Recently, Mitrinovic *et al.* carried out a detailed x-ray reflectivity study of the oil–water interface for eight linear alkanes from hexane to docosane [3]. They modelled the reflectivity curves with a hybrid model of the interface with an intrinsic interfacial width, σ_0 roughened by capillary waves, and based upon the error function profile, given by

$$\langle \rho(z) \rangle = \frac{1}{2}(\rho_1 + \rho_2) + \frac{1}{2}(\rho_1 - \rho_2) \operatorname{erf}\left(\frac{z}{\sqrt{2}\sigma}\right) \quad (21)$$

The single fitting parameter, σ , was interpreted as the sum of a capillary-wave contribution as defined in equation 15 and an intrinsic interfacial width, σ_0 , such that $\sigma^2 = w_c^2 + \sigma_0^2$. The addition of an intrinsic width to the capillary wave thickness leads to a broadened density profile but one that always gives a permittivity intermediate between that of the alkane and water. Such monotonic profiles will always give a more negative ellipticity than the capillary wave prediction and Mitrinovic's model is therefore not a good starting point for explaining my ellipsometry data. Nevertheless, it is worth noting that Mitrinovic was able to rationalize his results with a consistent physical model without invoking any 'drying' layer at the oil–water interface. The same model had been used to fit neutron reflectivity from the hexadecane–water interface with the same conclusion as with x-ray reflectivity – no interfacial drying [44].

Since the publication of the work presented in this chapter, there has been further discussion in the literature about the nature of water at hydrophobic interfaces. Ocko

et al. reanalyzed the work of Poynor *et al.* to include the reduced electron density of the methyl groups in comparison to the methylene groups [45]. This reanalysis led to a reduction in the observed electron density deficit at the interface between water and a solid hydrophobic surface and persuaded this group to postulate that the results were more consistent with local water orientation rather than depletion. Poynor *et al.* responded to this comment by measuring the x-ray reflectivity of the interface between ethanol and a methyl-terminated monolayer [46]. They found that the reduced electron density of the methyl groups completely explained the electron density gap in this wetting case but for water the methyl groups only accounted for half of the gap. Kashimoto *et al.* studied the heptane–water and perfluorohexane–water interfaces by x-ray reflectivity [47]. Their results were consistent with the subangstrom proximity of water to heptane, although they interpreted their reflectivity curves in terms of an intrinsic interfacial width in the same manner as ref [3]. The cause of the disagreement between the ellipsometry and x-ray reflectivity studies is currently unclear.

3.5 Conclusion

The coefficient of ellipticity, $\bar{\rho}$, for light reflected from the interface between oil and water is of the opposite sign to that expected for a sharp interface roughened by capillary waves. The values of $\bar{\rho}$ for a series of linear, branched and cyclic alkanes, as well as unsaturated oils were not strongly dependent on molecular architecture. I conclude that molecular packing or alignment at the interface is not the primary reason for the deviation from the capillary wave prediction for $\bar{\rho}$. I employed a stratified layer model to interpret the ellipsometric data from which I infer the “drying” layer at the interface is only 0.3–0.4 Å. This result may be understood by comparison with the excluded volume between adjacent hydrocarbon layers in alkane crystals. With this model, the ellipticity of the oil–water interface can be explained entirely by the van der Waals surface of the hydrocarbons without the imposition of an additional water layer of reduced density.

I also measured $\bar{\rho}$ for a series of oils containing polar functional groups in contact with water; $\bar{\rho}$ was correlated loosely with the interfacial tension. I employed the same model as above for the polar oils and found that the “drying” layer decreased in thickness as the favourable interaction between the two phases increased. This interaction, parameterized by the interfacial tension, is linked to the ability of the oil phase to form hydrogen bonds with water. In conclusion, if the oil phase is able to interact strongly with the water phase and form hydrogen bonds, then the drying layer thickness is reduced. To test the sensitivity of my interpretation to the model used, I also analysed our data with a model similar to that used in X-ray and neutron reflectivity. This model gave a separation between the midpoints of the water and oil density profiles of 2–3 Å for non-polar oils, with a reduced separation for polar oils. Though the density deficit is still small and the qualitative trends with polarity are the same in both models, the quantitative difference between the thickness of the ‘drying layer’ in the two models highlights the need for care in the treatment of capillary wave roughening.

References

- 1 J. S. Rowlinson and B. Widom, *Molecular Theory of Capillarity* 1st ed. (Dover, Mineola, N. Y., 2002).
- 2 K. Lum, D. Chandler, and J. D. Weeks, *J. Phys. Chem. B* **103**, 4570 (1999).
- 3 D. M. Mitrinovic, A. M. Tikhonov, M. Li, Z. Huang, and M. L. Schlossman, *Phys. Rev. Lett.* **85**, 582 (2000).
- 4 A. Zarbakhsh, J. Bowers, and J. R. P. Webster, *Meas. Sci. Technol.* **10**, 738 (1999).
- 5 M. M. Knock, G. R. Bell, E. K. Hill, H. J. Turner, and C. D. Bain, *J. Phys. Chem. B* **107**, 10801 (2003).
- 6 M. G. Brown, D. S. Walker, E. A. Raymond, and G. L. Richmond, *J. Phys. Chem. B* **107**, 237 (2003).
- 7 W. H. Steel, Y. Y. Lau, C. L. Beildeck, and R. A. Walker, *J. Phys. Chem. B* **108**, 13370 (2004).
- 8 D. Beaglehole, *J. Phys. Chem.* **93**, 2004 (1989).
- 9 A. Kereszturi and P. Jedlovsky, *J. Phys. Chem. B* **109**, 16782 (2005).
- 10 J. P. Nicolas and N. R. de Souza, *J. Chem. Phys.* **120**, 2464 (2004).
- 11 H. A. Patel, E. B. Nauman, and S. Garde, *J. Chem. Phys.* **119**, 9199 (2003).
- 12 J. L. Rivera, C. McCabe, and P. T. Cummings, *Phys. Rev. E* **67**, 011603 (2003).
- 13 S. Senapati and M. L. Berkowitz, *Phys. Rev. Lett.* **87**, 176101 (2001).
- 14 P. Ball, *Nature* **423**, 25 (2003).
- 15 D. Chandler, *Nature* **437**, 640 (2005).
- 16 L. R. Pratt and A. Pohorille, *Chem. Rev.* **102**, 2671 (2002).
- 17 R. M. A. Azzam and N. M. Bashara, *Ellipsometry and polarized light* 1st ed. (North-Holland, Amsterdam, 1977).
- 18 P. Drude, *Ann. Phys. Chem. (Leipzig)* **43**, 126 (1891).
- 19 J. Lekner, *Theory of Reflection*. (Martinus Nijhoff Publishers, Dordrecht, The Netherlands, 1987).
- 20 H. Bercegol, F. Gallet, D. Langevin, and J. Meunier, *J. Phys. (Paris)* **50**, 2277 (1989).

- 21 D. Beaglehole, *J. Phys. (Paris)* **supplement to volume 44**, C10 (1983).
- 22 J. Meunier, *J. Physique* **48**, 1819 (1987).
- 23 D. A. Tonova and A. A. Konova, *Thin Solid Films* **397**, 17 (2001).
- 24 A. Hirtz and G. H. Findenegg, *J. Phys.: Condens. Matter* **8**, 9541 (1996).
- 25 W. C. Bigelow, D. L. Pickett, and W. A. Zisman, *J. Colloid Sci.* **1**, 513 (1946).
- 26 S. N. Jasperson and S. E. Schnatterly, *Rev. Sci. Instr.* **40**, 761 (1969).
- 27 D. Beaglehole, Operating Theory of the Picometer Ellipsometer (Technical Note 1A)
- 28 G. Arfken, *Mathematical Methods for Physicists* 3rd ed. (Academic, Orlando, USA, 1985).
- 29 J.-W. Benjamins, B. Jonsson, K. Thuresson, and T. Nylander, *Langmuir* **18**, 6437 (2002).
- 30 D. E. Aspnes, *Thin Solid Films* **89**, 249 (1982).
- 31 K. R. Mecke and S. Dietrich, *Phys. Rev. E* **59**, 6766 (1999).
- 32 R. C. Weast, *Handbook of Chemistry and Physics*, (CRC Press, Boca Raton, 1981)
- 33 D. E. Small, *The Physical Chemistry of Lipids* 1st ed. (Plenum, New York, 1985).
- 34 Q. Lei and C. D. Bain, *Phys. Rev. Lett.* **92**, 176103 (2004).
- 35 P. W. Atkins, *Physical Chemistry* 3rd ed. (Oxford University Press, Oxford, 1994).
- 36 M. Mao, J. Zhang, R.-H. Yoon, and W. A. Ducker, *Langmuir* **20**, 1843 (2004).
- 37 J. W. G. Tyrrell and P. Attard, *Phys. Rev. Lett.* **87**, 176104 (2001).
- 38 R. Steitz, T. Gurberlet, T. Hauss, B. Klosgen, R. Krastev, S. Schemmel, A. C. Simonsen, and G. H. Findenegg, *Langmuir* **19**, 2409 (2003).
- 39 D. Schwendel, T. Hayashi, R. Dahint, A. Pertsin, M. Grunze, R. Steitz, and F. Schreiber, *Langmuir* **19**, 2284 (2003).
- 40 R. Helmy, Y. Kazakevich, C. Ni, and A. Y. Fadeev, *J. Am. Chem. Soc.* **127**, 12446 (2005).

- 41 M. Mezger, H. Reichert, S. Schoder, J. Okasinski, H. Schroder, H. Dosch, D. Palms, J. Ralston, and V. Honkimaki, *Proc. Natl. Acad. Sci.* **103**, 18401 (2006).
- 42 A. Poynor, L. Hong, I. K. Robinson, S. Granick, Z. Zhang, and P. A. Fenter, *Phys. Rev. Lett.* **97**, 266101 (2006).
- 43 T. R. Jensen, M. O. Jensen, N. Reitzel, K. Balashev, G. H. Peters, K. Kjaer, and T. Bjornholm, *Phys. Rev. Lett.* **90**, 086101 (2003).
- 44 A. Zarbakhsh, J. Bowers, and J. R. P. Webster, *Langmuir* **21**, 11596 (2005).
- 45 B. M. Ocko, A. Dhinojwala, and J. Daillant, *Phys. Rev. Lett.* **101**, 039601 (2008).
- 46 A. Poynor, L. Hong, I. K. Robinson, S. Granick, P. A. Fenter, and Z. Zhang, *Phys. Rev. Lett.* **101**, 039602 (2008).
- 47 K. Kashimoto, J. Yoon, B. Hou, C. Chen, B. Lin, M. Aratono, T. Takiue, and M. L. Schlossman, *Phys. Rev. Lett.* **101**, 076102 (2008).

Chapter 4

Adsorption of surfactants and proteins to the oil-water interface

4.1 Introduction

Milk proteins alone are unable to maintain a stable emulsion over the period required for a consumer product (see Chapter 1). Small-molecule surfactants can be added to extend shelf-life, but competition for interfacial area between surfactant and protein can serve to destabilize the emulsion. Thus there is the need to investigate and understand the interactions between proteins and surfactants in an emulsion, in order to produce a food product that both maintains its nutritive value and does not spoil rapidly.

The techniques that have been used to study emulsions have been reviewed in Chapter 1. Several of these procedures have been used to investigate the competitive adsorption of surfactants and proteins. Neutron reflectivity can deliver detailed compositional information about the adsorbed film at the air–water interface through isotopic labelling. Horne *et al* determined the effect of the concentration of C₁₂E₆ on the adsorbed amount and thickness of a β -lactoglobulin film [1]. At surfactant:protein molar ratios, $R < 0.2$, there was extensive adsorption of surfactant but minimal displacement of protein. At intermediate bulk compositions, there was an increase in film thickness until at $R > 0.6$ the protein was completely displaced by the surfactant. However, this approach is much less readily applied to the oil–water interface. Surface shear viscosity experiments can probe the disruption of protein films by surfactants [2], but cannot give detailed compositional information. Imaging techniques such as AFM allow the researcher to visualize the disruption of the protein film but require the transfer of the film to a mica surface, which limits the time resolution of the technique [3]. Ellipsometry may have the potential to study the competitive adsorption between surfactant and protein at this buried interface, as it is a rapid, non-invasive technique and is readily applied to the oil–water interface.

The aim of this chapter is to investigate the mechanism of the competitive adsorption of the nonionic surfactant $C_{10}E_8$ with the milk proteins β -casein and β -lactoglobulin at the hexadecane–water interface. In order to interpret the ellipsometry measurements, I first investigate separately the adsorption of pure $C_{10}E_8$ solutions and pure protein solutions. I use the insights gained from these studies to analyze the competitive adsorption behaviour of these proteins with $C_{10}E_8$.

4.2 Experimental

The procedures and protocols described in chapter 3 were also used to study surfactant and protein adsorption by ellipsometry and interfacial tensiometry. Octaethylene glycol monodecyl ether ($C_{10}E_8$) (>98%, Fluka), triolein (>99%, Fluka), β -casein (>90%, Sigma), β -lactoglobulin (3 \times crystallized, Sigma) and α,α,α -tris-(hydroxymethyl)-methylamine (>99.8%, Aldrich) (*tris*) were used as received. The proteins were dissolved in 10 mM *tris* buffer at pH 7.

4.3 Adsorption of $C_{10}E_8$ to hexadecane– and triolein–water interfaces

The coefficient of ellipticity for the adsorption of $C_{10}E_8$ from aqueous solution to the hexadecane–water interface was measured for a series of concentrations from 2.33 μM to 4.44 mM. The ellipticity was measured for thirty minutes at intervals of 25 s and the response is plotted as a function of time in figure 1.

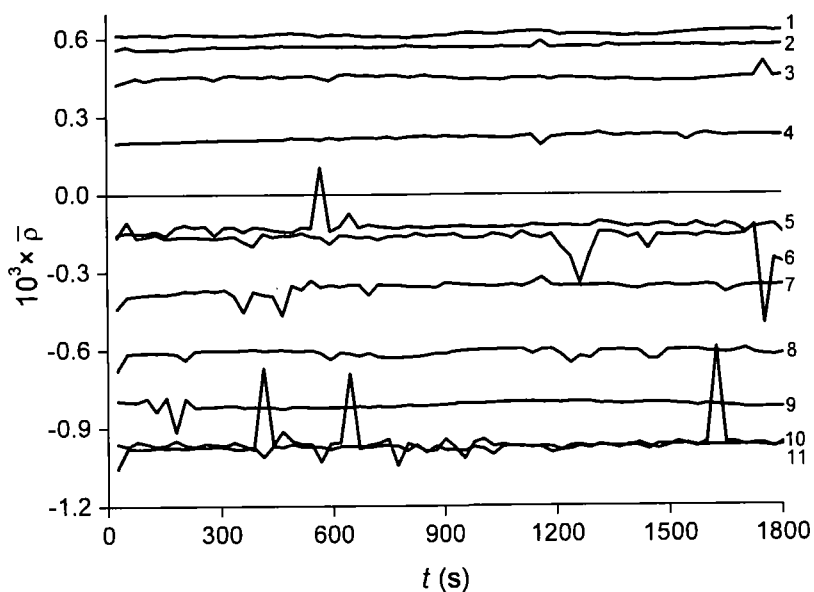


Figure 1. Coefficient of ellipticity, $\bar{\rho}$, plotted as a function of time, t , for the adsorption of a series of aqueous $C_{10}E_8$ solutions to the hexadecane–water interface. $[C_{10}E_8] = (1) 2.33 \mu\text{M}$, (2) $4.66 \mu\text{M}$, (3) $11.2 \mu\text{M}$, (4) $32.6 \mu\text{M}$, (5) $90.0 \mu\text{M}$, (6) $144 \mu\text{M}$, (7) $233 \mu\text{M}$, (8) $450 \mu\text{M}$, (9) $900 \mu\text{M}$, (10) 2.08mM , (11) 4.44mM .

The coefficient of ellipticity was essentially constant across the entire thirty-minute acquisition period for all concentrations. The occasional spikes and troughs occur when vibrations or air currents perturb the interface and cause the reflected beam to miss the detector. The lack of variation of the readings with time suggests that the surfactant in solution was in equilibrium with surfactant at the interface by the time the measurement was started. The nonionic C_nE_m surfactants are partially soluble in

oil, with the exact solubility dependent upon the relative lengths of the chain and headgroup. The lack of variation of the readings with time suggests that the dissolution of the surfactant into the oil phase does not have an effect upon the ellipticity. I also measured the coefficient of ellipticity for the adsorption of $C_{10}E_8$ to the triolein–water interface. The coefficient of ellipticity was also constant for thirty minutes for this interface for all concentrations. The average of the ellipticity over thirty minutes is plotted as a function of bulk concentration in figure 2 for each interface.

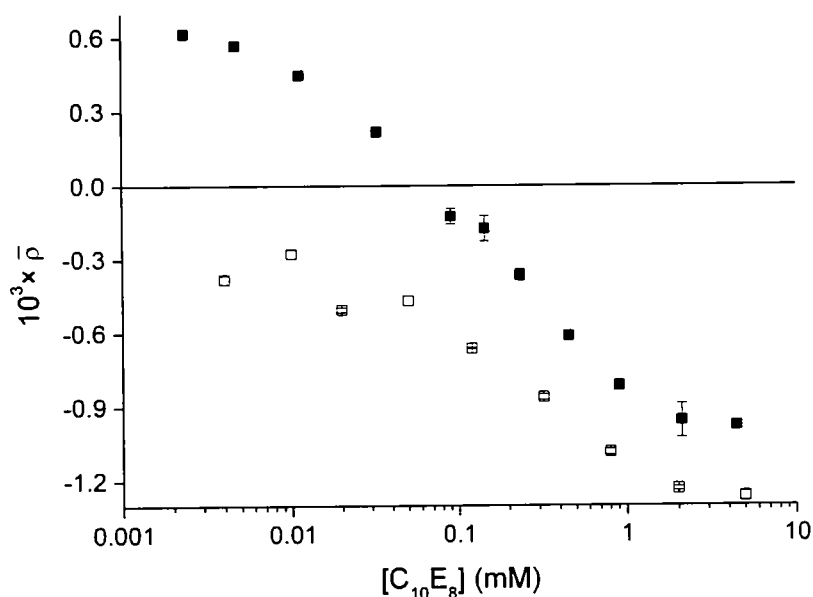


Figure 2. Coefficient of ellipticity, $\bar{\rho}$, plotted as a function of $C_{10}E_8$ concentration for the adsorption of a series of aqueous $C_{10}E_8$ solutions to the hexadecane–water interface (■) and the triolein–water interface (□).

At the hexadecane–water interface at low concentrations, the coefficient of ellipticity is positive and tends towards the value for a bare interface determined in chapter 3 ($\bar{\rho} = +0.93 \times 10^{-3}$). At higher concentrations, the ellipticity becomes negative, suggesting the formation of a film at the interface with a refractive index intermediate between the refractive indices of the bulk phases. Finally, above the critical micelle

concentration (cmc) ($[C_{10}E_8] = 1 \text{ mM}$) the ellipticity attains a limiting value of $\bar{\rho} = -0.97 \times 10^{-3}$. The formation of micelles in the bulk solution places a cap on the chemical potential of the surfactant and limits further adsorption [4]. The isotherm at the triolein–water interface displays similar behaviour. At high concentrations the ellipticity attains a limiting value of $\bar{\rho} = -1.26 \times 10^{-3}$ and at low concentrations the ellipticity tends to $\bar{\rho} = -0.3 \times 10^{-3}$. I have previously measured the ellipticity of the pure triolein–water interface as part of a previous data set. The ellipticity of the pure interface was measured to be $\bar{\rho} = (-0.6 \pm 0.05) \times 10^{-3}$. This value is significantly different from the value to which the data tends in figure 2. At low surfactant concentrations, depletion of the subsurface by the interface becomes appreciable and it is difficult to acquire equilibrium data below $1 \text{ }\mu\text{M}$ [5]. Nevertheless, the value of the ellipticity at the pure interface suggests that there may be a maximum in the ellipticity isotherm at low surface excess.

The ellipsometry isotherm in figure 2 provides more information when analyzed in conjunction with the surface excess isotherm. The interfacial tension of aqueous $C_{10}E_8$ solutions at the hexadecane–water interface was measured for a series of concentrations from $2.33 \text{ }\mu\text{M}$ to 4.44 mM . The interfacial tension decay curves are shown in figure 3.

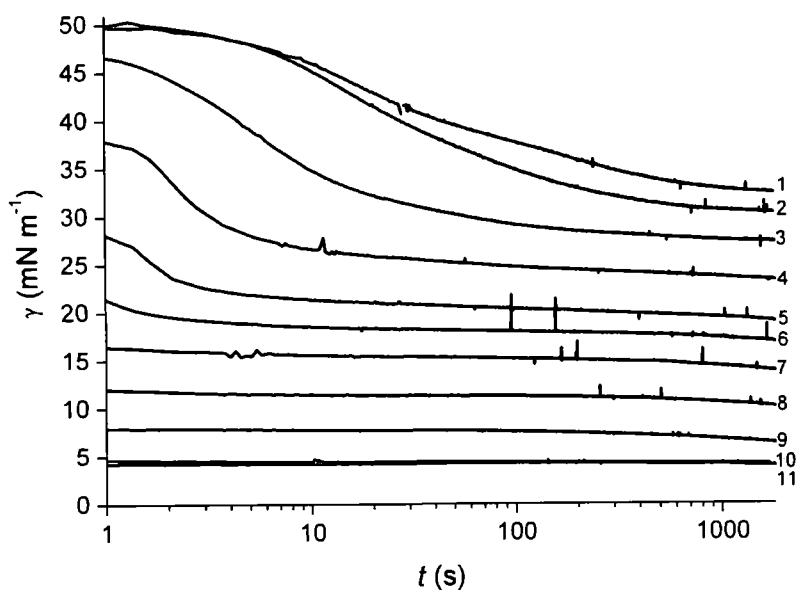


Figure 3. Interfacial tension at the oil–water interface, γ , plotted as a function of time, t , for the adsorption of a series of aqueous $C_{10}E_8$ solutions to the hexadecane–water interface. $[C_{10}E_8] = (1) 2.33 \mu\text{M}$, (2) $4.66 \mu\text{M}$, (3) $11.2 \mu\text{M}$, (4) $32.6 \mu\text{M}$, (5) $90.0 \mu\text{M}$, (6) $144 \mu\text{M}$, (7) $233 \mu\text{M}$, (8) $450 \mu\text{M}$, (9) $900 \mu\text{M}$, (10) 2.08 mM , (11) 4.44 mM .

At low bulk concentrations and at short adsorption times, the interfacial tension is close to the value for the bare hexadecane–water interface ($\gamma = 53.8 \text{ mN m}^{-1}$). The interfacial tension at $t = 0$ is equal to the bare interface value, but in practice the time resolution of the drop-shape analysis tensiometer is not sufficient to probe timescales of less than one second. As time passes, surfactant diffuses to the subsurface, adsorbs to the interface and lowers the interfacial tension. Higher bulk concentrations lower the interfacial tension more rapidly and reduce γ to lower values.

The relaxation rates of the interfacial tension at short times shown in figure 3 should be mirrored in the relaxation rates of the ellipticity (although the ellipticity responses will be more complex as they are dependent upon more than one parameter; surface excess, monolayer density, interfacial tension etc.). In practice, it takes from 2–5 minutes to prepare the ellipsometer to acquire readings. The interfacial tension is

almost constant at these timescales in figure 3, for all but the lowest two concentrations. Thus currently my methodology does not have sufficient kinetic resolution to probe the adsorption dynamics of surfactants. This issue will be addressed further in the outlook section below.

The time taken for a freshly-formed interface to reach equilibrium with the bulk solution is $\sim 5\tau$, where the characteristic diffusion time, τ , is defined as the time taken for a surfactant molecule to diffuse a distance equal to the depletion length, Γ/c , where c is the bulk concentration. τ is given by [5]:

$$\tau = \frac{\pi}{4D} \left(\frac{\Gamma}{c} \right)^2 \quad (1)$$

where D is the diffusion coefficient of the surfactant molecule. The diffusion coefficient of $C_{10}E_8$ is $4.5 \times 10^{-10} \text{ m}^2 \text{ s}^{-1}$ [6]. From the Gibbs equation, the values of Γ ranged from $1 \text{ } \mu\text{mol m}^{-2}$ at the lowest concentration studied to $2.7 \text{ } \mu\text{mol m}^{-2}$ at the cmc. I combined these estimates with equation 1 to give values for the time taken for each interface to reach equilibrium. The values of 5τ varied from $\sim 2 \text{ ms}$ above the cmc to 1700 s at the lowest concentration studied, and I averaged the interfacial tension measurements for 100 s after 5τ . Even at long times ($t > 1000 \text{ s}$), there is a slight drift in the interfacial decay curves. This drift is caused by impurities in the surfactant. Nonionic C_nE_m surfactants are considerably harder to purify than ionic surfactants as the impurities (usually surfactants with different values of n and m) have such similar bulk properties to the principal component. I also measured the interfacial tension for the adsorption of $C_{10}E_8$ to the triolein–water interface. There was slightly more drift in the long-time interfacial tensions for the triolein–water interface, which I account for as minor impurities in the triolein. These values are plotted as a function of bulk concentration in figure 4.

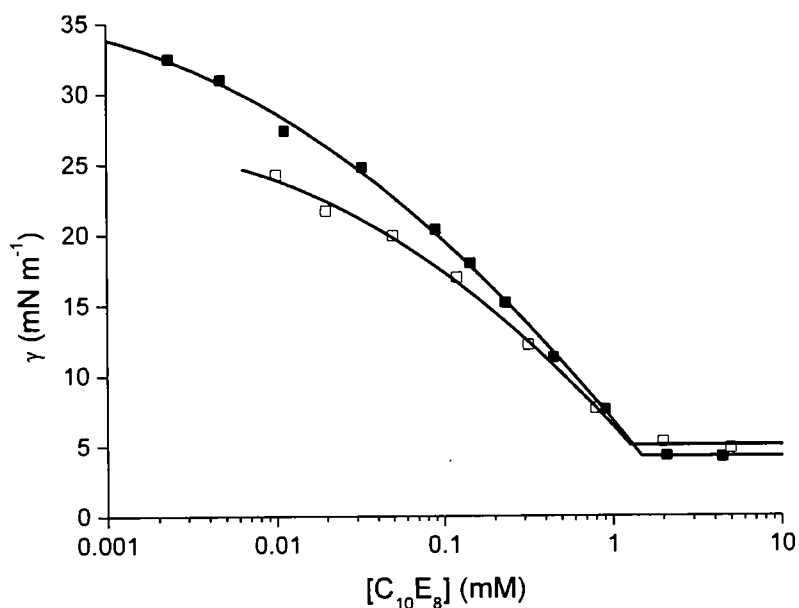


Figure 4. Interfacial tension, γ , plotted as a function of $C_{10}E_8$ concentration for the adsorption of a series of aqueous $C_{10}E_8$ solutions to the hexadecane–water interface (■) and the triolein–water interface (□).

Quadratic functions through the data below the cmc are also plotted in figure 4. I substituted the derivatives of the quadratic functions into the Gibbs adsorption isotherm (equation 9, chapter 1) to determine the surface excess from the interfacial tension isotherm. Figure 5 shows the ellipticity as a function of surface excess for each interface. The limiting surface coverage for $C_{10}E_8$ at the hexadecane–water interface was found to be $2.7 \mu\text{mol m}^{-2}$, whereas the limiting surface coverage for $C_{10}E_8$ at the triolein–water interface was found to be $2.4 \mu\text{mol m}^{-2}$. These results compare to a limiting value of $2.7 \mu\text{mol m}^{-2}$ at the air–water interface [7].

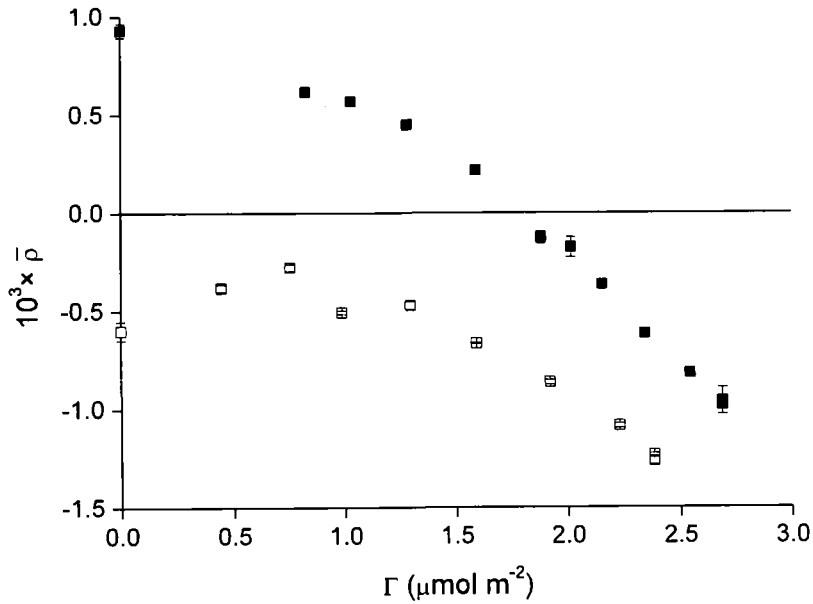


Figure 5. Coefficient of ellipticity, $\bar{\rho}$, plotted as a function of surface excess, Γ , for the adsorption of a series of aqueous $C_{10}E_8$ solutions to the hexadecane–water interface (■) and the triolein–water interface (□).

The construction of a model may give further information about the structure of the $C_{10}E_8$ monolayer. I treat the ellipticity as the sum of a term from interfacial roughening, $\bar{\rho}_r$, and a term from the monolayer itself, $\bar{\rho}_m$. As in chapter 3, $\bar{\rho}_r$ is given in terms of the interfacial tension, γ :

$$\bar{\rho}_r = -\frac{3\pi(\epsilon_1 - \epsilon_2)}{2\lambda\sqrt{\epsilon_1 + \epsilon_2}} \sqrt{\frac{\pi k_B T}{6\gamma}} \quad (2)$$

where ϵ_1 and ϵ_2 are the relative permittivities of oil and water, respectively, at wavelength λ . The ellipticity from the monolayer is modeled by the Drude equation, given by

$$\bar{\rho}_m = \frac{\pi}{\lambda} \frac{\sqrt{\epsilon_1 + \epsilon_2}}{(\epsilon_1 - \epsilon_2)} \int \frac{(\epsilon - \epsilon_1)(\epsilon - \epsilon_2)}{\epsilon} dz \quad (3)$$

I make the assumption that the monolayer can be treated as a number of adjacent isotropic slabs, i , of thickness d_i ; consequently, equation 3 simplifies to give

$$\bar{\rho}_m = \frac{\pi \sqrt{\varepsilon_1 + \varepsilon_2}}{\lambda (\varepsilon_1 - \varepsilon_2)} \sum_i \frac{(\varepsilon_i - \varepsilon_1)(\varepsilon_i - \varepsilon_2)}{\varepsilon_i} d_i \quad (4)$$

I treat $\bar{\rho}_m$ as the sum of three terms. The hydrocarbon chain is assumed to have the same permittivity as the oil phase, $\varepsilon = \varepsilon_1$, thus this region does not contribute to the ellipticity. The work presented in chapter 3 postulates that the positive ellipticity at a pristine oil–water interface arises from a vapour gap that is caused by the excluded volume between the hydrocarbon and water phases. A surfactant molecule at the interface would bridge this gap, thus as the surface excess of surfactant increases, the contribution of the gap to the ellipticity decreases accordingly. Consequently, I include a term in the model to account for the influence of this vapour gap, $\bar{\rho}_v$. The ratio of the surface excess and limiting surface excess of surfactant, Γ_{\max} , are used to calculate the area fraction of the surface that is covered by surfactant molecules. This area fraction is used to scale linearly the contribution of the vapour gap to the ellipticity as the surface excess increases:

$$\bar{\rho}_v = \bar{\rho}_{v0} \left(1 - \frac{\Gamma}{\Gamma_{\max}}\right) \quad (5)$$

where $\bar{\rho}_{v0}$ is the ellipticity of the pristine interface determined in chapter 3.

The final term arises from the ethylene oxide headgroup layer, $\bar{\rho}_h$. Water is likely to penetrate into this layer and consequently this region can be modeled in two ways. In the first instance, the layer is treated as an isotropic slab whose thickness is invariant with surfactant concentration. The volume fraction of the headgroup in the layer, ϕ , is dependent upon the surface excess, Γ , and the molar volume of the headgroup, V_m , according to:

$$\phi = \frac{\Gamma V_m}{d} \quad (6)$$

In the second possibility, the volume fraction is invariant with concentration and the thickness of the layer is given by:



$$d = \frac{\Gamma V_m}{\phi} \quad (7)$$

In either case, the remainder of the layer, $1-\phi$, is filled with water and the dielectric constant of the headgroup layer is given by the Lorentz–Lorenz effective medium approximation:

$$\frac{\varepsilon - 1}{\varepsilon + 2} = \phi \frac{\varepsilon_{PEO} - 1}{\varepsilon_{PEO} + 2} + (1 - \phi) \frac{\varepsilon_2 - 1}{\varepsilon_2 + 2} \quad (8)$$

The molar volume of a $(\text{CH}_2\text{CH}_2\text{O})$ group is $39.14 \text{ cm}^3 \text{ mol}^{-1}$ [8, 9] so the molar volume of the octaethylene oxide headgroup is $313.1 \text{ cm}^3 \text{ mol}^{-1}$. The permittivity of the headgroup, ε_{PEO} , is determined from the Clausius–Mossotti equation

$$\frac{\varepsilon_{PEO} - 1}{\varepsilon_{PEO} + 2} = \frac{R_m}{V_m} \quad (9)$$

where the molar refractivity, R_m , is $84.96 \text{ cm}^3 \text{ mol}^{-1}$ [8, 9].

The best least-squares fit to the constant thickness model is shown by the bold line in figure 6. The thickness of the headgroup region was 12 \AA .

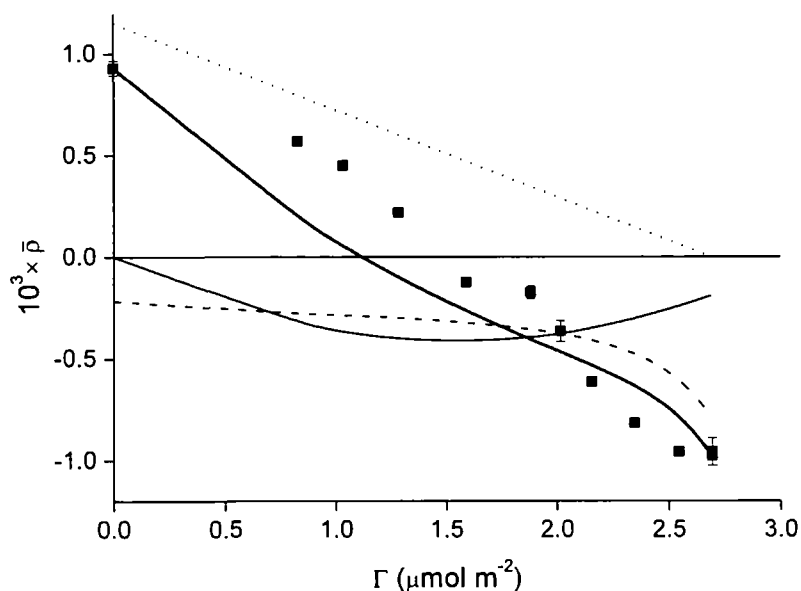


Figure 6. Coefficient of ellipticity, $\bar{\rho}$, plotted as a function of surface excess, Γ , for the adsorption of a series of aqueous $C_{10}E_8$ solutions to the hexadecane–water interface (■). (Bold solid line) Best fit to constant thickness model described in text. (Dashed line) roughness contribution ($\bar{\rho}_r$), (dotted line) excluded volume contribution ($\bar{\rho}_v$), (solid line) headgroup contribution ($\bar{\rho}_h$).

$\bar{\rho}_v$ decreases linearly to zero at the cmc by definition. The nonlinear nature of the roughness term causes $\bar{\rho}_r$ to decrease rapidly at high concentrations, where the surface excess approaches saturation but the surface tension continues to decrease. There is no evidence in the experimental data for this rapid decrease in $\bar{\rho}_r$, which may be suppressed by higher order terms (e.g. the bending modulus) that may be neglected at higher γ . $\bar{\rho}_h$ exhibits a minimum at $\Gamma \approx 1.6 \mu\text{mol m}^{-2}$. In the constant thickness model, the permittivity of the headgroup layer varies as the volume fraction of water in the layer changes. A minimum is observed where the dielectric constant of the layer passes through the geometric mean of the bulk phases at $\epsilon = 1.91$.

The best least-squares fit to the constant volume fraction model is shown in figure 7 with $\phi = 0.6$, although values from 0.5–0.7 did not change the fit significantly.

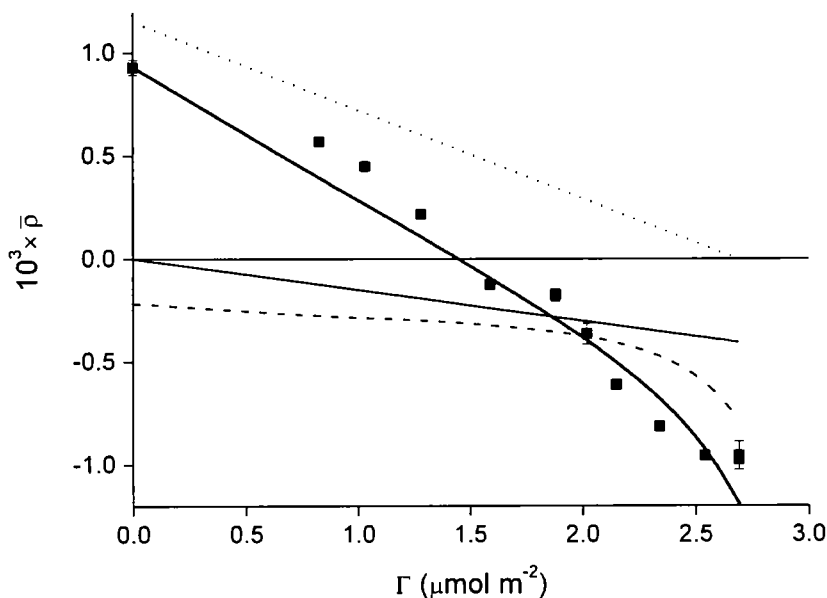


Figure 7. Coefficient of ellipticity, $\bar{\rho}$, plotted as a function of surface excess, Γ , for the adsorption of a series of aqueous $C_{10}E_8$ solutions to the hexadecane–water interface (■). (Bold solid line) Best fit to constant volume fraction model described in text. (Dashed line) roughness contribution ($\bar{\rho}_r$), (dotted line) excluded volume contribution ($\bar{\rho}_v$), (solid line) headgroup contribution ($\bar{\rho}_h$).

The roughness and excluded volume contributions are identical in each model. The headgroup contribution scales linearly with surface excess in this model. This model evidently follows the experimental data more accurately than the constant thickness model.

In a similar manner, I also created models to explain the ellipsometry data for the adsorption of $C_{10}E_8$ to the triolein–water interface. However, as the pristine triolein–water interface does not display a positive ellipticity, I did not include the excluded

volume contribution for this interface. The constant thickness and constant volume fraction models are shown in figure 8.

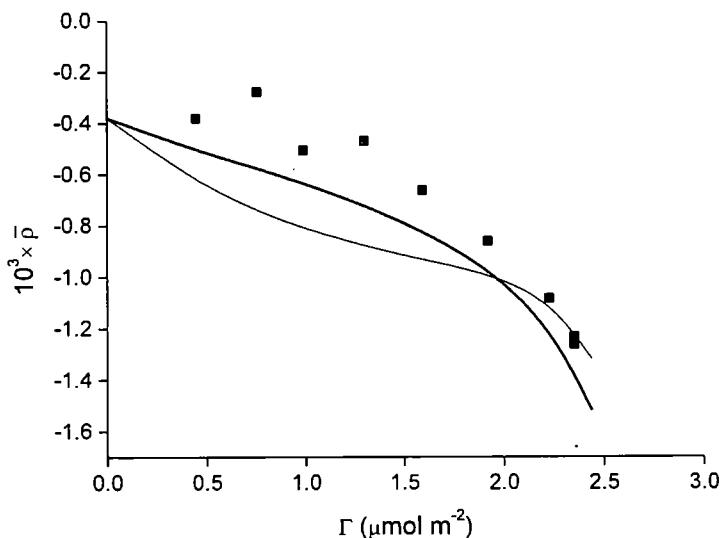


Figure 8. Coefficient of ellipticity, $\bar{\rho}$, plotted as a function of surface excess, Γ , for the adsorption of a series of aqueous C_{10}E_8 solutions to the triolein–water interface (■). (Solid line) Best fit to constant thickness model ($d = 9 \text{ \AA}$), (bold solid line) best fit to constant volume fraction model ($\phi = 0.7$).

The constant thickness model for the data at the triolein–water interface displays similar limitations to the model at the hexadecane–water interface. Although the constant volume fraction consistently underestimates the experimental results, it does display the correct monotonic decrease in ellipticity with increasing surface excess.

The constant volume models at both interfaces describe adequately the trends in the ellipsometry data, though the quantitative agreement is not perfect. The approximations in the model – especially the treatment of the depletion layer – and the unknown effects of trace impurities at the interface do not justify the addition of other terms to include, for example, anisotropy in the monolayer. In conclusion, there seems to be little variation in the behaviour of C_{10}E_8 at the hexadecane–water and

triolein–water interfaces, which suggests that the supernatant phase has little effect on the structure of the monolayer.

I will now compare my conclusions with the results of other workers on similar systems at the air–water interface. Goates *et al* studied the related nonionic surfactant $C_{12}E_8$ by vibrational sum-frequency spectroscopy and ellipsometry [9] at a surface coverage of $(2.7 \pm 0.1) \mu\text{mol m}^{-2}$. Their results suggested that the hydrophobic region of the monolayer had a density close to a liquid hydrocarbon. The maximum extended length of the polyethylene oxide chain places a minimum restriction on the volume fraction of 0.4. The results varied slowly with ϕ , but a good fit was obtained with a value of 0.5. Neutron reflection studies of $C_{12}E_8$ at the air–water interface by Lu *et al.* demonstrated a disordered hydrocarbon chain region at a surface excess of $\sim 2.7 \mu\text{mol m}^{-2}$ [10]. Neutron reflection together with isotropic labeling also allows the determination of the volume fraction profiles across the interface of individual segments of the surfactant, although the calculated profiles are convoluted with thermal roughening to give a Gaussian distribution. The headgroup region of $C_{12}E_8$ had a thickness of $\sim 17 \text{ \AA}$ whose volume fraction peaks at ~ 0.5 . The similarity of the behaviour of $C_{12}E_8$ at the air–water interface with the behaviour of $C_{10}E_8$ at the oil–water interface suggests that these simple C_nE_m surfactants are quite insensitive to the non-aqueous phase. The large ethylene oxide headgroups are only solvated by the aqueous phase. These headgroups control the film structure and preclude the formation of an anisotropic monolayer.

Some work has also been done with ellipsometry on the adsorption of surfactants at the oil–water interface. Knock *et al.* studied the adsorption of the cationic hydrocarbon surfactant hexadecyltrimethylammonium bromide (CTAB) to the hexadecane–water interface [11]. At low surface excess, the measured ellipticity was well-described by a model in which the hydrocarbon chain of the surfactant exhibited the same optical properties as hexadecane. The observed ellipticity was attributed to contributions from thermal roughening, the trimethylammonium headgroup and the bromide counterions. However, this model was less satisfactory at surface coverages close to the limiting surface excess unless the monolayer was treated as a uniaxial

film, whereby the alignment of the hydrocarbon chains along the surface normal introduced optical anisotropy. Benjamins *et al* investigated the adsorption of two nonionic surfactants to the decane–water interface [12]. They combined measurements taken with H₂O and D₂O in order to overcome the problem of correlation between the refractive index, n , and thickness of the interfacial layer, d ; ellipsometry yields one experimental parameter, the ellipsometric thickness, η , which is dependent upon both n and d . They assumed that the monolayer behaved as an isotropic slab between the bulk phases. The two water phases had sufficiently different refractive indices ($\Delta n = 0.005$) to allow them to extract both n and d (and hence the adsorbed amount). They determined the limiting surface excess for both the water-soluble surfactant C₁₈E₅₀ and the oil-soluble surfactant C₁₂E₅ and compared their results with the values from interfacial tensiometry. The values agreed to within 20% and 10%, respectively. This approach relies upon the assumption that the refractive index and the thickness of the oil film are independent of the solvent. H₂O and D₂O should hydrate the ethylene oxide groups to the same extent, but this situation would not result in the same refractive index for the interfacial film. Furthermore, this approach estimates the thickness of the interfacial film of C₁₂E₅ to be 15 nm, which is significantly longer than the fully-extended chain length of 3.5 nm [10]. Under the more reasonable assumption that the thickness of the film and the surface excess are identical, the surface coverage was overestimated by a factor of 4 compared to the value from interfacial tensiometry. Thus although this approach can generate reasonable values for the surface coverage, it is at the expense of the accuracy of other interfacial parameters such as the film thickness.

4.4 Protein adsorption to the hexadecane–water interface

The coefficient of ellipticity for the adsorption of β -casein from aqueous solution to the hexadecane–water interface was measured for a series of concentrations from 5.4 to 4800 mg L⁻¹. The coefficient of ellipticity for the adsorption of β -lactoglobulin was measured for a series of concentrations from 1.1 to 10000 mg L⁻¹. The measurements were taken for one hour for each solution and the results from the β -casein and β -lactoglobulin films are plotted in figure 9 and 10, respectively.

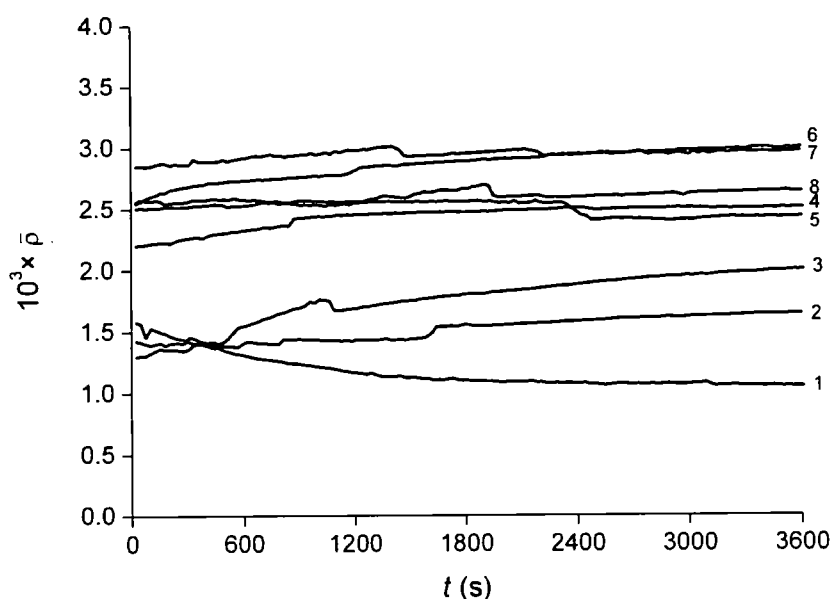


Figure 9. Coefficient of ellipticity, $\bar{\rho}$, plotted as a function of time, t , for the adsorption of a series of aqueous β -casein solutions to the hexadecane–water interface. $c =$ (1) 5.4 mg L⁻¹, (2) 11 mg L⁻¹, (3) 25 mg L⁻¹, (4) 100 mg L⁻¹, (5) 250 mg L⁻¹, (6) 520 mg L⁻¹, (7) 1000 mg L⁻¹, (8) 4800 mg L⁻¹.

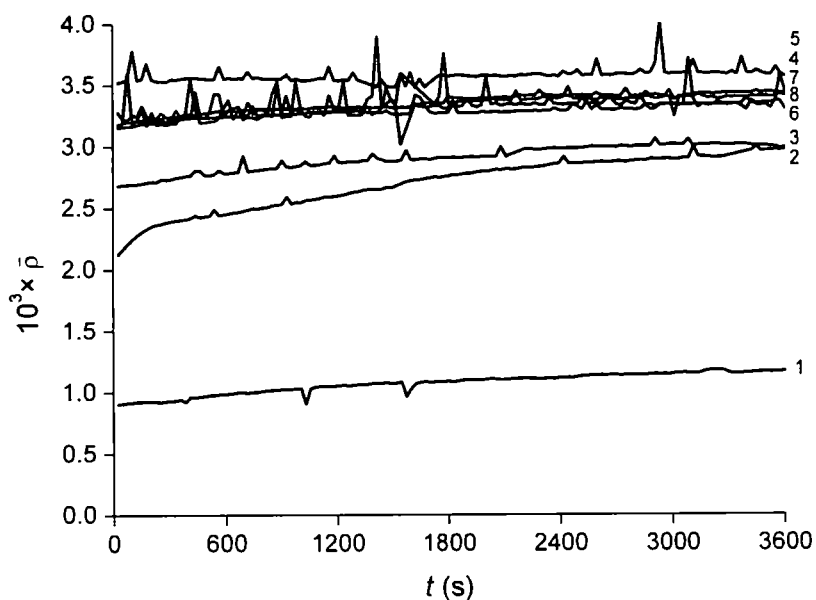


Figure 10. Coefficient of ellipticity, $\bar{\rho}$, plotted as a function of time, t , for the adsorption of a series of aqueous β -lactoglobulin solutions to the hexadecane–water interface. $c =$ (1) 1.1 mg L^{-1} , (2) 11 mg L^{-1} , (3) 49 mg L^{-1} , (4) 100 mg L^{-1} , (5) 500 mg L^{-1} , (6) 1000 mg L^{-1} , (7) 5000 mg L^{-1} , (8) 10000 mg L^{-1} .

The spikes and troughs occur when vibrations or air currents perturb the interface and cause the reflected beam to miss the detector. In most cases, the ellipticity rises asymptotically towards an equilibrium value during the course of the experiment as the protein adsorbs to the interface. The one exception to this observation is the lowest concentration of β -casein ($c = 5.4 \text{ mg L}^{-1}$), which drops over time to a value that is close to the value for the clean interface ($\bar{\rho} = 0.93 \times 10^{-3}$).

The average of the measurements over the last 100 s from figures 9 and 10 are plotted as a function of concentration in figure 11.

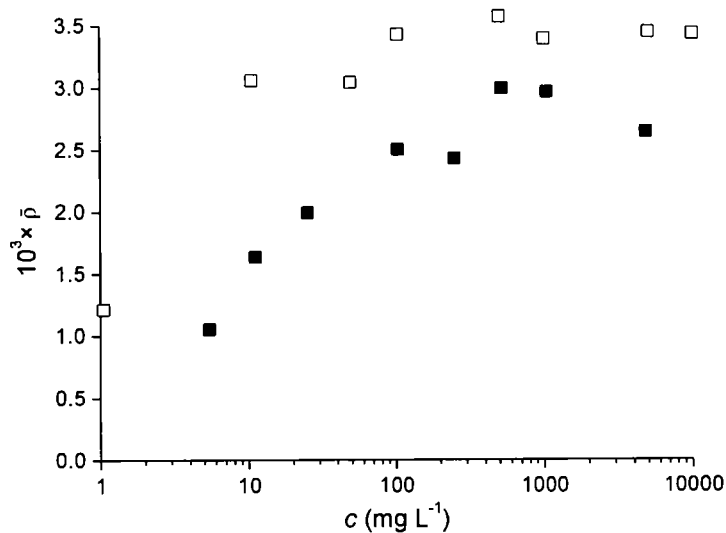


Figure 11. Coefficient of ellipticity, $\bar{\rho}$, plotted as a function of protein concentration, c , for the adsorption of a series of aqueous β -casein (■) and β -lactoglobulin (□) solutions to the hexadecane–water interface.

The ellipticity measurements for both proteins increase with increasing bulk concentration and reach a maximum at $c > 100 \text{ mg L}^{-1}$. This concentration is well below the typical concentrations of these proteins in bovine milk. The concentration of β -casein in milk is 9300 mg L^{-1} and the concentration of β -lactoglobulin is 3500 mg L^{-1} [13]. Neither the limiting bulk concentration nor the limiting surface coverage for the proteins is as sharply defined as for the surfactant monolayer. β -casein forms spherical micelles above a critical aggregation concentration which ranges from $500\text{--}2000 \text{ mg L}^{-1}$ [14], whereas β -lactoglobulin does not form micelles. The fact that both proteins reach their limiting values at similar concentrations suggests that the interface has become saturated with protein in both cases. The β -lactoglobulin film exhibits a greater ellipticity than the β -casein film, which suggests that β -lactoglobulin forms either a denser or a thicker film than β -casein. β -lactoglobulin also generates a larger ellipticity at a lower bulk concentration than β -casein. This result is surprising when one considers that β -casein is the most amphiphilic of the milk proteins and that β -casein tends to displace β -lactoglobulin from the air–milk

interface [15]. Nonetheless, the presence of the oil phase may cause β -lactoglobulin to form a denser film than β -casein and hence generate a more positive ellipticity.

As discussed above, ellipsometry yields one experimental parameter; the ellipsometric thickness, η , which is dependent upon both n and d . Thus it is not possible to determine unambiguously the surface coverage and the thickness of the protein film from these data alone. Nonetheless, it is possible to extract some useful qualitative data from my results. The protein molecules are undoubtedly perturbing the dielectric profile across the interface such that all the ellipticity readings are large and positive. If the protein unfolds at the interface, we expect that some of the sidechains of the hydrophobic residues may penetrate a short distance into the oil film but the majority of the protein will form a hydrated layer at the interface. A positive ellipticity at the oil–water interface can arise if the interfacial film has a refractive index that is either less than the refractive index of water ($n = 1.33$) or greater than the refractive index of hexadecane ($n = 1.43$). An intermediate value would lead to a negative ellipticity. The calculated refractive index for β -lactoglobulin is 1.58 [16], i.e. greater than hexadecane. If the portion of the protein dissolved in the oil phase has the same refractive index as the oil phase, it will not contribute to the ellipticity. In this model, the volume fraction of water in the protein film must be less than 60 % to ensure a positive ellipticity. However, if the protein dissolved in the oil phase does contribute to the ellipticity, then more extensive hydration is permitted. Given the difference in the refractive indices of the protein and oil phase, the second scenario is more likely.

I will now compare my results to other work from the literature. The work by Beaglehole *et al* on the adsorption of bovine serum albumin to the oleyl alcohol–water interface [17] was introduced in chapter 1. The protein formed a film with a refractive index intermediate between the two bulk phases; the refractive index of the oil phase ($n = 1.46$) is greater than the protein film. They assumed that the dielectric constant of the protein film, ϵ , was close to ϵ_2 . Consequently the Drude equation reduces to

$$\eta = \frac{\epsilon_2 - \epsilon_1}{\epsilon_2} \int (\epsilon - \epsilon_2) dz = \frac{\epsilon_2 - \epsilon_1}{\epsilon_2} \Gamma_\epsilon \quad (1)$$

where the dielectric excess, Γ_ϵ , is related to the adsorbed amount, Γ , through the expression

$$\Gamma = \frac{\Gamma_\epsilon}{\frac{dn}{dc}} \quad (2)$$

This model does not allow for any contribution to the ellipticity from protein in the oil phase. Beaglehole also assumed that the dielectric constant varies linearly over the concentrations adopted by the protein film. Under these assumptions, the adsorbed amount can be determined through the measurement of only one additional parameter; $\frac{dn}{dc}$. They measured this proportionality constant to be 0.9 mL g^{-1} at pH 3 from $0\text{--}14 \text{ mg mL}^{-1}$. This value is relatively large compared to the typical value for a protein of $\frac{dn}{dc} = 0.18 \text{ mL g}^{-1}$ [18], which corresponds to $\frac{d\epsilon}{dc} = 0.57 \text{ mL g}^{-1}$. They analyzed the ellipsometric response with these equations to give an adsorbed amount of 0.45 mg m^{-2} at a bulk concentration of 3.5 mg mL^{-1} . However, if the thickness of the protein film is assumed to be $\sim 5 \text{ nm}$, the concentration of the protein would be 90 mg mL^{-1} at the interface, and a thinner film would be even more concentrated. This concentration is outside the range over which the proportionality constant was measured. Consequently, this analysis relies on a considerable linear extrapolation of the refractive index of the protein film. Furthermore, this group did not take into account the effect of thermal roughening on the coefficient of ellipticity.

Bylaite *et al* measured the ellipsometric response of β -lactoglobulin at the interface between water and either olive oil or caraway essential oil [19]. In a previous study by Dalglish and Leaver [20], the thickness of a β -lactoglobulin film on latex was determined by dynamic light scattering to be 2 nm . Bylaite *et al* assumed that the protein film was the same thickness at the oil–water interface. Once the thickness is assumed, the refractive index of the layer can be calculated explicitly ($n = 1.48$). They then used the formula derived by Cuypers [21] to extract the adsorbed amount from the refractive index:

$$\Gamma = \frac{0.3d(\varepsilon - \varepsilon_2)}{(\varepsilon + 2)[r(\varepsilon_2 + 2) - v(\varepsilon_2 - 1)]} \quad (3)$$

where the specific refractivity, $r = 0.249 \text{ mL g}^{-1}$, and the partial specific volume, $v = 0.749 \text{ mL g}^{-1}$, were determined from the molar refractivity and specific volume of the amino acid sequence. Under these assumptions, they found that the protein film formed a dense layer with a surface excess of $1.60\text{--}1.66 \text{ mg m}^{-2}$ at a bulk concentration of $2\text{--}10 \text{ mg mL}^{-1}$. The diameter of a single β -lactoglobulin molecule is $\sim 36 \text{ \AA}$ [22], so the assumption that the film is thinner than this value is justified when one considers the evidence that the protein unfolds at the interface. It is unlikely that the protein forms films of the same thickness at the oil–water interface as on latex particles, particularly as the hydrophobic regions of the protein can penetrate the fluid but not the solid. Nonetheless, Bylaite *et al* state that the evaluation of the adsorbed amount is rather insensitive to the thickness value.

Russev *et al* studied the adsorption kinetics of a 0.1 mg mL^{-1} β -casein solution at the xylene–water interface [23]. This group also measured the adsorption of a β -casein solution at the same bulk concentration at the air–water interface. They assumed that β -casein formed identical films at these two interfaces and from this assumption they were able to determine explicitly the refractive index, n , and thickness, d , of the film. However, proteins are complex molecules, so the likelihood of the assumption that they behave identically at the air–water and oil–water interface being correct is tenuous. n and d were used to determine the adsorbed amount according to:

$$\Gamma = \frac{(n - n_2)d}{\frac{dn}{dc}} \quad (4)$$

where the variation of the refractive index with concentration, $\frac{dn}{dc}$, was taken from literature values to be 0.18 mL g^{-1} [18]. This analysis also relies on considerable extrapolation in the same manner as the work of Beaglehole *et al*. When they analyzed the refractive index and thickness adsorption curves, they found that the optimum model described the data in terms of a two-layer model; a dense inner layer with a surface concentration of 1.2 mg mL^{-1} , a thickness of 18 \AA and a refractive index of 1.45 which formed in 15 minutes and a more dilute outer layer with a

thickness of 54 Å and a refractive index of 1.37 which adsorbed over several hours. With either a single or double-layer model, the total adsorbed amount tended towards a limiting value of 2.3–2.5 mg m⁻².

It is useful to compare the adsorption isotherms determined ellipsometrically with other methods. Graham and Phillips used radiotracers and scintillation counting to determine the adsorbed amount of [1-¹⁴C] acetyl β-casein at the toluene–water interface [18]. They found that the adsorbed amount increased with bulk concentration to a plateau of ~3 mg m⁻² from 0.001–0.1 mg mL⁻¹. Above 0.1 mg mL⁻¹, the adsorbed amount rose again to 5 mg m⁻². Graham and Phillips assigned the adsorbed amount up to 3 mg m⁻² to an irreversibly adsorbed film, and subsequent adsorbed protein to reversibly adsorbed molecules in a second layer in the aqueous phase below the initial film.

Atkinson *et al* have studied β-casein and β-lactoglobulin films at the air–water interface by neutron reflectivity [24]. Both proteins formed a film at the interface which consisted of a dense, hydrophobic inner layer and a more diffuse, hydrophilic outer layer extending into the aqueous phase. They measured the surface properties of the films at bulk concentrations of 5–500 mg L⁻¹ and 10–1000 mg L⁻¹ for β-casein and β-lactoglobulin, respectively. The β-casein film exhibited surface coverages of 2.0–2.9 mg m⁻² over this concentration range. The inner layer of the film was 9–13 Å thick with a protein volume fraction of 90 % and the outer layer was 44–47 Å thick with a protein volume fraction of 20 %. The β-lactoglobulin film adsorbed at surface coverages of 1.6–2.0 mg m⁻². The inner layer was 10–13 Å thick with a protein volume fraction of 90 % and the outer layer was 20 Å thick with a protein volume fraction of 20 %. Under the assumption that both layers reside in the aqueous phase, the profile for β-casein would generate an ellipticity reading of $\bar{\rho} = (1.1–2.5) \times 10^{-3}$ and the profile for β-lactoglobulin would generate a reading of $\bar{\rho} = (2.4–3.3) \times 10^{-3}$. These modelled values are in the same range as my measured values, which suggests that these proteins also adopt a two-layer film at the oil–water interface with similar properties to the air–water interface.

The protein and surfactant films generate ellipticities of opposite sign. It should therefore be possible to draw meaningful conclusions from the ellipticities of mixed protein–surfactant films, despite the fact that quantification of the precise composition of the films would be subject to controversial assumptions. The extent to which ellipsometry can probe these mixed films will be addressed in the next section.

4.5 Surfactant and protein coadsorption

I investigated the effect of protein and surfactant coadsorption in two ways. In the first set of experiments, either β -casein or β -lactoglobulin was allowed to adsorb to the hexadecane–water interface in the absence of surfactant and, once the protein film had formed, $C_{10}E_8$ solution was injected into the subphase. In the second set of experiments, the surfactant and protein were co-dissolved in aqueous solution.

Injection of $C_{10}E_8$ into the subphase

In this set of experiments, the protein was left to adsorb to the hexadecane–water interface from a buffered 1000 mg L^{-1} solution (in the plateau region of the pure protein adsorption isotherm) in the absence of surfactant for thirty minutes. I then removed 0.5 mL of the aqueous subphase with a micropipette and replenished the solution with 0.5 mL of $C_{10}E_8$ solution (the volume of the aqueous section of the cell is 3.5 mL). The coefficient of ellipticity was then measured for a further 30 minutes. After 15 minutes, the coefficient of ellipticity was essentially constant in all cases except three (*vide infra*). The average of the coefficient of ellipticity over the final 15 minutes is plotted as a function of $C_{10}E_8$ concentration in figure 12 for the experiments employing β -lactoglobulin as the protein.

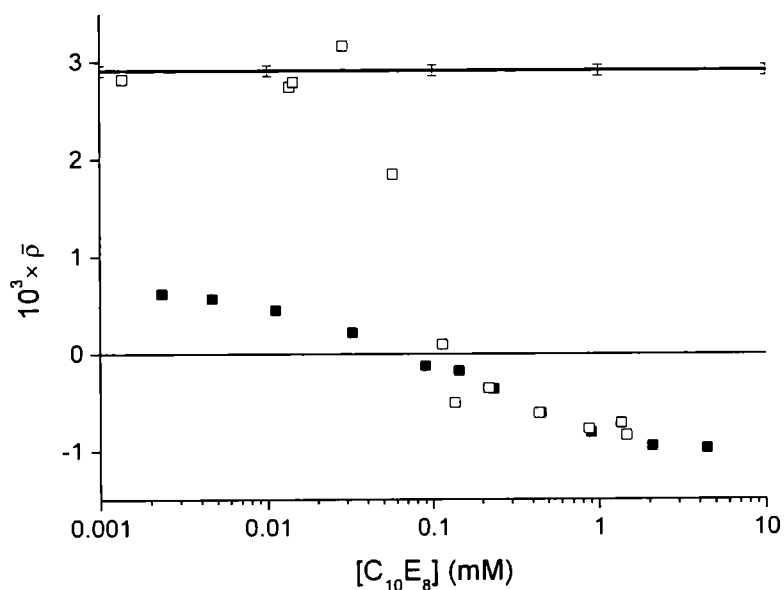


Figure 12. Coefficient of ellipticity at the hexadecane–water interface, $\bar{\rho}$, plotted as a function of the final concentration of $C_{10}E_8$. (■) Pure $C_{10}E_8$, (□) β -lactoglobulin film adsorbed from 1000 mg L^{-1} solution in the presence of $C_{10}E_8$ injected into the subphase, (solid line) 1000 mg L^{-1} pure β -lactoglobulin solution in the absence of surfactant.

At $[C_{10}E_8] < 0.01 \text{ mM}$ ($R < 0.2$), the measured ellipticity is close to the value for the pure protein film, which suggests that the surfactant has a negligible effect on the protein film below this concentration. At $[C_{10}E_8] > 0.1 \text{ mM}$ ($R > 2$), the ellipticity follows closely the isotherm of the pure surfactant, which suggests that above this concentration the surfactant has completely displaced the protein film at the interface. Between these two regimes, both protein and surfactant are present at the interface. However, it is not possible by ellipsometry alone to determine the composition of the film in this region.

The coefficient of ellipticity is plotted as a function of $C_{10}E_8$ concentration in figure 13 for the experiments employing β -casein as the protein.

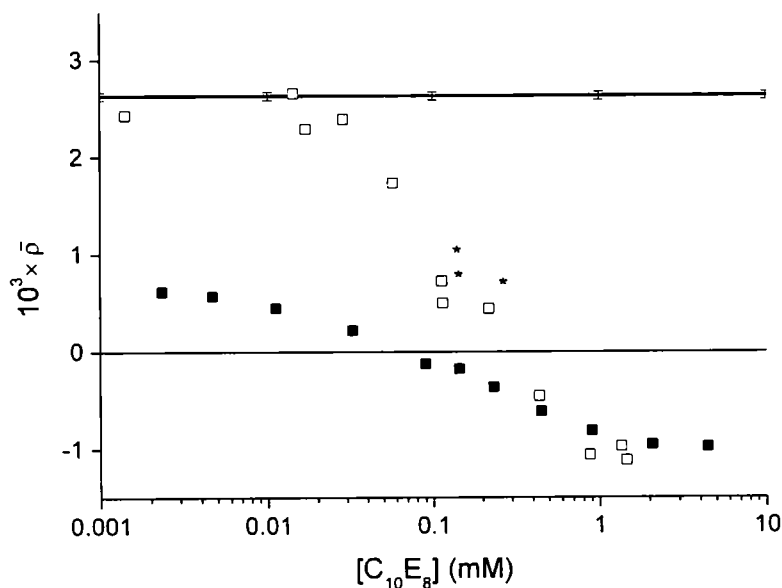


Figure 13. Coefficient of ellipticity at the hexadecane–water interface, $\bar{\rho}$, plotted as a function of the final concentration of $C_{10}E_8$. (□) β -casein film adsorbed from 1000 mg L^{-1} solution in the presence of $C_{10}E_8$ injected into the subphase (■) pure $C_{10}E_8$, (solid line) 1000 mg L^{-1} pure β -casein solution in the absence of surfactant.

The behaviour of the β -casein films is qualitatively similar to the β -lactoglobulin films, although the ellipticity does not approach the isotherm of the pure surfactant until $[C_{10}E_8] > 0.4 \text{ mM}$ ($R > 10$), which suggests that the β -casein film is more resistant to displacement by surfactant than the β -lactoglobulin film.

The molar ratio at which the surfactant begins to displace both proteins ($R > 0.2$) is very similar to the molar ratio at which $C_{12}E_6$ begins to displace β -lactoglobulin from the air–water interface [1]. This observation suggests that the nature of the supernatant phase is not critical for this phase of the displacement. In contrast, greater molar ratios are required to completely remove the protein from the oil–water interface. If the two-layer model for protein adsorption is correct, these observations can be rationalised in the following way. The surfactant removes the outer, more dilute region of the protein film at lower concentrations. As this part of the film is

entirely located in the aqueous phase, the nature of the supernatant phase is irrelevant. The removal of the denser layer that is adjacent to, or penetrates into, the oil phase requires a greater surfactant concentration than the outer film. Furthermore, a greater surfactant concentration is required to remove the film from the oil–water interface than the air–water interface, which suggests that the inner film is more strongly bound to the oil phase than the air phase, and may even be dissolved in the oil phase.

The three data points marked by the asterisk in figure 13 were not constant over the period of measurement. The coefficient of ellipticity for these measurements are plotted as a function of time in figure 14. The injection of the surfactant into the subphase defines $t = 0$.

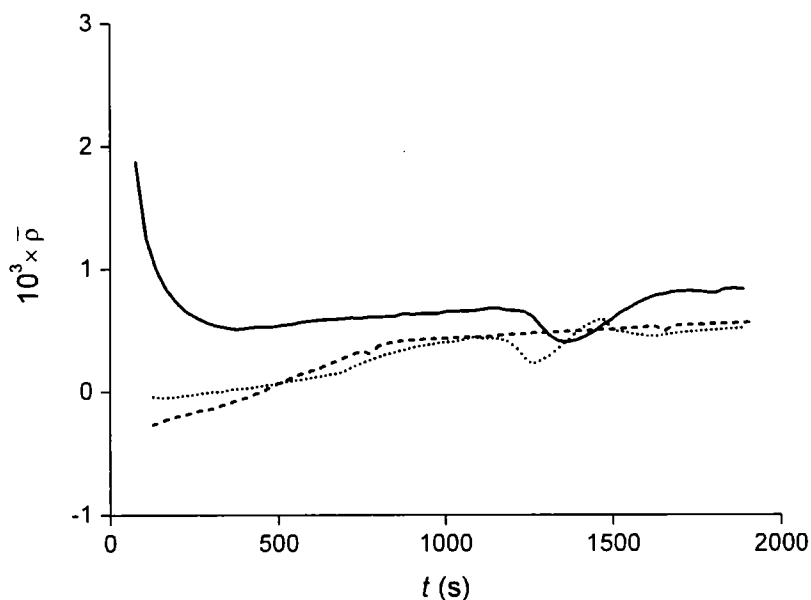


Figure 14. Coefficient of ellipticity, $\bar{\rho}$, plotted as a function of time, t , for the adsorption of $C_{10}E_8$ solutions beneath a β -casein film adsorbed from 1000 mg L^{-1} solution at the hexadecane–water interface. (Solid line) $[C_{10}E_8] = 0.113 \text{ mM}$, (dashed line) $[C_{10}E_8] = 0.114 \text{ mM}$, (dotted line) $[C_{10}E_8] = 0.228 \text{ mM}$.

All three curves should extrapolate back to the value for the unperturbed protein film ($\bar{\rho} = 2.6$) at $t = 0$. Thereafter, at these concentrations the coefficient of ellipticity exhibits maxima and minima at seemingly random times. These variations in the ellipticity may be due to variations in the average thickness of the protein/surfactant film that is illuminated by the laser beam. In the second stage of the orogenic mechanism described by Mackie [3], the β -casein film is ruptured by surfactant. Surfactant-rich domains are surrounded by protein-rich networks that become thicker over time. In the case of β -lactoglobulin, however, the film does not become thicker and the displacement occurs over a very narrow range of surface pressure. Therefore, the behaviour in figure 14 may be the result of these networks being carried into and out of the laser beam. However, in the absence of imaging capabilities, this conclusion is only tentative.

Surfactant and protein co-dissolved in solution

In this set of experiments, the protein and surfactant were co-dissolved in *tris* buffer solution. The protein concentration was 1000 mg L^{-1} . The coefficient of ellipticity at the hexadecane–water interface was then measured for 90 minutes. The coefficient of ellipticity is plotted as a function of time in figure 15 for the experiments employing β -lactoglobulin as the protein and in figure 16 for the experiments employing β -casein as the protein.

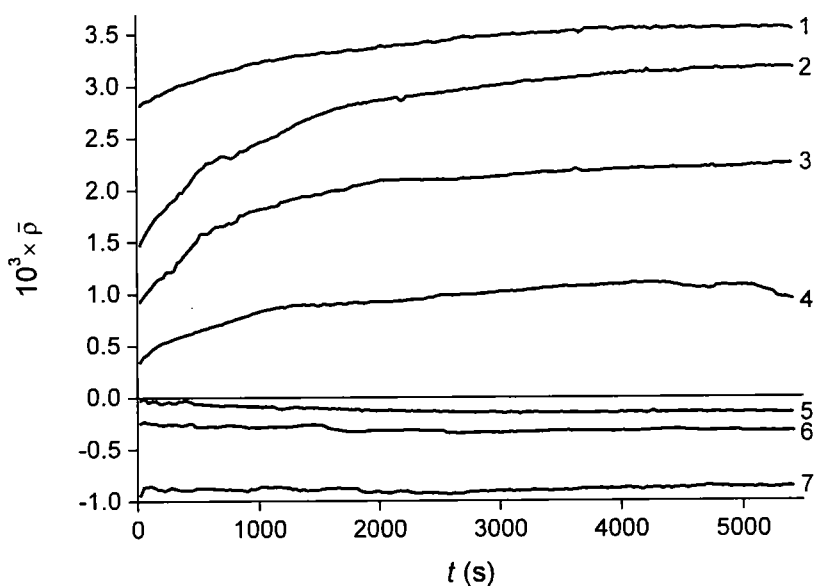


Figure 15. Coefficient of ellipticity, $\bar{\rho}$, plotted as a function of time, t , for the adsorption of a series of aqueous β -lactoglobulin and $C_{10}E_8$ solutions to the hexadecane–water interface. $[C_{10}E_8] = (1) 1.6 \mu\text{M}, (2) 16 \mu\text{M}, (3) 35 \mu\text{M}, (4) 70 \mu\text{M}, (5) 110 \mu\text{M}, (6) 160 \mu\text{M}, (7) 1600 \mu\text{M}$. Protein concentration = 1000 mg L^{-1} .

In figure 15 at $[C_{10}E_8] \leq 70 \mu\text{M}$ ($R \leq 1.3$), the ellipticity readings increase over the course of the experiment towards limiting values. This slow variation in the ellipticity is analogous to the behaviour of the pure protein solutions in figure 10. This observation suggests that at these low surfactant concentrations the protein is still able to adsorb to the surface and denature. At $[C_{10}E_8] \geq 110 \mu\text{M}$ ($R \geq 2$), the readings are essentially constant over the course of the experiment, at the values expected in the absence of protein. The more rapid diffusion of surfactant molecules in comparison to protein molecules means that the $C_{10}E_8$ monolayer reaches equilibrium before the start of the measurement, as exemplified by figure 1. This observation suggests that in this regime, the surfactant controls the interfacial behaviour.

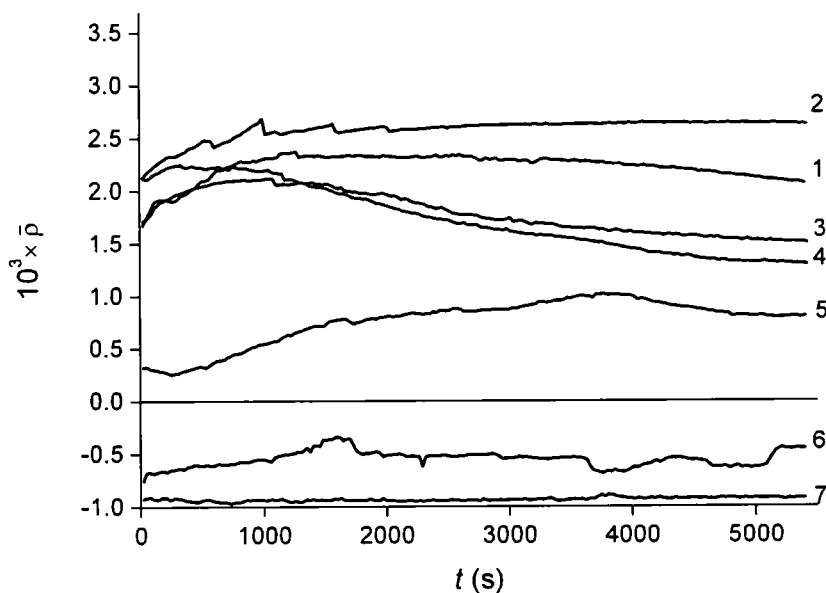


Figure 16. Coefficient of ellipticity, $\bar{\rho}$, plotted as a function of time, t , for the adsorption of a series of aqueous β -casein and $C_{10}E_8$ solutions to the hexadecane–water interface. $[C_{10}E_8] = (1) 1.6 \mu\text{M}, (2) 16 \mu\text{M}, (3) 35 \mu\text{M}, (4) 70 \mu\text{M}, (5) 110 \mu\text{M}, (6) 160 \mu\text{M}, (7) 1600 \mu\text{M}$. Protein concentration = 1000 mg L^{-1} .

The behaviour of the β -casein and $C_{10}E_8$ solutions is qualitatively similar to the results from the β -lactoglobulin and $C_{10}E_8$ solutions; there is a shift in the kinetic curves from time-variant to time-invariant behaviour at $[C_{10}E_8] \geq 160 \mu\text{M}$ ($R \geq 4$), which again suggests a change in the species that dominates the surface. However, in contrast to the β -lactoglobulin solutions, some of the ellipticity regions decrease with time, and the data are markedly less regular. Furthermore, these solutions were turbid. There has been little work done on the effect of surfactants on the self-aggregation of proteins. However, Semenova *et al* have proposed the following mechanism for the aggregation of sodium caseinate in the presence of the nonionic surfactant polyglycerol palmitate [25]. The surfactant and protein combine due to the hydrophobic effect and the concomitant release of large numbers of hydrating water molecules into bulk solution. These surfactant–protein complexes then form

aggregates whose radius of gyration is ~ 200 nm. The presence of these aggregates may explain the more complex behaviour in figure 16. Non-aggregated protein can diffuse and adsorb to the surface more rapidly than aggregated protein. The protein–surfactant complex then adsorbs to the interface over longer timescales and the presence of the surfactant in the film reduces the coefficient of ellipticity accordingly. The average of the coefficient of ellipticity for the last ten minutes of each experiment in figures 15 and 16 are plotted as a function of $C_{10}E_8$ concentration in figure 17.

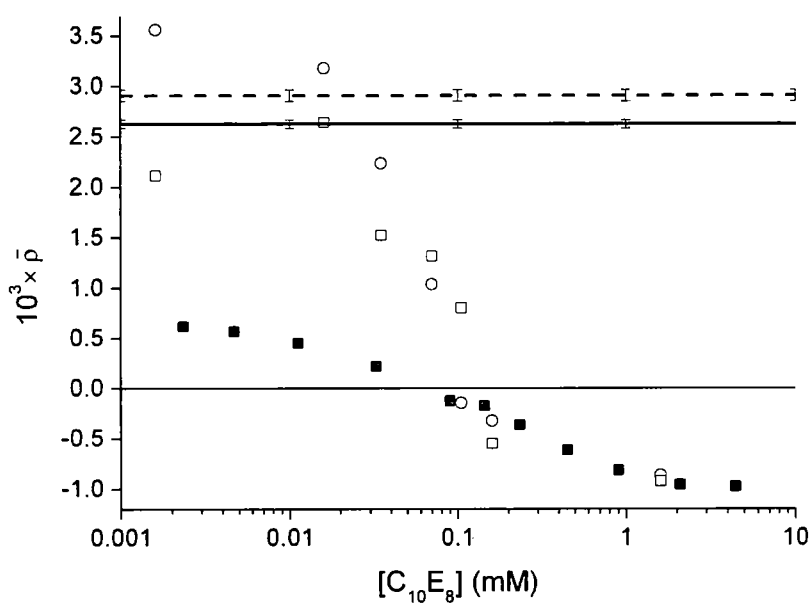


Figure 17. Coefficient of ellipticity at the hexadecane–water interface, $\bar{\rho}$, plotted as a function of the concentration of $C_{10}E_8$. (■) Pure $C_{10}E_8$, (□) β -casein and $C_{10}E_8$, (solid line) pure β -casein, (○) β -lactoglobulin and $C_{10}E_8$, (dashed line) pure β -lactoglobulin. Protein concentration = 1000 mg L^{-1} in all cases.

As noted above, at $[C_{10}E_8] > 100 \text{ } \mu\text{M}$, the measured ellipticity for each protein follows the isotherm for pure $C_{10}E_8$ solutions, which suggests that the protein does

not adsorb to the interface in the presence of surfactant at this concentration. Conversely, at $[C_{10}E_8] < 20 \mu\text{M}$, the measured ellipticity is large and positive and similar to the values for the pure protein films. Between these limiting concentrations, there is a changeover where the measured ellipticity is intermediate between these two regimes.

When one compares the co-adsorption behaviour in figure 17 to the adsorption of surfactant into the protein film in figures 12 and 13, it is evident that the long-time behaviour of these systems is largely independent of the approach that is used to prepare the surfaces. At low surfactant concentrations, the protein dominates the surface, whereas at sufficiently high surfactant concentrations, the surfactant dominates the surface. In the intermediate regime, the average ellipticity readings for the two experiments are similar; however, this observation alone does not necessarily imply that the surface films are identical, particularly in light of the interesting kinetic behaviour shown in figure 14. Nonetheless, there is only a narrow concentration range where both species are present at the interface.

Further work with a chemically-specific technique would be useful to determine whether the structure and composition of the mixed film is dependent upon the pathway used to create the film. This question is evidently of interest to the formulators of food emulsions.

4.6 Conclusion

In this chapter, I have employed ellipsometry to study the adsorption to the hexadecane–water interface of a simple nonionic hydrocarbon surfactant and two milk proteins, as well as the competitive adsorption of each protein with the surfactant. In my study of the adsorption of $C_{10}E_8$, I created two simple physical models in order to interpret the ellipsometry results. In the simplest model that describes the experimental results, the hydrocarbon chains in the monolayer are disordered and the polyethylene oxide headgroups are hydrated with approximately 40 % of the headgroup layer occupied by water. I observed very similar behaviour for

$C_{10}E_8$ films at the triolein–water interface, and other workers have seen similar behaviour for the related surfactant $C_{12}E_8$ at the air–water interface, which suggests that the nature of the supernatant phase has only a subtle effect on the surfactant monolayer.

Proteins and surfactant films generate ellipticities of opposite sign which gives some potential to probe mixed protein–surfactant films. The technique is rapid and relatively simple to implement, which allows researchers the opportunity to highlight concentration ranges of interest for study by more complex techniques that display chemical specificity. In the study where $C_{10}E_8$ was injected into the subphase, there appears to be interesting behaviour for the β -casein films in the intermediate concentration range which may be a consequence of the orogenic mechanism for the displacement of protein films by surfactant. The fact that a greater molar ratio of surfactant to protein is required to remove the protein film from the oil–water interface compared to the air–water interface also suggests that the interaction of the oil phase with the protein is relevant to the stability of emulsions. Finally, the ellipsometric response from the mixed protein–surfactant films is independent of the procedure adopted to produce the films. Further work with chemically-specific techniques would be useful to determine the effect of the adsorption pathway in the structure and composition of these mixed films.

4.7 Outlook

Although this cell and the light guides can be used to measure the coefficient of ellipticity at the oil–water interface, there are several limitations to this design. First, even though the interface is pinned, the angle of the reflected light beam tends to drift over time and the tilt angle of the cell must be readjusted intermittently to ensure the beam enters the photomultiplier tube. Second, it takes several minutes to realign the beam once the oil phase has been introduced on top of the aqueous phase. Thus this arrangement is unable to probe adsorption on short timescales. Third, the current setup has no temperature control. Finally, it is difficult to alter the composition of the

aqueous phase quickly and accurately and without perturbing the interface mechanically.

With these limitations in mind, I suggest below two alternative developments that would make simpler the study of the oil–water interface by ellipsometry. The first geometry integrates the ellipsometer with the drop-shape analysis tensiometer, as shown in figure 18.

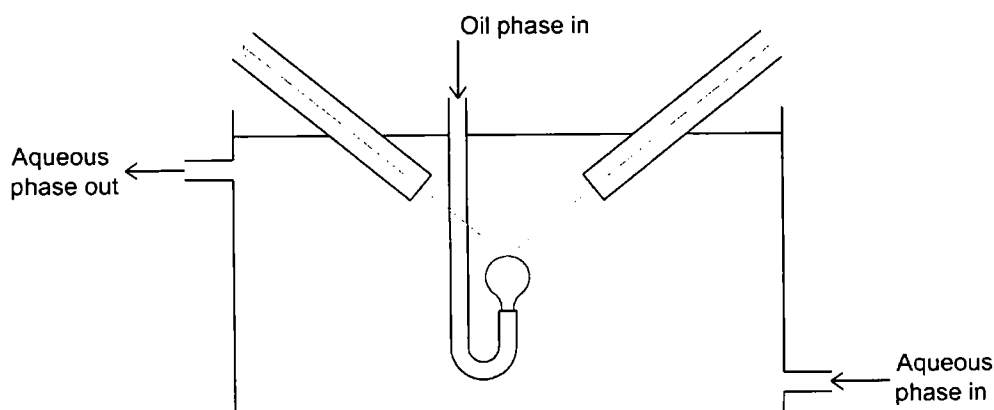


Figure 18. Schematic showing the potential integration of the ellipsometer with the drop shape analysis tensiometer.

If the ellipsometer and light guides were sufficiently well-aligned, it would be possible to create reproducibly a rising drop whose surface coincided with the beam. The drop-shape analysis tensiometer produces a fresh interface for each drop so short timescales could be measured and the aqueous phase could be replaced without perturbing the interface mechanically. This design also has the benefit that the ellipticity could be measured simultaneously with the interfacial tension.

The largest complications for this design are technical. First, the beam must coincide accurately with the surface of the drop. Furthermore, for efficient surfactant solutions, the interfacial tension and hence the shape of the drop change rapidly over time. A feedback mechanism between the video camera and a z-axis translation stage would be required to adjust the position of the drop relative to the beam. Second, the beam will diverge after reflection from the interface. This problem could be solved by using

a focusing lens before the sample to limit the lateral extent of the beam focus and a collimating lens after the sample to direct the divergent beam into the PMT. A similar approach has been used in this group to measure ellipsometry from a liquid jet [26].

The second design discards the light guides and employs a fused silica hemisphere to introduce the laser beam to the oil–water interface at the correct angle of incidence, as shown in figure 20.

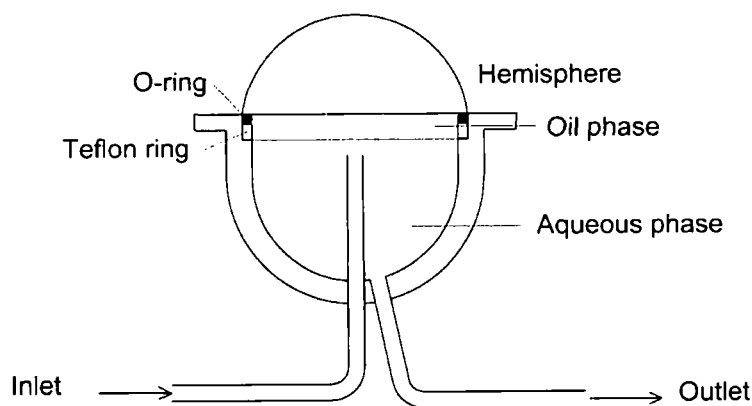


Figure 20. Schematic showing a sealed cell for studying the oil–water interface by ellipsometry.

This design would allow rapid and controllable exchange of the aqueous phase and would make the alignment of the laser beam simpler. It may also allow measurements of the kinetics of adsorption of soluble surfactants; if the aqueous phase is continually exchanged there is a stagnation point immediately above the inlet tube and the aqueous phase flows radially away from this point. However, there are three difficulties that must be overcome in this design. First, the hemisphere must be sufficiently optically isotropic that it does not introduce artefacts into the ellipsometry reading. Second, it will be more difficult to introduce the two phases into the sealed cell than in the current design. Finally, it will be more difficult to control the planarity of the oil–water interface; a focusing lens may be required to collect the divergent light.

References

- 1 D. S. Horne, P. J. Atkinson, E. Dickinson, V. J. Pinfield, and R. M. Richardson, *Int. Dairy J.* **8**, 73 (1998).
- 2 E. Dickinson, *Colloids and Surfaces B: Biointerfaces* **20**, 197 (2001).
- 3 A. R. Mackie, A. P. Gunning, P. J. Wilde, and V. J. Morris, *Langmuir* **16**, 2242 (2000).
- 4 M. Sekine, R. A. Campbell, D. S. Valkovska, J. P. R. Day, T. D. Curwen, L. J. Martin, S. A. Holt, J. Eastoe, and C. D. Bain, *Phys. Chem. Chem. Phys.* **6**, 5061 (2004).
- 5 C. D. Taylor, D. S. Valkovska, and C. D. Bain, *Phys. Chem. Chem. Phys.* **5**, 4885 (2003).
- 6 P. R. Griffiths, *Private Communication*.
- 7 H.-C. Chang, C.-T. Hsu, and S.-Y. Lin, *Langmuir* **14**, 2476 (1998).
- 8 P. W. Atkins, *Physical Chemistry* 3rd ed. (OUP, Oxford, 1986).
- 9 S. R. Goates, D. A. Schofield, and C. D. Bain, *Langmuir* **15**, 1400 (1999).
- 10 J. R. Lu, Z. X. Li, R. K. Thomas, E. J. Staples, L. Thompson, I. Tucker, and J. Penfold, *J. Phys. Chem.* **98**, 6559 (1994).
- 11 M. M. Knock, G. R. Bell, E. K. Hill, H. J. Turner, and C. D. Bain, *J. Phys. Chem. B* **107**, 10801 (2003).
- 12 J.-W. Benjamins, K. Thuresson, and T. Nylander, *Langmuir* **21**, 149 (2005).
- 13 G. Bobe, G. L. Lindberg, A. E. Freeman, and D. C. Beitz, *J. Dairy Sci.* **90**, 3955 (2007).
- 14 Y. D. Livney, A. L. Schwan, and D. G. Dalgleish, *J. Dairy Sci.* **87**, 3638 (2004).
- 15 S. A. Holt and J. W. White, *Phys. Chem. Chem. Phys.* **1**, 5139 (1999).
- 16 T. Nylander and N. M. Wahlgren, *J. Colloid Interface Sci.* **162**, 151 (1994).
- 17 D. Beaglehole, F. Lawson, G. Harper, and M. Hossain, *J. Colloid Interface Sci.* **192**, 266 (1997).
- 18 D. E. Graham and M. C. Phillips, *J. Colloid Interface Sci.* **70**, 415 (1979).
- 19 E. Bylaite, T. Nylander, R. Venskutonis, and B. Jonsson, *Colloids and Surfaces B: Biointerfaces* **20**, 327 (2001).

- 20 D. G. Dalgleish and J. Leaver, in *Food Polymers, Gels and Colloids*, edited by E. Dickinson (Royal Society of Chemistry, Cambridge, 1991), p. 113.
- 21 P. A. Cuypers, J. W. Corsel, M. P. Janssen, J. M. M. Kop, W. T. Hermens, and H. C. Hemker, *J. Biol. Chem.* **258**, 2426 (1983).
- 22 D. W. Green and R. Aschaffenburg, *J. Mol. Biol.* **1**, 54 (1959).
- 23 S. C. Russev, T. V. Arguirov, and T. D. Gurkov, *Colloids and Surfaces B: Biointerfaces* **19**, 89 (2000).
- 24 P. J. Atkinson, E. Dickinson, D. S. Horne, and R. M. Richardson, *J. Chem. Soc. Faraday Trans.* **91**, 2847 (1995).
- 25 M. G. Semenova, L. E. Belyakova, Y. N. Polikarpov, M. M. Il'in, T. A. Istarova, M. S. Anokhina, and E. N. Tsapkina, *Biomacromolecules* **7**, 101 (2006).
- 26 T. Battal, C. D. Bain, M. Weiss, and R. C. Darton, *J. Colloid Interface Sci.* **263**, 250 (2003).

Chapter 5

Development of evanescent wave Raman scattering at the oil–water interface

5.1 Introduction

Vibrational spectroscopy has the potential to give detailed information on the structure of thin films at the oil–water interface, but to obtain suitably resolved spectra the technique must deliver a certain level of sensitivity and surface-specificity. The very strong absorbance of water in infrared spectroscopy dominates the spectrum and can totally mask regions of interest whereas water has a relatively low Raman cross-section. As a result Raman spectroscopy is favoured in studies of biological systems in their natural aqueous environment. The most common form is confocal Raman spectroscopy where scattered Raman photons are collected through the same optics used to deliver the pump laser beam. However, spatial resolution normal to the interface is in the micron range and hence is not sufficiently good to study exclusively monolayers and protein films. Evanescent wave Raman scattering has been developed in the Bain group to study thin films at the solid–solid and solid–liquid interfaces as it gives both superior surface selectivity and improved sensitivity compared to confocal Raman scattering. Beattie *et al.* confined fatty acid monolayers between CaF_2 and MgF_2 and studied the effect of pressure on the conformation of the molecules [1]. Evanescent wave Raman scattering is particularly useful in this instance as it offers a wealth of structural information. Greene and Bain exploited the surface sensitivity of TIR Raman scattering to study the surface of polymer laminates and foliar cuticles [2]. Lee and Bain investigated phase transitions of planar supported lipid bilayers confined at the silica–water interface [3] and even acquired spectra of peptides incorporated into the bilayer [4]. However, to date it has not been used to probe the liquid–liquid interface and there are numerous technical difficulties that must be resolved. Although the technique has some degree of surface-specificity, the spectrum will have contributions from the fused silica substrate, the ambient water phase within the evanescent wave and, most pertinently, the oil film. The signal from

the oil phase is likely to dominate the region of interest for any species adsorbed at the oil–water interface and hence I require a thin oil film (< 100nm thick) to prevent the oil spectrum from swamping the signal from the thin interfacial layer. Even in the case of a thin oil film a reference spectrum of the oil in contact with pure water will be required so that the oil bands can be removed from spectra of surfactants or proteins at the oil–water interface.

Previous spectroscopic studies of the oil–water interface

There have been a considerable number of studies with interfacial tensiometry, and to a lesser extent ellipsometry, of species adsorbed at the oil–water interface but relatively few studies that give direct access to molecular information. Takenaga and Nakanga demonstrated the first use of evanescent wave Raman scattering in their study of cetyltrimethylammonium bromide (CTAB) and methyl orange adsorbed at the interface between CCl_4 and aqueous solution [5]. They used the resonant enhancement of the dye molecules to provide Raman spectra of an adduct of CTAB and methyl orange in the monolayer. However they were only able to draw conclusions about the orientation of the dye at the interface as only these molecules were sufficiently enhanced. Furthermore, the behaviour of a monolayer at the water– CCl_4 interface is not necessarily representative of its behaviour an organic oil–water interface. Fujiwara and Watarai used the same technique to study the adsorption of a cationic manganese–porphyrin complex at the toluene–water interface and to determine the mean tilt angle of the complex at the interface [6]. More recently Fujiyoshi *et al.* have developed fourth-order Raman spectroscopy to study oxazine 170 dye molecules at the hexadecane–water interface [7]. Fourth-order Raman spectroscopy is an even-order nonlinear technique (χ^4) so a transition is only allowed if inversion symmetry is broken, such as at an interface. However this technique relies on the second-harmonic generation of the dye molecules to be effective and consequently it is a fairly restrictive probe of adsorption at the oil–water interface.

Sperline and Freiser coated a ZnSe internal reflection element (IRE) with a very viscous aliphatic hydrocarbon gel (Apiezon M) and contacted the IRE to a

cetylpyridinium chloride (CPC) solution [8]. They used infrared attenuated total reflection spectroscopy to observe adsorption of the surfactant to the gel–water interface.

Zarbakhsh *et al.* have pioneered the use of neutron reflectivity to study liquid–liquid interfaces [9, 10]. As well as their studies of the neat interface, which I have discussed previously, they have also studied the adsorption of surfactants and polymers to the hexadecane–water interface. They used isotopic substitution to investigate the structure of hexadecylphosphorylcholine films and proposed a trilayer of surfactant molecules to explain their results.

Schlossman's group have used x-ray reflectivity to study adsorption to liquid–liquid interfaces [11]. In particular, they have investigated the ordering of oil soluble surfactants at the hexane–water interface, including alcohols, carboxylic acids and partially fluorinated alcohols.

Although AFM is not a spectroscopic technique, it can offer information on the behaviour of proteins and emulsifiers at the oil–water interface. Mackie *et al.* allowed β -casein or β -lactoglobulin films to adsorb at the tetradecane–water interface and then transferred the films to mica by Langmuir-Blodgett (LB) deposition [12]. These LB films were then studied by AFM and compared with films drawn from interfaces with the non-ionic surfactant Tween 20 in the aqueous phase. They found that the protein films were displaced from the interface by the surfactant in a process dubbed orogenic displacement. This process involves the nucleation of surfactant domains within the protein film, the subsequent spread of the surfactant domains and increase in the protein film thickness and finally the complete breakup of the protein network. Although AFM allows detailed structural studies, it does not deliver molecular information, nor can the oil–water interface be studied *in situ*.

The Richmond group have carried out a series of studies on the adsorption of surfactant molecules to the CCl_4 – D_2O interface with vibrational sum-frequency spectroscopy (VSFS) [13–15]. They used a TIR geometry to enhance the electric fields at the interface and to boost the sum-frequency signal and under these conditions they were able to observe a change in the molecular conformation with

increasing surface coverage. Organic oils absorb infrared light so Knock *et al.* employed a 50- μm thick hexadecane film in their VSFS study of CTAB adsorbed at the oil–water interface [16]. They were also able to observe a change in the molecular conformation with increasing surface coverage.

Total internal reflection fluorescence spectroscopy (TIRFS) is closely related to evanescent wave Raman scattering as it relies on an evanescent wave to provide surface-sensitivity for a technique that is not inherently surface-specific. Yamashita *et al.* used the technique to examine solvent relaxation processes of 12-(9-anthroyloxy) stearic acid (12-AS) and 4-(9-anthroyloxy) butanoic acid (4-ABA) at the heptane–water interface [17]. They found that the fluorophore 12-AS is preferentially solvated by heptane in the ground state but by water in the excited state, whereas 4-ABA does not undergo preferential solvation. Although TIRFS can be used to study processes at the nanosecond timescale, it does require that the surfactant possesses a fluorophore.

In summary, there are a number of different techniques with which to study the oil–water interface, but no single approach can claim to answer exclusively all potential questions about surfactant and emulsifier adsorption. Fluorescence and resonance Raman spectroscopies are limited to the study of dye molecules. Although nonlinear techniques do not require dye molecules, they are only sensitive to preferentially oriented molecules and are technically difficult to implement. Scattering techniques are not intrinsically chemically specific and x-ray and neutron scattering also require central facilities. Consequently we hope that evanescent wave Raman scattering can offer additional insights to complement these techniques.

5.2 Thin oil film concept and theory

The formation of a stable, thin, subaqueous oil film supported on a planar solid substrate is nontrivial and there are a number of criteria that must be satisfied. First, to prepare a very thin oil film one must spin-coat oil onto the substrate (*vide infra*). Consequently, the oil film must not dewet from the substrate in air. Second, the oil film is then contacted to the aqueous phase, so it is desirable that the oil should have either a high viscosity or a melting point, T_m , between room temperature and the

freezing point of water, i.e. $273 \text{ K} < T_m < 293 \text{ K}$. This restriction will ensure that the aqueous phase can be introduced to the oil film without mechanically washing the oil away. Finally, the oil film should be thermodynamically stable under the aqueous phase to prevent the aqueous phase breaking through and displacing the oil from the substrate. I will first discuss the basis of these restrictions before describing my attempts to satisfy them.

The first and final criteria require that the oil film is stable in air and under aqueous solution. These requirements are controlled by the same thermodynamic restrictions and I will discuss them together. The stability of a spread film is controlled by the surface free energies and the interaction free energies across the film. Surface free energies arise from incomplete balancing of intermolecular energies at a surface. For a stable film, the surface free energies must satisfy the following inequality

$$\sigma_{si} > \sigma_{so} + \sigma_{oi} \quad (1)$$

where σ is the interfacial tension and the subscripts s , o and i refer to the solid, oil and ambient phases respectively. In practice, it is not possible to measure directly the surface energy of a solid, but the state of the inequality in equation 1 can be determined by measuring the contact angles of the liquid phases on the solid in air, if the contact angles are greater than zero. In figure 1, the geometry for a drop of water on a solid substrate in air is shown.

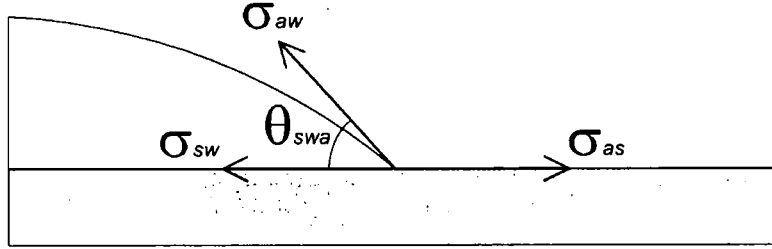


Figure 1. Geometry for a drop of water on a solid substrate. σ is the interfacial tension, θ is the three-phase contact angle and the subscripts a , w and s refer to the air, water and solid phases, respectively.

At equilibrium, the forces at the three-phase contact must be balanced, hence

$$\sigma_{as} = \sigma_{sw} + \sigma_{aw} \cos \theta_{swa} \quad (2)$$

An equivalent relationship holds for a drop of oil on the solid in air:

$$\sigma_{as} = \sigma_{so} + \sigma_{ao} \cos \theta_{soa} \quad (3)$$

Equating equations 2 and 3 gives

$$\sigma_{sw} - \sigma_{so} = \sigma_{ao} \cos \theta_{soa} - \sigma_{aw} \cos \theta_{swa} \quad (4)$$

hence the inequality in equation 1 can be written

$$\sigma_{ao} \cos \theta_{soa} - \sigma_{aw} \cos \theta_{swa} > \sigma_{ow} \quad (5)$$

The quantities in equation 5 are directly accessible by experiment. Representative values of these quantities are $\sigma_{ao} = 27 \text{ mN m}^{-1}$ (for a typical hydrocarbon such as hexadecane), $\sigma_{aw} = 72 \text{ mN m}^{-1}$ and $\sigma_{ow} = 54 \text{ mN m}^{-1}$. Consequently, to satisfy the inequality for a stable oil film under water I require an oleophilic and hydrophobic surface, such that $\theta_{soa} \approx 0^\circ$ and $\theta_{swa} > 112^\circ$. The stability of the oil film in air can be directly determined by observing whether an oil droplet spreads on the surface. If the oil wets the solid in air, the equality in equation 3 does not hold and this analysis is

not quantitatively accurate. Nevertheless, in this scenario the formation of a thin oil film under water is more favourable than equation 5 would suggest so a qualitative appreciation of the film stability can still be attained.

The second process that controls whether a spread film is stable is the effect of the long range van der Waals interaction free energies across the film between the solid and ambient phases. The interaction free energy between two surfaces is typically expressed in terms of the Hamaker constant, A , and in the case of two phases separated by a film of thickness D , the free energy per unit area, W , is given by [18]

$$W = -A/12\pi D^2 \quad (6)$$

Consequently the sign of the Hamaker constant will parameterize whether the film is stable ($A < 0$) or if it thins and subsequently dewets ($A > 0$). The magnitude and sign of the Hamaker constant can be determined by making use of Lifshitz theory. This theory is derived from an electrostatic argument whereby the influence of the induced dipoles that are the origin of the van der Waals forces are affected by the dispersion of the adjoining media. In the nonretarded case the theory gives

$$A = A_{v=0} + A_{v>0} \quad (7)$$

where the zero-frequency part, $A_{v=0}$, is given in terms of the static dielectric constants, ϵ , of each phase [18].

$$A_{v=0} = \frac{3k_B T}{4} \left(\frac{\epsilon_i - \epsilon_o}{\epsilon_i + \epsilon_o} \right) \left(\frac{\epsilon_s - \epsilon_o}{\epsilon_s + \epsilon_o} \right) \quad (8)$$

The frequency-dependent part, $A_{v>0}$, is defined in terms of the high frequency refractive index [18]

$$A_{v>0} = \frac{3h\nu_e}{8\sqrt{2}} \frac{(n_i^2 - n_o^2)(n_s^2 - n_o^2)}{\sqrt{(n_i^2 + n_o^2)(n_s^2 + n_o^2)} \left(\sqrt{(n_i^2 + n_o^2)} + \sqrt{(n_s^2 + n_o^2)} \right)} \quad (9)$$

where ν_e is the main electronic absorbance in the UV (typically $3 \times 10^{15} \text{ s}^{-1}$). Representative values for this equation at room temperature are $\epsilon_{\text{water}} = 80$, $\epsilon_{\text{oil}} \approx 2$ (for a typical hydrocarbon such as hexadecane), $n_{\text{water}} = 1.33$ and $n_{\text{oil}} \approx 1.4$.

Consequently for a stable oil film under water I require a solid substrate that has a refractive index that is greater than that of the oil film.

The relationship in equation 6 neglects the fact that for film thicknesses above ~ 5 nm there will be a significant time delay between the creation of a dipole in one medium and the creation of induced dipoles in the other media. This delay is due to the finite speed of light and is known as retardation. Retardation increases the rate at which the magnitude of the interaction free energies decay as the intervening film thickens. Thus the exponent in equation 6 is in reality greater than two [18]. Although retardation affects the magnitude of the interaction free energies, it does not change the sign and it does not change the conclusions of the argument given above.

In practice, the stability requirements can be relaxed partially if there is hysteresis between the advancing and receding contact angles of the oil on silica in water. In this case it is worth considering the potential breakup pathways of a metastable oil film into droplets. Two mechanisms are discussed in the literature: spinodal dewetting and heterogenous nucleation [19-21]. Spinodal dewetting ensues if $A > 0$, whereby fluid in the film flows from a thick region to a thinner region. This flow sets up an oscillation in the film and eventually dewetting occurs by the formation and spreading of circular holes in the film. However, the spinodal mechanism operates at characteristic length scales of less than 5 nm, such that a thicker film is spinodally stable even if $A > 0$. Heterogenous nucleation occurs when the wettability of a surface varies across the surface. This variation in the wettability causes a surface tension gradient that causes the film to flow to the more wettable region in an analogous manner to Marangoni flow.

5.3 Spin coating

Spin-coating is used extensively to prepare thin films on solid substrates, particularly in the study of polymer films. The planar sample is held on a platform by suction and the platform is spun at high speed – typically a few thousand revolutions per minute. A solution of the polymer in a volatile solvent is applied to the spinning surface and

the solvent is allowed to evaporate. This technique can be used to prepare films that are tens of nanometers to microns thick.

I spin-coated neat oil and toluenic oil solutions onto silicon wafers first. The high reflectivity of silicon at optical frequencies compared to optical substrates aids in the characterisation of the film thickness. As noted below, the film thickness is predominantly independent of the substrate, therefore the oils and oil solutions should behave almost identically on the optical substrates.

I spin-coated hexadecane films on silicon at 2000 or 6000 rpm for various spinning times and determined the thicknesses either by white-light reflectivity for films thicker than ~200 nm or by ellipsometry at an angle of incidence, $\phi = 70^\circ$, for thinner films. The thickness, h , is plotted as a function of spinning time in figure 2. Also shown in figure 2 are theoretical plots calculated from a model by Emslie *et al.* for spin-coating a disc with a neat, viscous liquid, which for long spinning times is given by [22]

$$h = \frac{1}{2\omega} \sqrt{\frac{3\nu}{t}} \quad (10)$$

where ω is the angular velocity of the disc, ν is the kinematic viscosity of the fluid and t is the spinning time. It is apparent from figure 2 that a spinning time of ~300s at 6000 rpm will form ~100 nm hexadecane films on silicon.

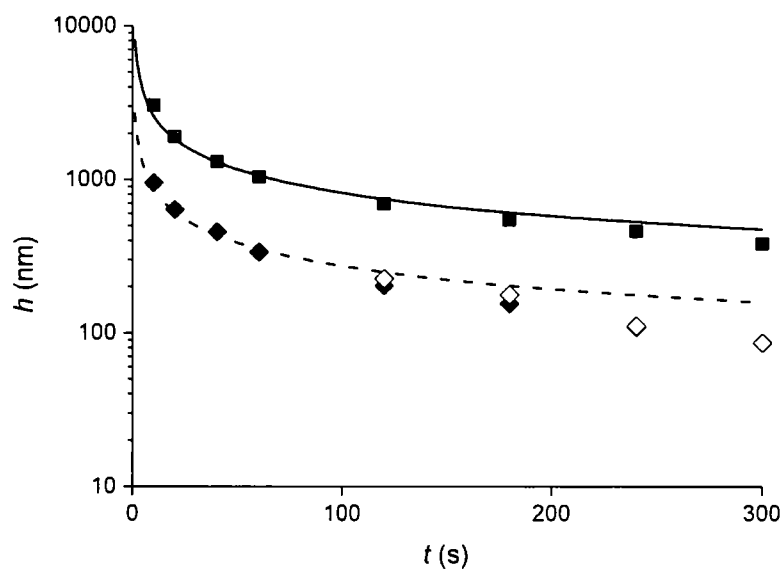


Figure 2. Thickness, h , of hexadecane films ($\nu = 3.92 \times 10^{-6} \text{ m}^2 \text{ s}^{-1}$) spin-coated on hydrophilic silicon at 2000 (■) and 6000 (◇, ◆) rpm as a function of spinning time, t . (■, ◆) Determined by white light reflectivity. (◇) Determined by ellipsometry. Theoretical thicknesses for films spin-coated at 2000 rpm (dashed line) and 6000 rpm (solid line) from a model due to Emslie *et al.* [22].

I also spin-coated solutions of squalene in toluene at various concentrations and determined the film thicknesses as described above. Squalene is considerably more viscous than hexadecane, so spin-coating the neat oil is not feasible for reasonable spin times or angular velocities. Coating the surface with an oil dissolved in a volatile solvent ensures a rapidly-formed, even covering of the surface by the solute. It is evident from figure 3 that ~100-nm squalene films can be readily formed on solid substrates.

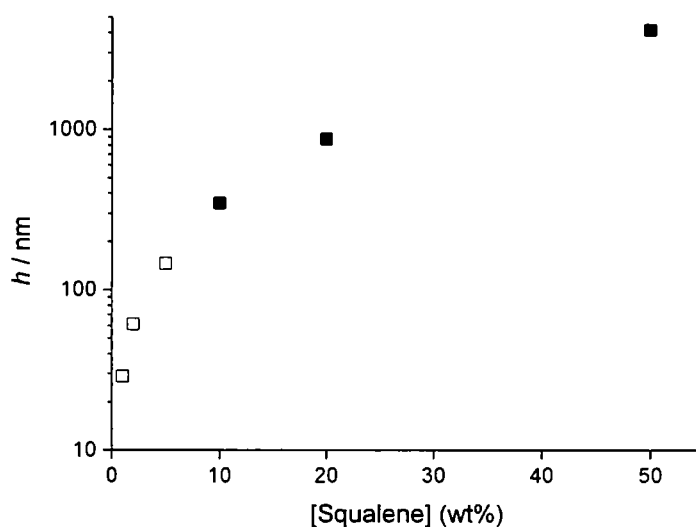


Figure 3. Thickness, h , of squalene films spin-coated on hydrophilic silicon at 2000 rpm from toluenic solution as a function of concentration in solution. Spinning time = 30 s. (■) Determined by white light reflectivity. (□) Determined by ellipsometry.

Once I had ascertained that I could readily form sufficiently thin oil films on solid substrates, I attempted to form stable, subaqueous oil films, using many variations of oil, hydrophobing solution and substrate. I will describe these in turn.

5.4 Hydrophobing optical substrates

The first combinations that I tried involved hexadecane as the oil phase and fused silica as the substrate. Hexadecane melts at 18 °C so it can be easily frozen whilst the aqueous phase is introduced. This property inspired Bowers *et al* to spin-coat hexadecane onto silicon hydrophobed with trimethylsilyl chloride in their study of neutron reflection from the oil–water interface [23]. Silicon is evidently unsuitable as a substrate for evanescent wave Raman scattering, but as silicon wafers have a thin, oxidized layer the surface of a silicon wafer is similar to fused silica at the molecular level. Both surfaces have free hydroxyl groups that can react with chlorosilanes, so the behaviour of Bower’s surfaces should be transferable to my surfaces. I will first

describe the generic technique that I used to hydrophobe all my surfaces and then I will present and discuss the results for each system.

Hydrophobing procedure

The fused silica windows were cleaned with hot “piranha” solution (~70 % concentrated sulphuric acid (Aldrich) : 30 % hydrogen peroxide solution (35 wt%, Aldrich)) for ~45 mins. **WARNING: Piranha solution can react violently with organic materials.** Piranha solution renders fused silica hydrophilic by removing all organic surface contaminants and exposing the surface hydroxyl groups. The windows were rinsed thoroughly with ultrahigh purity (UHP) water (MilliQ, Millipore) and left submerged in UHP whilst the hydrophobing solutions were prepared. The clean hydrophilic silica windows were made hydrophobic by immersion in a 5-mM solution of the alkylsilyl chloride in toluene (>99.5 %, Aldrich) at room temperature for a period of up to 24 hours. At the end of this period the windows were sonicated for 5 minutes at a time in the following solvents: 2× toluene, 2× methanol, 1× UHP water. Finally, the windows were dried with dry N₂ and used immediately. The windows were either used to determine the static contact angle of oil and UHP water on the surface (FTA200, First Ten Ångstroms) or were spin-coated with an oil solution to determine the stability of an oil film under water. Table 1 lists the different alkylsilyl chlorides employed along with the advancing contact angles of water and hexadecane.

Alkylsilylchloride	Type	$\theta_{sva}(^\circ)$	$\theta_{soa}(^\circ)$
C ₁₀ H ₂₁ (CH ₃) ₂ SiCl ^a	Dimethyl monochloride	93	0
(C ₂ H ₅) ₂ SiCl ₂ ^b	Dichloride	85	0
C ₁₀ H ₂₁ SiCl ₃ ^c	Trichloride	97	21
C ₁₈ H ₃₇ SiCl ₃ ^d	Trichloride	102	34

Table 1. Static contact angles for water and hexadecane on hydrophobically-modified silica. a: (>97%, Fluka), b: (95%, Aldrich), c: (97%, Aldrich), d: (>90 %, Aldrich).

Oil film stability

The stability of the oil film under water was determined by multiple angle of incidence (MAI) ellipsometry in the following manner. First, I investigated the effect of freeze-thaw action on the hexadecane film. The hydrophobic silica window was spin-coated with hexadecane at 6000 rpm for 20 s and then the film thickness was characterized with MAI ellipsometry in a thermostatted cell at room temperature. In figure 4, $\text{Im}(r_p/r_s)$ is plotted as a function of angle of incidence, φ , (■) for a representative window hydrophobed with decyldimethylchlorosilane. The data were fit to a three-layer optical matrix model consisting of the silica substrate (2), the oil film (1) and air (0) using the film thickness, h , as the single fitting parameter. The model is described by [24]:

$$\frac{r_p}{r_s} = \frac{(r_{01,p} + r_{12,p}e^{-2i\beta})(1 + r_{01,s}r_{12,s}e^{-2i\beta})}{(r_{01,s} + r_{12,s}e^{-2i\beta})(1 + r_{01,p}r_{12,p}e^{-2i\beta})} \quad (11)$$

where $\beta = \frac{2\pi h n_1 \cos \theta_1}{\lambda}$, $r_{ij,k}$ are given by the Fresnel equations in chapter 2 and λ is the wavelength of the incident light.

The modelled thickness of the film on hydrophobic silica was 580 nm, which is consistent with the thickness of a film spun on silicon at the same angular velocity and spinning time. This result suggests that the spin-coating is independent of the substrate, as long as the oil wets the substrate, as suggested above. I then placed the window in a cell thermostatted at 278 K which rapidly froze the oil film within a few seconds (T_m of hexadecane = 291 K). The temperature of the cell was increased to 298 K, the oil film was allowed to thaw slowly over several minutes and the film thickness was recharacterized by ellipsometry. These data are also plotted in figure 4 (□) and correspond to a 560-nm thick film. Although there is a slight reduction in film thickness, it is apparent that the hexadecane film is resistant to freeze-thaw action. However, if the window is placed in the thermostatted cell at room temperature and the temperature subsequently reduced so that the oil is frozen slowly over a few minutes, the film ruptures as the oil contracts.

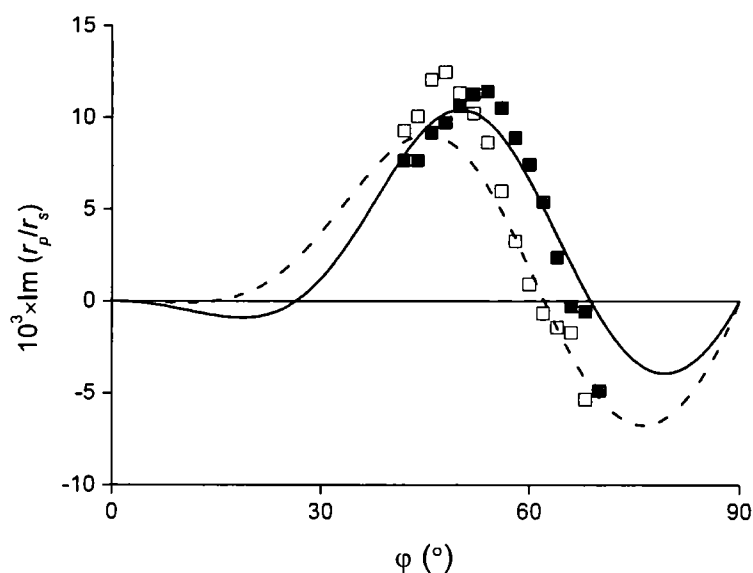


Figure 4. Imaginary part of the ratio of reflection coefficients of p - and s -polarized light, $\text{Im}(r_p / r_s)$, as a function of angle of incidence, ϕ , for (■) a fresh hexadecane film on hydrophobic silica in air and (□) the same film subjected to one freeze–thaw cycle. The solid and dashed lines represent modelled results for a 580- and 560-nm thick film, respectively.

A new film was spin-coated and frozen onto a freshly-hydrophobed silica window using the same spinning parameters. Cold water ($T < 291$ K) was slowly introduced onto the frozen film. At this stage, crystals of the frozen hexadecane film were visibly present. The temperature was raised to room temperature and the oil film was allowed to melt prior to characterisation by MAI ellipsometry. The laser beam was introduced into the water phase using the light guides described in chapter 3. The measured ellipticity is plotted in figure 5 and compared to the modelled ellipticity for a 580-nm thick oil film (solid line). The angle of incidence is limited to a narrow range of 53–66° by the geometry of the experiment.

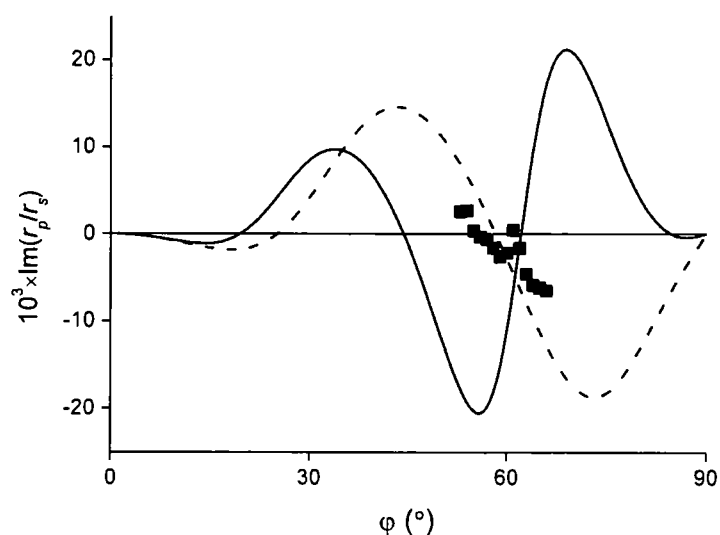


Figure 5. Imaginary part of the ratio of reflection coefficients of p - and s -polarized light, $\text{Im}(r_p / r_s)$, as a function of angle of incidence, ϕ , for a hexadecane film on hydrophobic silica in water. The solid and dashed lines represent modelled results for a 580 and 360-nm thick film, respectively.

The oil film does not appear to be stable under water. The best fit to the ellipsometry data corresponds to a film that is ~ 360 nm thick (dashed line), however the fit is poor. On inspection with a magnifying glass, beads of oil were visible on the surface of the window, which suggests that the film has broken and beaded up on the silica surface. Once I had ascertained that it was possible to determine the stability of the film by visual inspection, I resolved to use a microscope rather than MAI ellipsometry as a more efficient technique for all subsequent investigations.

None of the hydrophobic surfaces described in table 1 were able to maintain a stable oil film under water. In the two cases where the surface was much more hydrophobic (the trichlorosilanes) hexadecane did not spread on the surface in air. It is well documented that a hydrocarbon will not wet a methyl-terminated surface but will wet a methylene surface [25]. Consequently I resolved to improve the wetting characteristics by forming a more oleophilic and hydrophobic monolayer and to use squalene as the oil phase. Squalene has an interfacial tension with water of 21 mN m^{-1} so the inequality in equation 5 can be satisfied with a less hydrophobic

monolayer. Finally I decided to enhance the effect of the long range van der Waals forces by using a substrate with a refractive index greater than 1.5.

The first substrate I tried was cubic zirconia (CZ). There is very little data in the literature about hydrophobing CZ so I tried various alternative hydrophobing solutions. CZ does not have free hydroxyl groups at the surface therefore it cannot react directly with alkylsilyl chlorides. Work done by Folkers *et al.* suggests that a reasonably strong Lewis acid-base interaction between CZ and phosphonic or carboxylic acids means a hydrophobic monolayer can be formed with these acids [26]. I also tried using OTS to hydrophobe the surface of CZ. Although OTS cannot bond directly with CZ, the silane polymerizes readily and therefore only requires a few anchor points to the CZ to form a hydrophobic surface. The results are shown in table 2.

Hydrophobing agent	Type	$\theta_{swa}(\circ)$
$C_{17}H_{35}CO_2H$	Carboxylic acid	100
$C_{18}H_{37}PO_3H_2$	Phosphonic acid	105
$C_{18}H_{37}SiCl_3$	Silyl trichloride	114

Table 2. Static contact angles for water on hydrophobically-modified cubic zirconia.

I was unable to form a spread film on either the phosphonic or stearic acid surface as the oil dewet rapidly in air. Occasionally the oil remained spread on the surface treated with OTS, despite the fact that the oil should not wet the methyl-terminated surface. I contend that because OTS can only interact weakly with the CZ surface the monolayer is disordered and the oil can penetrate the monolayer and interact with the methylene groups. Indeed I was able to form a stable oil film once and acquire spectra of the oil–water interface. An image of the oil film is shown in figure 6, and spectra of the oil–water interface are shown in figures 7 and 8.

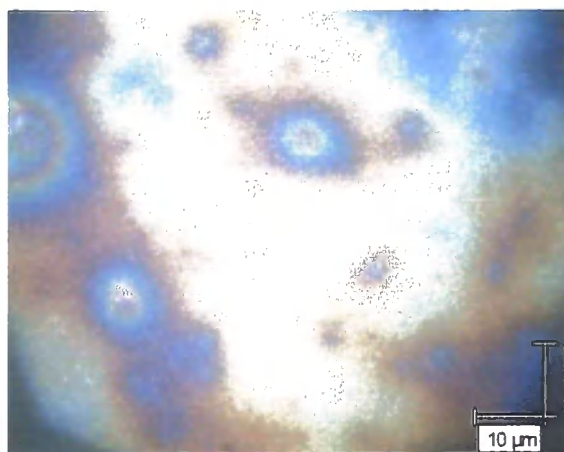


Figure 6. White light microscope image of a 200-nm subaqueous squalene film supported on hydrophobically-modified cubic zirconia.

The film in figure 6 is not homogenous but the film is intact throughout the field of view of the microscope. It is immediately apparent if the film has ruptured, as shown below in figure 9. Therefore the traces below are genuine spectra of the oil–water interface.

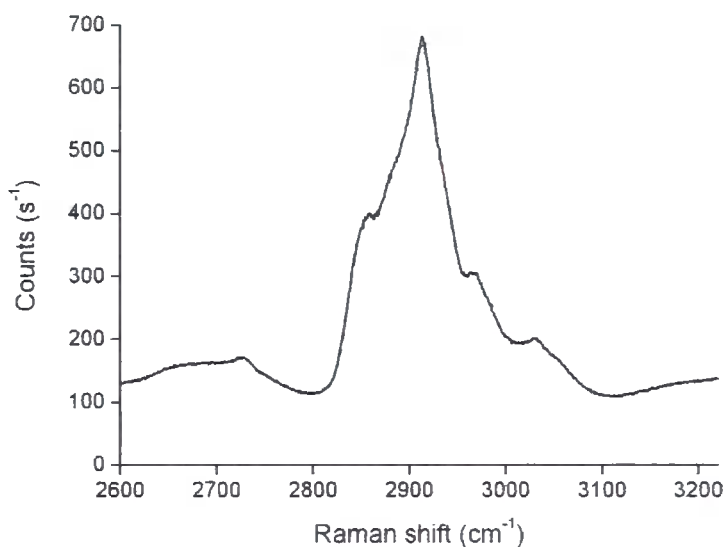


Figure 7. TIR Raman spectrum in the C–H stretching region of a 200-nm subaqueous squalene film supported on hydrophobically-modified cubic zirconia. Laser power = 200 mW.

The spectrum in figure 7 is dominated by the C–H stretching modes from 2800–3100 cm^{-1} . The broad band extending from 2600–2800 cm^{-1} arises from the cubic zirconia substrate and the band beginning at 3100 cm^{-1} is the water O–H bend. By comparison with previous work done on surfactant adsorption to the silica–water interface, I expect that a monolayer of a simple surfactant such as CTAB adsorbed at the oil–water interface would give maximum peak heights in the C–H stretching region of $\sim 30 \text{ s}^{-1}$ under these conditions.

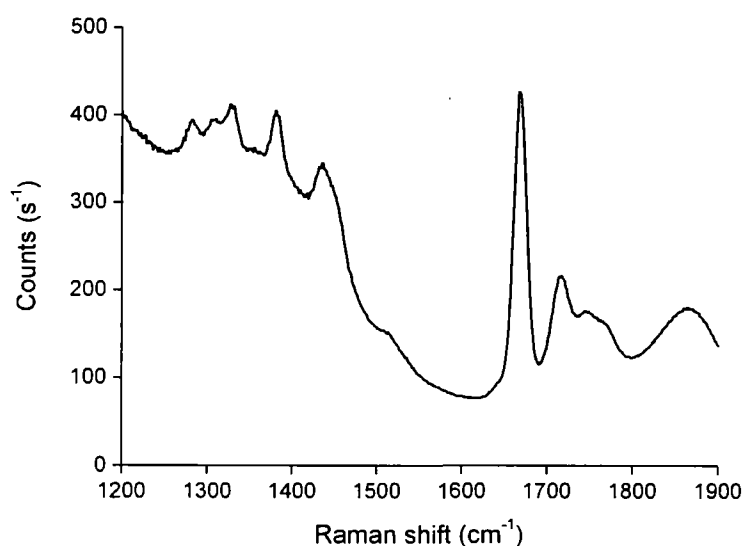


Figure 8. TIR Raman spectrum in the fingerprint region of a 200-nm subaqueous squalene film supported on hydrophobically-modified cubic zirconia.

The broad feature from 1200–1600 cm^{-1} in figure 8 is a cubic zirconia band. The C–H bending and twisting modes from the oil film are superimposed on top of the CZ band from 1280–1450 cm^{-1} . The sharp peak at $\sim 1680 \text{ cm}^{-1}$ arises from the unsaturated C=C bond in squalene. The remaining bands arise from CZ. In this region there is a region from 1500–1650 cm^{-1} where the background signal is relatively weak and flat. It may be possible to register signal from a protein monolayer at the oil–water interface in this region. However I was unable to form a stable film with CZ again and so I was unable to test this theory. It appears that slight differences in the CZ surface, the hydrophobing solution and the conditions used to prepare the

SAM have a large effect on the stability of the oil film. Nonetheless, I decided that developing a disordered trichlorosilane monolayer was the appropriate approach. Therefore I decided to use the high index glass SF10 as the solid substrate. This glass has the advantages of a high refractive index like CZ but also free hydroxyl groups on the surface so I could form monolayers repeatably. In order to introduce disorder into the monolayer I used mixtures of alkyl trichlorosilanes with different chain lengths. This approach has been used by Bain and Whitesides when working with thiols on gold [25] and by Offord and Griffiths working with silanes on silicon [27]. Close to the substrate the mixed monolayer is believed to be close-packed. However, the difference in the chain lengths of the constituents introduces free volume into the outer part of the monolayer. This free volume causes the outer part of the monolayer to be more disordered and liquid-like [25]. Both groups found that in a plot of the contact angle of hexadecane against the composition of the mixed monolayer there was a sharp minimum in the oil contact angle. Although there was also a minimum in the water contact angle, this dip was not so pronounced. Consequently the mixed monolayers were both oleophilic and hydrophobic.

I hydrophobed SF10 with neat solutions of OTS and decyltrichlorosilane (DTS) and with mixtures of these two silanes at different compositions. The contact angles are given in table 3.

Alkylsilylchloride	$\theta_{swa}(\text{°})$	$\theta_{soa}(\text{°})$
$\text{C}_{10}\text{H}_{21}\text{SiCl}_3$ (DTS)	115	15
$\text{C}_{18}\text{H}_{37}\text{SiCl}_3$ (OTS)	114	33
2:1 (DTS:OTS)	106	8
5:1 (DTS:OTS)	117	8

Table 3. Static contact angles for water and oil on hydrophobically-modified SF10 glass.

Despite early promise, the mixed monolayer approach did not work either. On most occasions the squalene films dewetted in air. I believe this is because the high surface

tension of squalene ($\sigma_{ao} = 31 \text{ mN m}^{-1}$) means that squalene cannot spread on this surface in air. On the few occasions when the squalene film remained wetted in air, the film dewetted under water. Images of the squalene film dewetting from the glass surface are shown in figure 9.

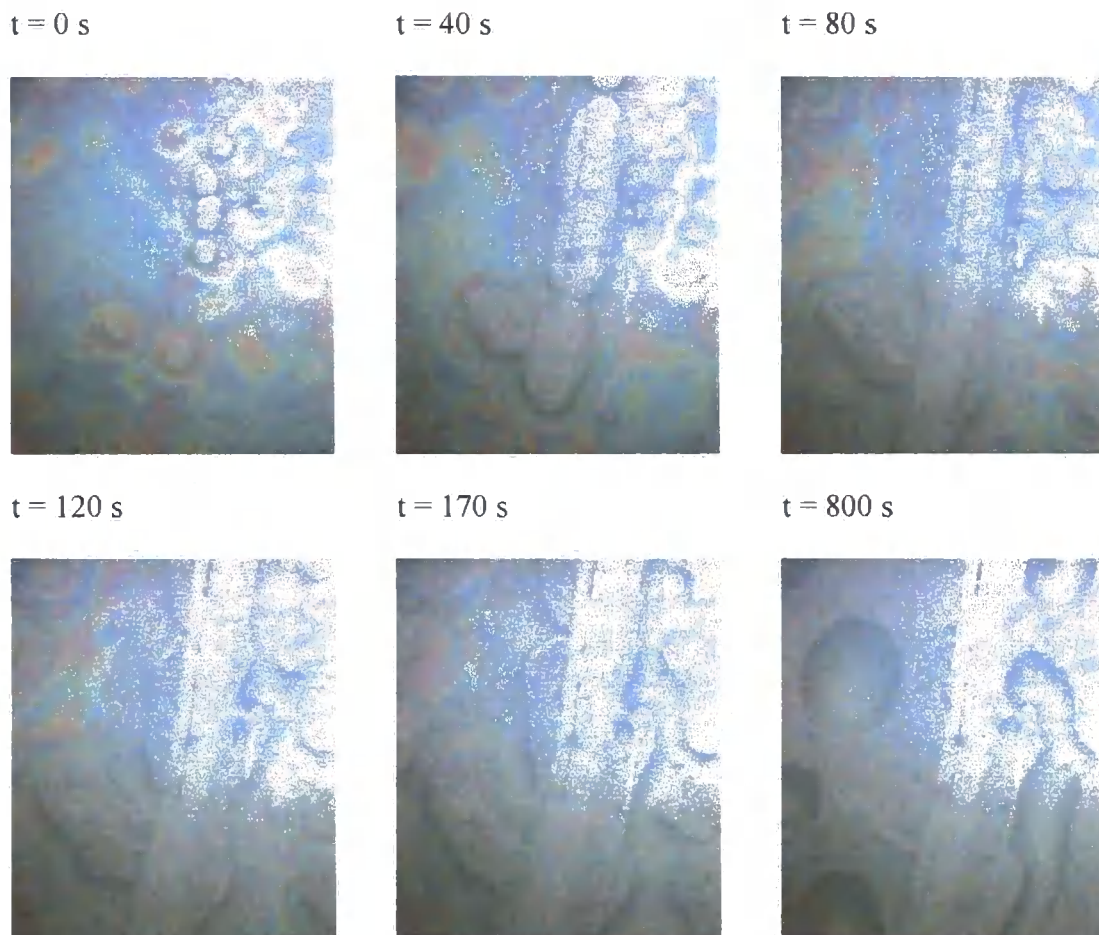


Figure 9. Images of a subaqueous squalene oil film dewetting from glass.

5.5 Outlook

Despite significant effort I have been unable to maintain a thin, stable oil film under water. It appears that any such film would be right at the limit between thermodynamic stability and instability, and subtle differences in the preparation and deposition of the oil film are sufficient to drive any film to break up through heterogenous nucleation. Although I believe that it should still be possible to form a thin, stable oil film, the experimental conditions would have to be extremely precisely controlled. Determining such conditions would still involve a considerable undertaking, although I hope that the work I have done to date will at least point future researchers in the correct direction. In the event, I decided to put this work aside and focus on developing the study of the oil-water interface with ellipsometry and ultraviolet resonance Raman scattering. The latter approach in particular offers a partial alternative to the visible Raman scattering approach outlined at the beginning of this chapter as the resonance enhancement means that we should be able to discriminate between the bulk oil phase and the monolayer. However, this approach only works for species that are resonant in the UV such as proteins and not for typical surfactant species which are not resonant until the vacuum UV region.

References

- 1 D. A. Beattie, S. Haydock, and C. D. Bain, *Vib Spectrosc* **24**, 109 (2000).
- 2 P. R. Greene and C. D. Bain, *Spectroscopy Europe* **16**, 8 (2004).
- 3 C. Lee and C. D. Bain, *Biochim. Biophys. Acta* **1711**, 59 (2005).
- 4 C. Lee, D. Phil. thesis, (Oxford, 2005)
- 5 T. Takenaka and T. Nakanaga, *J. Phys. Chem.* **80**, 475 (1976).
- 6 K. Fujiwara and H. Watarai, *Langmuir* **19**, 2658 (2003).
- 7 S. Fujiyoshi, T. Ishibashi, and H. Onishi, *J. Phys. Chem. B* **110**, 9571 (2006).
- 8 R. P. Sperline and H. Freiser, *Langmuir* **6**, 344 (1990).
- 9 A. Zorbakhsh, A. Querol, J. Bowers, and J. R. P. Webster, *Faraday Discussions* **129**, 155 (2005).
- 10 A. Zorbakhsh, A. Querol, J. Bowers, M. Yaseen, J. R. Lu, and J. R. P. Webster, *Langmuir* **21**, 11704 (2005).
- 11 M. L. Schlossman, *Physica B* **357**, 98 (2005).
- 12 A. R. Mackie, A. P. Gunning, P. J. Wilde, and V. J. Morris, *Langmuir* **16**, 2242 (2000).
- 13 J. C. Conboy, M. C. Messmer, and G. L. Richmond, *J. Phys. Chem.* **100**, 7617 (1996).
- 14 M. C. Messmer, J. C. Conboy, and G. L. Richmond, *J. Am. Chem. Soc.* **117**, 8039 (1995).
- 15 M. R. Watry and G. L. Richmond, *J. Am. Chem. Soc.* **122**, 875 (2000).
- 16 M. M. Knock, G. R. Bell, E. K. Hill, H. J. Turner, and C. D. Bain, *J. Phys. Chem. B* **107**, 10801 (2003).
- 17 T. Yamashita, T. Uchida, T. Fukushima, and N. Teramae, *J. Phys. Chem. B* **107**, 4786 (2003).
- 18 J. N. Israelachvili, *Intermolecular and Surface Forces* 1st ed. (Academic Press, London, 1987).
- 19 R. Konnur, K. Kargupta, and A. Sharma, *Phys. Rev. Lett.* **84**, 931 (2000).
- 20 A. Oron, S. H. Davis, and S. G. Bankoff, *Rev. Mod. Phys.* **69**, 931 (1997).
- 21 A. Sharma, *Eur. Phys. J. E* **12**, 397 (2003).
- 22 A. G. Emslie, F. T. Bonner, and L. G. Peck, *J. Appl. Phys.* **29**, 858 (1958).

- 23 J. Bowers, A. Zarbakhsh, J. R. P. Webster, L. R. Hutchings, and R. W. Richards, *Langmuir* **17**, 140 (2001).
- 24 R. M. A. Azzam and N. M. Bashara, *Ellipsometry and Polarized Light* 1st ed. (North-Holland, Amsterdam, 1977).
- 25 C. D. Bain and G. M. Whitesides, *J. Am. Chem. Soc.* **111**, 7164 (1989).
- 26 J. P. Folkers, C. B. Gorman, P. E. Laibinis, S. Buchholz, G. M. Whitesides, and R. G. Nuzzo, *Langmuir* **11**, 813 (1995).
- 27 D. A. Offord and J. H. Griffin, *Langmuir* **9**, 3015 (1993).

Chapter 6

Development of a UV resonance Raman microspectrometer

6.1 Introduction

Ultra-violet resonance Raman spectroscopy (UVRRS) is a relatively new addition to the suite of techniques that have been developed since the Raman effect was first discovered in 1928 [1]. Resonance Raman spectroscopy relies upon the large enhancement in the number of Raman photons scattered by a molecule when the energy of the excitation light source lies close to an electronic resonance within the molecule. Most simple emulsifiers and proteins do not absorb light at visible frequencies and this restriction necessitates the use of UV lasers to study the resonance Raman spectra of these molecules. Although several groups have done considerable quantities of work on the resonance Raman response of simple molecules in the gas phase and polycyclic aromatic hydrocarbons, proteins and nucleic acids in solution [2, 3], no work has been done with UVRRS at interfaces. Lee has highlighted the limitations of visible evanescent wave Raman scattering for studying the structure and function of peptides in planar supported lipid bilayers [4]. The signal from these peptides is extremely weak relative to the bilayer and the supporting substrate. The resonance enhancement from a UV laser will boost this signal considerably and allow us to obtain deeper insights into the behaviour of peptides in membranes. Furthermore, the enhancement of the Raman signal from proteins adsorbed at the oil–water interface means that it may be possible to distinguish the protein signal from the oil signal without the use of a very thin oil film.

UVRRS has been used by several groups to probe the excited states of simple molecules in the gas phase. These studies investigate the excited state geometries, dynamics and potential energy surfaces of photodissociated molecules such as methyl iodide and ammonia [2]. Resonance Raman excitation profiles (the dependence of the Raman cross-section upon the excitation frequency) are also frequently used to determine the electronic transition frequency in the deep UV. However the most

relevant studies to this thesis have investigated proteins and peptides via the enhancement of either the backbone amide bands or aromatic sidechains. The weak $n-\pi^*$ transition of the amide bond occurs at ~ 210 nm and the stronger $\pi-\pi^*$ transition occurs at 185 nm, except in the case of the proline residue where the amide band is red-shifted by ~ 10 nm [3]. Chi *et al* used 206.5 nm light to collect resonant Raman spectra of a series of proteins with known secondary structures [5]. They used the amide I, II and III bands and the $C_{\alpha}-H$ amide bending mode to determine directly the secondary structure of these proteins in aqueous solution. Lednev *et al* used 194-nm light in a similar manner to probe the secondary structure of hen egg white lysozyme as a function of temperature during denaturation [6].

The resonant enhancement of the aromatic sidechains of tryptophan, tyrosine, phenylalanine and, to a lesser extent, histidine have also been used to report on the environment of these residues within a protein. The aromatic $\pi-\pi^*$ transitions of these residues occur at different wavelengths within the deep UV region. Consequently Balakrishnan *et al* demonstrated that by tuning the excitation frequency they could selectively enhance the different vibrational modes of the aromatic groups [7]. Spiro's group used the same techniques to study structural changes of carboxyhemoglobin during protein folding.

A tunable source also allows the user to determine resonant Raman excitation profiles (RREPs) as well as Raman spectra. The electronic absorption bands which determine these RREPs are themselves dependent on the local environment in which the residue finds itself. For example, Balakrishnan *et al* found that the RREPs of phenylalanine residues in carboxyhemoglobin were red-shifted relative to phenylalanine in solution, and they ascribed this shift as indicative of the hydrophobic environment within the protein [7].

Nelson's group has pioneered the use of UVRRS of living cells, particularly within bacteria. They used 251-nm light to enhance the Raman signal from nucleic acids within the bacteria and were able to describe the spectra in terms of the known Raman cross-sections of the individual nucleic acid bases [8]. Neugebauer *et al* probed both the aromatic amino acid residues and nucleic acids within

Staphylococcus Epidermis with 244-nm light to investigate changes during bacterial growth [9]. Both groups employed a flow system to limit photo damage to individual cells.

Despite the obvious benefits of UV resonant Raman spectroscopy, there are nonetheless several impediments to the successful acquisition of high-quality spectra. First, from the technical point of view many of the materials and optics used in a conventional Raman spectrometer will not work in the UV region. The materials used in reflective and anti-reflective coatings, detectors, filters and polarizing optics are not as efficient in the UV, if they work at all. Second, UV laser sources not only enhance the Raman effect but can also form radical species. Furthermore if the electronic ground state is sufficiently depopulated during excitation the Raman bands can saturate, whereby increasing the intensity of the incident light no longer increases the Raman signal. Consequently previous workers have used flow cells to exchange the material excited by the UV laser [5-7]. We expect that these issues will be exacerbated when taking spectra from an interface. Fewer molecules are present overall compared to bulk studies so the Raman signal is relatively weak, and the molecules are confined to the interface so cannot be rapidly replenished by convection as in bulk studies. Czaja *et al* managed to acquire UVRR spectra from individual plant cells with a controlled line-scan along a cell wall [10]. They determined empirically that exposure of the sample to $\sim 40 \mu\text{W}$ of 244-nm laser light focused to a spot size of 2–3 μm produced no damage for $\sim 1\text{--}2$ s. For longer illumination times they observed heat-induced damage and a reduction in the Raman signal. We expect that we will require a similar solution to the problem of photo-degradation of a confined sample.

In the remainder of this chapter I will describe the design and building of a custom UV resonant Raman spectrometer to collect Raman photons scattered by an evanescent wave. The work in this chapter was carried out jointly with Dr Eric Tyrode, a post-doctoral researcher in the Bain group.

6.2 Development of the optical bench

Coherent Indigo-S Solid State UV laser

The laser we used is a commercial Coherent Indigo-S Solid-State UV laser. A schematic of the Indigo-S is shown in figure 1.

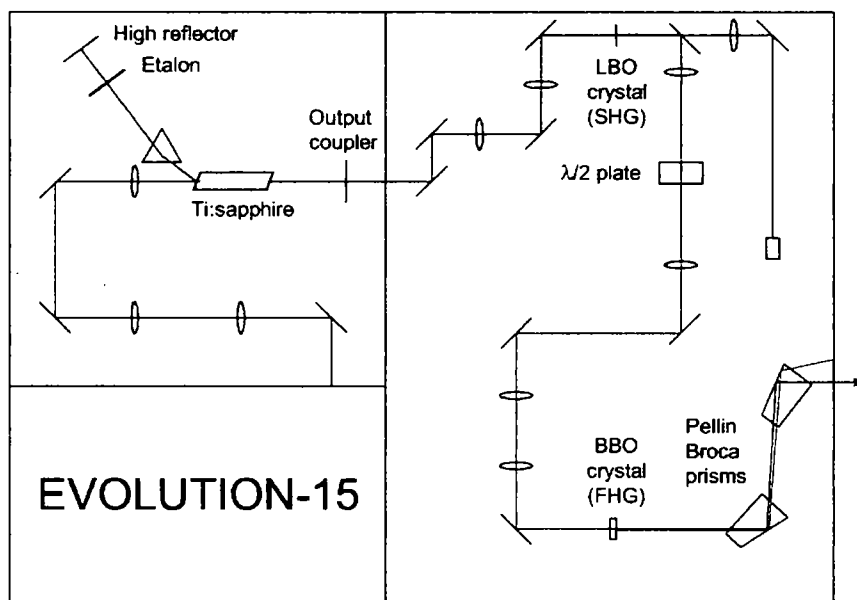


Figure 1. Schematic of the Coherent Indigo-S Solid-State UV laser. The different frequencies produced in the laser head are denoted as follows: (Green) Nd-YLF pump beam at 527nm. (Red) Ti:sapphire fundamental at 840–900 nm. (Light blue) Second harmonic at 420–450 nm. (Dark blue) Fourth harmonic at 210–225 nm.

A Coherent Evolution-15 diode-pumped, Q-switched, intracavity-doubled Nd-YLF laser operating at 4 kHz with a 260-ns pulse width produces a 527-nm beam at an average power of up to 15 W. This green light pumps a Ti:sapphire oscillator to produce an average power of up to 1.8 W of the fundamental Ti:sapphire beam. This light has a 35-ns pulse width and can be tuned in the range from 840–900 nm by varying the position of the high-reflecting cavity mirror of the oscillator. A high refractive index glass prism and etalon within the cavity reduce the line width of the fundamental beam to less than 10 pm. This fundamental beam is then focused onto a

lithium barium borate (LBO) nonlinear crystal. All the nonlinear crystals in the laser must be phase-matched to produce a sufficient intensity of the second harmonic. At a particular angle of incidence the refractive indices of the fundamental and second harmonic will be identical. Consequently all of the second harmonic light that is produced as the fundamental traverses the crystal will interfere constructively and the maximum intensity of second harmonic light will be outputted from the nonlinear crystal. However, the second-harmonic output is a sharply-peaked function with respect to the incident angle so the exact rotation of the crystal is crucial. The second harmonic is tunable between 420 and 450 nm and produces laser light at an average power of up to 400 mW. This second harmonic light can then either be mixed with fundamental light in a barium borate (BBO) crystal to produce the third harmonic by sum-frequency generation, or it can be frequency-doubled in another BBO crystal to produce the fourth harmonic of the Ti:sapphire fundamental. The third harmonic is tunable between 280 to 300 nm and produces an average power of up to 65 mW. The fourth harmonic is tunable from 210 to 225 nm and produces an average power of up to 25 mW. The third and fourth harmonics are not available simultaneously. Finally the different harmonics are separated by a pair of Pellin-Broca prisms and the UV light is emitted from the laser head with a horizontal polarization relative to the plane of the optical bench. Tuning the excitation wavelength is straightforward. First the wavelength of the Ti:sapphire fundamental is changed by moving the high reflecting mirror in the oscillator cavity with a computer-controlled actuator. Next the phase matching angles of the nonlinear crystals are adjusted manually in series to maximize the second harmonic or sum-frequency generation. Finally the angles of the Pellin-Broca prisms are adjusted manually to allow emission of light from the laser head. The large number of different wavelengths created within the laser means that we always wore laser safety goggles that had a sufficient optical density for all wavelengths that could be created by the laser. Furthermore, the particular dangers of deep UV radiation meant that we always wore full lab coats and nitrile gloves whenever the laser was energized.

Delivery optics and microscope design

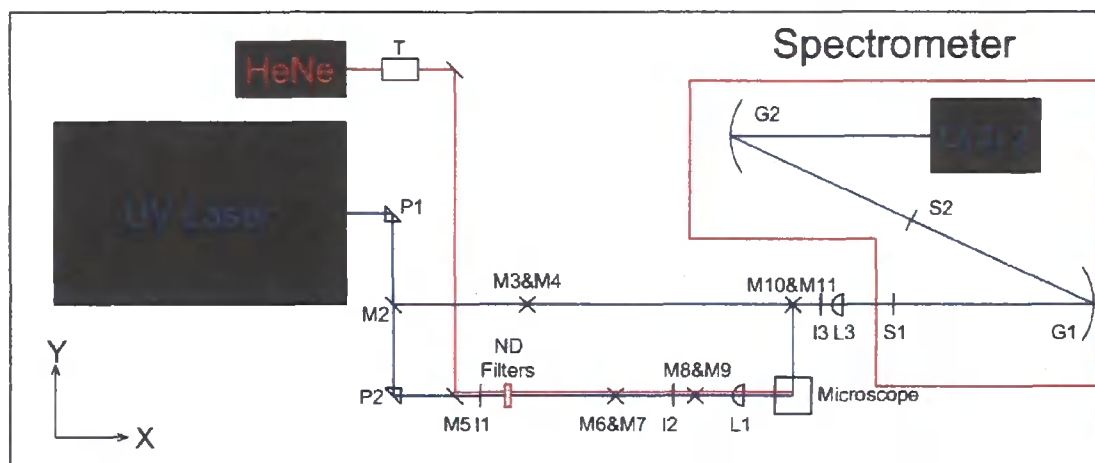


Figure 2. Schematic of the Durham UV resonance Raman spectrometer, version 1. T = beam expander, P = prism, M = mirror, I = iris, L = lens, S = slit, G = grating. Top view.

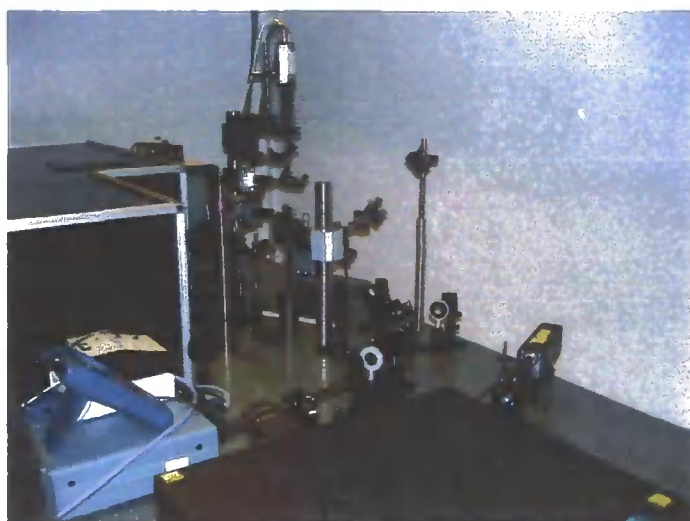


Figure 3. Photograph of the Durham UV resonance Raman spectrometer.

The UV light is delivered to the sample along the path shown in figure 2. The UV-grade fused silica right angle prisms (P90-100-193-248-UV, CVI Laser) were anti-reflection (AR) coated by CVI to give a reflectivity of 0.5% between 193 and 248 nm. The benefit of using right angle prisms over mirrors in the deep UV is that AR

coatings are considerably more efficient than reflection coatings at these frequencies, and of course no energy is lost during total internal reflection at the hypotenuse. Prisms were not used exclusively however as they are harder to mount and align than conventional mirrors. Most of the mirrors were aluminium (DUVA-PM-1025-UV, CVI Laser) and were coated by CVI to give a reflection efficiency of $> 90\%$ from 185 nm to 250 nm. We also used a 0.8-mW HeNe laser (1507P, JD Uniphase) to align the delivery optics and microscope and by flipping M5 up or down either the HeNe or UV beam could be directed towards the sample. The UV and the HeNe beams were overlapped through a pair of irises (ID25/M, Thorlabs) to ensure the beams were coaxial. M1–5 are only used for alignment purposes and are lower quality UV-enhanced aluminium mirrors (Optarius). M9 and L1 (+75 mm, UV-grade fused silica, AR coated 193–248 nm, PLCX-25.4-38.6-UV-193-248, CVI Laser) are used to focus the UV beam onto the sample at the required angle of incidence and are mounted on a z translation stage to move the excitation beam relative to the microscope field of view.

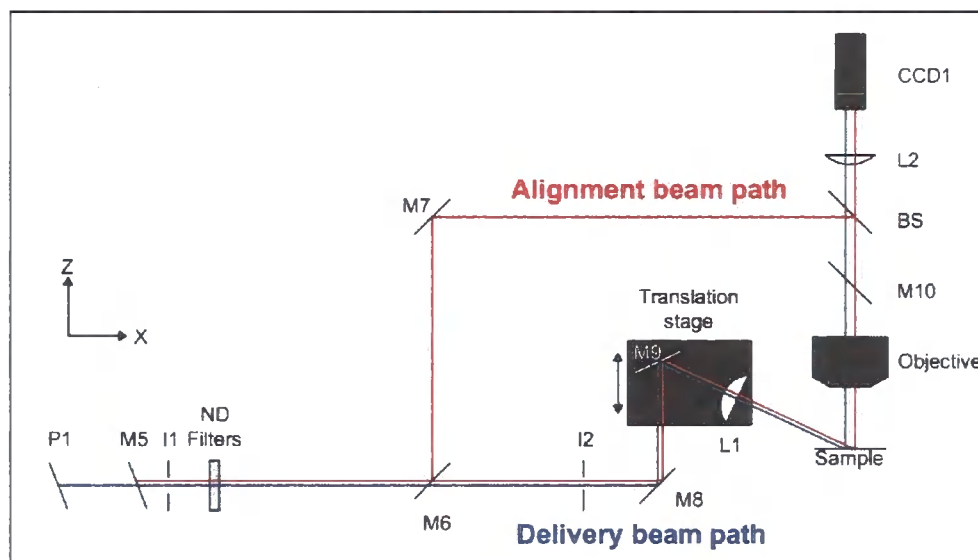


Figure 4. Schematic of the delivery optics and microscope of the Durham UV resonance Raman spectrometer. The overlapping HeNe and UV beams have been offset for clarity. Side view.

The custom microscope and the delivery optics are shown in figure 4. The microscope was designed to perform two functions – to collect a large fraction of the scattered Raman light, and to ensure that the surface under investigation could be positioned repeatably at the same height. To satisfy the first criterion we used an infinity-corrected reflecting Schwarzschild objective with a high NA (NA = 0.5, working distance = 23 mm, Davin Optronics). Unlike conventional refractive objectives, reflecting objectives are achromatic, hence light of all frequencies should be collimated to the same extent which minimizes aberrations in the spectrograph. The surface under investigation needs to be positioned at the same height repeatably to ensure that all the light collected from the surface by the objective is collimated when it exits from the objective. If this is not the case, the position of the focus on the detector will move from experiment to experiment causing errors in the resolution of spectral bands. The procedure for aligning the microscope is described in detail below.

Light collected by the objective is directed upwards towards M10. M10 is mounted on a custom-made dovetail so that it can be easily slid in and out of the beam path. This scattered light is then folded by M11 and M12 and focused onto the entrance slit, S1, of the custom double spectrograph by L3 (+200 mm, UV-grade fused silica, AR coated 193–248 nm, PLCX-50.8-103.0-UV-193-248, CVI Laser). This lens is f-number matched to the spectrograph to ensure maximum throughput.

Diffraction and grating physics

The principal component of a spectrograph or monochromator is the dispersing element, so first I will describe the basic physical principles of diffraction. When polychromatic light is incident upon a grating – that is an extended pattern of grooves on a surface where the spacing of the grooves is of the order of the wavelength of the incident light – it will be dispersed into its constituent frequencies. This process is widely used in spectrographs and monochromators to analyze polychromatic light. A cross-section of a simple planar grating is shown in figure 5.

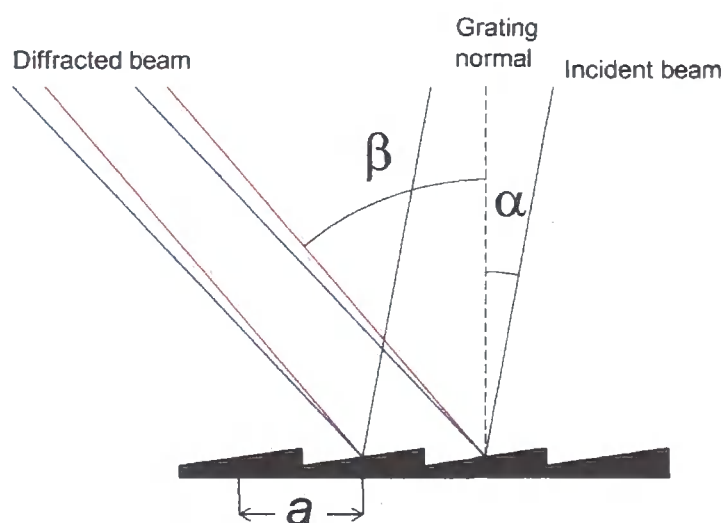


Figure 5. Cross section of a diffraction grating. Only $m = +1$ is shown for clarity.

Light diffracted from a grating consists of a superposition of the beams scattered across the grating surface. This superposition will result in constructive interference if the path length difference is a multiple of the wavelength, λ . By trigonometry from figure 5 [11]:

$$a(\sin \alpha + \sin \beta) = m\lambda \quad (1)$$

where m is an integer known as the order of diffraction. $m = 0$ corresponds to specular reflection, with higher orders being diffracted at greater angles from the surface normal. It is evident from equation 1 that light of different wavelengths that strike the grating at the same incident angle will be diffracted at different angles, resulting in the dispersion of light. Furthermore, a grating with a greater groove density will separate adjacent frequencies over a greater distance than a less powerful grating. In a spectrometer, the diffraction efficiency of the grating into a certain order is critical as signals can often be very weak. Therefore gratings are blazed to work for a limited range of frequencies and to diffract light primarily into one order. Blazing is achieved by changing the morphology of the grooves [11].

Light can also be dispersed by shining it through a prism. The variation of the refractive index of the prism with wavelength varies the angle of refraction of the

different frequencies of light. The dispersing power of a prism – that is the spatial separation of the constituent frequencies of the incident light – is typically not as great as a diffraction grating. Consequently the resolution of a prism spectrograph will not be as good as a grating spectrograph.

Double spectrograph design

There are four main issues to consider when designing a Raman spectrometer. The spectrometer must collect as much Raman light as possible, reject the Rayleigh light, minimize stray light and have sufficient resolution and dispersion. I will discuss each of these in turn and describe how they were implemented in the Durham UV resonance Raman spectrometer.

1. Light collection

The Raman effect is a relatively weak effect in comparison to Rayleigh scattering and fluorescence, so as little as possible of the Raman light must be lost. We used a high NA objective to collect ~7 % (0.84 sr) of the light emitted by the sample. Although higher NA objectives are available (such as water-immersion objectives), they are extremely expensive and have shorter working distances. We require a relatively large working distance to ensure that light can be delivered to the interface above the critical angle. To improve further the efficiency of the spectrograph, we chose a CCD camera (Newton, DU940N-BU2, Andor) with a high quantum efficiency in the UV (35–70% from 210–250 nm) and all mirrors were coated to maximize reflectivity in this frequency range. Finally the pre-slit lens and the CCD window were anti-reflection coated for deep UV wavelengths.

However, it is the diffraction gratings that typically determine the performance of a spectrograph. In a conventional Czerny-Turner arrangement, as shown in figure 6, plane gratings are employed [11].

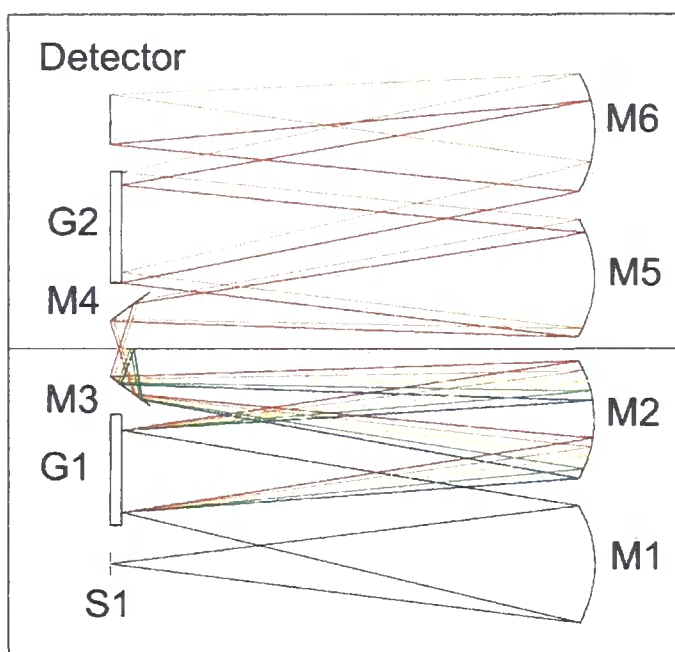


Figure 6. Schematic of a typical Czerny-Turner double spectrograph.

Consequently, off-axis paraboloidal mirrors are required to collimate or focus the light from one region of the spectrometer to the next. As discussed below, in the UV region double or even triple monochromators are required to achieve sufficient rejection of the Rayleigh line, so there could be up to ten mirrors. As the reflectivity of each mirror may be only 90%, in the case of a triple spectrometer ~1% of the Raman light collected by the objective will reach the detector. Therefore we elected to use concave gratings (264510 2953 224, Zeiss). These gratings act both to disperse and focus the light so no focusing mirrors are required in the spectrograph. They are also specifically designed to work with array detectors such as CCD cameras as they generate flat-field images directly, without the need for the correction of aberrations required in Czerny-Turner spectrographs [12]. The gratings also offer high efficiencies in the UV. I will discuss the behaviour of these gratings in more detail below.

2. Rayleigh line rejection

Rayleigh scattering is much more intense than Raman scattering, so it is essential that Rayleigh light is prevented from reaching the detector. In the low Raman shift region the Rayleigh light would swamp any Raman signal as the tail of the laser line may extend with significant intensity to up to $\sim 2000 \text{ cm}^{-1}$ from the peak. Even in the high wavenumber region, stray reflections of the Rayleigh light result in a high background count and therefore a low signal-to-noise ratio. In conventional Raman spectrometers the excitation laser emits in the visible or infrared regions of the electromagnetic spectrum and holographic notch or edge filters are used at the entrance to a spectrograph to reject the Rayleigh line. These optics offer the dual benefits of a high optical density at the laser wavelength and a sharp cutoff so that the Raman signal at low Raman shifts (typically down to $\sim 50 \text{ cm}^{-1}$) can still be probed. However, these holographic filters are inefficient in the deep UV. For example, a Semrock RazorEdge 224.3-nm long-pass filter only transmits 40% of the light at a Raman shift of 1600 cm^{-1} from 224.3 nm and 62% of the light at 3000 cm^{-1} . Furthermore, an edge filter that blocked the laser line at 225 nm would block the Stokes-shifted Raman light at 3000 cm^{-1} if the excitation wavelength were at 210 nm. Therefore we would need a whole suite of edge filters to cover the excitation range of our laser. As a result, many workers utilize double or even triple spectrometers to reject the Rayleigh line, as discussed in the introduction to this chapter. We elected to use a double spectrometer setup as the best compromise between Rayleigh light rejection and high efficiency.

3. Minimizing stray light

Stray light arises when ambient light or light from the laser line is scattered within the spectrometer onto the detector into a region where only Raman light is expected. This stray light will either cause a general rise in the background noise level or it will result in unexpected peaks or bands appearing in the Raman spectrum. Therefore it is highly desirable that as little stray light as possible reaches the detector. We limited the amount of ambient light by enclosing the spectrometer in a sealed box and

performing all experiments in a completely darkened room. We limited the amount of stray light from the laser line with a double spectrograph.

4. Spectrometer resolution and dispersion

The resolution of a spectrometer is its ability to separate two adjacent Raman bands into two images on the detector. It is a function of both the dispersion of the gratings and the relative size of the CCD pixels compared to the image projected onto them. I will discuss these two factors in turn.

The dispersion of a single grating is determined by the groove spacing. Our Zeiss concave gratings have a line spacing of 2500 grooves mm^{-1} and are specified to give a reciprocal linear dispersion (RLD) of 0.7 nm mm^{-1} . We are using two gratings in an additive configuration which halves the RLD to 0.35 nm mm^{-1} . The pixels on our Andor Newton camera are $13.5 \mu\text{m} \times 13.5 \mu\text{m}$, therefore the limiting resolution is $\sim 5 \text{ pm pixel}^{-1}$. At 225 nm this corresponds to a limiting resolution of $\sim 1 \text{ cm}^{-1} \text{ pixel}^{-1}$.

The gratings disperse an image onto the CCD, therefore the size of the image and the number of pixels that it covers will determine the actual resolution of an instrument. The image that is projected onto the chip is either determined by the size of the illuminated area of the sample or the size of the slit at the entrance to the spectrometer. If the collected light beam underfills the slit, the image of the illuminated area of the sample will be projected onto the CCD chip, consequently the size of the image at the chip will be the size of the illuminated area multiplied by the magnification factor of the objective and spectrometer system. The gratings have a magnification factor of unity, the reflective objective has a focal length of 13 mm and the pre-slit lens has a focal length of 200 mm, so the overall magnification factor is ~ 15 . Therefore if the sample is illuminated by a 10- μm diameter laser spot, the image at the chip will be ~ 11 pixels wide, corresponding to a limiting resolution of $\sim 11 \text{ cm}^{-1}$ at 225 nm. However, a tightly-focused laser beam creates a region of high intensity on the sample, and in the UV this situation can often lead to unwanted photochemical effects on the sample. Furthermore the cross-section of the laser beam is asymmetric so the spot size was $\sim 40 \times 200 \mu\text{m}$. In this case the image at the slit would be 0.6 mm wide, and to achieve a reasonable resolution the slit must be closed down to a width

of less than 200 μm . However, as the slit is closed less light reaches the detector. This point is demonstrated by the following model [13]. Assume that the sample image has dimensions $h \times w$ and the light from the image is collected by an objective parameterized by $f_1/\#$. The collimated beam is focused by a positive lens with a fixed $f/\#$ given by $f_2/\#$ onto a spectrometer slit of fixed dimensions $a \times b$. Consequently the magnification of the image, M , is given by

$$M = \frac{f_2/\#}{f_1/\#} \quad (2)$$

As the power of the objective is increased the amount of light transmitted by the slit into the spectrometer, P , passes through three regimes. In the first regime the image completely underfills the slit, in the second regime the image is vignetted by the slit in the horizontal axis and in the third regime the image completely overfills the slit. The expressions for the power transmitted by the slit in each of these regimes are given by

$$P \propto \frac{1}{(f_1/\#)^2} \quad f_1/\# > \frac{w(f_2/\#)}{a} \quad (3a)$$

$$P \propto \frac{a}{Mw(f_1/\#)^2} \quad \frac{w(f_2/\#)}{a} \geq f_1/\# \geq \frac{h(f_2/\#)}{b} \quad (3b)$$

$$P \propto \frac{ab}{M^2wh(f_1/\#)^2} \quad f_1/\# < \frac{h(f_2/\#)}{b} \quad (3c)$$

The relative power into the spectrometer is plotted as a function of $f_1/\#$ in figure 7 for our spectrometer.

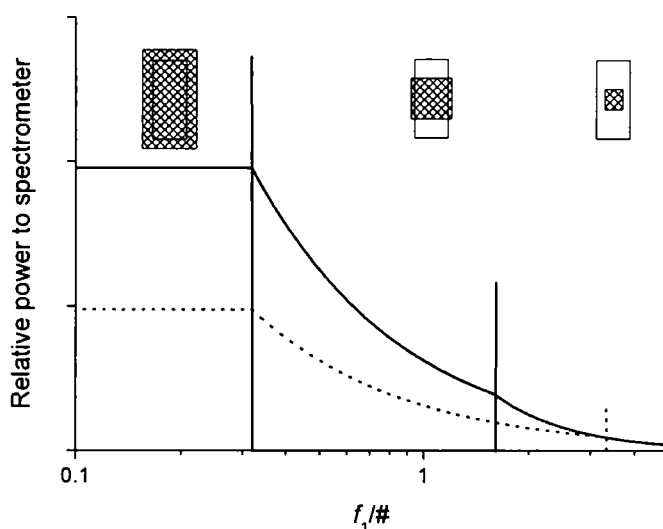


Figure 7. Relative power into the spectrometer plotted as a function of the $f/\#$ of the objective. Source size = $40\ \mu\text{m} \times 200\ \mu\text{m}$, (solid line) slit size = $200\ \mu\text{m} \times 5000\ \mu\text{m}$, (dashed line) slit size = $100\ \mu\text{m} \times 5000\ \mu\text{m}$. The inset images are cartoons of the image (hatched area) on the slit.

An objective with an $f/\#$ greater than 0.8 will underfill the 200- μm slit but the slit is not totally overfilled until an objective with an $f/\# < 0.3$ is used. Consequently our objective with an $f/\# = 0.87$ will only be vignetted by the slit in the horizontal axis when the slit is less than 200 μm wide.

The layout of the interior of the spectrometer is shown in figure 2. The entrance slit to the spectrometer was a commercial optical slit assembly with a maximum aperture of 3 mm (SPS-716-1, PI Acton). The slit is controlled by a micrometer to an accuracy of $\sim 5\ \mu\text{m}$. The second slit, S2, consisted of two razor blades placed 25 mm apart and mounted on two orthogonal manual linear translation stages (Newport). The second grating, G2 and the CCD camera, CCD 2, were each mounted on two orthogonal manual linear translation stages and a manual rotation stage (Newport). We later coupled stepper motors to the linear translation stages to automate the spectrometer. This process will be described in more detail below.

Behaviour and alignment of the double spectrometer

As noted above, we chose to employ concave holographic gratings in a double spectrometer configuration. These gratings were originally designed to be used in a single spectrograph so it was unclear how they would behave in series. The dispersion geometry of a single grating is shown in figure 8.

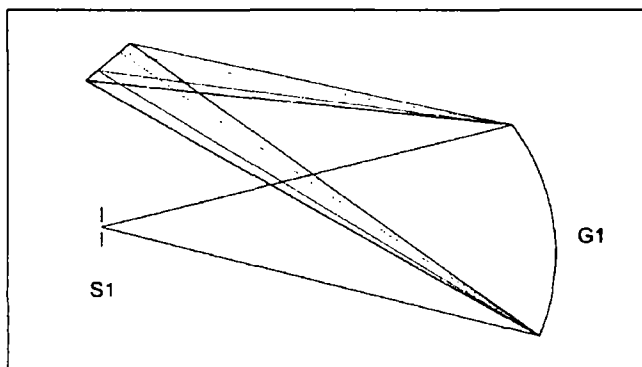


Figure 8. Dispersion geometry of a single Zeiss concave holographic grating.

Polychromatic light strikes the grating, is dispersed into its constituent frequencies and is focused to an image line. From this geometry we were able to ascertain where to place the second slit, the second grating and the CCD. The geometry of these components is displayed in figure 9. The second slit needs to be able to travel along the image line of the first grating to block the Rayleigh light with one edge and it needs to be sufficiently wide to allow enough Raman light through so that the doubly-dispersed light completely fills the CCD chip. The CCD chip is ~28 mm long so the width of the second slit was set at 30 mm. Although the slit size could be reduced to ~15 mm, in practice we found that this did not reduce stray light and made alignment more difficult. It is apparent that only the very central wavelength incident on the second grating will completely fill the grating; regions of the light cone for wavelengths that are higher or lower than this will be lost. By underfilling the grating slightly, the losses are not too severe. This problem also occurs with plane gratings in a Czerny-Turner configuration. The Zeiss concave grating is designed to minimize aberrations such as astigmatism and spherical aberration and consequently the line

spacing is a complicated nonlinear pattern. We had initially assumed that by inverting the second grating we could ensure that the light incident on the CCD was doubly dispersed with higher wavelengths shifted in the positive y direction. However in this configuration the light actually underwent subtractive dispersion. As an alternative we remounted the second grating in the same orientation as the first grating. We now discovered that the spectrograph grating exhibited double dispersion but the dispersion at the CCD was actually in the *negative* y direction. This result is caused by the concave grating acting as a concave mirror whereby the image at S2 is inverted as well as being doubly dispersed, as shown in figure 9.

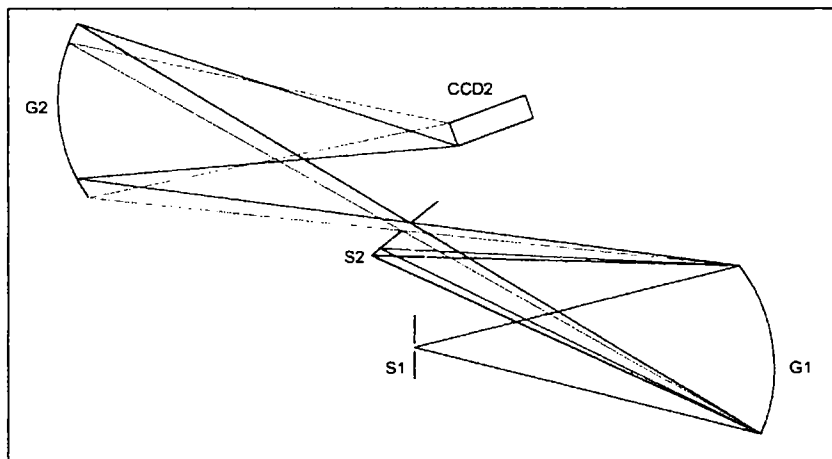


Figure 9. Illustration of the dispersion of the second grating in the spectrometer.

The different frequencies are therefore diffracted at different angles from those expected when the grating is illuminated with polychromatic light that is all incident at the same angle. In contrast, in a conventional Czerny-Turner double spectrograph the gratings are planar so this anomaly does not occur. Although this result was unexpected, it has no bearing on the ability of the double spectrometer to operate efficiently and effectively, as evinced below.

CCD camera: principle of operation

We employed an Andor Newton CCD (charge-coupled device) camera to detect the Raman scattered light. As the behaviour of a CCD is integral to the design of the spectrometer I will briefly describe its principle of operation [14]. A CCD is a silicon semiconductor chip which consists of a large 2D-array of pixels (2048×512 for the Andor Newton DU940N). Below each column of pixels is the shift register, which is another row of pixels which is masked from the incident light. A photon incident upon a pixel may produce a photoelectron and the probability of this event is termed the quantum efficiency. Therefore during the course of an acquisition charge builds up on the chip and at the end of the acquisition the charge on each pixel is stepped down the chip vertically and is then shifted horizontally into the amplifier node. The amplified signal is converted into counts and is sent to a PC. The number of photoelectrons per count for the Andor Newton in high sensitivity mode is 4.6 electrons per count.

One key advantage of the CCD is that it can deliver high signal-to-noise ratios. Noise can be produced from a number of sources. The first source is shot noise from the signal. This form of noise is always present and is a statistical property of the light itself, caused by the fact that photons are discrete entities. Although it cannot be eliminated, for a given signal of N photoelectrons, shot noise scales as $N^{1/2}$, so acquiring for longer times will increase the signal-to-noise ratio. The second source of noise is from the dark current. Even in the absence of incident light a CCD will experience a current from thermal generation. This source of noise also scales as the square root of the dark current and can be minimized by operating the camera at low temperatures. The chip is cooled by a thermoelectric cooler and we operated the CCD at a temperature of -65°C .

Noise also arises during the readout process from the CCD amplifier and the analogue-to-digital conversion from photoelectrons to counts. Therefore we operated the camera at a relatively low vertical shift speed of 50 kHz to minimize readout noise (the Andor Newton allows rates of up to 2 MHz for fast processes). Furthermore, we tried to limit the number of accumulations for a given total readout

time to ensure that each pixel accumulated as much charge as possible without becoming saturated before it was read.

The charge from the pixels can be read out and binned in a number of different ways. In our case we dispersed the Raman light along the long axis of the chip (the spectral axis), with the image of the slit extending along the short axis (the spatial axis). If each pixel is read individually an image of the light incident on the CCD is produced. This mode is useful to determine where the light is on the chip but is not very useful to produce a spectrum. Alternatively the charge from all the pixels in a given column can be summed in a process known as full vertical binning (FVB). This process will yield a spectrum, however as all the pixels are being read the background signal and hence the shot noise will be higher. Therefore typically one only reads from the illuminated part of the chip, if possible. This capture area extends the full length of the chip in the spectral direction but is limited in the spatial axis. I will term the product of this process a single track spectrum during this thesis.

Operating program

Although our spectrometer was custom-made, we wished to imbue it with all the benefits of a commercial system, including a user-friendly operating system and a high degree of automation. The laser itself was controlled independently by the software provided by Coherent Inc., but the control of all the remaining components was aggregated into a single program that we wrote in Labview (National Instruments). A screenshot of the front panel of the program is displayed in figure 10.

(Next page) Figure 10. Screenshot of the front panel of the spectrometer operating program, written in Labview.

Camera Controls

Read Mode

Background and signal together

Acquisition Mode

Cosmic Ray Removal

Accumulations

Exposure Time / s

Spectrometer Controls

Position

Raman shift

Motor select

Steps

Raman shift offset

Motor Position	
Sample x	30400
Sample y	29500
Slit lower	90000
Slit upper	93000
Grating upper	54000
Grating lower	65000
CCD upper	42000
CCD lower	24000

Raster during acquisition

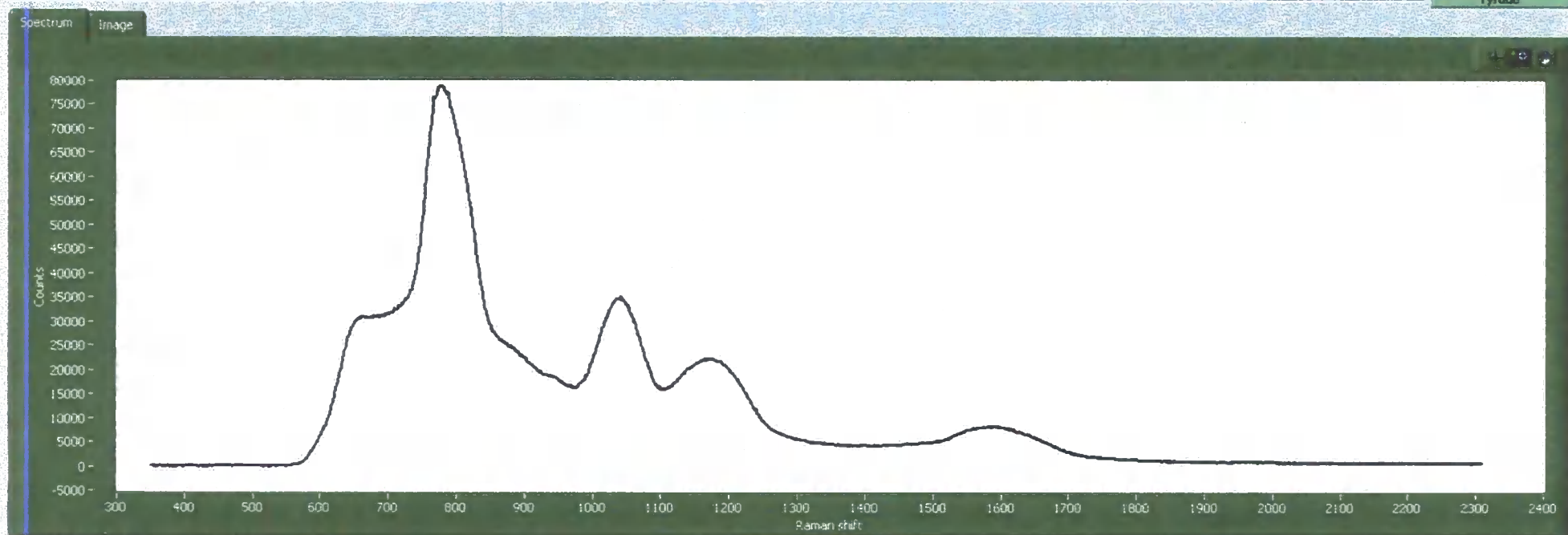
Raster limits

Xmin	29500
Xmax	30500
Ymin	29500
Ymax	30500

Camera condition

Temperature

© James Day & Eric Tyrade



The program controls and reads from the CCD camera, the laser shutter, the laser power meter, the spectrometer motors and the sample motors. The CCD camera is controlled by a series of functions written in Labview by the camera manufacturers (Andor SDK). We implemented some of these functions into our program to drive and read from the CCD camera. The user can control some of these functions from the front panel, as shown in figure 10. The read mode menu ring allows the user to choose between full vertical binning (FVB), single track and image. If the user is using the single track read mode the program also allows the user to specify the position and height of the capture box on the CCD chip and adjusts the extent of the CCD image accordingly. The acquisition mode menu ring allows the user to choose either a single spectrum or a series of accumulations. In the latter case, a software function can also be activated that removes from the spectrum any spikes caused by cosmic rays. The remaining buttons control the acquisition time, the number of accumulations (if applicable), whether to take a dark signal or a sample signal with the laser activated, and whether to save the spectrum. The program automatically subtracts the dark signal from the sample signal to give the spectrum.

The laser shutter is configured so the shutter is open to allow light to pass when the software is acquiring Raman light from the sample but closed when acquiring the dark signal.

The laser power meter (Nova II, Ophir) is also provided with a library of functions in Labview. We used these functions in the program to acquire the average laser power whilst the shutter is open.

We wished to motorize the spectrometer so that when we changed the laser excitation frequency we could rapidly and repeatably realign the spectrometer components to the correct position. We therefore coupled the linear translation stages to stepper motors. The hardware power supply and hardware control for these motors were designed and built by the electrical workshops. The motors were driven with eighth-stepping to give 1600 steps per revolution, giving a distance per step of 0.3 μm and 0.6 μm for the larger and smaller stages, respectively. The motors are controlled by eight digital inputs and return five digital outputs. Four of these input lines select one

or none of the motors. One line controls the direction of rotation of the motor, one line enables the motors, one line determines whether the motors are controlled by software or hardware and one line delivers the square-wave pulses required to drive the stepper motors. The frequency of these pulses determines the speed of the motors. Four of the five outputs describe whether an individual motor has reached a hardware limit and one output describes whether all motors have initialized to the home position. We wrote to and read from the digital lines controlling the motors and the shutter through a digital acquisition card (PCI 6221, National Instruments) connected to a connector block (SCB68). Upon initialization the motors are all driven to the home position, which is defined by the position of a microswitch attached to the linear stages. Once the motors are initialized they are released from hardware to software control. The program is designed to allow the user to specify the laser excitation wavelength and the spectral region of interest. The motors are then driven to the correct positions, which we determined during the alignment of the spectrograph (*vide infra*). The program also allows the user to jog any motor a desired number of steps for fine-tuning. These jog movements are controlled by software limits to ensure the motors do not drive the stage actuators beyond their limits. Only one motor is driven at a time in software control mode.

The sample motors behave in a similar manner to the spectrometer motors. However, they also allow the user to raster the sample during acquisition. This rastering process ensures the sample area illuminated by the laser is constantly moving so that photodegradation of the sample is limited. The raster path and parameters are defined in figure 11 and the logic controlling the raster is given in table 1.

The control program loops at 10 Hz. At the start of each cycle, the program checks which motor was moving in the previous cycle and the direction of the motor. The program then compares the current position of the sample stage with the limit parameters, x_{\min} , x_{\max} , y_{\min} , y_{mid} , and y_{\max} , and determines which motor to drive according to the logic in table 1. This logic produces the raster path described in figure 11.

Sample holder

A sketch of the sample holder is shown in figure 12.

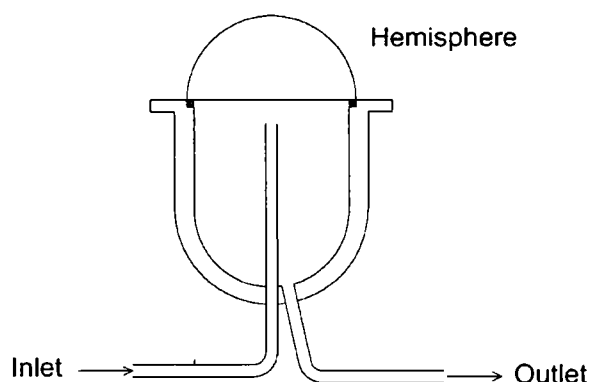


Figure 12. Sketch of the hemisphere sample holder.

The main body of the cell is made of glass. The joint between the cell and the 10-mm diameter UV-grade fused silica hemisphere (ISP Optics) is sealed by a Viton O-ring. The inlet tube is connected to a syringe pump (Model 11 Plus, Harvard Apparatus, Holliston, Ma.) with valves and Teflon tubing (Omnifit) and the outlet tube leads to a waste beaker.

Generic laser beam alignment

I used the following technique to align any laser beam in the work described in this thesis. First, I determined the coordinates of the two points in space that I wanted the beam to pass through. An upright ruler was positioned at each of these points in turn and the two mirrors preceding the two points were adjusted iteratively to walk the beam into alignment. The mirror closest to the laser source was used to align the beam on the ruler at the point closest to the laser source, and *vice versa*. I iterated this process until the beam intersected the ruler at the correct coordinates in each position. This process works because two points define a line and two mirrors are required to control two targets. In some cases, I aligned the beam as described above and then placed two well-separated irises in the beam path such that the beam passed directly through the centre of each iris. These irises allow the alignment to be checked and adjusted more easily than with a ruler.

To align a lens, I first aligned the beam from the source to the focal point in the absence of the lens. I then inserted the lens in the beam and adjusted the position and tilt of the lens until the beam both intersected the focal point and the back reflection from the side of the lens closest to the source was coaxial with the incident beam.

Microscope alignment

We aligned the microscope in the following manner (see figure 4 for an illustration of the components). First, the sample origin was defined at a fixed point in space (180 mm above the optical bench and at an arbitrary position in the xy plane). Using a plumb line, we located and marked the position on the laboratory ceiling immediately above the sample origin. The HeNe beam was aligned through I1 and I2 (see figure 4) and the sample origin. We placed a roughened silicon wafer at the sample origin and positioned the objective to ensure that the collected light was centered on the mark on the ceiling and the objective was level in the xy plane. We adjusted the objective's z -translation stage to ensure that the light emitted by the objective was collimated. We then positioned L2 (+125 mm, fused silica, Newport) and ensured that the light transmitted by L2 was centered on the mark on the ceiling. The position of CCD 1

was adjusted to ensure that the image of the sample was centered on the monitor screen and at its minimum size. Once CCD 1 was aligned, we positioned the 50% beamsplitter (NT43-736, Edmund Optics) and M7 to reflect the scattered light towards M7. Finally M6 was flipped into place to activate the “alignment” beam path, and M6 and M7 were adjusted to ensure the image of the laser light on the sample was also in the centre of monitor.

We aligned the sample in the following manner: the UV laser was blocked at the laser head and the alignment beam path was activated by flipping M5 and M6 into the beam path and removing M10 from the collection path (figure 4). The sample was raised until the image of the incident beam on the monitor was minimized. Once this has been done the sample is at the correct height. We then activated the delivery path by sliding M5 and M6 out of the beam path. One can see the scattered UV light by placing a roughened silicon wafer at the focus of the laser and consequently one can adjust the focus of lens 1 as required. M9 and L1 were then moved up or down on the translation stage to bring the image of the scattered UV light into the center of the monitor. This step is important as there is not enough scatter from a typical sample to see the UV beam at the sample surface. Finally M10 was slid back into the beam path to deliver the scattered light to the spectrometer. The position of the excitation beam in the centre of the hemisphere is critical when the incident beam is above the critical angle. If the beam is not in the centre of the hemisphere, it will not strike the curved surface of the hemisphere at normal incidence. Consequently the beam will be refracted and may be incident at the sample interface at less than the critical angle. If this is the case, the collected light will be scattered overwhelmingly by the bulk fluid and the signal from the surface will be swamped.

Aligning the double spectrograph

The double spectrograph is all aligned relative to the entrance slit, S1 (see figure 2). Once we had positioned S1, the first grating, G1, was positioned at the correct distance from the slit (445 mm, as defined by the manufacturers). M2 was flipped into the UV laser beam path and the periscope consisting of M3 and M4 was adjusted

to raise the beam to the same height above the optical table as the centre of G1. M11 was flipped out of the beam path and the beam was aligned through the slit to the centre of G1. We adjusted the orientation of G1 to ensure that the laser beam was focused in the correct position in the vicinity of S2. The geometry of the concave grating is shown in figure 13:

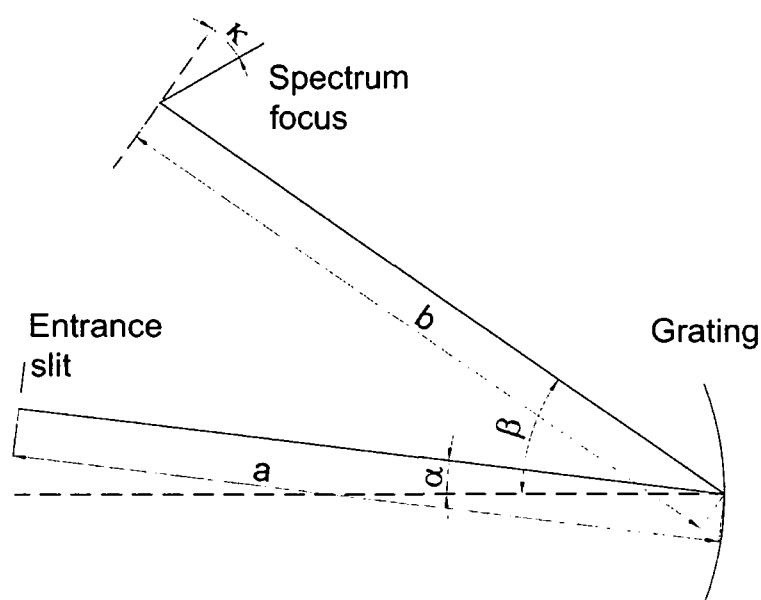


Figure 13. Geometry of Zeiss holographic concave grating.

The specification of the holographic grating, as given by the manufacturer, is shown in table 2.

Specification	Value
a (entrance slit to grating)	445 mm
b_{290} (focal distance at 290 nm)	432 mm
RLD (reciprocal linear dispersion)	0.7 nm mm^{-1}
α (incidence angle)	6.7°
β_{210} (diffraction angle at 210 nm)	24.2°
β_{350} (diffraction angle at 350 nm)	49.4°
κ_{290} (angle of focal plane at 290 nm)	20.0°

Table 2. Specification of Zeiss holographic concave grating.

From these specifications, I calculated the parametric equations for the focal distance, $b(\lambda)$, and the diffraction angle, $\beta(\lambda)$,

$$b^2(\lambda) = 2.041 \times 10^{12} \lambda^2 - 1.606 \times 10^6 \lambda + 0.4808 \quad (4)$$

$$\theta(\lambda) = 17.5 - \arccos\left(\frac{0.6459 - 7.747 \times 10^5 \lambda}{b(\lambda)}\right) \quad (5)$$

where the units of b and λ are m and the units of θ are degrees.

Once we had aligned G1, we positioned the second slit, S2, at the focus of G1. We then placed the second grating G2 at 445 mm from S2 and orientated G2 to ensure the laser beam passed down the table in the xy plane. Finally we positioned the CCD camera, CCD 2, at the focus of G2.

To calibrate and align accurately the motorized components S2, G2 and CCD 2 we used a sample of 50 % MeCN (aq) in the sample holder with an angle of incidence of 65° (below the critical angle). MeCN exhibits strong, well-spaced peaks with Raman shifts that are well-documented. We optimized the position of each motorized component in turn and adjusted the angle of the CCD camera to ensure the MeCN peaks were as sharp as possible across the whole chip. We then took a spectrum for calibration. The strongest peaks in each region were used to plot a third-order polynomial to convert from pixel to Raman shift. We changed the wavelength of the laser in 5-nm increments and repeated this procedure throughout the tuning range of the 4th harmonic of the Indigo-S laser. Typical spectra of acetonitrile solutions in the high and low wavenumber regions are shown in figure 14 and 15, respectively.

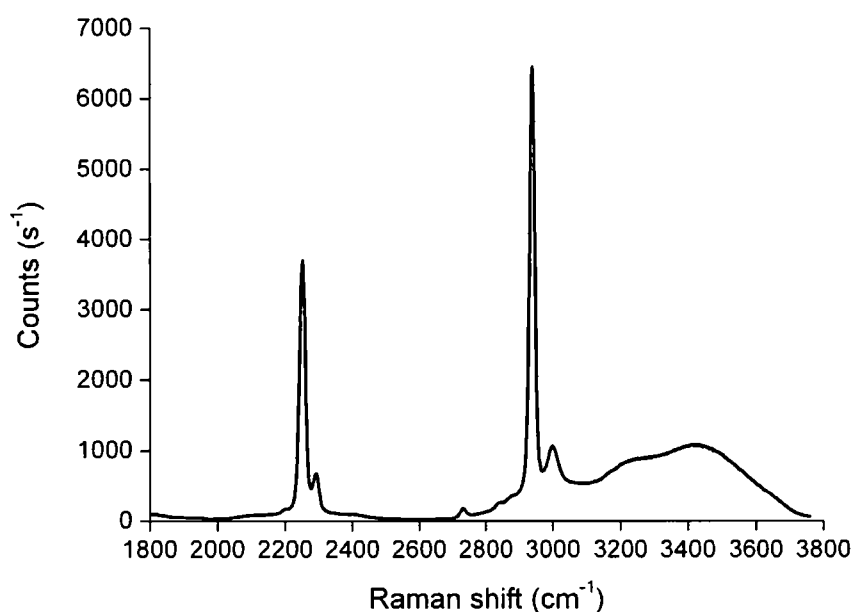


Figure 14. Spectrum of 50% v/v MeCN (aq) in the high wavenumber region. Conditions: $\lambda = 225$ nm, slit = 100 μm , acquisition time 10 s, angle of incidence = 65° .

The broad feature from $3100\text{--}3700\text{ cm}^{-1}$ is the OH stretching range of water. The peaks at 2940 cm^{-1} and 3000 cm^{-1} are the symmetric and asymmetric CH_3 modes, respectively. The peak at 2292 cm^{-1} arises from the CN stretch, the bands around 1400 cm^{-1} arise from CH bending modes and the peak at 918 cm^{-1} is the CC stretching mode. The peak at 2252 cm^{-1} is a combination of the CH bend and CC stretch that is enhanced by a Fermi resonance [15]. Although this spectrum exhibits strong peaks with good resolution, it is apparent from the baseline that the Rayleigh scattering has not been completely removed by S2. In particular the broad band centred at $\sim 1680\text{ cm}^{-1}$, which I believe is a ghost side band caused by an aberration in the grating, masks the amide I region. The problems from this relatively intense baseline are more apparent when the angle of incidence is increased above the critical angle. This situation will be discussed below.

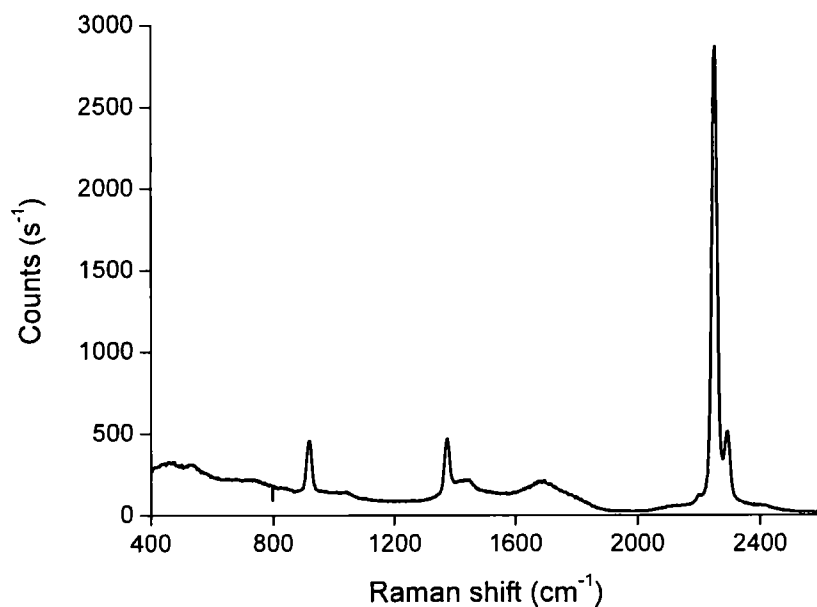


Figure 15. Raman spectrum of 50% v/v MeCN (aq) in the low wavenumber region. Conditions: $\lambda = 225$ nm, slit = 100 μm , acquisition time 10 s, angle of incidence = 65°.

6.3 UV resonance Raman spectra from an unenhanced monolayer

We increased the angle of incidence above the critical angle for the fused silica–water interface and acquired Raman spectra scattered by the evanescent wave. Raman spectra of water and a 1 mM CTAB solution are shown in figure 16.

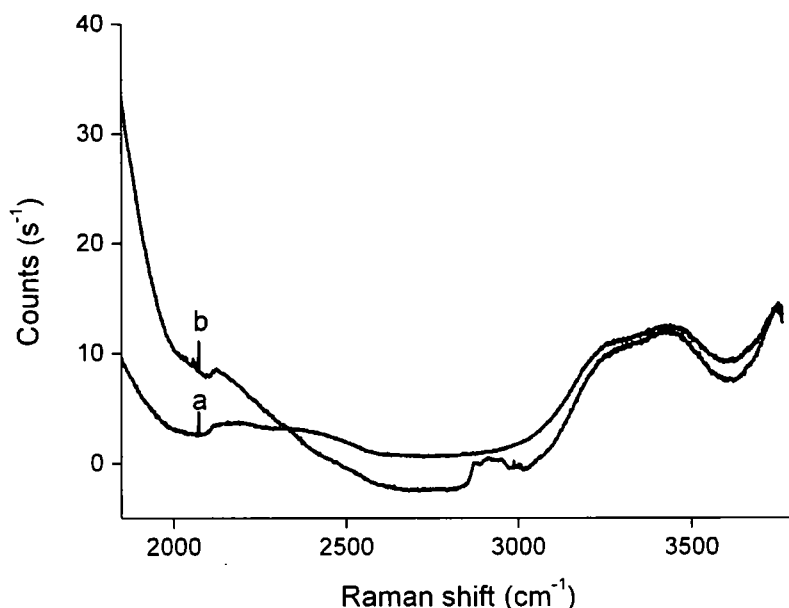


Figure 16. Raman spectra of (a) water and (b) 1 mM CTAB (aq.) in the high wavenumber region. Conditions: $\lambda = 225$ nm, slit = 500 μm , acquisition time = 20 min, angle of incidence = 70° .

In the spectrum of the CTAB solution in figure 16 the C–H stretching peaks of the surfactant monolayer can be clearly distinguished at 2800–3000 cm^{-1} . To our knowledge, this is the first reported UV Raman spectrum of a monolayer. This spectrum is very encouraging and an important step on the way to our ultimate goal of acquiring spectra of peptides and proteins adsorbed in lipid bilayers and at the oil–water interface. However, the incomplete rejection of the Rayleigh line that was alluded to above causes a number of problems at these signal levels. First the baseline below ~ 1800 cm^{-1} in the water background spectrum in figure 16 is at least an order of magnitude more intense than the CH_2 bending modes that would be expected at ~ 1400 cm^{-1} . Second, some of the laser light that reaches the spectrometer arises from

scattering of the laser by irregularities in the silica surface. If the laser beam strikes a different part of this surface the amount of scattering will vary. This effect is apparent when one compares the baselines of the water and surfactant spectra in figure 16. Furthermore the baseline of the CTAB spectrum becomes negative from 2700–3000 cm^{-1} . This result suggests that the ambient light has varied between the dark acquisition and the sample acquisition. Consequently, better ambient light rejection is required. The large variations in the baseline mean that it would be impossible to obtain a good subtraction spectrum from these data. We therefore elected to try and solve these problems next.

6.4 Design of the prism prefilter

The broad peak at $\sim 1680 \text{ cm}^{-1}$ in figure 15 is caused by an inconvenient ghost image from an aberration in the concave grating. In the setup described above, all the Rayleigh light (except that lost through incomplete reflection by the collection optics) strikes the first grating, and we rely on S2 to prevent this light reaching the detector. However, this setup will only work if all the Rayleigh light is scattered along one path centred on the 0 cm^{-1} Raman shift. If some of this light is scattered along a different path, it will pass through S2, strike the detector and cause unexpected peaks in the Raman spectrum. We therefore decided to incorporate a prism prefilter before our main spectrometer to prevent most of the Rayleigh light from entering the spectrometer. The prism prefilter is inspired by a design by Kaminaka and Mathies [16], although our filter is slightly different as it does not employ a Czerny-Turner configuration, nor do we use reflective optics. We chose this design to maximize throughput as the only losses should occur at the two prism–air interfaces. The prefilter is shown in figure 17.

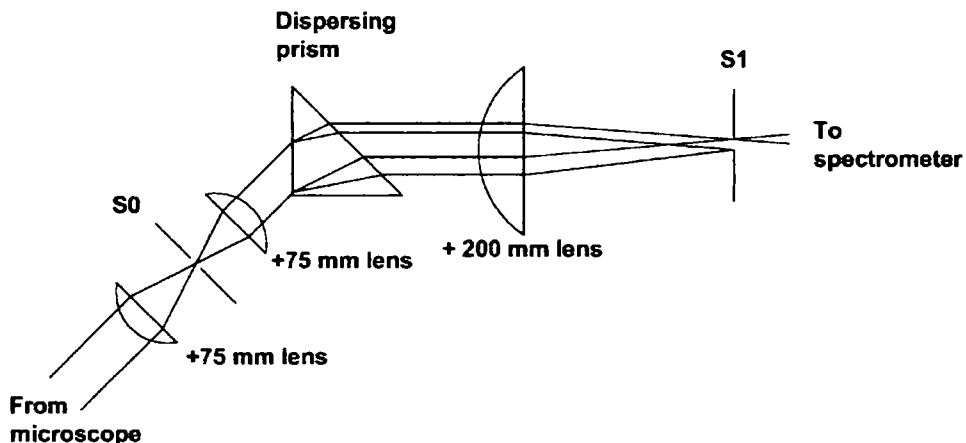


Figure 17. Prefilter design. The dispersion of the prism has been magnified for clarity.

The collimated beam from the microscope is focused through a slit, S0. This slit acts as the entrance slit for the spectrometer also and determines the spectral resolution. The light is recollimated and passed through a right-angle prism. The dispersed light is then focused onto another slit S1. This slit blocks the Rayleigh light but allows the Raman light to pass through to the spectrometer. We chose a right-angle prism as the best compromise between throughput and dispersion. A close-up of the dispersing prism is shown in figure 18.

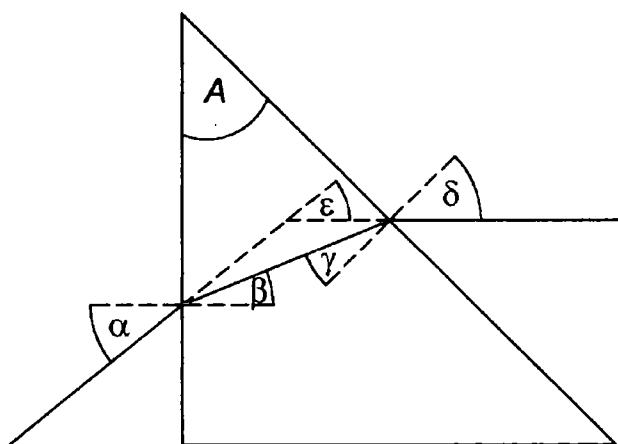


Figure 18. Refraction of a light ray through a dispersing prism.

If the entrance angle, α , and exit angle, δ , differ the prism will magnify or demagnify the beam with the magnification factor, M , given by

$$M = \frac{\cos\beta \cdot \cos\delta}{\cos\alpha \cdot \cos\gamma} \quad (6)$$

We wished to avoid this situation as it would change the f-number of the beam entering the spectrometer. α and δ are the same when

$$\alpha = \sin^{-1}(n \sin(A/2)) \quad (7)$$

where n is the index of refraction of fused silica and A is the apex angle of the prism. Increasing A and α will increase the dispersion, however more light will be reflected from the two silica–air surfaces. The reciprocal linear dispersion for the prism prefilter is given by

$$\frac{d\lambda}{dx} = \frac{\cos\beta \cdot \cos\delta}{f \sin(A)} \frac{d\lambda}{dn} \quad (8)$$

where f is the focal length of the focusing lens and the variation of the refractive index of fused silica is given by [17]:

$$n^2 - 1 = \frac{0.6961663\lambda^2}{\lambda^2 - (0.0684043)^2} + \frac{0.4079426\lambda^2}{\lambda^2 - (0.1162414)^2} + \frac{0.8974794\lambda^2}{\lambda^2 - (9.896161)^2} \quad (9)$$

where λ is in microns.

I have plotted the RLD and the reflectivity per surface for s - and p -polarized light at 225 nm in figure 19. At $A = 45^\circ$, $R_s = 7\%$, $R_p = 2\%$ and the RLD at 225 nm is 6.4 nm mm^{-1} . This prism gives a good compromise between high dispersion and high throughput.

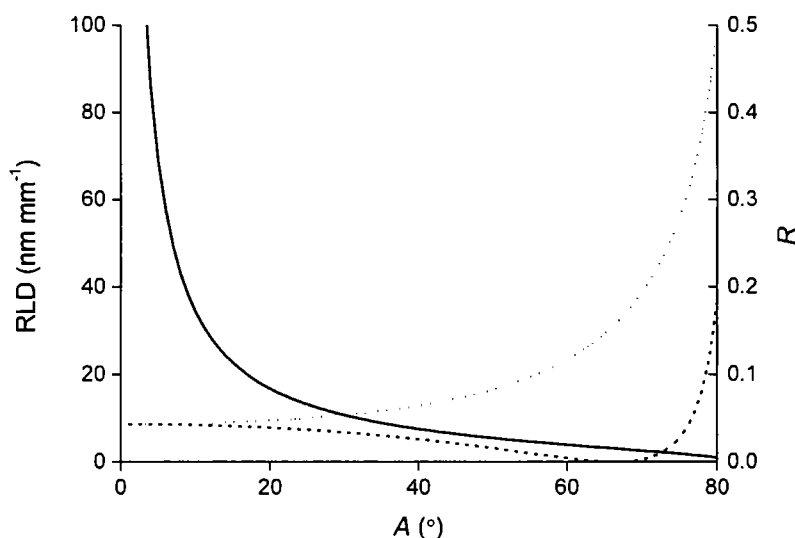


Figure 19. Reciprocal linear dispersion, RLD, (solid line) and reflectivity per surface for *p*- (dashed line) and *s*-polarized light (dotted line) for a fused silica prism with apex angle, A . $\lambda = 225$ nm.

No *p*-polarized light is reflected at the Brewster angle, so a Brewster's angle prism would be essentially lossless for this polarization of light. However we wanted to acquire spectra with unpolarized as well as polarized light so we decided not to use a Brewster angle prism.

As n varies with frequency it is not possible to position the prism to have a magnification of unity for all frequencies simultaneously. We aligned the prism so that 225-nm light is not magnified, so that the largest increase in the magnification factor is less than 1%.

In figure 20 I have plotted the RLD of the prism prefilter in units of $\text{cm}^{-1} \text{mm}^{-1}$ as a function of wavelength:

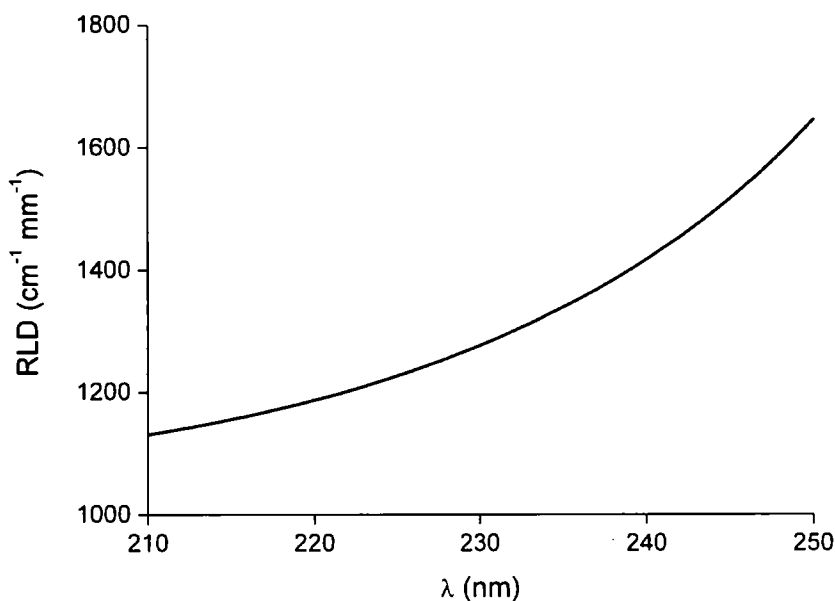


Figure 20. Reciprocal linear dispersion, RLD, plotted as a function of wavelength for a fused silica prism with apex angle = 45° .

From figure 20 it is apparent that a slit width of 3 mm is sufficient to transmit the spectrum from $1000\text{--}4000 \text{ cm}^{-1}$, even at an excitation wavelength of 210 nm.

The prism prefilter deviates the path of the scattered light by $\epsilon = 26^\circ$, as shown in figure 18. We initially placed the prism prefilter at the appropriate angle before the spectrometer and adjusted the steering mirrors to deliver the beam into the spectrometer. However, the throughput of this alignment was considerably poorer than our original design for the following reason. The laser beam has a line cross-section in the horizontal plane caused by the BBO crystal. When this line was focused onto the sample, the minimum image size was $\sim 10 \mu\text{m} \times 300 \mu\text{m}$. In the original design the long axis of this image was projected parallel to the spectrometer slit and little light was lost even with a tightly-closed slit. In contrast, with the prefilter in place this image was rotated by 26° such that the long axis of the image was no longer parallel to the slit and a significant intensity of light was lost. This problem is exacerbated by the fact that most of the scattered intensity is localized towards one end of the long axis of the image. Thus to solve this problem we changed

the angle of the image formed at the sample. Version 2 of the optical bench layout is shown in figure 21. In this design the long axis of the image projected onto S0 is parallel to the slit.

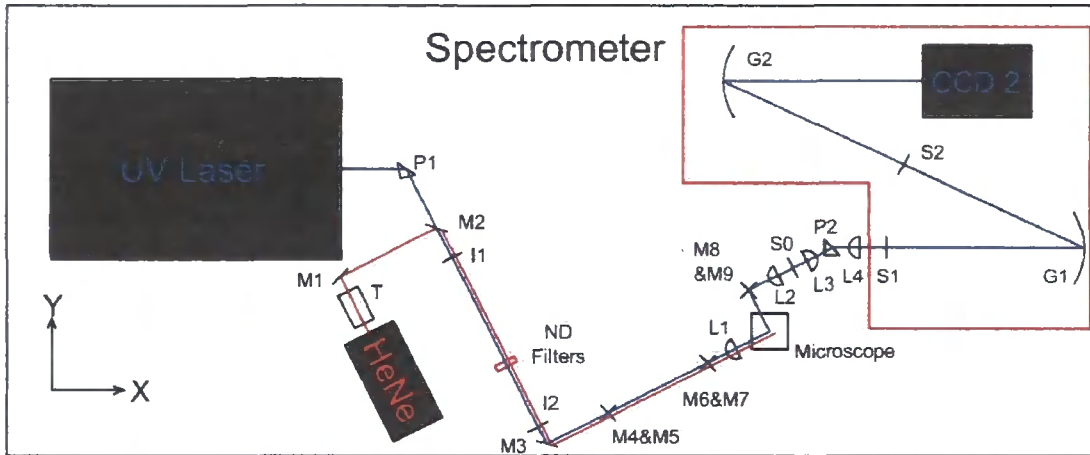


Figure 21. Schematic of the Durham UV resonance Raman spectrometer, version 2.

The effect of the prefilter can be seen by comparing the two spectra of polytetrafluoroethene (PTFE) in figure 22, taken with S1 fully open and partially closed to block the Rayleigh line.

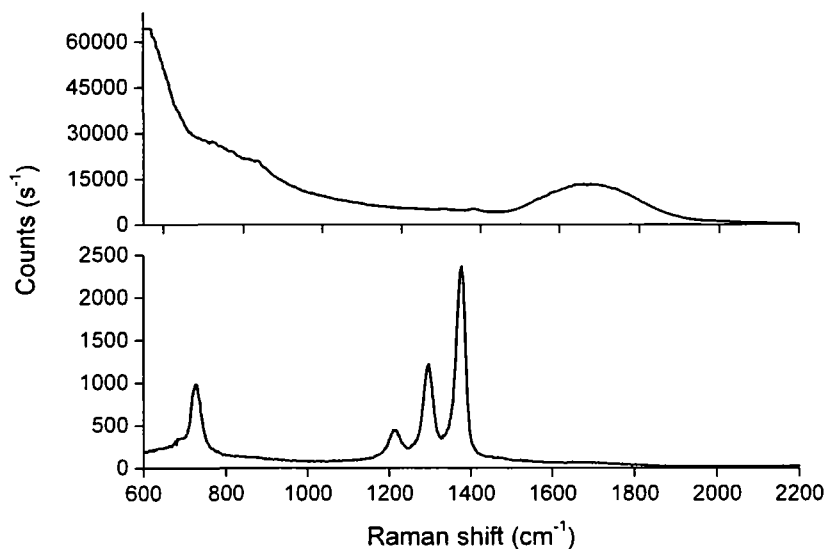


Figure 22. Raman spectra of PTFE. (Upper) S1 fully open. (Lower) S1 partially closed. Conditions $\lambda_0 = 225$ nm, power = 500 μ W, S0 = 250 μ m, acquisition time = 1 s.

PTFE bands occur at 729 cm^{-1} (symmetric CF_2 stretch), 1215 cm^{-1} (antisymmetric CF_2 stretch), and 1295 and 1379 cm^{-1} (C–C stretching modes). The PTFE peaks can only just be distinguished from the baseline with S1 fully open and the aberration centred at ~ 1680 cm^{-1} is clearly visible. When S1 is partially closed the Rayleigh scatter is prevented from entering the spectrometer. The PTFE peaks are the dominant features in the spectrum and the grating aberration is no longer apparent.

6.5 Spectrometer throughput and resolution

The intensity of laser light scattered by a roughened silicon wafer was measured at S0 and at CCD2 (see figure 21). The measured efficiency of the spectrometer varied between 25 and 30% across the tuning range of the laser.

I acquired spectra of the CN stretch of acetonitrile for a series of slit widths (S0). The peak intensity and the full-width at half maximum (FWHM) from these spectra are plotted in figure 23.

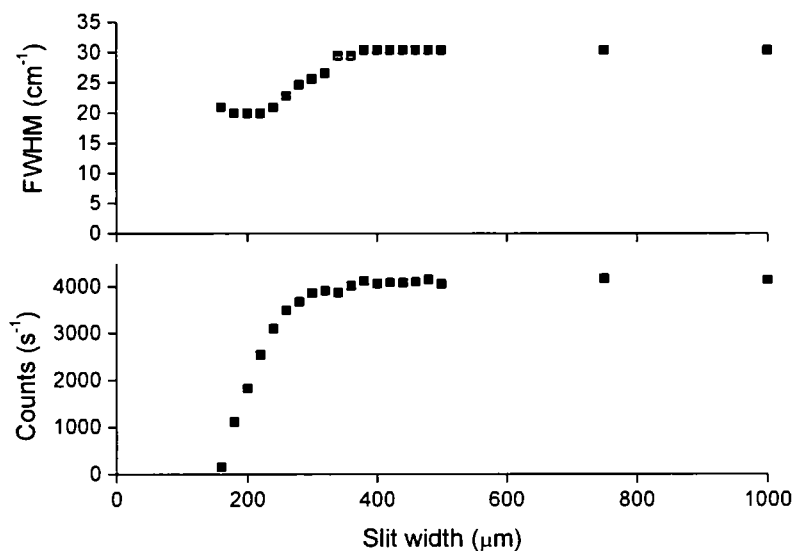


Figure 23. Peak intensity and FWHM of acetonitrile in the CN-stretching region as a function of slit width. Conditions $\lambda_0 = 225 \text{ nm}$, power = $350 \mu\text{W}$, acquisition time = 5 s.

The signal drops to zero at a slit width of $180 \mu\text{m}$. The lateral position and focus of the image have been optimized on the slit, so the sudden cut-off in intensity is surprising. I believe this effect is due to the fact that the image of the laser beam on the sample does not have a Gaussian intensity envelope; the greatest intensity is not in the middle of the beam. Thus although the slit is $180\text{-}\mu\text{m}$ wide, most of the intensity is striking either side of the slit.

The optimum slit width is $\sim 250 \mu\text{m}$. At this slit width the peak intensity is 80% of the maximum intensity and the FWHM is $\sim 22 \text{ cm}^{-1}$. This resolution is relatively poor: ideally we require a FWHM of $< 10 \text{ cm}^{-1}$. The image of the laser beam at the sample has a width of $\sim 40 \mu\text{m}$. The microscope objective and +75 mm lens magnify this image by a factor of 5.8 onto S0 to give an image of $\sim 230 \mu\text{m}$. If the size of the image of the laser beam at the sample was reduced, the resolution would improve accordingly.

6.6 Truncated hemisphere design

The sample holder design shown in figure 12 is not ideally suited to raster the sample relative to the incident laser beam. When the sample holder is moved laterally (in the xy -plane), the laser beam no longer strikes the curved surface of the hemisphere at normal incidence. Furthermore, the hemisphere and the microscope objective are no longer coaxial. Both these factors serve to degrade the Raman spectrum as the light no longer follows the optimal beampath to the detector. In order to address these issues, we designed a new sample cell that employed a truncated hemisphere. This cell is shown in figure 24.

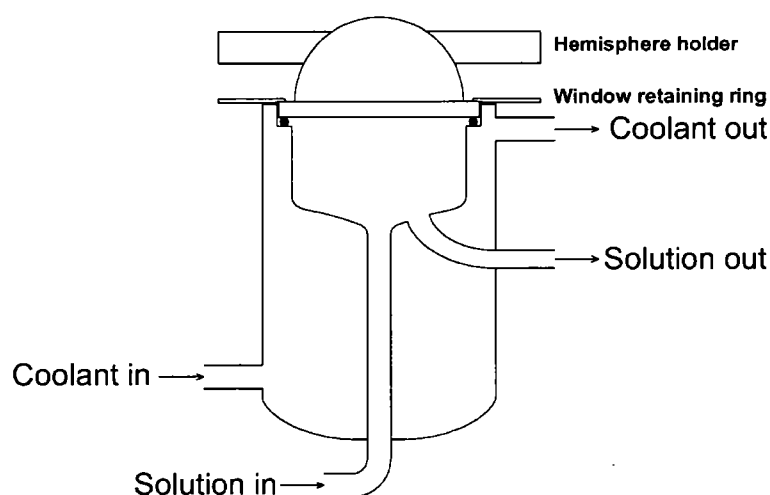


Figure 24. Sketch of the truncated hemisphere sample holder.

The cell is constructed from glass and is jacketed to allow temperature control. The volume of the cell that contains the sample is sealed by a 3-mm thick, 38-mm

diameter, UV-grade, fused silica window (Global Optics, UK) and a Viton O-ring. A truncated hemisphere (Global Optics, UK) with a radius of curvature of 17 mm sits on top of the window. The planar face of the hemisphere has been truncated by 3 mm such that the centre of the hemisphere is coincident with the bottom face of the window. Squalane was used as an index-matching fluid as it is viscous enough to provide sufficient lubrication between the two optics. The squalane was filtered through alumina to remove absorbing contaminants. The truncated hemisphere is held fixed in the *xy*-plane relative to the microscope objective, whereas the rest of the sample cell can move relative to the objective. This design ensures that the sample can be rastered up to 2 mm in any direction from the centre.

6.7 Indolicidin adsorbed in a planar-supported lipid bilayer

Indolicidin is a water-soluble, antimicrobial tridecapeptide that contains five tryptophan residues [18]. The indole rings in the sidechains of tryptophan are resonantly-enhanced at 225 nm, so this peptide is a good candidate to test the capabilities of the UV Raman spectrometer. The sample cell in figure 24 was cleaned in Decon solution and rinsed thoroughly in UHQ water. The window and truncated hemisphere were cleaned in chromosulphuric acid to remove organic contaminants, rinsed thoroughly in UHQ water and dried in a stream of dry nitrogen. 1-palmitoyl-2-oleoyl-*sn*-glycero-3-phosphocholine (POPC) was dissolved in 10 mM *tris* buffer at pH 7 and sonicated for 15 minutes to produce multilamellar vesicles. This solution was passed eleven times through a 100-nm filter to produce small unilamellar vesicles. This solution was introduced to the cell and the vesicles were allowed to fuse to the silica surface for one hour to form planar-supported lipid bilayers. Once a spectrum of the lipid bilayer had been acquired, a 10- μ M solution of indolicidin was introduced into the cell and another spectrum was acquired. The Raman spectra in the fingerprint region of pure water, the POPC bilayer and the POPC bilayer in the presence of indolicidin are shown in figure 25.

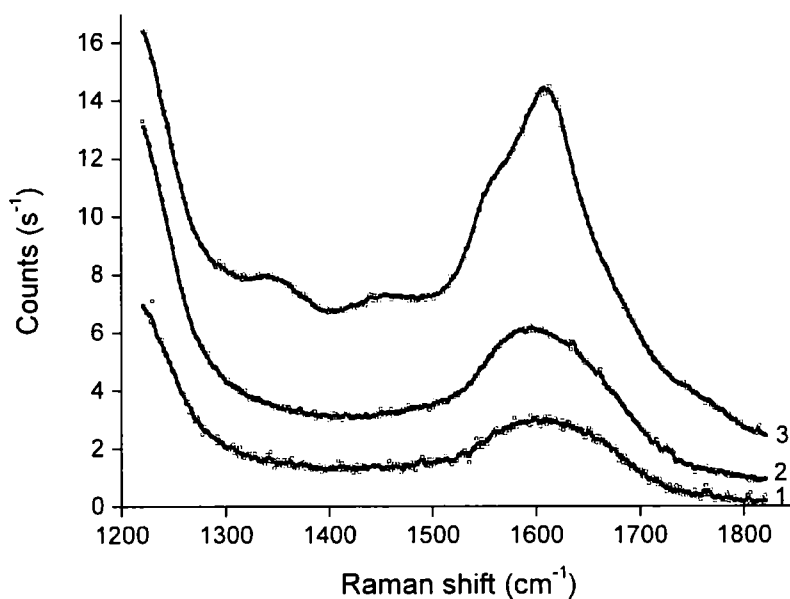


Figure 25. Raman spectrum of (1) water, (2) POPC, (3) POPC + indolicidin in the low wavenumber region. Conditions: $\lambda = 225$ nm, power = $270 \mu\text{W}$, acquisition time 1200 s, angle of incidence = 74° . (\square) Raw data, (solid line) data smoothed by 5-point adjacent averaging. The spectra have been offset vertically for clarity.

The broad feature in the water spectrum centred at 1620 cm^{-1} and the tail of the band below 1300 cm^{-1} arise from the silica substrate. The water bend is too weak to be resolved at this signal-to-noise ratio. The POPE spectrum is similar to the water spectrum; neither the methylene bending modes nor the carbonyl stretch of the lipid can be distinguished. In contrast, the spectrum of the sample that contains indolicidin is markedly different from the other two spectra. The difference spectrum of spectrum 3 and spectrum 1 is shown in figure 26.

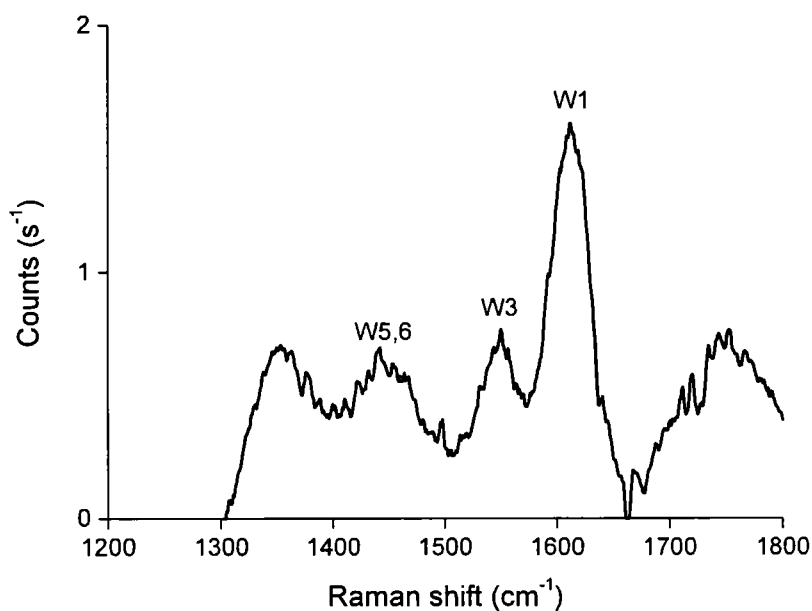


Figure 26. Difference spectrum of (POPE+indolicidin) – water. Conditions as in figure 25.

Although the spectrum in figure 26 is quite noisy, the tryptophan peaks W1, W3 and W5,6 can be clearly distinguished at 1620 cm^{-1} , 1550 cm^{-1} and 1450 cm^{-1} , respectively. These Raman shifts correspond well with reported values in the literature [7]. Below 1300 cm^{-1} , the strong band from the silica substrate masks further tryptophan peaks. As the experimental technique is refined, it is hoped that superior background matching will allow these bands to be identified too.

The signal-to-noise level in figure 26 is quite poor, but it is reassuring that we are able to discriminate the resonantly-enhanced peaks from the peaks from the substrate and the bilayer. Nevertheless, the technique must be refined further to allow us to acquire quantitative measurements from these systems.

6.8 Spatial filter

The minimum image size of the laser beam at the sample is $40\ \mu\text{m} \times 250\ \mu\text{m}$. The large size of this image has two drawbacks. First, the width of the beam limits the spectral resolution, as discussed above. Second, the laser beam illuminates a large surface area, which limits the efficacy of the raster approach to reduce sample damage. The large image size arises from the poor beam quality of the UV laser; spatial walkoff in the nonlinear BBO crystal generates an elliptical beam cross-section [19] with side lobes surrounding the main beam. I constructed a spatial filter to clean up the beam-shape, as shown in figure 27.

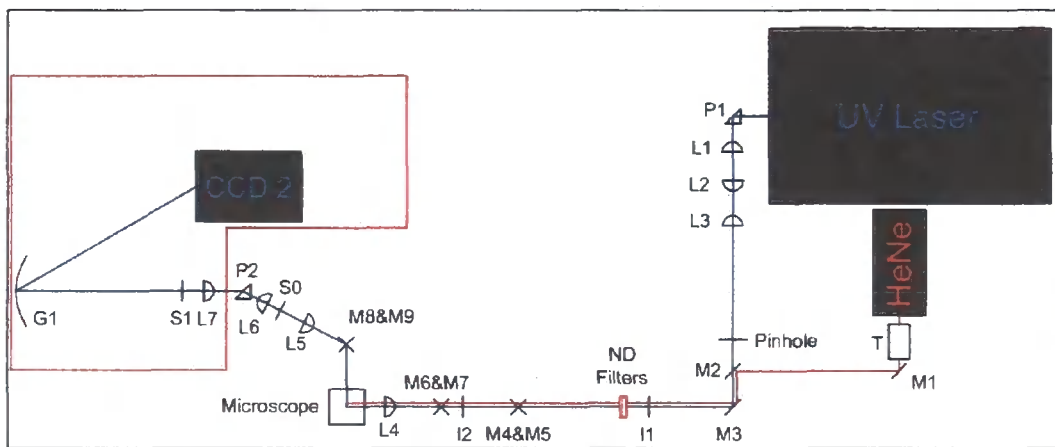


Figure 27. Schematic of the Durham UV resonance Raman spectrometer, version 3.

L1 (+ 15 mm) and L2 (+ 200 mm) act as a Keplerian telescope to expand the beam by a factor of ~ 13 . L3 (+ 200 mm) focuses the beam onto the 50- μm pinhole. The laser beam overfills the pinhole in order to eliminate the side lobes. The cleaned laser beam is focused by L4 (+ 75 mm) to generate an image of the pinhole on the sample that is reduced by a factor of ~ 2.7 . With this spatial filter in place, the image at the sample is approximately $20\ \mu\text{m} \times 25\ \mu\text{m}$, where the elliptical cross-section solely arises from the non-normal incident angle. As the image of the beam at the sample no longer has such an extreme aspect ratio, the beam path does not need to be tilted as in version 2 in figure 21.

The other alterations in version 3 concern the spectrometer and the design of the prefilter. The spectrometer has been reduced to a single grating. Although the previous doubly-additive configuration generated twice the dispersion, the aberrations created when focusing to an image limited the resolution. Thus to improve throughput but maintain resolution I have adopted a single grating configuration.

The configuration of the prefilter is critical. The prefilter is constructed from refractive optics which generate chromatic aberrations. In the wrong configuration, the difference in the position of the focus at S1 for 225-nm and 245-nm light can vary by up to 30 mm. This aberration greatly affects the tilt angle of the focal plane of the concave grating and means that the CCD detector can not effectively capture the Raman spectrum. The optimum combination of lenses that minimized the chromatic aberration of the prefilter and satisfied the acceptance $f/\#$ of the grating was as follows: $L5 = +100$ mm, $L6 = +75$ mm, $L7 = +75$ mm.

6.9 Comparison with other UV Raman spectrometers

Asher's group have been at the forefront of the development of UV resonant Raman spectroscopy for twenty years. Their most recent spectrometer is based on a modified Czerny-Turner configuration [20]. The key feature of their spectrometer is the use of partially subtractive dispersion to minimize stray light from the Rayleigh line. In an additive configuration, stray light from the Rayleigh line which is not diffracted along the 0 cm^{-1} light path by the first grating will not be prevented from striking the second grating and will appear as an artefact in the Raman spectrum. This situation occurs with our spectrometer without the prefilter, as discussed above and demonstrated in the upper spectrum of figure 21 between 1600 and 1800 cm^{-1} . Bykov *et al* used a second grating in a partially subtractive configuration with a dispersion six times that of the first grating. The vast majority of the artefactual stray light from the first grating is dispersed along the 0 cm^{-1} light path of the second grating and hence is shifted out of the Raman spectrum. This spectrometer achieved a throughput of $\sim 18\%$ and a spectral resolution of $\sim 7.5\text{ cm}^{-1}$ at 204 nm . Lednev *et al* also used a double Czerny-Turner arrangement in a partially subtractive configuration and

achieved a throughput of $\sim 12\%$ and a spectral resolution of $\sim 6 \text{ cm}^{-1}$ at 202 nm [6]. Although the partially subtractive configuration is effective at blocking the Rayleigh line, we decided not to use this approach as the number of reflective surfaces in the spectrometer necessarily limits the throughput.

Aki *et al* adopted an alternative approach to eliminate the Rayleigh light [21]. They used a liquid filter to prevent 244-nm Rayleigh light from entering their single Czerny-Turner spectrograph. The liquid filter consisted of a 10-mm thick rectangular cuvette filled with a 4:1 v/v methanol:butyl acetate solution. This solution acts as an edge-pass filter – transmitting the Stokes Raman light but absorbing the Rayleigh and anti-Stokes light. This concept of a liquid filter was developed initially by Kleinmeyer *et al* for lasers in the range of 288 nm to 342 nm [22]. Although McKenzie has demonstrated the effectiveness of a 0.5% acetone/water filter to suppress 193-nm Rayleigh light [23] we elected not to use liquid filters in our spectrometer for two reasons. First, the search for a filter solution suitable for the frequency range of our laser may be long and ultimately fruitless. We would require a separate solution for each excitation wavelength of our laser. Second, the cutoff of liquid filters is not as sharp as a holographic edge or notch filter and throughput is reduced even at high Raman shifts.

Bykov *et al* have also discussed the possibility of using the Schumann-Runge absorption bands of O_2 as a Rayleigh filter [20], although this approach has not been realized to date. The excitation light could be tuned to one of these bands and the scattered light passed down an unevacuated pathway into the spectrometer. However these bands span the 175–205 nm region so this approach is not appropriate for our UV laser.

Finally I will discuss the specifications for a typical commercial UV Raman spectrometer manufactured by Jobin-Yvon. The T64000 uses a triple Czerny-Turner configuration to minimize stray light. The first two gratings are used in a fully subtractive mode to remove the Rayleigh line and the third grating is used to redisperse the light and produce a spectrum. As only one grating is used to disperse the light onto the CCD camera, the RLD is that of a single spectrograph. The

spectrometer comprises three gratings with $\sim 40\%$ efficiency in the deep UV and ten coated aluminium mirrors with $\sim 90\%$ efficiency which results in an overall throughput of $\sim 2\%$. This efficiency is evidently not sufficient for studies of monolayers and bilayers.

6.10 Conclusion

We have designed and built a UV resonance Raman spectrometer to acquire spectra from proteins and peptides adsorbed within a bilayer or at the oil–water interface. Our UV laser source is tunable within the range 210–225 nm and requires that the spectrometer is also tunable across this region. The incident light is delivered to the sample above the critical angle to make the procedure surface-sensitive. Scattered light from the sample is collected with a custom-made microscope and delivered to the spectrograph. Our spectrometer is built around two holographic concave gratings to minimize the number of optics and maximize throughput. All movable parts within the spectrometer are motorized for accurate and repeatable repositioning. The sample holder is also motorized so that the sample can be rastered relative to the incident beam. This step is essential to prevent photochemical degradation of the sample. We found that an additive double spectrograph configuration was not able to limit stray light sufficiently so we included a low dispersion prism prefilter prior to the main spectrometer to eliminate the Rayleigh light. The throughput and resolution of this spectrometer are sufficient to detect the unenhanced Raman signal from surfactant monolayers adsorbed at the interface between fused silica and aqueous solution and the enhanced signal from tryptophan residues in the peptide indolicidin adsorbed in a lipid bilayer.

References

- 1 D. A. Long, *The Raman Effect* 1st ed. (John Wiley & Sons, Ltd., Chichester, 2002).
- 2 S. A. Asher, *Ann. Rev. Phys. Chem.* **39**, 537 (1988).
- 3 E. V. Efremov, F. Ariese, and C. Gooijer, *Analytica Chimica Acta* **606**, 119 (2008).
- 4 C. Lee, D. Phil. thesis, (Oxford, 2005)
- 5 Z. Chi, X. G. Chen, J. S. W. Holtz, and S. A. Asher, *Biochemistry* **37**, 2854 (1998).
- 6 I. K. Lednev, V. V. Ermolenkov, W. He, and M. Xu, *Anal. Bioanal. Chem.* **381**, 431 (2005).
- 7 G. Balakrishnan, Y. Hu, S. B. Nielsen, and T. G. Spiro, *Appl. Spec.* **59**, 776 (2005).
- 8 Q. Wu, W. H. Nelson, S. Elliot, J. F. Sperry, M. Feld, R. Dasari, and R. Manoharan, *Anal. Chem.* **72**, 2981 (2000).
- 9 U. Neugebauer, U. Schmid, K. Baumann, W. Ziebuhr, S. Kozitskaya, V. Deckert, M. Schmitt, and J. Popp, *ChemPhysChem* **8**, 124 (2007).
- 10 A. D. Czaja, A. B. Kudryavtsev, and J. W. Schopf, *Appl. Spec.* **60**, 352 (2006).
- 11 C. Palmer, *Diffraction Grating Handbook* 6th ed. (Newport Corporation, Rochester, NY, 2005).
- 12 J. Reader, *J. Opt. Soc. Am.* **59**, 1189 (1969).
- 13 Newport Corporation, Getting Light Into A Monochromator, <http://www.newport.com/Getting-Light-into-a-Monochromator/383722/1033/catalog.aspx>
- 14 Andor Technology plc, User's Guide to the Andor Newton (2007)
- 15 J. R. Reimers and L. E. Hall, *J. Am. Chem. Soc.* **121**, 3730 (1999).
- 16 S. Kaminaka and R. A. Mathies, *Appl. Spec.* **52**, 469 (1998).
- 17 I. H. Malitson, *J. Opt. Soc. Am.* **55**, 1205 (1965).
- 18 M. E. Selsted, M. J. Novotny, W. L. Morris, Y. Q. Tang, W. Smith, and J. S. Cullor, *J. Biol. Chem.* **267**, 4292 (1992).

- 19 J. Friebe, K. Moldenhauer, E. M. Rasel, W. Ertmer, L. Isaenko, A. Yelisseyev, and J.-J. Zondy, *Optics Communications* **261**, 300 (2006).
- 20 S. Bykov, I. K. Lednev, A. Ianoul, A. Mikhonin, C. Munro, and S. A. Asher, *Appl. Spec.* **59**, 1541 (2005).
- 21 M. Aki, K. Shinzawa-Itoh, S. Yoshikawa, and T. Kitagawa, *J. Phys. Chem. B* **104**, 10765 (2000).
- 22 J. A. Kleinmeyer, J. C. Fister III, J. Zimmerman, and J. M. Harris, *Appl. Spec.* **50**, 1597 (1996).
- 23 R. L. McKenzie, *Opt. Lett.* **18**, 995 (1993).

Chapter 7

Confocal Raman spectroscopy of lubricants in a soft elasto-hydrodynamic tribological contact

7.1 Introduction

Understanding the behaviour of a lubricating fluid in the contact region between soft, pliable surfaces is of prime importance in many industrial and biological spheres. For example, animal joints operate through the interaction between relatively soft cartilage surfaces and are lubricated by synovial fluid [1], if this fluid is lost or altered the patient can suffer from arthritis. Contact lenses also require significant lubrication to avoid irritation and inflammation, and the behaviour of food in the rubbing contact between the tongue and the mouth during eating is believed to have a direct relevance to the appreciation of food texture and taste [2]. While a significant body of work has been done on the behaviour of hard contacts owing to their critical importance and ubiquity in engineering bearings, there has been much less focus on soft contacts. In this chapter I will present work carried out on a three-month placement at Unilever R&D, Colworth, to commission and demonstrate proof-of-principle for a combined tribology and confocal Raman spectroscopy experimental rig for studying soft contacts.

Classically, the friction between two sliding objects (or tribopair) is described by Amonton's laws of friction [1]. The first law states that the friction force, F , is proportional to the normal load, L , on the objects, and the constant of proportionality is known as the coefficient of friction, μ , i.e. $\mu = F / L$. The second law states that the friction force is independent of the nominal area of contact between the objects. For a sliding contact between two surfaces moving relative to each other at a speed U and lubricated by a fluid with a dynamic viscosity η , μ varies with the product $U\eta$ in a characteristic manner that is known as a Stribeck curve, as shown in figure 1.

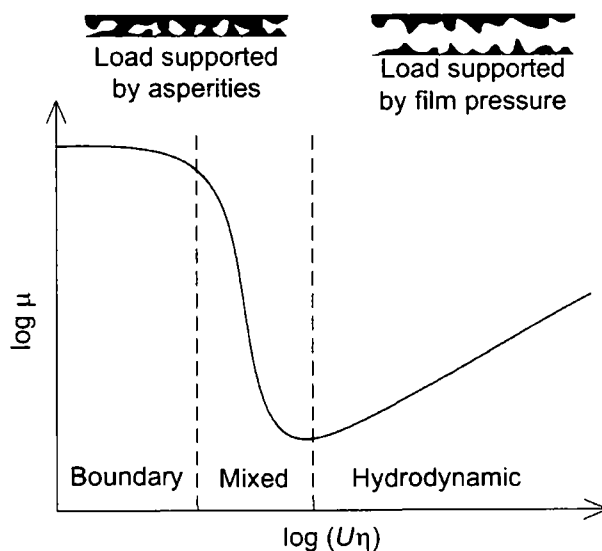


Figure 1. Schematic of a typical Stribeck curve, showing the variation of friction coefficient with the product of the entrainment velocity, U , and the lubricant viscosity, η . Note the log-log scale.

At low values of $U\eta$, a simple lubricant is readily squeezed out of the contact and the whole normal load is supported by the contacts between asperities on the two surfaces. This regime is known as the boundary regime and in the absence of surfactant molecules μ is relatively large. However, if the lubricant contains surfactant that can adsorb at the surfaces within the contact, μ can be reduced by an order of magnitude [1]. Consequently, the coefficient of friction in the boundary regime on the Stribeck curve varies greatly depending on the nature of the lubricant. At high values of $U\eta$ the contact is in the hydrodynamic regime, where the entire load is supported by the fluid. In this regime the friction force arises from causing the lubricant to flow and hence the friction coefficient depends solely on the viscosity of the fluid for a given tribopair. At intermediate values of $U\eta$, the contact is in the mixed regime between the boundary and hydrodynamic regimes. The contacts studied in this work can be classed in the isoviscous-elastic hydrodynamic lubrication (EHL) regime, where a complete lubricating film is formed and the pressures in the contact are high enough to deform the solid surfaces but not high enough to alter the viscosity

of the lubricant [3]. Although the friction coefficient in these soft contacts can be readily determined by experiment or from theory, ascertaining more detailed information on the behaviour of the contact is more challenging. Key questions one may ask about these contacts include: what is the thickness of the lubricating film within the contact and, in a multicomponent system such as an emulsion, what is the composition within the contact? Raman spectroscopy is evidently ideally suited to answer these questions.

There have been several previous studies on tribology in soft EHL contacts at Unilever, Colworth, comprising both numerical and experimental techniques. De Vicente *et al.* solved the isoviscous 2D Reynolds equation and the elasticity equation to give the film thickness, Poiseuille (rolling) and Couette (sliding) shear stresses and Poiseuille and Couette friction coefficients across the contact [4]. They successfully compared the calculated values of the friction coefficient with experimental results in the EHL regime. As well as studying the friction properties of non-Newtonian polymer solutions [5] and food hydrocolloids [6], de Vicente *et al.* investigated lubrication by emulsions and, in particular, the effect of the viscosity ratio of the aqueous and oil phases [7]. They found that the behaviour of the friction coefficient suggested that the most viscous phase may dominate the contact to the exclusion of the less viscous phase, but as their technique did not have chemical specificity they were unable to confirm this hypothesis. The use of a spectroscopic technique to determine explicitly the composition within the contact is evidently desirable. In addition to the body of work on the tribology of EHL contacts, various other experimental techniques have been employed to probe lubricant properties in the contact [8]. Capacitance and optical interferometry measurements have been used since the 1960s to determine the thickness of thin films and the advent of ultra-thin film interferometry in the 1990s extended the measurable film thickness down to ~2 nm. However, both substrates must conduct electricity for capacitance measurements and optical interferometry requires adequate optical contrast between the substrates and the lubricant and hence neither of these techniques is directly applicable in the model system used in this work. Light microscopy has been used to image directly shear-banding in EHL films [9, 10] and emulsions close to the contact [11]. IR,

Raman and fluorescence spectroscopies have also been used to determine lubricant composition in the contact (though not in soft-EHL contacts). Can used polarized FTIR reflection absorption spectroscopy and an IR microscope to examine molecular alignment of polymers and liquid crystals in a hard EHL contact [12]. Raman spectroscopy has been used to map the pressure variation in the contact by measuring peak shifts in the lubricant [13]. However, a shift of 0.1 cm^{-1} was found to correspond to a pressure change of $\sim 30 \text{ MPa}$, so this technique cannot be used to map pressure changes in the soft EHL system employed here as the Young's modulus of the PDMS elastomer is $\sim 4 \text{ MPa}$ [14]. Confocal Raman spectroscopy has also been applied by Bae *et al.* to study PDMS liquid confined between mica sheets in the surface forces apparatus [15]. Finally, Beattie *et al.* used evanescent wave Raman scattering and sum-frequency spectroscopy to study monolayers of Zn arachidate confined between MgF_2 and CaF_2 and subjected to a pressure of 60 MPa [16]. Changes to the spectra under load suggested a structural change in the monolayer, although the exact nature of this change was unclear.

In the rest of this chapter, I will first describe the design and the commissioning of the tribo-Raman experimental rig before presenting Raman spectra, white-light images and friction data from a soft-EHL contact. The proof-of-principle will be demonstrated with a single phase lubricant followed by results from oil-in-water emulsions.

7.2 Experimental rig

The experimental rig was designed by Jeroen Bongaerts, Paul Pudney and Chris Marriott at Unilever R&D, Colworth, to measure the friction coefficient and to acquire simultaneously Raman spectra of a lubricated soft-EHL contact. Although the rig had been designed and built prior to my arrival at Colworth, it had not been operated and no tribology measurements or Raman spectra had been acquired. Thus my project was to commission the system and demonstrate proof-of-principle and then develop the technique to provide in-contact Raman spectra and images of more complex lubricants. The rig consists of a mini-traction machine (MTM, PCS Instruments), a custom-made sample cell and a confocal Raman microspectrometer (Olympus BX 60 microscope coupled to a Kaiser Holoprobe 5000R spectrometer), all mounted on a large granite slab that can be tilted to an angle of 30° from horizontal, as shown in figure 2.

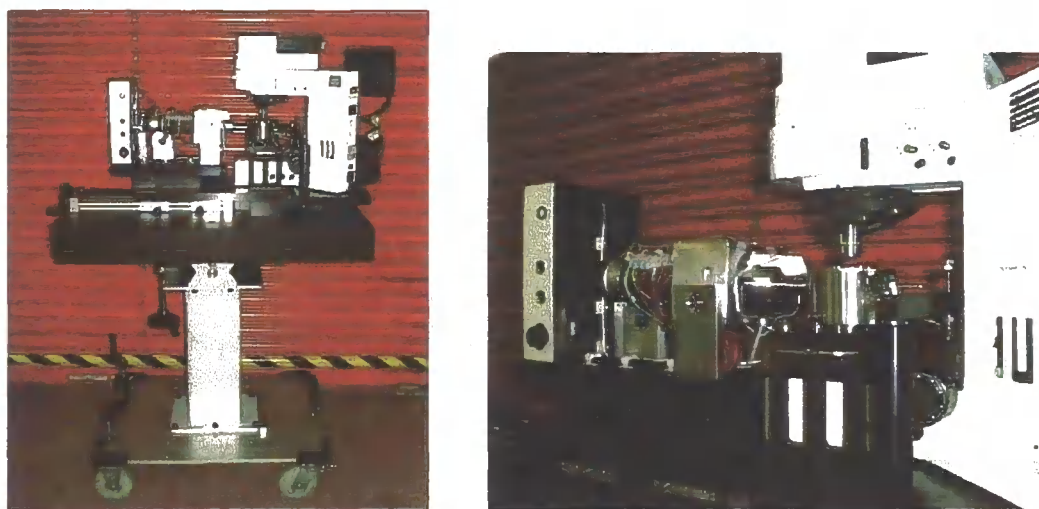


Figure 2. The tribology-Raman experimental rig and a close-up of the MTM, sample cell and microscope.

The tribological contact is formed in the sample cell between a polydimethylsiloxane (PDMS) elastomer ball attached to the MTM and a fused silica window, as shown in figure 3.

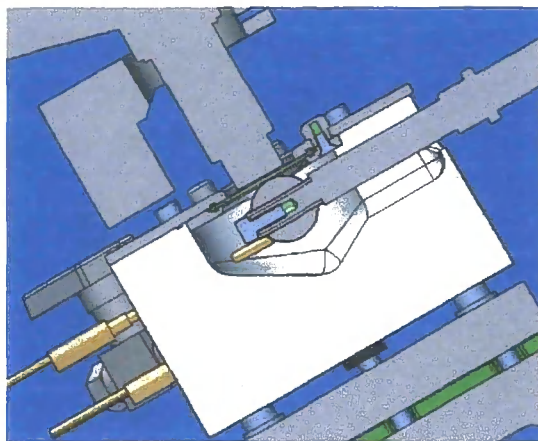


Figure 3. Cut-away CAD image through the sample cell, showing the contact between the PDMS ball and fused silica window. Image created by C. Marriott, Unilever, Colworth.

When the table is tilted the sample cell is filled so that the contact is fully flooded with liquid. It is well-known that incomplete flooding of the contact in the EHD regime (starvation) can significantly reduce the thickness of the lubricating film and increase the friction coefficient [17]. This tilting arrangement eliminates any artefacts in the friction coefficient from starvation effects. The MTM applies a constant normal load to the ball, measures the normal load with a strain gauge, rotates the ball at a constant angular velocity and measures the lateral traction force on the ball resulting from friction in the contact with a force transducer. As the window is fixed, $U_w = 0$, and the ball is rotating at a speed $U = U_b$, the MTM operates at a constant slide-to-roll ratio, $SRR = 2$, where $SRR = 2|U_b - U_w|/(U_b + U_w)$. The microscope objective is attached to a piezo-driven stage (PIFOC, PI, Karlsruhe, 100- μm range) for fine focusing in the z direction and positioned above the fused silica window to take images and spectra of the contact. The MTM rig is mounted on a motorized xy translation stage with submicron resolution (Proscan, Prior Scientific, Cambridge) so that the PDMS ball can be moved relative to the microscope objective in the xy plane. This arrangement allows the acquisition of spectra and images from different areas of the contact. The MTM and sample cell are also mounted on a coarser manual translation stage to allow the cell to be wheeled under the microscope objective.

The confocal Raman spectrometer consists of an optical microscope connected by fibre optic cables to a 785-nm diode laser (Tiger, Sacher) and a spectrometer. A Kaiser Holoprobe sampling accessory is fixed to the top of the microscope to couple the laser light into the microscope and to deliver the scattered light to the spectrometer. The layout of the Holoprobe sampling accessory is shown in figure 4.

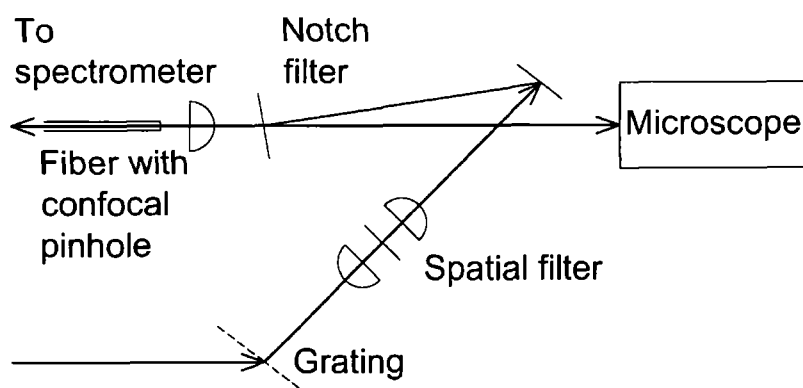


Figure 4. Schematic of the Kaiser Raman Holoprobe sampling accessory.

Laser light from the input fibre optic cable is dispersed by a grating and focused through a spatial filter to remove all Raman light scattered by the optical fibre, leaving just the Rayleigh line. This step is essential or the bands from the silica fibre optic cable swamp the peaks from the sample. The cleaned beam is folded into the microscope by a series of mirrors and focused with a long working distance oil immersion objective specifically designed to image through fused silica at 785 nm (River Diagnostics, 100 \times , $NA = 0.85$). The returning scattered light passes through a holographic notch filter to remove the Rayleigh line and is then focused into a fibre optic through a pinhole and passed to the spectrometer. This pinhole controls the confocal spatial resolution as shown in figure 5. Different pinholes can be employed in order to vary the spatial resolution. Only light that originates from close to the focal plane of the objective can pass through the pinhole. A similar mechanism operates to control the resolution in the focal plane itself.

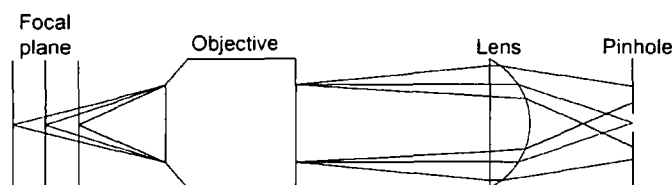


Figure 5. Schematic showing how a pinhole controls the spatial resolution.

The dispersive holographic grating in the spectrometer is fixed but split into two sections that disperse high and low frequency Raman light, respectively, onto the CCD chip. This process eliminates the need to move the grating to scan the whole region of interest from $50 - 3500 \text{ cm}^{-1}$ but does not allow the user to measure the anti-Stokes Raman light without replacing the entire grating.

7.3 Materials and methods

The PDMS (Sylgard 184, Dow Corning) balls were cast in a custom-built mould and had a radius of 9.5 mm. The base and curing agent were used in a mass ratio of 10:1 and were cured for 2 hours in an oven at $70 \text{ }^\circ\text{C}$. Scanning electron microscope (SEM) images of the ball surface were taken by Steve Furzeland and analyzed by Michael van Ginkel. The root-mean-square (rms) roughness was $\sim 350 \text{ nm}$ and the periodic tooling marks occur approximately every $25 \text{ }\mu\text{m}$. An SEM image and profile of the ball surface are shown in figure 6.

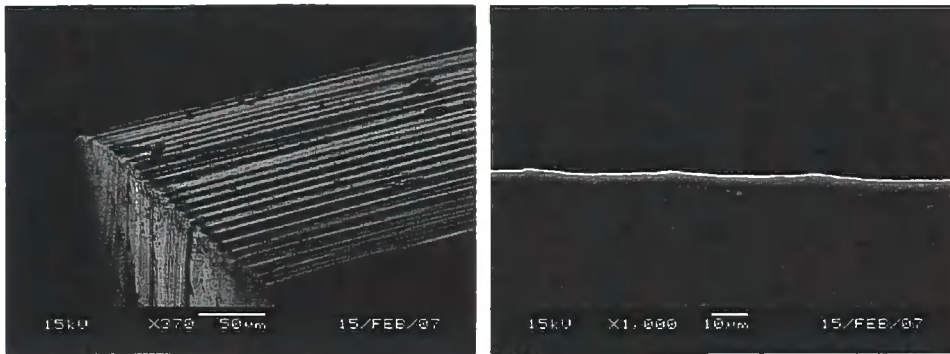


Figure 6. SEM image and profile of the surface of a PDMS ball. rms roughness \approx 350 nm.

The fused silica windows (35 mm diameter, 1 mm thick) were either used as received or made hydrophobic by coating with an OTS monolayer. Glycerol (Aldrich, 99.5%) and corn syrup solutions were made using UHP water. Sunflower oil (SFO) was used as the oil phase. The oil and aqueous phases of the emulsions were prepared separately then emulsified with a Silverson L4R emulsifier at a mass ratio of 1:4. All emulsions were stabilized with 1 wt% Tween 60 (Fluka). All emulsions in this work will be referred to by the glycerol concentration in the aqueous phase.

The normal and traction forces measured by the MTM were calibrated before use with weights of known mass. Before each set of experiments, the sample cell, fused silica window and PDMS ball were cleaned thoroughly in a weak detergent solution, rinsed thoroughly in UHP water, rinsed in isopropanol, rinsed thoroughly in UHP water again and dried in a stream of dry nitrogen. After reassembling the sample cell, the table was tilted to 30° and the lubricant was fed into the sample cell by syringe. For experiments where $U\eta < 0.1 \text{ Nm}^{-1}$ the cell was completely filled with lubricant. If the cell was filled completely for $U\eta > 0.1 \text{ Nm}^{-1}$, the spindle of the MTM drew the lubricant up into the entrance of the cell. This fluid in the cell entrance tended to exert a lateral force on the traction transducer that was greater than the friction force. Therefore at these high values of $U\eta$ the volume of fluid in the cell was reduced to ensure the force measured by the transducer arose purely from friction. Although at rest the contact was no longer fully flooded, once the ball was rotating the whole window was coated in lubricant and the degree of starvation in the contact was

minimal under these conditions. The sample cell was then wheeled under the microscope objective. The microscope was focused into the contact in three progressively finer ways. First, the sample cell was raised towards the objective with metal strips inserted below the cell. Then the microscope was pressed down more tightly onto the experimental rig by the restraining bolt. As the microscope rests on rubber pads, pressing the microscope down causes the pads to compress and brings the objective closer to the contact. The pitch of the restraining bolt was $\sim 1.25 \text{ mm turn}^{-1}$, which provided sufficient resolution to focus the microscope efficiently. Finally the objective piezo-driven mount was used to fine-tune the position of the microscope focus. Raman spectra from the microscope were cycled at a frequency of 1 Hz as the objective was focused in the contact and the intensity of the fused silica, lubricant and PDMS peaks were used to determine the position of the focus in the z direction. I will describe the procedure to determine the extent of the contact below.

A normal load of 1 N was applied during all tribological measurements and the traction force was averaged over at least 50 s. Raman spectra were acquired at 4 cm^{-1} resolution. All experiments were done at room temperature ($\sim 22 \text{ }^\circ\text{C}$).

7.4 Confocality of the microscope objective

An oil immersion objective was used in this experiment as it improves the depth resolution of the Raman microscope relative to an air immersion objective. Everall [18] and Baldwin and Batchelder [19] have calculated the effects of refraction on the depth resolution in a confocal Raman microscope and in a more recent paper Everall has further highlighted the introduction of spectral artefacts from out-of-focus sample regions [20]. In an attempt to image a point in a sample at a distance Δ below the interface, the marginal rays are refracted through a greater angle than the paraxial rays. The depth resolution, D , i.e. the size of the region illuminated by the laser, is defined by [18]

$$D = \Delta \{ [NA^2(n^2 - 1)/(1 - NA^2)]^{1/2} - n \} \quad (1)$$

where $n = n_2/n_1$ is the ratio of the refractive indices of the sample, n_2 , and the incident medium, n_1 .

Previous work on this microscope with a 15- μm pinhole and a short working distance oil-immersion objective demonstrated that the depth resolution of the confocal microscope is $\sim 2\ \mu\text{m}$, where the resolution is defined as the distance it takes for a signal to decrease to half its maximum value as the focus moves away from a planar interface. However, it quickly became apparent that I was not achieving this level of depth resolution with the new long working distance oil immersion objective. In figure 7, the normalized intensity of the $1053\ \text{cm}^{-1}$ peak from a glycerol solution collected using the long working distance oil immersion objective and a 20- μm pinhole is plotted as a function of z .

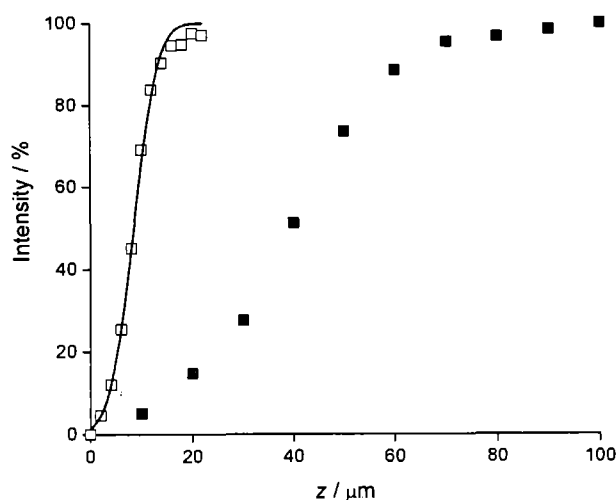


Figure 7. Normalized intensity of the $1053\ \text{cm}^{-1}$ peak from a 96 wt% glycerol solution collected with a long working distance oil immersion objective and a 20- μm pinhole plotted as a function of z . (■) Without beam expander. (□) With beam expander. The fit to the data with equations 3, 4 and 5 is shown as a solid line.

The depth resolution of the long working distance objective is $\sim 35\ \mu\text{m}$. The depth of field, d , of an objective is described by

$$d = \frac{\lambda(n^2 - NA^2)^{1/2}}{NA^2} \quad (2)$$

where $\lambda = 785$ nm is the wavelength of the incident light. If the objective is fully or overfilled with light, $NA = 0.85$ and $d = 1.3$ μm . The diameter of the laser beam entering the objective was ~ 2 mm. In this case $NA = 0.21$ and $d = 26$ μm , which is close to the depth of field I observed experimentally. The larger the depth of field, the stronger the fused silica and PDMS peaks will be in spectra of the contact. To improve the depth resolution we needed to expand the laser beam. Therefore we designed a support cage for a beam expander and inserted it between the Holoprobe sampling accessory and the main body of the microscope, as shown in figure 8. The support cage employed finely threaded screws to control the tilt and pitch of the beam expander. A $5\times$ beam expander (BE05M-B, Thor Labs) was connected to an xy positioning stage (ST1XY-S/M, Thor Labs) within the support cage.

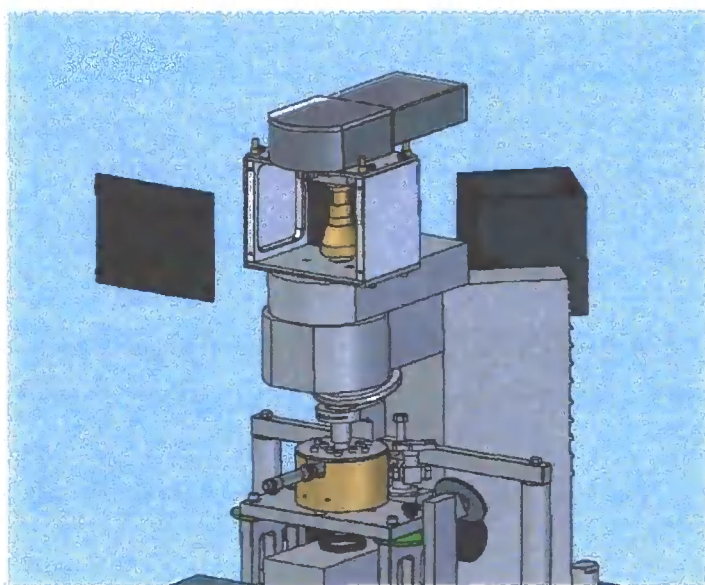


Figure 8. CAD image of the Raman microscope with the custom-built beam expander cage in place. Image created by C. Marriott, Unilever Colworth.

The normalized intensity of the 1053 cm^{-1} peak from a glycerol solution collected with the laser beam expanded prior to the long working distance oil immersion objective is also shown in figure 7. The depth resolution has been improved from \sim

35 μm to $\sim 8 \mu\text{m}$. The image of the laser spot on the sample overfills the pinhole, so the depth resolution could be improved further with a smaller pinhole, but at the cost of reduced signal. I decided that this depth resolution was sufficient for the experiments on the tribology-Raman rig.

The sigmoidal shape of the depth resolution in figure 7, $F(z)$, can be described by the convolution of the laser focus kernel $K(a)$ with the planar interface, $H(a)$, given by

$$F(z) = \int_{-\infty}^{\infty} P(a)K(z-a)da \quad (3)$$

where $H(a)$ is the Heaviside step function

$$H(a) = \begin{cases} 1 & a > R \\ 1/2 & a = R \\ 0 & a < R \end{cases} \quad (4)$$

where R is the position of the interface and I approximate $K(a)$ by a Gaussian profile, in accordance with [21].

$$K(a) = \frac{1}{\sigma} e^{-\frac{\pi^2 a}{\sigma^2}} \quad (5)$$

where σ is the standard deviation of the Gaussian distribution. Equations 3, 4 and 5 were fitted to the experimental profile by least-squares fitting with $\sigma = 9.6 \mu\text{m}$.

7.5 Single phase lubricants

I took Raman spectra and made tribology measurements of a single phase system in the contact before investigating the properties of emulsions as lubricants. In figure 9, the friction coefficient between a PDMS ball and a hydrophilic fused silica window is plotted as a function of $U\eta$ for a series of aqueous solutions. The viscosities of the lubricants at room temperature are given in table 1.

Lubricant	η / mPa s
Water	1.0
52 wt% glycerol (aq)	6.7
84 wt% glycerol (aq)	84
92 wt% glycerol (aq)	380
90 wt% corn syrup (aq)	1500
95 wt% corn syrup (aq)	6900

Table 1. Dynamic viscosities of the lubricants used to construct the Stribeck master curves in figures 8 and 9. Viscosities measured by Phil Houston, Unilever R&D, Colworth.

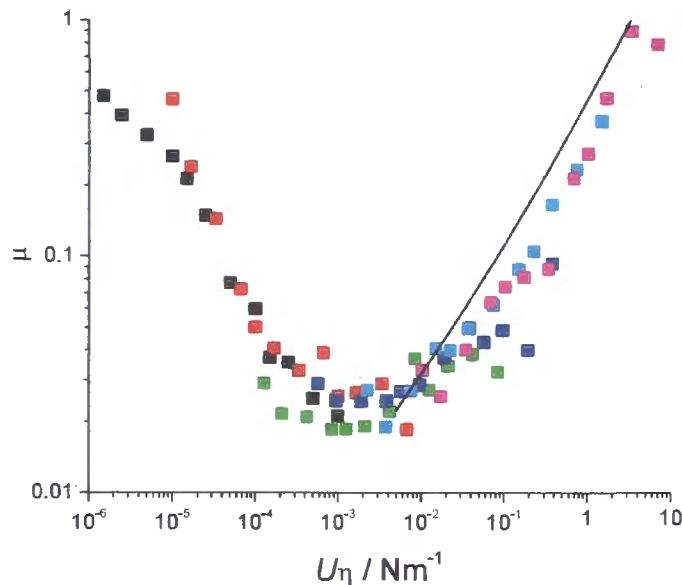


Figure 9. Stribeck curve of the coefficient of friction between a hydrophilic fused silica window and a PDMS ball plotted against the product of the entrainment velocity, U , and the dynamic viscosity, η . (■) Water, (■) 52 %, (■) 84 %, (■) 92 % glycerol (aq), (■) 90 %, (■) 95 % corn syrup (aq). Solid line: equation 6.

The values of μ from the different lubricants all map onto a single master curve. At $U\eta > 10^{-2}$, the friction coefficient rises monotonically and the contact is in the EHL regime. Below this value of $U\eta$, the contact is in the mixed regime. For this

hydrophilic–hydrophobic tribopair the boundary region is not reached for the values of $U\eta$ accessible on the MTM with aqueous solutions. This behaviour has been observed previously by Bongaerts *et al.* for the contact between hydrophobic PDMS (water contact angle in air, $\theta \approx 100^\circ$) and PDMS rendered less hydrophobic by exposure to oxygen plasma ($\theta \approx 42^\circ$) [14]. They suggested that in a hydrophobic contact the water can be fully excluded at low $U\eta$, leading to a high friction coefficient with a value close to the friction coefficient for a dry contact. In contrast, in a hydrophilic contact pockets of water remain trapped between the rough surfaces, aiding lubrication. Also shown on the graph as a solid line is the theoretical friction coefficient calculated from the relationship determined by de Vicente *et al.* from a power law fit to numerical results [4]:

$$\mu = SRR \left(3.8 \bar{U}^{0.71} \bar{W}^{-0.76} + 0.96 \bar{U}^{0.36} \bar{W}^{-0.11} \right) \quad (6)$$

where $\bar{U} = \frac{U\eta}{E'R'}$ and $\bar{W} = \frac{W}{E'R'^2}$ are the dimensionless speed and load parameters,

respectively. E' is the reduced Young's modulus, given by $\frac{1}{E'} = \frac{(1-\nu_1^2)}{E_1} + \frac{(1-\nu_2^2)}{E_2}$,

where ν is Poisson's ratio and E is the Young's modulus for the substrates. R' is the

reduced radius, given by $\frac{1}{R'} = \frac{1}{R_1} + \frac{1}{R_2}$. The theoretical model overestimates the

friction coefficient by a factor of ~ 1.5 but predicts the correct slope.

In figure 10, the friction coefficient between a PDMS ball and a hydrophobic fused silica window is plotted as a function of $U\eta$ for the same series of aqueous solutions. A curve representing a fit to the data from the hydrophilic–hydrophobic tribopair in figure 9 is also shown as a broken line. In the EHL regime the friction coefficient is independent of the hydrophobicity of the fused silica window. However, the behaviour in the mixed regime is markedly different: the mixed regime only lasts for $10^{-4} < U\eta < 10^{-2}$ and a plateau is observed at $U\eta < 10^{-4}$. This plateau is characteristic of the boundary region. The high value of the friction coefficient in the boundary region is likely due to the lubricant being completely excluded from the contact and the adhesive nature of PDMS on glass [14].

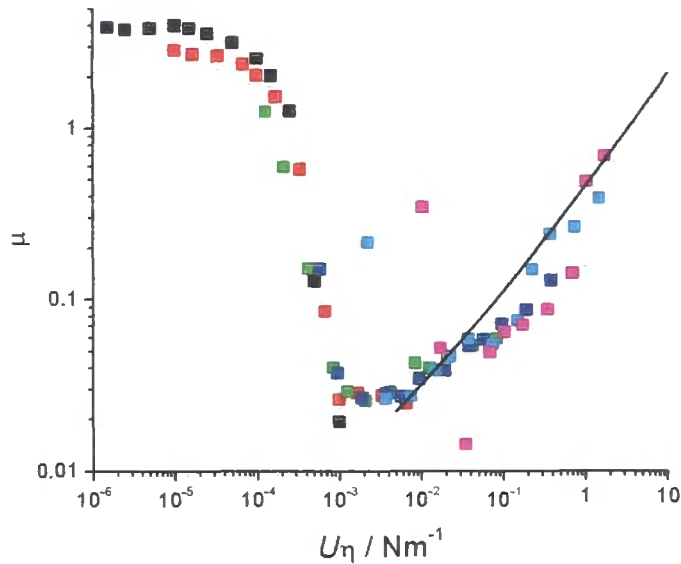


Figure 10. Stribeck curve of the coefficient of friction between a hydrophobic fused silica window and a PDMS ball plotted against the product of the entrainment velocity, U , and the dynamic viscosity, η . (■) Water, (■) 52 %, (■) 84 %, (■) 92 % glycerol (aq), (□) 90 %, (■) 95 % corn syrup (aq). Solid line: equation 8.

The refractive indices of fused silica, PDMS, glycerol and water at 785 nm are 1.454 [22], 1.43 [23], 1.467 [24] and 1.328 [25], respectively. Consequently there is very little refractive index contrast between PDMS, fused silica and concentrated glycerol solutions and it is difficult to see the contact with conventional brightfield microscopy. However, for $U\eta > 10^{-2}$, a cavitation region forms beyond the contact outlet which can be seen. In this region the pressure in the fluid is either very low or negative which leads to the formation of cavitation fingers. Examples of these fingers are shown in figure 11. The cavitation region has also caused the lubricant film to dewet the fused silica window beyond the contact at $U = 500 \text{ mm s}^{-1}$

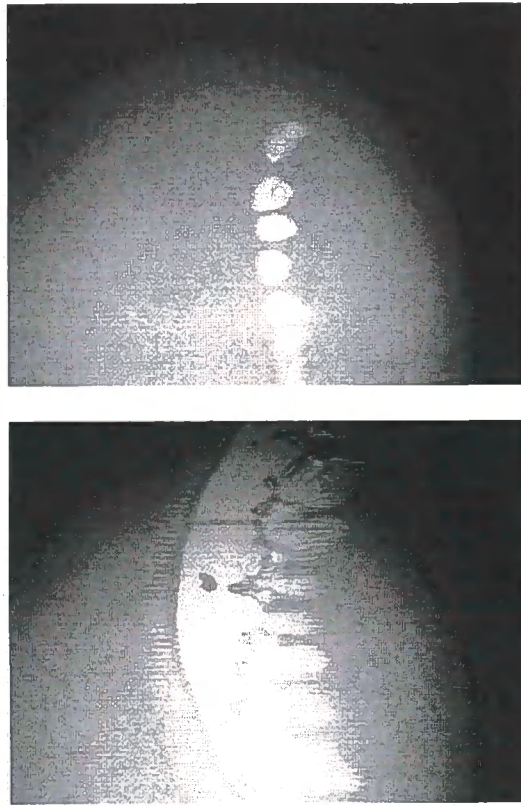


Figure 11. Brightfield images of 85 wt% glycerol (aq) in a soft tribological contact with a 5× objective. Left: $U = 50 \text{ mm s}^{-1}$, right: $U = 500 \text{ mm s}^{-1}$. Image size is $\sim 1.5 \text{ mm} \times 1 \text{ mm}$.

The Raman spectra of glycerol, the PDMS ball and the fused silica window in the fingerprint region are shown in figure 12 and the glycerol and PDMS modes are assigned in tables 2 and 3.

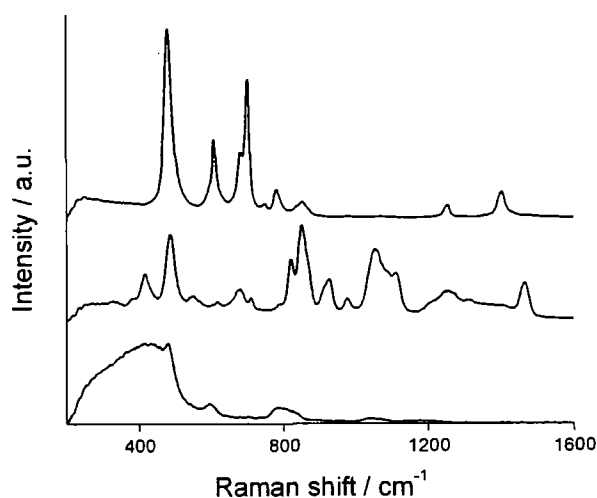


Figure 12. Raman spectra of PDMS (top), glycerol (centre), and quartz (bottom) in the fingerprint region.

Raman shift / cm^{-1}	Mode assignment
821, 850	C–C–O in phase stretch
1059	Primary alcohol C–C–O out of phase stretch
1114	Secondary alcohol C–C–O out of phase stretch
1249	CH ₂ wag
1311	CH ₂ twist
1466	CH ₂ scissor

Table 2. Normal mode assignment of bands in the Raman spectrum of glycerol.

Raman shift / cm^{-1}	Mode assignment
488	Si–O–Si symmetric stretch
688	Si–CH ₃ symmetric rock
709	Si–C stretch
790	CH ₃ asymmetric rock and Si–C antisymmetric stretch
861	CH ₃ symmetric rock
1263	CH ₃ symmetric bend
1413	CH ₃ antisymmetric bend

Table 3. Normal mode assignment of bands in the Raman spectrum of PDMS [15].

Although there will not be any changes to the composition in the contact, it is still instructive to take spectra of a single phase system in the contact. As well as mapping the shape of the contact, it proved possible to map the thickness of the contact with Raman spectroscopy. The poor optical contrast meant that it was very difficult to determine visually the position of the microscope focus within the contact. However, the relative intensities of the PDMS and glycerol peaks do give the shape of the contact. The objective was focused at a constant height below the window such that the focus was within the PDMS ball. The normalized intensities of the 1053 cm^{-1} glycerol peak and the 616 cm^{-1} PDMS peak are plotted as a function of x and y in figure 13, where x is the coordinate across the contact parallel to the axis of rotation and y is the coordinate perpendicular to the axis of rotation and consequently runs from the inlet to the outlet of the contact.

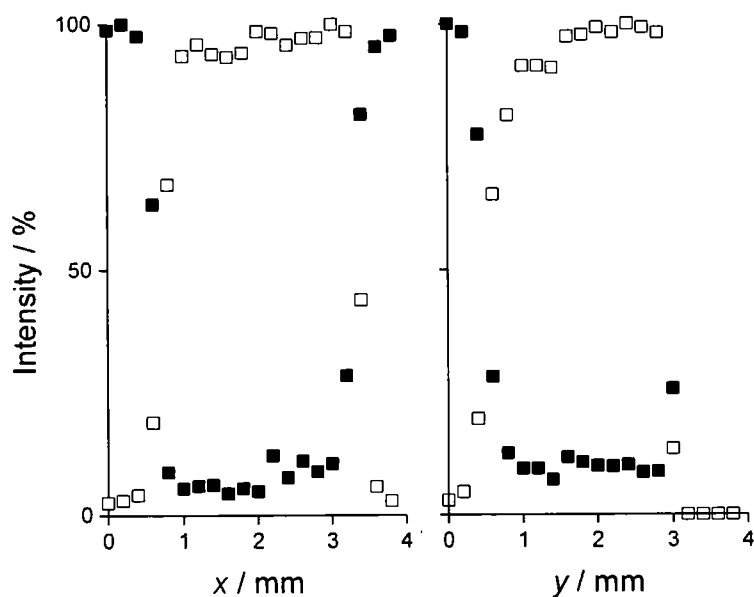


Figure 13. The normalized intensities of the 1053 cm^{-1} glycerol peak (■) and the 616 cm^{-1} PDMS peak (□) are plotted as a function of x and y . 92 wt% glycerol solution. $U = 1000\text{ mm s}^{-1}$.

The edges of the contact are immediately apparent even with this coarse approach. This technique was used to find the contact in all future work. At $y > 3\text{ mm}$ the signal

from both species is ~ 0 . Beyond this position is the cavitation region. In practice I found that any air bubbles in the lubricant congregated and coalesced in this low-pressure region and over time a macroscopic air bubble was formed. Consequently there was no signal in this region.

I found that at low U and for thin films the laser melted the PDMS ball as the heat from the laser does not dissipate quickly. The PDMS residue fused to the window and fluoresced strongly. This effect can be limited by reducing the laser power at the cost of significantly reducing the signal. However, the laser intensity scales linearly with the laser power, whereas the film thickness varies exponentially with U so this solution does not allow Raman spectra to be taken at significantly lower speeds. The normalized intensity of the 1053 cm^{-1} glycerol peak from a representative depth profile through the contact is plotted as a function of z in figure 14.

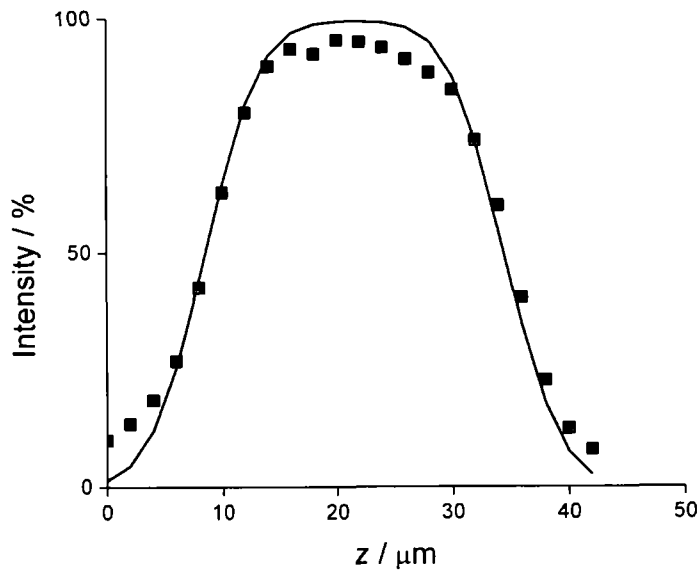


Figure 14. Normalized intensity of the 1053 cm^{-1} glycerol peak as a function of z into a 96 wt% glycerol solution in a soft EHL contact. $U = 250\text{ mm s}^{-1}$. The fit to the data with equations 3, 5 and 9 is shown as a solid line.

In the contact there are two interfaces, so the profile can be described with a top hat function, according to

$$H(a) = \begin{cases} 1 & R_1 < a < R_2 \\ 1/2 & a = R_1, R_2 \\ 0 & a < R_1, a > R_2 \end{cases} \quad (7)$$

where R_1 and R_2 are the positions of the two interfaces. The depth profile through the contact was fitted by least-squares and the thickness of the contact, $t = R_2 - R_1$, is plotted in figure 15 across the contact from the inlet to the outlet. The cavitation region lies at $y > 3$ mm.

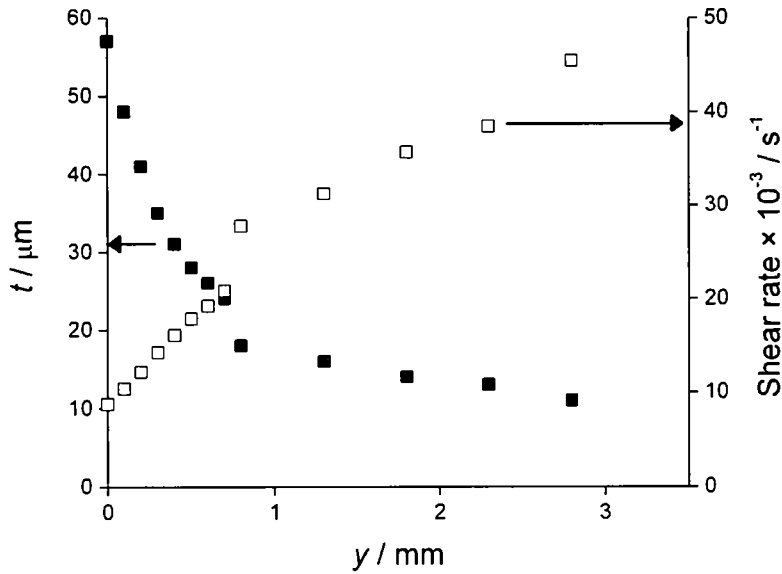


Figure 15. Thickness and shear rate of a 96 wt % glycerol film in a soft EHL contact. The fluid flows from left to right and the cavitation region lies at $y > 3$ mm. $U = 250$ mm s⁻¹.

The shear rate, $\dot{\gamma}_{yz}$, is defined as $\dot{\gamma}_{yz} = \frac{\partial v_y}{\partial z} + \frac{\partial v_z}{\partial y}$. In the contact $\frac{\partial v_y}{\partial z}$ is negligible, so

$\dot{\gamma}_{yz} = U/t$. The shear rates across the contact are also shown in figure 15. The shear stress in this isoviscous contact can also be calculated from the product of the viscosity and the shear rate because the pressures in the contact are too low to alter the viscosity. I also measured the thickness of the film in the contact as a function of $U\eta$ at constant x and y . The film thickness is plotted as a function of $U\eta$ in figure 16.

The theoretical central film thickness, h_c , and minimum film thickness, h_m , from ref [4] are also plotted in figure 16. These thicknesses are given by [4]:

$$h_c = 3.3R'\bar{U}^{0.60}\bar{W}^{-0.14} \quad (8)$$

$$h_m = 2.8R'\bar{U}^{0.66}\bar{W}^{-0.22} \quad (9)$$

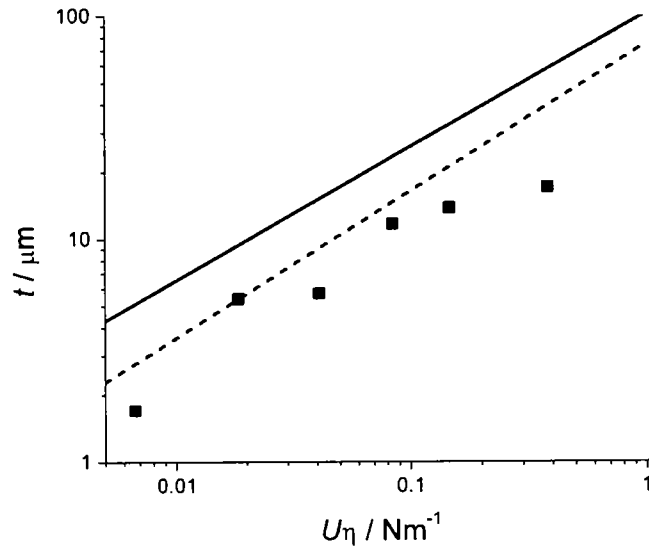


Figure 16. Film thickness plotted as a function of U_η . The theoretical central (solid line) and minimum film thicknesses (broken line) from ref [4] are also shown.

It is evident that the theoretical model overestimates the film thicknesses by a factor of $\sim 2-3$. It is not surprising therefore that the model overestimates the friction coefficient in figure 9, however the origin of this disagreement is unclear at the present time.

In anticipation of the work on emulsions presented below, I also took spectra of sunflower oil in the contact. Sunflower oil is a complex mixture of various fatty acids in predominantly triglyceride form with $\sim 68\%$ linoleic acid ($C_{18:2}$) and $\sim 19\%$ oleic acid ($C_{18:1}$) [26]. A representative spectrum is presented in figure 17 and the peaks are assigned in table 4.

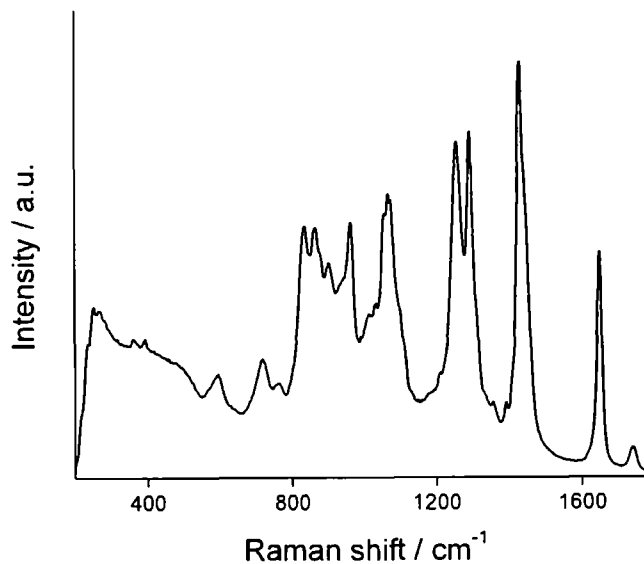


Figure 17. Raman spectrum of sunflower oil in the fingerprint region.

Raman shift / cm^{-1}	Mode assignment
727	CH_2 rock
840–970	C–C–O in phase stretch
1080	C–C–O out of phase stretch
1264	CH_2 wag
1302	CH_2 in phase twist
1440	CH_2 scissor
1658	C=C stretch
1747	C=O stretch

Table 4. Normal mode assignment of bands in the Raman spectrum of sunflower oil.

7.6 Emulsions

Still images taken from videos of an oil-in-water (O/W) emulsion in a PDMS–hydrophilic silica contact are shown in figure 18. The 1% Tween 60 solution aqueous phase and the sunflower oil phase were emulsified at a ratio of 4:1 by weight. Although the optical contrast is low, it is sufficient to distinguish the emulsion oil droplets approaching and receding from the contact. At this speed and for this lubricant it appears that there is a single phase pool close to the contact, as observed

by Yang *et al.* [11]. The frame rate of the video camera was not fast enough to capture video at higher U .

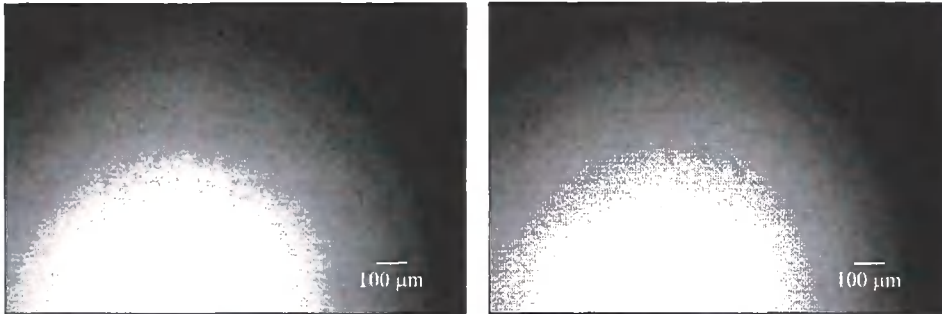


Figure 18. Sunflower oil-in-water emulsion in a tribological contact. The emulsion is comprised of 20% sunflower oil as the oil phase and is stabilized by 1% Tween 60. Left: contact outlet, right: contact inlet. $U = 1.5 \text{ mm s}^{-1}$. The surface of the ball is rotating from right to left. $5\times$ objective.

In figure 19A, the friction coefficient of an O/W emulsion comprised of 20% oil phase and 1% Tween 60 is plotted as a function of U . The friction coefficient of SFO and the aqueous master curve from figure 9 are also plotted in figure 19. The master curve has been plotted with a viscosity equal to the aqueous phase (1.5 mPa s). At $U \leq 50 \text{ mm s}^{-1}$, the friction coefficient of the emulsion follows the friction coefficient of neat SFO suggesting that there is only sunflower oil in the contact, whereas at $U \geq 250 \text{ mm s}^{-1}$ the friction coefficient of the emulsion follows the aqueous master curve, suggesting that the oil phase may be excluded from the contact at these speeds. At ($50 < U < 250$) mm s^{-1} , the friction coefficient behaves like neither phase.

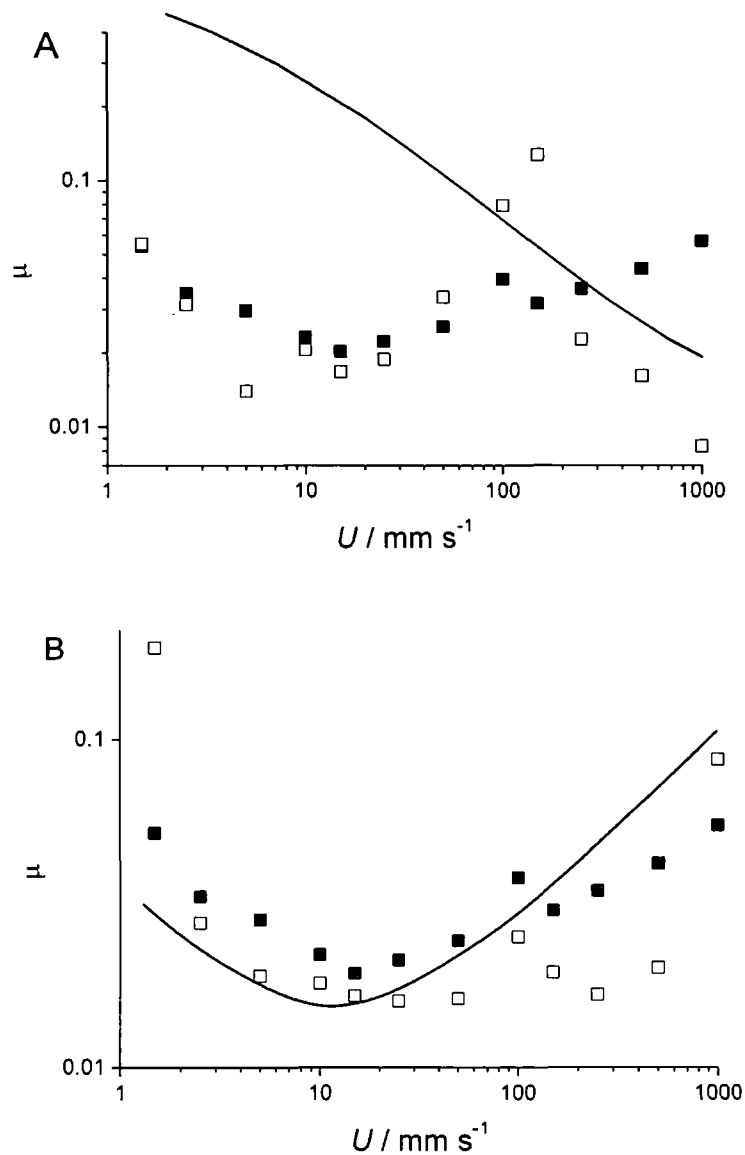


Figure 19. Friction coefficient of pure sunflower oil (■) and O/W emulsions (□) in a soft tribological contact. The emulsion is comprised of 20% sunflower oil as the oil phase and is stabilized by 1% Tween 60. (A) Aqueous phase = 20 wt% glycerol solution. (B) Aqueous phase = 92 wt% glycerol. The solid line is the master curve derived from figure 9.

In comparison, the friction coefficient of a 92 wt% glycerol O/W emulsion is plotted as a function of U in figure 19B. It is difficult to tell from this graph whether the

emulsion is behaving like the oil, the aqueous phase or neither. Raman spectroscopy should help to resolve this issue.

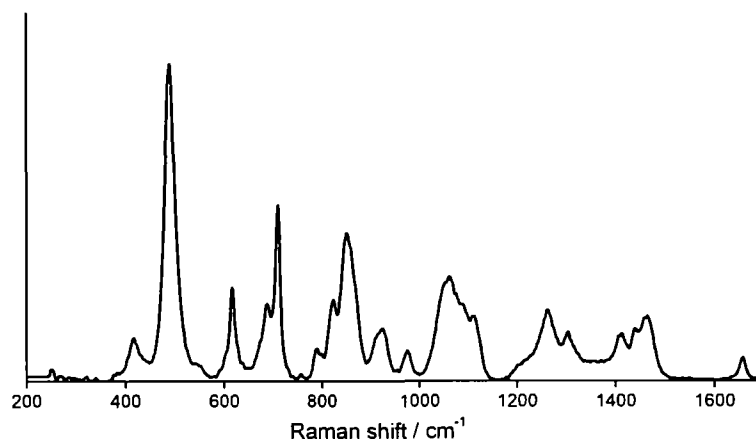


Figure 20. Raman spectrum of an O/W emulsion comprised of 20 wt% SFO in a 74 wt% glycerol–water solution, stabilized with 1 wt% Tween 60. $U = 1000 \text{ mm s}^{-1}$.

A representative Raman spectrum of an O/W emulsion comprised of 20 wt% SFO in a 74 wt% glycerol–water solution, stabilized with 1 wt% Tween 60 is plotted in figure 20. The bands can be readily ascribed to sunflower oil, glycerol or PDMS by comparison with the spectra in figures 12 and 17. The Tween 60 signal is too weak to show up on this scale. I determined the composition of the emulsion in the contact relative to the bulk by fitting a combination of the individual components to the emulsion spectrum. In figure 21 I have plotted the concentration of the oil phase of the emulsion in the centre of the contact as a function of entrainment velocity.

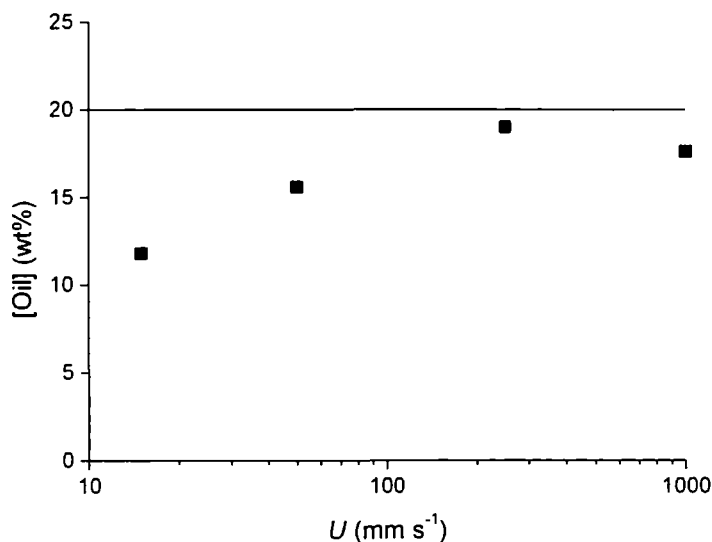


Figure 21. The oil concentration of the lubricant within the contact as a function of U . The lubricant is an O/W emulsion comprised of 20 wt% SFO in a 92 wt% glycerol–water solution, stabilized with 1 wt% Tween 60.

At low speeds, the oil concentration is lower within the contact than the bulk concentration of 20%. At $U = 15 \text{ mm s}^{-1}$, for example, the oil concentration is 12%. This observation suggests that at low speeds fewer oil droplets enter the contact, possibly due to the fact that the film thickness at low speeds is much smaller than the droplet size. To investigate this hypothesis further, I determined the droplet sizes in the emulsion by light scattering with a Malvern Mastersizer 2000. The volume-weighted mean, $D[4,3]$, of the droplets are given in table 5.

Glycerol concentration / wt%	$D[4,3] / \mu\text{m}$
40	4.7
52	3.6
60	2.4
76	2.7
92	1.3

Table 5. Volume-weighted mean, $D[4,3]$, of the oil droplets in oil-in-water emulsions with varying concentrations of glycerol in the continuous phase.

As a first approximation, I assume that the aqueous phase controls the viscosity of the emulsion in the contact and hence the thickness of the contact. Consequently $U \eta$ varies from 0.004 to 0.4 Nm⁻¹ in figure 21. From figure 16 I can estimate that the thickness of the contact for the emulsions in figure 21 varies from 1–20 μm. As the emulsion droplets are ~ 1 μm in diameter, this simple calculation supports my hypothesis that at low speeds the separation of the solid walls is sufficiently small to restrict the oil droplets from entering the contact. It would appear that the oil droplets behave like undeformable spheres. What is not observed here is a phase-inversion or even a complete breakdown of the emulsion within the contact, which would result in oil-dominated friction behaviour. Such behaviour has been reported previously, depending on the tribological conditions. For example de Vicente *et al.* [6] have found for unstabilized O/W emulsions (i.e., no surfactants are added for stabilisation) that the significantly more viscous of the two phases dominates the lubricated contact in terms of its friction, suggesting that only the most viscous phase is present within the contact. The viscosity ratio between the oil and aqueous phase for this emulsion is $\eta_{oil}/\eta_{aq} \approx 2$ i.e., the oil is slightly more viscous. Here, we do not observe an oil dominated contact, but rather an aqueous-phase dominated contact.

I also studied a different O/W emulsion with a larger viscosity ratio between the two phases $\eta_{oil}/\eta_{aq} \approx 14$. I took spectra of the contact at 500-μm intervals in the y direction to determine the composition of the contact from the inlet to the outlet. I analyzed these spectra with the procedure described above to obtain the composition profile within the contact. This profile is plotted in figure 22.

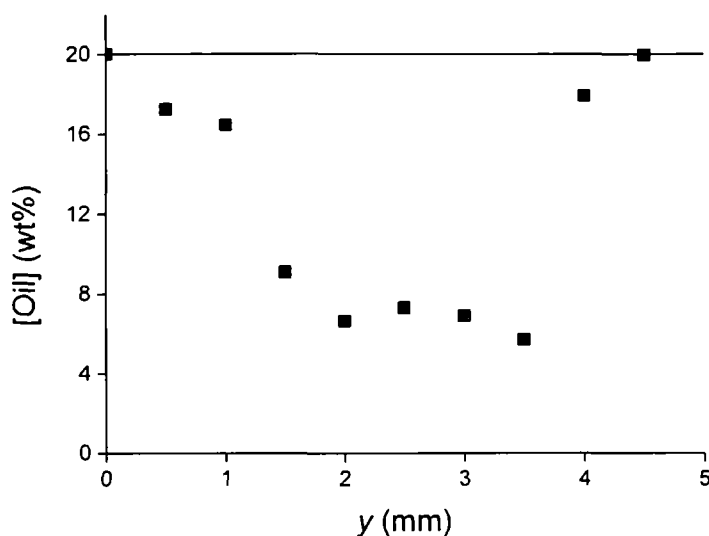


Figure 22. The oil concentration of the lubricant across the contact. The lubricant is an O/W emulsion comprised of 20 wt% SFO in a 52 wt% glycerol–water solution, stabilized with 1 wt% Tween 60. $U = 1000 \text{ mm s}^{-1}$.

Outside the contact the emulsion composition is equal to that of the bulk. However, within the contact, the oil concentration decreases to ~ 5 wt%, a significant reduction compared to the bulk concentration of 20 wt%. Again, emulsion breakdown is not observed at these conditions, even with a large viscosity ratio $\eta_{oil}/\eta_{aq} \approx 14$. I attribute the absence of rubbing-induced emulsion break-down to a combination of high sliding speed and the presence of a surfactant that stabilizes the emulsion. The surfactant significantly lowers interfacial tension, reduces droplet coalescence and facilitates droplet break up, which prevents a large pool of oil being formed at high rubbing speeds. Furthermore, the thickness of the lubricating film at these conditions is $\approx 2 \mu\text{m}$, which is of the order of the droplet size. These results indicate that fewer oil droplets enter the contact and instead they move around it. Another factor influencing emulsion break down is the hydrophobicity of the rubbing contact, which in this experiment was a mixed hydrophobic–hydrophilic contact. The formation of a large pool of oil will be easier against a hydrophobic surface than against a hydrophilic surface (assuming the oil phase wets PDMS).

There are two issues to overcome before Raman spectra of emulsions in the contact can be obtained across the full range of interest. First, the lubricating film must currently be thicker than $\sim 1 \mu\text{m}$ to give a reasonable Raman signal. In practice this restriction requires that the contact is in the EHL regime with $U\eta > 0.01 \text{ Nm}^{-1}$. A higher viscosity oil, such as castor oil, could be used to ensure the contact is in the EHL regime at a greater range of speeds and viscosity ratios between the continuous and dispersed phases. Second, the problem with the PDMS ball being burnt by the laser must be overcome. An alternative elastomer such as polyurethane may prove more resistant than PDMS.

7.7 Conclusion

During my three-month placement, I commissioned and developed a tribological Raman microscopy instrument that combines friction measurements with *in-situ* confocal Raman microscopy. We have demonstrated that friction data can be obtained throughout the boundary, mixed and EHL lubrication regimes. For the first time, it is possible to take Raman spectra and friction measurements simultaneously from complex lubricants. I obtained film thickness profiles of the lubricant within the contact in the full-film lubrication regime, without the need for reflective surfaces. Film thickness data provide the local shear-rate profile within the contact, which is valuable information when investigating lubrication by non-Newtonian lubricants. I found that the film thickness was smaller than numerical calculations predict, which we attribute to starvation of the lubricated contact. This conclusion is supported by the observed friction values in the EHL regime and visual observation of an air pocket at the outlet of the rubbing contact. This example shows that combining friction data, experimental film thickness data and visual inspection of the rubbing contact results in a much more complete picture of what occurs within the lubricating contact.

I also determined the composition of a model O/W emulsion within the contact from the Raman spectra. The composition depended on both the rubbing speed and the

location within the rubbing contact. A change of composition of the emulsion within the contact has major implications for the lubricating properties of soft surfaces by emulsions. Whether oil or an aqueous phase dominates the contact will determine much of the tribological properties. Furthermore, related aspects, such as cooling of the contact and the deposition of material onto the surfaces will depend crucially on the phase that is in direct contact with the rubbing surfaces. The ability to obtain friction forces, film thickness and composition will help enormously when trying to understand the lubricating properties of complex fluids.

References

- 1 J. Williams, *Engineering Tribology* 1st ed. (Cambridge University Press, Cambridge, 2005).
- 2 M. A. Malone, I. A. Appelqvist, and I. T. Norton, *Food Hydrocolloids* **17**, 763 (2003).
- 3 B. J. Hamrock, *Fundamentals of Fluid Film Lubrication* 1st ed. (McGraw-Hill, Inc., New York, 1994).
- 4 J. de Vicente, J. R. Stokes, and H. A. Spikes, *Tribol. Lett.* **20**, 273 (2005).
- 5 J. de Vicente, J. R. Stokes, and H. A. Spikes, *Tribol. Int.* **38**, 515 (2005).
- 6 J. de Vicente, J. R. Stokes, and H. A. Spikes, *Food Hydrocolloids* **20**, 483 (2006).
- 7 J. de Vicente, H. A. Spikes, and J. R. Stokes, *Trans. ASME, J. Tribology* **128**, 795 (2006).
- 8 H. A. Spikes, *Proc. Instn. Mech. Engr.* **213**, 335 (1999).
- 9 S. Bair, F. Qureshi, and M. Khonsari, *Trans. ASME, J. Tribology* **116**, 705 (1994).
- 10 S. Bair, F. Qureshi, and W. O. Winer, *Trans. ASME, J. Tribology* **115**, 507 (1993).
- 11 H. Yang, S. R. Schmid, R. A. Reich, and T. J. Kasun, *Trans. ASME, J. Tribology* **128**, 619 (2006).
- 12 P. M. Cann, M. Aderin, G. J. Johnston, and H. A. Spikes, in *Wear Particles, Proceedings of the 18th Leeds-Lyon Symposium on Tribology, Lyon, September 1991*, edited by D. Dowson (Elsevier, 1992).
- 13 S. Coulon, I. Jubault, A. A. Lubrecht, F. Ville, and P. Vergne, *Tribol. Int.* **37**, 111 (2004).
- 14 J. H. H. Bongaerts, J. R. Stokes, and K. Fourtouni, *Tribol. Int.* **40**, 1531 (2007).
- 15 S. C. Bae, H. Lee, Z. Lin, and S. Granick, *Langmuir* **21**, 5685 (2005).
- 16 D. A. Beattie, S. Haydock, and C. D. Bain, *Vib. Spectrosc.* **24**, 109 (2000).
- 17 T. Lubrecht, D. Mazuyer, and P. Cann, *Comptes Rendus De L'Academie des Sciences Serie IV Physique Astrophysique* **2**, 717 (2001).

- 18 N. J. Everall, *Appl. Spec.* **54**, 1515 (2000).
- 19 K. J. Baldwin and D. N. Batchelder, *Appl. Spec.* **55**, 517 (2001).
- 20 N. Everall, *Appl. Spec.* **62**, 591 (2008).
- 21 F. Garcia-Vicente, J. M. Delgado, and C. Rodriguez, *Phys. Med. Biol.* **45**, 645 (2000).
- 22 Melles Griot Catalogue
- 23 A. M. Cardenas-Valencia, J. Dlutowski, D. Fries, and L. Langebrake, *Appl. Spec.* **60**, 322 (2006).
- 24 J. Rheims, J. Koser, and T. Wriedt, *Meas. Sci. Technol.* **8**, 601 (1997).
- 25 J. E. Bertie and Z. Lan, *Appl. Spec.* **50**, 1047 (1996).
- 26 R. D. O'Brien, *Fats And Oils* 2nd ed. (CRC Press, Boca Raton, 2004).

